Report No. CG-D-27-96, I
DOT-VNTSC-USCG-96-2.1

PB97-134688

U.S. Coast Guard
1994 Oil Pollution Research Grants
Publications - Part I

U.S. Department of Transportation
Research and Special Programs Administration
John A. Volpe National Transportation Systems Center
Cambridge, MA 02142

FINAL REPORT
September 1996

This document is available to the U.S. public through the
National Technical Information Service, Springfield, Virginia 22161

Prepared for:

U.S. Coast Guard
Research and Development Center
1082 Shennecossett Road
Groton, Connecticut 06340-6096

REPRODUCED BY: NTIS
U.S. Department of Commerce
National Technical Information Service
Springfield, Virginia 22161

NOTICE

This document is disseminated under the sponsorship of the Department of Transportation in the interest of information exchange. The United States Government assumes no liability for its contents or use thereof.

NOTICE

The United States Government does not endorse products or manufacturers. Trade or manufacturers' names appear herein solely because they are considered essential to the objective of this report.

Technical Report Documentation Page

1. Report No. CG-D-27-96, I	PB97-134688
3. Recipient's Catalog No.	
4. Title and Subtitle: U.S. Coast Guard 1994 Oil Pollution Research Grants Publications - Part I	5. Report Date: September 1996
	6. Performing Organization Code: DTS-72
7. Author(s)	8. Performing Organization Report No.: R&DC 24/96, DOT-VNTSC-CG-96-2.1
9. Performing Organization Name and Address: U.S. Department of Transportation, Research and Special Programs Administration, John A. Volpe National Transportation Systems Center, Cambridge, MA 02142	10. Work Unit No. (TRAIS)
	11. Contract or Grant No.
12. Sponsoring Agency Name and Address: U.S. Coast Guard, Research and Development Center, 1082 Shennecossett Road, Groton, Connecticut 06340-6096	13. Type of Report and Period Covered: Final Report, August 1994 - September 1995
	14. Sponsoring Agency Code

15. Supplementary Notes

The R&D Center's technical point of contact is Kenneth Bitting, 860-441-2733.

16. Abstract

The Oil Pollution Research Grant Program was created by the Oil Pollution Act of 1990, P.L. 101-380 (OPA 90), 33 U.S. C. 28761(c)(8) and 2761(c)(9). The OPA established a regional research program and authorized those agencies represented on the Interagency Coordinating Committee on Oil Pollution Research, including the U.S. Coast Guard (USCG), to make grants to universities and other research institutions to perform research related to regional effects of oil pollution . The USCG established such a grant program, and the Volpe National Transportation Systems Center (Volpe Center), a component of the Research and Special Programs Administration of the Department of Transportation (DOT), was chosen to administer this program on behalf of the USCG.

In August 1994, the Volpe Center awarded nine one-year grants. Coast Guard funds were matched by funds from the university or non-profit research institution.

This report contains the final reports, presented in two parts, for research performed under these grants.

17. Key Words: oil pollution research, oil pollution grants	18. Distribution Statement: Document is available to the U.S. public through the National Technical Information Service, Springfield, Virginia 22161

19. Security Classif. (of this report)	20. SECURITY CLASSIF. (of this page)	21. No. of Pages	22. Price
UNCLASSIFIED	UNCLASSIFIED	230	

Form DOT F 1700.7 (8/72) Reproduction of form and completed page is authorized

FOREWARD

PUBLICATIONS OF THE U.S. COAST GUARD 1994 OIL POLLUTION RESEARCH GRANTS

On March 24, 1989 the EXXON VALDEZ ran aground on Bligh Reef in Prince William Sound, Alaska producing the largest oil spill in U.S. history. Following this event, the Coast Guard reexamined its mission needs and technology to formulate an R&D effort for the 1990's. Workshops were held within the Coast Guard and with other Federal agencies and private sector organizations to identify spill response needs and R&D efforts that would support those needs. One of the workshops was a U.S. Coast Guard sponsored Interagency Planning Workshop on oil spill research and development on September 26-27, 1989. This workshop exchanged information and initiated the development of a coordinated national plan for oil spill research and development under Title VII of the Oil Pollution Act of 1990.

The Oil Pollution Research Grant Program was created by the Oil Pollution Act of 1990, P.L. 101-380 (OPA 90), 33 U.S.C. 2761 (c)(8) and 2761 (c)(9). The OPA established a regional research program and authorized those agencies represented on the Interagency Coordinating Committee on Oil Pollution Research, including the U.S. Coast Guard (USCG), to make grants to universities and other research institutions to perform research related to regional effects of oil pollution. The USCG established such a grant program, and the Volpe National Transportation Systems Center (Volpe Center), a component of the Research and Special Programs Administration of the Department of Transportation (DOT), was chosen to administer this program on behalf of the USCG.

The Volpe Center mailed Grant Applications to about 145 universities and non-profit research institutions on December 21, 1993. The mailing list included institutions from all the Coast Guard regions. On March 7, 1994 the Volpe Center received 14 applications from four regions. These proposals were reviewed by the Volpe Center and the Coast Guard Research and Development Center and the recommendations forwarded to the Interagency Committee on Oil Pollution Research for approval. Nine one year Grants were awarded in August 1994. Coast Guard funds were matched by funds from the university or non-profit research institution.

This report contains the Final Reports for research performed under these Grants. The results are presented in two volumes. For further information contact Kenneth Bitting at the U.S. Coast Guard Research and Development Center, Groton, Conn . (860) 441-2733.

Additional copies of this document are available through the National Technical Information Service, Springfield, Virginia 22161.

PROTECTED UNDER INTERNATIONAL COPYRIGHT
ALL RIGHTS RESERVED.
NATIONAL TECHNICAL INFORMATION SERVICE
U.S. DEPARTMENT OF COMMERCE

METRIC/ENGLISH CONVERSION FACTORS

ENGLISH TO METRIC

LENGTH (APPROXIMATE)

1 inch (in) = 2.5 centimeters (cm)
1 foot (ft) = 30 centimeters (cm)
1 yard (yd) = 0.9 meter (m)
1 mile (mi) = 1.6 kilometers (km)

AREA (APPROXIMATE)

1 square inch (sq in, in^2) = 6.5 square centimeters (cm^2)
1 square foot (sq ft, ft^2) = 0.09 square meter (m^2)
1 square yard (sq yd, yd^2) = 0.8 square meter (m^2)
1 square mile (sq mi, mi^2) = 2.6 square kilometers (km^2)
1 acre = 0.4 hectare (ha) = 4,000 square meters (m^2)

MASS - WEIGHT (APPROXIMATE)

1 ounce (oz) = 28 grams (gm)
1 pound (lb) = .45 kilogram (kg)
1 short ton = 2,000 pounds (lb) = 0.9 tonne (t)

VOLUME (APPROXIMATE)

1 teaspoon (tsp) = 5 milliliters (ml)
1 tablespoon (tbsp) = 15 milliliters (ml)
1 fluid ounce (fl oz) = 30 milliliters (ml)
1 cup (c) = 0.24 liter (l)
1 pint (pt) = 0.47 liter (l)
1 quart (qt) = 0.96 liter (l)
1 gallon (gal) = 3.8 liters (l)
1 cubic foot (cu ft, ft^3) = 0.03 cubic meter (m^3)
1 cubic yard (cu yd, yd^3) = 0.76 cubic meter (m^3)

TEMPERATURE (EXACT)

°C=5/9(°F - 32)

METRIC TO ENGLISH

LENGTH (APPROXIMATE)

1 millimeter (mm) = 0.04 inch (in)
1 centimeter (cm) = 0.4 inch (in)
1 meter (m) = 3.3 feet (ft)
1 meter (m) = 1.1 yards (yd)
1 kilometer (km) = 0.6 mile (mi)

AREA (APPROXIMATE)

1 square centimeter (cm^2) = 0.16 square inch (sq in, in^2)
1 square meter (m^2) = 1.2 square yards (sq yd, yd^2)
1 square kilometer (km^2) = 0.4 square mile (sq mi, mi^2)
10,000 square meters (m^2) = 1 hectare (ha) = 2.5 acres

MASS - WEIGHT (APPROXIMATE)

1 gram (gm) = 0.036 ounce (oz)
1 kilogram (kg) = 2.2 pounds (lb)
1 tonne (t) = 1,000 kilograms (kg) = 1.1 short tons

VOLUME (APPROXIMATE)

1 milliliter (ml) = 0.03 fluid ounce (fl oz)
1 liter (l) = 2.1 pints (pt)
1 liter (l) = 1.06 quarts (qt)
1 liter (l) = 0.26 gallon (gal)
1 cubic meter (m^3) = 36 cubic feet (cu ft, ft^3)
1 cubic meter (m^3) = 1.3 cubic yards (cu yd, yd^3)

TEMPERATURE (EXACT)

°F=9/5(°C) + 32

QUICK INCH-CENTIMETER LENGTH CONVERSION

INCHES	0		1		2		3		4		5		
CENTIMETERS	0	1	2	3	4	5	6	7	8	9	10	11	12	13

QUICK FAHRENHEIT-CELSIUS TEMPERATURE CONVERSION

°F	-40°	-22°	-4°	14°	32°	50°	68°	86°	104°	122°	140°	158°	176°	194°	212°
°C	-40°	-30°	-20°	-10°	0°	10°	20°	30°	40°	50°	60°	70°	80°	90°	100°

For more exact and or other conversion factors, see NIST Miscellaneous Publication 286, Units of Weights and Measures. Price $2.50. SD Catalog No. C13 10286.

Updated 8/1/96

TABLE OF CONTENTS

Part 1

Section Page

A HYDRODYNAMIC MODEL OF OIL CONTAINMENT BY A BOOM: PHASE I 1
Stephan Grilli, Z. Hu, and M.L. Spaulding, University of Rhode Island

1. Introduction and Literature Review 5
2. General Equations for the Dynamics of Vortex Sheets 26
3. Equations for Numerical Model 38
4. Model Test and Validation 52
5. Conclusions and Future Developments 68
6. Bibliography 71

DEVELOPMENT OF A RAPID CURRENT CONTAINMENT BOOM: PHASE I 75
M. Robinson Swift, Barbaros Celikkol, Philip Coyne, University of New Hampshire

1. Introduction 77
2. Concept Development 82
3. Oil Containment Performance Testing 91
4. Theoretical Considerations 98
5. Velocity Distribution 102
6. Flexible 3-Dimensional Physical Models 106
7. Summary and Conclusions 112
8. References 113

SOURCE IDENTIFICATION OF OIL SPILLS BASED ON THE ISOTOPIC COMPOSITION OF INDIVIDUAL COMPONENTS IN WEATHERED OIL SAMPLES 115
R. Paul Philp, University of Oklahoma

1. Summary 117
2. Introduction 118
3. Experimental 120
4. Results and Discussion 121
5. Conclusions 128
6. References and Figures 130

PREVENTING OIL SPILLS BY EVALUATING, MONITORING, AND MANAGING PORT AND WATERWAY RISK 145
John R. Harrald, The Louisiana State University National Ports and Waterways Institute

1. Introduction 147
2. Risk and "Acceptable Risk" 148
3. Risk Scenarios and System States 148

TABLE OF CONTENTS (cont.)

Part 1

Section Page

1. A System Based Risk Assessment Methodology 153
2. Conclusions 166
3. Appendix 1 Evaluating and Monitoring Waterway Risk in the Port of New Orleans: Phase II 168

Part 2

Section Page

EFFECTS OF THE WATER ACCOMMODATED FRACTION OF CRUDE OIL AND DISPERSED OIL ON THE EARLY LIFE STAGES OF TWO MARINE SPECIES 223
Michael M. Singer, Ronald Tjeerdema, University of California

1. Introduction 226
2. Specifications of Standard Test Solution Preparation Protocol for Water-Accommodated Fractions (WAFs) of Oil 228
3. Specification of Standard Test Preparation Protocol for Chemically Dispersed Oil (CDO) 237
4. Analytical Methods 242
5. Toxicity Testing 255
6. Appendix 1 Draft Protocol for Preparation of a Water-Accommodated Fraction of Crude Oil 271
7. Appendix 2 Draft Protocol for Preparation of Chemically Dispersed Crude Oil 273

INFLUENCE OF DISPERSANTS ON PETROLEUM BIOAVAILABILITY WITHIN A MARINE FOOD CHAIN 277
Martha F. Wolfe, Ronald Tjeerdema, University of California

1. Introduction 281
2. Materials and Methods 285
3. Results 292
4. Discussion 296
5. Conclusions 300
6. Appendix 305

TABLE OF CONTENTS (cont.)

Part 2

Section Page

PETROLEUM PC-BASED SHIPBOARD PILOTING EXPERT SYSTEM (SPES) 321
Martha Grabowski, Rensselaer Polytechnic Institute

1. Introduction 324
2. Functional Requirements 326
3. Architecture 329
4. Hardware Environment 331
5. Software Environment 332
6. Interface Concept 332
7. Operational Example 334
8. Phase 1 Design and Development 336
9. Comparison of PC-Based SPES to its Predecessors 341
10. Future Work and Issues to be Considered 342

DECISION SUPPORT TECHNOLOGY FOR OIL SPILL RESPONSE CONFIGURATION PLANNING 347
Roberto DeSimone, SRI International

1. Introduction 350
2. Spill Response Planning Systems 353
3. Dynamic Replanning 356
4. Knowledge-Base Maintenance 362
5. Conclusions 366
6. Appendix A - Screen Displays for IMO and VNTSC Demonstrations 368

OIL SPILL PREVENTION THROUGH THE IMPROVED MANAGEMENT OF HUMAN ORGANIZATION ERRORS IN THE OPERATIONS OF TANKERS AND BARGES 389
Karlene H. Roberts, University of California

A HYDRODYNAMIC MODEL OF OIL CONTAINMENT BY A BOOM: PHASE I

Stephen Grilli, Z. Hu, and M.L. Spaulding, University of Rhode Island

Abstract

This report presents results obtained at the University of Rhode Island, Department of Ocean Engineering, as part of a research project titled : "A hydrodynamic model of oil containment by a boom : Phase I". This project was supported by Grant No. DTRS-5794-G-00076 of the Department of Transportation (United States Coast Guards District No. 1) FY 1994 Oil Pollution Research Grant Program. A 50% budget match was provided by the University of Rhode Island.

This project officially started on August 15th, 1994, originally for a period of one year, but was extended until November 15th, 1995 due to a late start. A second year grant was obtained as part of the same program with FY 1995 funding and is currently in progress. This report only covers developments and computations carried out during the first year of the project, using a numerical model hereafter referred to as *Phase I model.*

An extensive literature review was first conducted for problems of interfacial instabilities between two fluids and, more specifically, for oil containment failure problems. Based on this review, a hierarchy of modeling strategies was proposed both for this project and for its possible extensions. These are hereafter referred to as Phase I, II and III models. Phase I model was developed, implemented, and tested as part of the FY94 project. The Phase II model is being developed as part of the FY95 project. A summary of the literature review and proposed modeling strategies is given in Chapter 1.

The Phase I model is based on using piecewise-constant vortex sheets (VS) to represent the dynamics of the oil-water interface in a contained oil slick. Both finite and semi-infinite VS's are used in the model. Biot-Savart's law is used to calculate flow velocities induced by vorticity distributions in the VS's. Self-induced velocity contributions of VS elements are explicitly calculated in the model. This represents a significant improvement compared to most earlier approaches proposed for modeling interfacial instability using VS's. An evolution equation is derived for updating VS's vorticity which includes the effects of inertia, gravity, oil and water density differences, and surface tension at the interface. VS dynamics equations used in Phase I model are detailed in Chapter 2.

Higher-order modeling of the VS's geometry is introduced, based on 4th-order sliding polynomials and cubic spline elements, to accurately calculate tangential derivatives needed along VS's for expressing the evolution equation. Vortex regridding techniques are introduced and tested in the model to control model resolution in specific interfacial regions. Both implicit and explicit time updating schemes are developed, implemented, and tested for calculating new positions and vorticity of VS's at a later time. In the model, the initial quasi-steady shape of the oil slick is calculated based on satisfying both kinematic and dynamic conditions along the interface, for a flow velocity below the critical threshold. The numerical implementation of the Phase I model is detailed in Chapter 3.

Chapter 4 presents application cases used to test and validate the model. The idealized case of a periodic Kelvin-Helmholtz instability is first presented to test and validate the principal numerical algorithms. The pure headwave instability case (i.e., without a boom) is then presented. Model calculations are found to be both stable and accurate, without need

for smoothing or for other transformations of model outputs often used in earlier studies. In all cases, computations of interfacial instabilities can be pursued for a longer time than with earlier approaches. Computational results are qualitatively similar to other published material.

Applications of the model to more realistic cases for which experimental data is available or will be performed, will be addressed in Phase II of this project.

Chapter 1

Introduction and literature review

The present project is aimed at developing a hydrodynamic model of *oil containment* by a boom and to use the model to investigate oil containment failure mechanisms identified and studied in both the research and professional community over the past 25 years. In the objectives originally proposed for this project, it was envisioned that this model and its future improvements would help us gain fundamental insight into oil containment failure mechanisms and outline strategies and methods to limit the occurrence or the intensity of these failures in actual field situations. Due to both its more catastrophic nature and its dominance for high viscosity oils found in actual spills, the failure mode referred to as *critical accumulation* was selected as the main object of the study. Three technical tasks were proposed : (i) numerical model selection and design; (ii) model testing and validation; and (iii) application to critical accumulation failure.

Task (i) was achieved by conducting an extensive review and analysis of the oil containment literature, including theoretical, analytical, and numerical aspects (Subramanya and Grilli, 1994). At the conclusion of this review, a tentative numerical modeling strategy was identified, hereafter referred to as the *Phase I model* and a hierarchy of models was also proposed for future developments (hereafter referred to as Phase II and III models).

In this report, we present key elements of the literature review in Chapter 1. In Chapters 2 and 3, we detail and discuss equations and numerical procedures selected for the implementation of the Phase I model. Finally, in Chapter 4, we conduct the validation and testing of the Phase I model (Task (ii)) both for a purely interfacial instability problem (periodic Kelvin-Helmholtz instability) and for a headwave instability (i.e., without a boom). Detailed results for more realistic problems including critical accumulation failure of oil containment by a boom (Task (iii)) will be addressed in Phase II of this project, using an improved version of the model [1]. Preliminary qualitative results, however, are given in Section 5 that illustrate computations with the present model for a case involving both a headwave instability and a boom.

[1] It was indeed found while conducting this study that a more accurate numerical model than originally anticipated is needed to realistically address such problems.

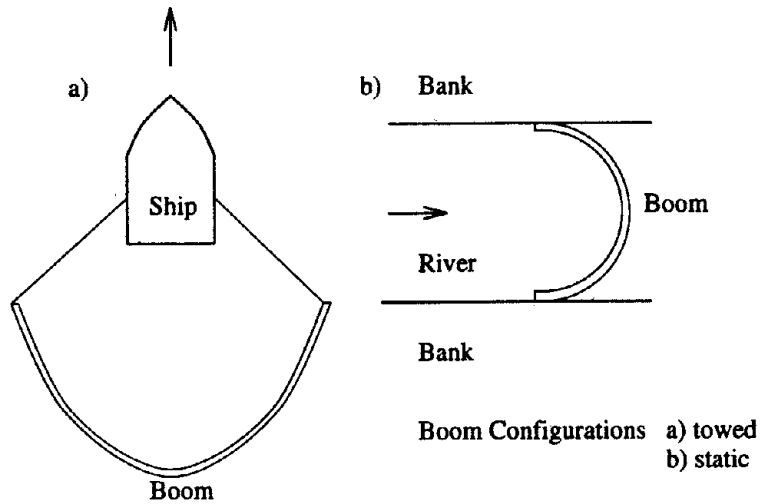

Figure 1.1: Planview of typical set-up for oil containment by : (a) a towed boom (ocean); or (b) a static boom (river).

1.1 Overview of the Problem

Oil booms or barriers are one of the most commonly used techniques to collect and contain oil on the sea surface, or to protect specific areas against slick spreading. In the collecting mode, such floating boom systems are usually set–up on the free surface in a U configuration and towed towards the oil slick.

The containment of oil by a boom is illustrated by the sketches in Fig. 1.1 which correspond to both an *ocean situation* in which a boom is towed by a boat at speed U over an essentially non-moving water mass (zero current), and a *river situation* in which a fixed boom is placed across a river flow with current U. In both cases, the boom takes a catenary shape and oil accumulates inside the boom. Maximum accumulation of oil occurs at the catenary's apex where maximum relative water velocity also occurs. Considering this and the small curvature of the boom geometry around the apex point, it is acceptable as a first approximation to simplify and analyze this essentially three-dimensional problem as a *two-dimensional* one in the vertical plane intersecting the boom at the catenary's apex (Fig. 1.2). It is also acceptable to assume that, for both cases in Fig. 1.1, the boom does not move and the water flows under the boom at a velocity U, equal to the relative boom-water velocity.

In order to collect as much oil as possible in the shortest possible time, it is desirable to have a tow velocity as large as possible. Various hydrodynamic instabilities at the oil–water interface, however, contribute to a fairly low practical limit on the tow velocity, on the order of 0.5 m/s.

For the idealized problem sketched in Fig. 1.2, observations show that interfacial waves start developing at the oil–water interface for relative current speeds, $U > U_{cr} \simeq 0.15$ m/s. For larger speed, these waves grow unstable and, in most cases, lead to substantial

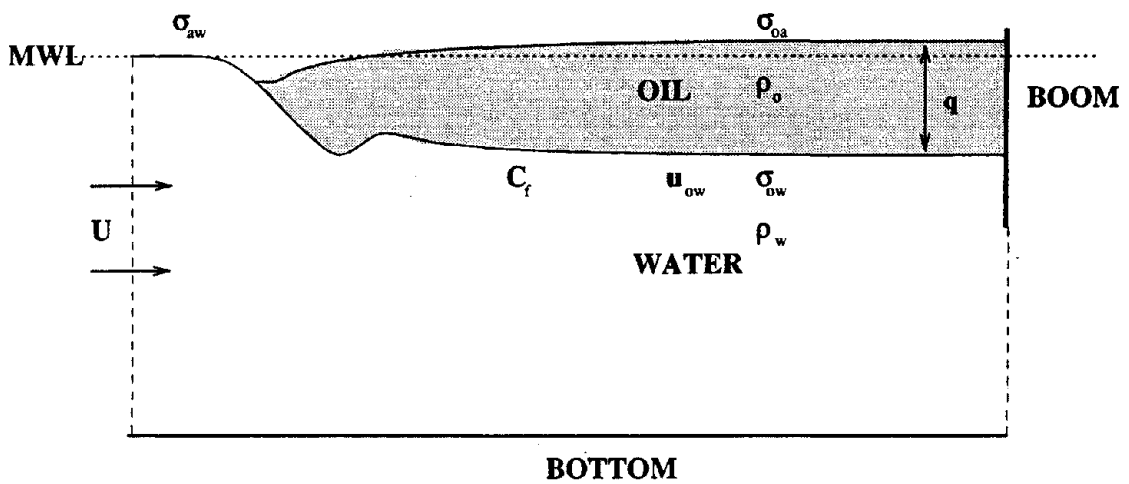

Figure 1.2: Sketch for initiation of oil containment failure by *critical accumulation*, with mention of important parameters : U, oil-water relative current velocity; $\mathbf{u}_{ow}$, oil-water relative velocity; ρ_o, ρ_w, oil and water density, respectively; σ_{ow}, σ_{oa}, σ_{aw}, interfacial tension coefficients for oil-water, oil-air, and air-water, respectively; C_f, oil-water interfacial friction coefficient; q, oil slick depth at the boom; MWL, Mean Water Level.

or even total loss of oil by entrainment of oil particles under the boom (e.g., Wicks, 1969; Wilkinson, 1972,1973; Lau and Kirchifer, 1974; Agrawal and Hale, 1974). In the literature, such instabilities are referred to as *boom containment failure modes* and three main types of containment failures have thus far been identified. These are defined in the following,

- **Drainage Failure** An increase in relative oil-water velocity U leads to an increase in interfacial friction stresses, causing a shortening and a thickening of the slick. An increase in slick thickness beyond the barrier draft d leads to drainage failure.

  Cross and Hoult (1971) studied the steady–state profiles of contained oil slicks and formulated an equation for the maximum slick length l as a function of barrier draft d,

  $$l = \frac{156.25\, g\,(1-s)}{U^2}\, d^2 \tag{1.1}$$

  where, $s = \rho_o/\rho_w$ (ρ_o being the oil density and ρ_w the water density). This equation is applicable only for low current speeds and smooth oil-water interfaces. If slick length is larger than l, containment failure will occur by drainage under the boom.

  For larger current speed, the oil-water interface is no longer smooth (see below) and the interfacial friction coefficient C_f increases. For such cases, Delvigne (1989) finds empirically that maximum slick length depends on oil volume Q as, $l \propto Q^{2/3}$.

- **Entrainment Failure** For high relative oil–water velocities and low viscosity oils ($\nu_o < 3,000$ cs), large interfacial stresses occur and induce shear instabilities of the

oil-water interface. Such instabilities are characterized by the formation of small fast-moving interfacial waves which, for sufficiently large U (on the order of 0.25 m/s), may become unstable and break, and lead to subsequent entrainment of oil droplets in the underlying flow. The droplets either reattach to the slick (if the slick is long enough) or pass under the barrier, leading to *progressive* containment failure by droplet entrainment.

Significant work on droplet entrainment was done by Agrawal and Hale (1974), Wilkinson (1970), and Leibovich (1976).

Note that drainage and entrainment failure may simultaneously occur in some situations.

- **Critical Accumulation** Prior to Delvigne's (1989) experiments, entrainment failure was thought to be the primary dynamic failure mode for contained oil slicks. Delvigne, however, showed that for oils with large viscosities, $\nu_o \geq 3,000$ cs, another, more catastrophic, failure mechanism occurs at a lower velocity U than the other two modes. Previous studies did not reveal this failure mechanism because the oil viscosities used in the experiments were too low.

  In this failure mode, referred to as *critical accumulation*, the oil–water interface, when exposed to a relative oil–water flow velocity exceeding a certain critical velocity, $U_{cr} \simeq 0.15$ m/s, develops slow-moving large scale oscillations which eventually cause all of the oil to escape under the barrier, *independent* of barrier draft d.

  A more detailed analysis of Delvigne's experiments reveals that critical accumulation is characterized by the formation of a headwave at the front of the slick (Fig. 1.3) which grows in amplitude as a function of time and propagates downstream towards the boom, causing the slick to become both shorter and thicker and eventually leading to almost total loss of oil under the boom. Quite remarkably, for large enough viscosity, Delvigne's experiments showed a lack of dependence of U_{cr} on oil viscosity ν_o, density difference, $\Delta\rho_{ow} = \rho_w - \rho_o = \rho_w(1 - s)$, oil volume Q, and water depth h.

  Finally, it should be emphasized that, due to weathering and emulsification, real slicks can quickly reach large viscosities, on the order of 10,000 cs (e.g., Johnston *et al.*, 1993) and, hence, their containment by a boom is likely to fail by critical accumulation, for tow velocities beyond the critical value.

Of the three failure modes mentioned above, for high viscosity oils that are found in actual slicks, critical accumulation seems to be the dominant failure mode for large tow or current speeds[2].

[2]Note that, in addition to these failure modes which occur in calm weather, the effectiveness of the boom in containing oil can be severely limited by the hydrodynamic behavior of both the boom and the slick under extreme weather conditions that may create high seas. These factors will not be considered in the present study.

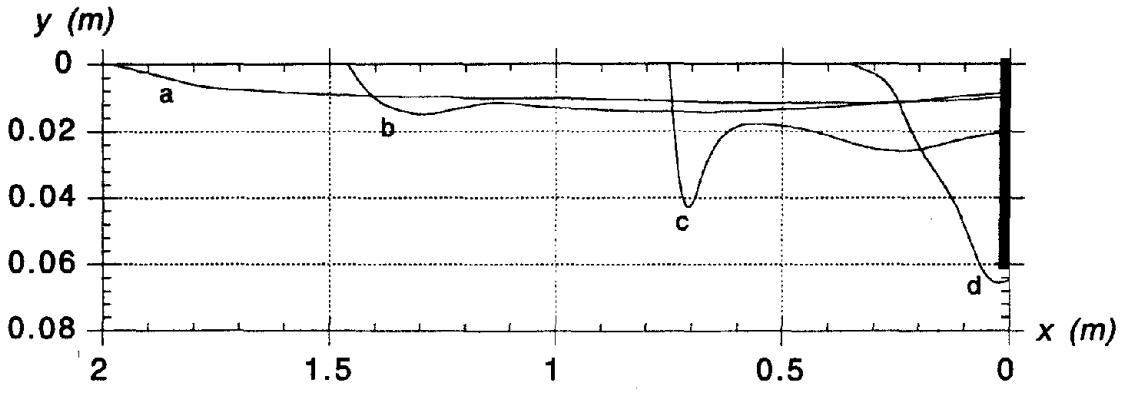

Figure 1.3: Experimental shapes of oil slicks measured in Delvigne's (1989) experiments with Arabian light emulsion ($\nu_o = 2,300$ cs) for relative oil-water velocity U = a : 0.065; b : 0.095; c : 0.128; and d : 0.145 m/s. The figure shows the increase in size of the headwave and the shortening of the slick as U increases from curve a to c and, finally, the failure by critical accumulation with the oil slick draining under the boom in curve d.

Many experimental and theoretical studies were pursued in the 1970's to understand the physics of oil containment by a boom and circumstances leading to containment failure. More recently, there has been a renewed interest in studying the problem and a few attempts were made to better understand the problem by the use of numerical modeling tools. In Section 1.2, we present a literature review of the oil containment problem including qualitative, experimental, and numerical studies. It will be shown, in particular, that interfacial waves occurring during the failure modes discussed above are both initiated and sustained by *shear instability* at the oil-water interface, usually referred to as a *Kelvin-Helmholtz (KH) instability*. Hence, modeling KH instability in the context of oil containment by a boom, will be one of the main objectives of the present study. This will be detailed in Section 1.3.

1.2 Literature review

Research in the area of boom–slick–current interaction has primarily been experimental, with few researchers adopting theoretical approaches to the problem. Recently, efforts have been made to study the phenomenon using numerical methods but with limited success.

In the following sections, in an attempt to better understand the physics of the problem and formulate an effective modeling strategy, the existing literature has been reviewed and significant studies summarized based on the approach adopted by the researchers, namely *qualitative, experimental, theoretical* or *numerical.*

1.2.1 Qualitative studies

Wilkinson

Wilkinson (1972) studied the effect of hydrodynamic forces on an oil slick contained in a two–dimensional channel and showed that, even for inviscid flows, the slick thickness would be finite in the presence of a current.

He conjectured that the oil slick can be divided into *two zones* : (i) one in which dynamic forces are dominant; and (ii) the other in which viscous effects dominate. The relative extents of each of these zones were determined by examining the orders of magnitude of the forces acting on the slick. The force balance in the frontal zone (headwave) was examined by equating pressure forces acting at sections upstream of and across the slick to the change in momentum of the flow between the two sections (viscous forces were assumed negligible). The following conclusions were drawn regarding contained oil slicks,

- The *frontal thickness* of a slick will never be greater than approximately one–third of the stream depth.
- Containment failure occurs when the *Froude number* of the flow upstream of the slick exceeds a critical value (0.498–0.527).

The frontal region of the slick is thus analogous to a hydraulic jump in which the head loss or rate of energy dissipation can be defined in terms of an upstream Froude number.

When the slick is of considerable length and overlies deep water, its final thickness may greatly exceed the frontal thickness. The form of the frontal zone is determined largely by interfacial stresses and interfacial slopes, which typically vary between 0.0005 and 0.004 (Cross and Hoult, 1970) and imply a more or less uniform interfacial stress.

The slick length and therefore the quantity of oil that can be contained by a barrier are also limited and depend upon the Froude number of the flow upstream of the slick and the interfacial and boundary stresses acting beneath the slick. A strong dependence of the interfacial friction coefficient C_f on the Reynolds number **Re** of the underlying flow is observed.

Leibovich

Leibovich (1976) studied *entrainment failure* of oil slicks and suggested that it was caused by the breaking of Kelvin–Helmholtz (KH) interfacial waves. Using linear stability theory, Leibovich demonstrated that thin slicks are more stable than thick slicks (unlike earlier conclusions by Jones, 1972). The surface tension at the oil–air interface, σ_{oa} was found to have a stabilizing influence on the development of interfacial waves in thin slicks.

Drazin's (1970) theory of *finite amplitude* KH waves was used to explain the departure of experimental values of U_{cr} from those predicted by the linear stability analysis. Stabilizing factors leading to the formation of equilibrium finite amplitude KH waves are buoyancy, $\Delta\rho_{ow}$, and surface-tension at the oil–water interface, σ_{ow}.

The formation of the *headwave* and its role in entrainment failure was also considered in this study. Three possible causes were proposed to explain the initiation of entrainment failure at the headwave,

- Benjamin (1968) studied gravity currents in cavity flows and observed *headwave instability* downstream of the point of maximum thickness (an inviscid theory, however, was used [3]).
- Adverse pressure gradient on the lee of the headwave, contributing to separation and eddy formation.
- The locally high values of the relative oil-water velocity at the interface, $\boldsymbol{u}_{ow}$, at the point of maximum thickness of the slick may cause the early *separation of oil droplets*, even though $\boldsymbol{u}_{ow}$ may be smaller than the critical value elsewhere along the slick.

Milgram and Van Houten

Milgram and Van Houten (1978) studied the respective magnitudes of *frictional and pressure forces* along the oil–water interface using a combined theoretical–experimental approach.

In this study, potential flow theory is assumed for the water and the shape of the oil–water interface is measured in experiments. Dynamic pressure due to the underlying flow is calculated on the interface using a Green's function approach. An equation relating interfacial shape, dynamic pressure, and shear stress is derived to calculate the shear stress distribution and conclusions are then drawn about the relative effects of shear and pressure forces along the oil–water interface.

A more detailed discussion of numerical methods employed and results obtained in this study are given later in this review.

Di Pietro and Cox

Di Pietro and Cox (1980) showed the existence of a region at the very tip of the slick where *surface tension* is more important than gravity and viscous forces. This region is shown to be (physically) necessary to connect the monolayer (defined as the thin layer of oil preceding the slick) and the bulk of the slick. This is also an area where the interface slope is large.

The form of a slick upstream of a barrier is computed assuming : (i) small velocity variations across the oil layer; (ii) monolayer and bulk layer lengths much larger than capillary scale; (iii) small interface slopes; (iv) inertia effects are neglected in the oil slick; (v) negligible pressure variations in the underlying flow; (vi) laminar flow in boundary layers.

This theory is important from the current perspective as it forms a plausible starting point for numerical simulations. Initial conditions based on the analytical form can be

[3]Note that Milgram and Van Houten (1978) showed the importance of viscous shear along the slick interface and hence the selection of a purely dynamic approach may not be appropriate.

used as input to the proposed model and evolution tracked for increasing U. The excellent description of the oil–water–air junction will be important to prevent numerical instabilities from creeping in due to incorrectly posed initial conditions (see also Section 3.2).

Delvigne

Delvigne (1980) identified a third failure mechanism for oil slick containment by a barrier and called it *critical accumulation* (hereafter referred to as CA). CA appears to occur for oil viscosities, $\nu_o \geq 3,000$ cs and flow velocities $U \geq 0.15$ m/s. Prior studies considered oils where viscosities were too low and water depths too limited to reveal this mechanism. In his experiments, Delvigne used oil viscosities as high as 33,000 cs and flow velocities up to 1 m/s.

Oil viscosity considerably influences both the length and shape of a contained oil slick and the occurrence of interfacial instabilities. In fact, oil viscosity is a key parameter for the occurrence of any of the three modes of failure, in the range of flow velocities at which failure commences. In real oil spills, however, oil viscosity often rapidly increases as a result of weathering and emulsification. Whereas most crude oils and products originally have $\nu_o \leq 1,000$ cs, emulsification takes place within a few hours of the spill and results in a viscosity on the order of 1,000 cs. Continual weathering of slicks eventually increases this viscosity to the order of 10,000 cs and, in the long term, almost solid tar balls can be formed.

Oil slick behavior behind a barrier can be described as a function of viscosity ν_o and flow velocity U. Three different scenarios are possible,

- *Low viscosity oils* with $\nu_o \leq 400$ cs exhibit failure normally by the droplet entrainment mechanism. Increasing values of U result in shorter slick lengths and fast moving interfacial waves (due to KH instability) which become unstable at a certain velocity, leading to oil droplets being torn from the slick and passing under the barrier or reattaching to the slick further downstream.

- *Moderately viscous oils* with ν_o in the $400 - 3,000$ cs range normally have a smooth interface, with a headwave at the upstream edge of the slick. Slow interfacial waves develop at higher current velocities, and slick shortening and thickening take place (see Fig. 1.3). If the barrier draft is adequate to prevent drainage failure, droplet entrainment begins as a result of headwave instability.

- *Highly viscous oils* with $\nu_o \geq 3,000$ cs show smooth interfaces and the formation of a headwave. In long slicks, regularly spaced interfacial waves are observed downstream of the headwave, which appear to be almost stationary. Slick length gradually decreases with increasing U. At some critical velocity U_{cr} the slick collapses to a vanishingly small length and passes under the barrier, regardless of barrier draft.

1.2.2 Some related phenomena

Owing to the complicated nature of the modeling problem of an oil containment by a boom, researchers have attempted to compare the slick–water–boom interaction problem to other physical phenomena and gather insight from studies in those fields. Two phenomena, analogous to the present problem, are gravity currents and hydraulic jumps.

Gravity currents

A gravity current (or density current) is the name given to the phenomena characterized by the relative flow of fluids of differing densities past each other. A typical gravity current consists of a heavier fluid flowing over the bottom, displacing a fluid of smaller density. The front of the fluid progresses with nearly constant speed and is characterized by the existence of a large headwave, typically twice the height of the interface average depth, and an undulating turbulent downstream side indicative of some kind of wave instability and/or breaking. Further downstream, the interface becomes nearly horizontal. Typical instances of gravity currents in nature include the case of salt water intrusion into fresh water, turbidity currents, and meteorological cold-fronts.

Wicks (1969) first observed the similarity of our problem to an upside down gravity current and posed that results for gravity currents would be similarly applicable to the problem of a contained slick floating on water.

Benjamin (1968) studied gravity currents using inviscid fluid theory with simple extensions to account for dissipation. Two approaches were investigated, without and with dissipation. The salient features of his paper and relevant conclusions of his study are,

- The interface between two fluids is shown to be unstable to all possible stable disturbances.
- The existence of a headwave is shown to be impossible if the flow is energy conserving and its existence is thus linked to the dissipative process.
- An analytical solution for the interface, is derived using complex mapping and assuming only dynamic effects. An included angle of 60° at the front of the gravity current is deduced [4].

Hydraulic jumps

Wilkinson (1972) pointed out the similarity of the slick water interface to a hydraulic bore. Wei *et al.* (1995) studied undular bores at the ocean surface. These results, when turned upside down, are remarkably similar to interfacial profiles measured by Delvigne (1989) (see Figs. 1.3 and 1.4). Since the results for the undular bore were computed using a fully nonlinear potential flow model (i.e., a theory that does not include friction), it is reasonable

[4]Note that Milgram and Van Houten (1978) demonstrated the need to also consider viscous effects when computing interfacial profiles.

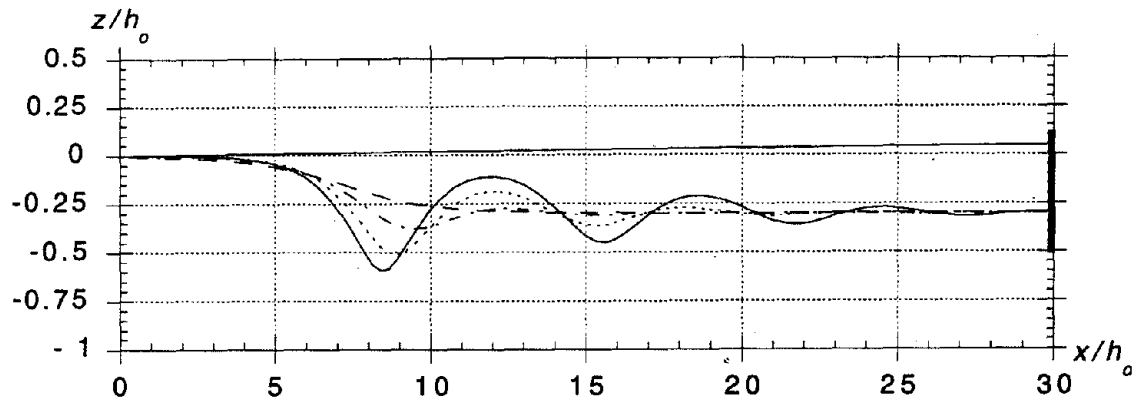

Figure 1.4: Qualitative similarity between headwave instabilities and the time development of an upside down undular bore calculated by Wei *et al.* 1995.

to infer that dynamic forces (i.e., boundary conditions on the oil water interface) dictate to a large extent the formation of the interfacial waves.

1.2.3 Experimental results

Following is a summary of significant experimental studies to date and their results that can provide a ready reference for the researcher in the field of current–slick interaction.

Milgram and Van Houten

In Milgram and Van Houten's (1978) study the *shape* of the oil–water interface in an oil slick was experimentally measured, for different oil characteristics and current speeds, and related by quasi-hydrostatic equilibrium equations to the friction coefficient and the dynamic pressure distribution along the interface (see Sections 1.2.4 and 3.2).

The experiments were carried out at MIT's precision flume (6.25 m by 0.61 m by 0.46 m), with an operating water depth of 0.53 m and a barrier draft of 0.175 m. Wall effects, shown to cause premature containment failure in the flume due to the generation of side vortices, were reduced by using a layer of rubberized horsehair on the upstream side of the barrier. Uniform current speeds were first established in the water before layering oil onto the test section and waiting for equilibrium. Equilibrium was reached in the slick after damping of waves moving back and forth in the oil was achieved. Since the speed of such waves is limited to $\sqrt{gq(1-s)}$, where q is the oil layer thickness, equilibrium in thin slicks was only reached after quite a long time, particularly since s varied between 0.804 and 0.88 in the experiments. Measurements of interfacial shape were directly made on the flume glass sidewalls, using photographic techniques. Smoothing of photographs of the interface was performed afterwards. Oil viscosity in the experiments varied between 3.61 and 125.36 cs and current speeds of 0.16 m/s to the upper limit of entrainment failure were tested.

The main experimental results obtained were as follows,

- The oil was found to move very slowly, with the formation of vertical circulation cells within the slick. This justifies assuming *quasi-hydrostatic pressure* in the oil for the theoretical analyses, particularly for high viscosity oils (see Section 3.2).

- Smooth interface shapes were only observed for $U \leq 0.20$ m/s. At higher velocities, interfacial waves developed. These were shown to be *KH instability* waves, owing to their constant phase speed and the formation of a headwave at the location of higher Reynolds numbers in the underlying flow.

- Leibovich's (1976) observation of increased stability for thinner oil layers was verified.

- The upstream end of the slick was marked by a visible ridge on the water surface, referred to as *Thoreau-Reynolds ridge*.

- A surface film formed upstream of the oil slick, referred to as the *monolayer* (Di Pietro and Cox, 1980). A boundary layer of water formed underneath the film, with the stress in the boundary layer being balanced by the surface tension gradient in the oil film.

- *Interfacial friction* was found to increase with increasing interfacial slope and current speed, and to have a strong dependence on pressure gradient.

- *Droplet entrainment* occurred due to the formation of large scale unstable KH waves on the interface. The rate of droplet entrainment increased with the water velocity u_{ow} directly below the interfacial boundary layer and with the thickness of the boundary layer. Thin boundary layers and high water speeds maximized droplet entrainment.

- Decreasing interfacial *surface tension* only had marginal effect on the interface geometry. Surface tension, however, was found important for the evolution of finite amplitude KH waves (Drazin, 1970). Increasing oil viscosity also helped damping the shorter waves occurring on the interface.

Delvigne

Delvigne (1989) primarily addressed the problem of containment of highly viscous oils ($\nu_o \geq 3,000$ cs) in nonlimiting water depths, for large values of U (up to 1 m/s) not addressed in prior experiments. He succeeded in demonstrating the occurrence of a new (dominant) failure mechanism, *critical accumulation*, and described the experimental results and the factors deemed to be important for this kind of failure mode.

Experiments were performed in two flumes with widths of 0.5 and 2.0 m, water depths ranging from 0.3 to 0.7 m and barrier draft from 0.07 to 0.13 m. Different oil types were used to obtain a continuous range of viscosity. Oil was poured on the water, current velocities were established, and slick length and form were measured. Different scaling rules were applied for different failure modes : (i) drainage failure was scaled using a Froude number

scaling, on account of its sensitivity to barrier draft and slick length; (ii) droplet entrainment and critical accumulation on the other hand were simulated using full scale, because of their dependence on viscosity and current speed.

The main experimental results obtained were as follows,

- The proportionality of maximum slick length for *drainage failure* to the square of the barrier draft (first proposed by Cross and Hoult, 1970; see Eq. (1.1)) was self evident in the results.

  For low current speed, maximum slick length was proportional to U^{-2} but for larger current speed, the interfacial friction coefficient C_f increases due to interfacial KH waves and maximum slick length was proportional to $Q^{2/3}$ (where Q is the oil volume per unit width of slick).

- Agrawal and Hale's (1974) postulated dependence of *critical velocity* U_{cr} for droplet entrainment failure on the Weber number was not supported by experimental results. Values of U_{cr} were also found to be lower than those observed by Agrawal and Hale. The trend of decreasing U_{cr} with increasing ν_o was substantiated.

- *Critical accumulation* always occurred in experiments for $\nu_o \geq 3,000$ cs and for current speeds greater than 0.15 m/s. Both entrainment and critical accumulation failures simultaneously occurred for $2,000 \leq \nu_o \leq 3,000$ cs.

- U_{cr} for critical accumulation was found to be *independent* of ν_o, $\Delta\rho_{ow}$, Q and water depth h.

Johnston et al.

Johnston *et al.*'s (1993) study was aimed at providing a better hydrodynamic understanding of containment of highly viscous oil slicks. A theoretical model describing the phenomenon was introduced where the importance of oil circulation on the *critical accumulation* failure mechanism was stressed.

Experiments were performed in a flume 24 m by 0.4 m by 0.4 m. Water depths ranged from 0.18 m to 0.3 m and model boom drafts ranged from 0.05 m to 0.08 m. Uniform current characteristics were obtained using a pump and a specially designed inlet manifold. Water level control was achieved using a weir type mechanism and flow rates were adjusted using valves in the inlet line. Oil viscosities of $\nu_o = 500$ to 10,000 cs with relative densities $s =$ 0.900 to 0.985 were tested. The high sensitivity of oil viscosity to temperature changes was used to alter viscosity in the experiments, with negligible change in oil density. Parameters measured included, slick length, thickness, visual observation of behavior, interface shape (measured using capacitance gages). The air-oil interface was assumed to be constant in time and the rise of the interface as a result of the density differences was assumed to have little effect on the dynamics of the oil–water interface.

The main experimental results obtained were as follows,

- Water-in-oil *emulsions* exhibit non-Newtonian behaviors and some of them belong to a specific type of non–Newtonian fluid, known as *Bingham plastics*. The experimental program was geared towards the study of slicks having Bingham plastic characteristics.

- At relatively low values of U (0.10 to 0.26 m/s, depending on oil viscosity and density), the slick interface became dynamic. A *surge* developed at the frontal region (headwave) and pulsed towards the boom. As the oil slick thickness increased, its length reduced. The phenomenon reversed itself as interfacial waves were reflected from the boom.

- The *intensity of the surge* was dependent on flow velocity, oil viscosity, and oil density. For intermediate viscosities (2,000 to 8,000 cs) interfacial waves (surge) periods were small and the pressure build up at the boom seemed to be relieved by the upstream movement of the leading edge of the slick. For higher viscosities ($\geq$ 8,000 cs) the wave period considerably increaseed and circulation in the oil was often inadequate to account for the pressure buildup, leading to a major leakage followed by the slick reforming and a new circulation setting in.

In the light of these experimental findings, the surging phenomenon is posed as a possible precursor to the failure mode by critical accumulation. This is consistent with Delvigne's (1989) findings. A scoop boom was used to facilitate circulation and found to be of limited use since dynamic effects propagated from the front of the slick. A proposed explanation to the *critical accumulation failure* is : as the circulation in the oil becomes insufficient to relieve the shear stresses along the oil–water interface, a shear instability is caused in the slick interface, leading to containment failure.

Song et al.

Song *et al.* (1993) investigated the experimental behavior of contained oil slicks made with diesel fuel and soy bean oil. An analysis based on the approach by Milgram and Van Houten (1978) was performed to predict the interfacial friction coefficient.

Results are basically consistent with prior observations, linking slick length to slick volume and density, and to U. Only drainage and droplet entrainment failure mechanisms were explored since oil viscosities investigated were quite low (4.02 and 99.7 cs). The influence of the densimetric Froude number on the flow field was found to be significant.

1.2.4 Numerical Models

To our knowledge, only four previous studies qualify as numerical models of oil slick containment. In fact, among those, the older works by Zalosh (1974,1976) and by Milgram and Van Houten (1978), represent detailed and thorough investigations, using approaches that accurately address the physics specific to the oil containment problem. On the other

hand, recent modeling works, originated in the early 1990's, which rely on supposedly more accurate but more general Computational Fluid Dynamics techniques, have only met with limited success, owing to the simplifying assumptions made by the researchers for the representation of the interface or due to the modeling techniques chosen.

We will see, in particular, that recent numerical models proposed by Bai and Kim (1992) and Clavelle and Rowe (1993) concentrated primarily on calculating fluid behavior in the bulk of the oil and water domains while ignoring surface tension and KH interfacial waves along the slick-water interface. Because domain-discretization-type methods were used in these models (i.e., Finite Difference Method and Finite Volume Method), they also lacked resolution in the discretization of the geometry of interfaces which are the regions of the flow where accuracy is most needed in order to understand and predict oil-containment instability.

A review of the numerical techniques used thus far is however of great interest as it helps to guide the formulation of our modeling strategy.

Zalosh

In our opinion, despite being the older, only the work by Zalosh (1974,1976) (which for unknown reason seems to have long been forgotten in most of the existing oil containment literature) put emphasis on the important parameters identified in both the qualitative and experimental studies discussed above, that affect interfacial instabilities occurring during containment of an oil slick by a boom, i.e., fluid density difference, surface tension, unsteadiness of KH instability waves, detailed shape of interfaces.

Zalosh studied the headwave instability of an oil slick due to an underlying current velocity U (i.e., for the case of a pure headwave instability without a boom), by developing a numerical model assuming inviscid fluid. In the model, the oil-water, oil-air and air-water interfaces were represented by vortex sheets (VS) discretized using point vortices and semi-infinite VS's used to represent interfaces far away from the slick leading edge. An evolution equation including gravity and surface tension effects was developed and used to compute the geometry of the oil-water interface as a function of time. An implicit numerical scheme was used to solve the time-evolution equation. Using this approach, model results showed some sawtooth instabilities which required geometric smoothing algorithms during time marching computations.

Using this model, Zalosh predicted the occurrence of KH instability waves in the headwave region, for flow velocity beyond a critical value, and initial stages of roll-up of VS's. Some unacceptable simplifications and a few mistakes in the equations, however, prevented quantitatively realistic results for a sufficiently long time. Since our model uses an approach similar to Zalosh's, detailed discussions of this model's equations and numerical procedures can be found in Chapters 2 and 3.

An oil droplet formation algorithm was then formulated and applied to the numerically modeled headwave region. The computed velocity for the onset of significant droplet entrainment was found in good agreement with laboratory experiments. A theoretical analysis

was thus conducted for the droplet entrainment rates which were found to approximately agree with experiments but did not vary with current velocity.

Milgram and Van Houten

Milgram and Van Houten (1978) studied the mechanics of a restrained layer of floating oil above a water current U by performing a quasi-hydrostatic mathematical analysis in the oil layer, combined with an ideal fluid approximation in the water. Since this analysis is the basis of our computations of initial steady-state shape of oil slicks, basic equations for these computations are detailed in Section 3.2 and only a brief summary of this study is given here.

Milgram and Van Houten treated the oil slick instability problem as a combination of potential flow in the underlying water layer (infinite depth) and hydrostatic force equilibrium in the oil slick. This is supported by experimental evidence discussed above showing that circulation in the oil slick is quite slow and essentially stationary.

Assuming potential flow theory in the water, a Green's function Boundary Integral Equation can be expressed for the potential ϕ and the tangential velocity U_{ws} at points (x_l, y_l) along the slick interface boundary Γ_s can be found by taking the tangential derivative of the potential, as,

$$\frac{\partial \phi}{\partial s}(x_l, y_l) = U_{ws}(x_l, y_l) = \frac{U}{2} cos\theta + \int_{\Gamma_s} U_{ws}(x, y) \frac{\partial G}{\partial n} d\Gamma(x, y) \tag{1.2}$$

where $G(\boldsymbol{x}, \boldsymbol{x}_l)$ is the Green's function (see Eq. (3.32)). The dynamic free surface boundary condition (Bernoulli eq.) yields the dynamic pressure p_D along the interface as a function of U_{ws} (see Eq. (3.25)).

Neglecting oil momentum fluxes and dynamic pressures, the pressure in the oil layer can be assumed hydrostatic. The forces on an element of oil slick interface are shown in Fig. 3.2 and the force equilibrium equations relating the mean shear stress τ_s, the dynamic pressure and the hydrostatic forces to interface shape and slick depth can be expressed (see Eqs. (3.26) to (3.28)).

Hence, given an initial slick shape measured in experiments $(\eta(x), q(x))$, U_{ws} is calculated by Eq. (1.2) and yields the dynamic pressure which then lets us determine the value of the friction coefficient C_f using the force equilibrium equations.

Milgram and Van Houten showed various experimental results and corresponding values of C_f and thus discussed the relative importance of interfacial shear stress and dynamic pressure in determining slick thickness distribution. The results show that the rear portion of the slick is governed purely by shear stress as is the forward portion for lower current speed. For higher current speed, both dynamic pressure and shear stress are important in determining the shape of the forward portion. Large friction coefficients are shown to be due to flow over a rough interface resulting from the generation of KH waves on the interface.

Bai and Kim

Bai and Kim (1993) formulated a numerical method to determine the thickness of a contained slick and simulate the long scale gravity, inertial, and viscous effects occurring on the oil–water interface while neglecting the unsteady short–scale motion governed by surface tension, viscous and buoyancy effects (i.e., KH instability waves).

As before, the oil layer is modeled following the quasi-hydrostatic approach proposed by Milgram and Van Houten (1978) and the outer water flow (i.e., flow outside the interfacial Boundary Layer) is modeled using a Green's function approach assuming ideal fluid. The modeling of the inner water layer (i.e., the interfacial Boundary Layer) is performed by solving Navier–Stokes (NS) equations, with kinematic viscosity terms only (i.e., a Stokes flow model; see e.g. Eqs. (1.5)).

The outer layer (far from the interface) is modeled using a streamfunction ψ (also see Section 3.2). Boundary conditions at the oil-water interface are linearized to yield the following simplified problem,

$$\begin{aligned}
\nabla^2\psi &= 0 && \text{for } y < 0 \\
\frac{\partial\psi}{\partial y} &= \frac{g}{U^2}\psi && \text{for } x < 0, y = 0 \text{ on } \Gamma_f \\
\frac{\partial\psi}{\partial y} &= \frac{gs}{U^2}\psi - \frac{g(1-s)}{U}(q-\eta) && \text{for } x \geq 0, y = 0 \text{ on } \Gamma_s
\end{aligned} \tag{1.3}$$

where Γ_f denotes the air-water interface and Γ_s the oil-water interface.

Closure for the above system of equations is provided by determining $q(x)$ from the hydrostatic force equilibrium along the oil slick interface (see Eqs. (3.26) to (3.28)) and from the viscous model of the interface Boundary Layer. The viscous model within the Boundary Layer is based on a finite difference solution of the NS equations and on the continuity equation for incompressible fluids. The details of the model are not clear from the paper but, apparently, a system of Ordinary Differential Equations is derived, following Kantarovich's variational approach, and is then solved by Newton–Raphson iterations.

In the numerical results, Bai and Kim note that the use of the molecular water viscosity in the NS equations modeling yields computed oil slick thicknesses far smaller than observed in practice, e.g., by Milgram and Van Houten. This is attributed to the assumption made in the model of neglecting (turbulent) Reynolds stresses. A rather heuristic increase in the molecular viscosity coefficient applied in some computations shows that the computed interface shape can be "made" qualitatively similar to results obtained experimentally by Milgram and Van Houten.

Clavelle and Rowe

Following Johnson *et al.* (1993), Clavelle and Rowe (1993) posed that *critical accumulation* failures occur due to the inability of the internal circulation in the oil to account for the interfacial shear stress, at current speeds exceeding 0.15 m/s. To account for internal

circulation within the oil and for the non-uniform flow beneath the slick, an approximate solution to the Navier–Stokes (NS) equations for layered fluids is applied to the problem.

The solution approach involves the use of a finite difference–based numerical model referred to as *SOLA-VOF*. This model uses fractional Volume Of Fluids (VOF) to establish and keep track of the density interface location more accurately than in pure VOF methods. A function $F(x, y, t)$ is defined within each computational cell with values between 0 and 1 for water and oil, respectively, and a temporal dependence specified by the standard kinematic condition,

$$\frac{\partial F}{\partial t} + u\frac{\partial F}{\partial x} + v\frac{\partial F}{\partial y} = 0 \tag{1.4}$$

The flow in both fluids is described by the full two-dimensional NS momentum equations and by the continuity equation,

$$\begin{aligned}
\frac{\partial u}{\partial t} + u\frac{\partial u}{\partial x} + v\frac{\partial u}{\partial y} &= g_x - \frac{1}{\rho}\frac{\partial p}{\partial x} + \nu\left(\frac{\partial^2 u}{\partial x^2} + \frac{\partial^2 u}{\partial y^2}\right) \\
\frac{\partial v}{\partial t} + u\frac{\partial v}{\partial x} + v\frac{\partial v}{\partial y} &= g_y - \frac{1}{\rho}\frac{\partial p}{\partial y} + \nu\left(\frac{\partial^2 v}{\partial x^2} + \frac{\partial^2 v}{\partial y^2}\right) \\
\frac{\partial u}{\partial x} + \frac{\partial v}{\partial y} &= 0
\end{aligned} \tag{1.5}$$

where ρ and ν denote the density and the kinematic viscosity of the considered fluid (oil or water), and (g_x, g_y) denotes the gravitational acceleration vector.

Steps in the numerical implementation are essentially : (i) finite difference approximations to the momentum equations (1.5) are used to determine the velocities at the next time step; (ii) pressure is iteratively adjusted in the VOF's cells and the resulting corrections to the velocities are added to those computed in step (i); (iii) the time derivative of function F is used to time step the system to later time; (iv) numerical dissipation is used in the computational model to approximately simulate turbulence.

Due to the computationally expensive nature of such simulations, only coarse grid sizes were used by Clavelle and Rowe. Hence, poor resolution is obtained for the oil-water interface. In the applications presented in the paper, free surface boundary conditions were not implemented. Results show that only qualitative agreement is obtained with interface shapes measured by Delvigne (1989) for the critical accumulation failure mode.

1.3 Statement of the problem

The literature review identified key parameters and physical phenomena responsible for the three failure modes of oil containment by a boom. More specifically, in the light of Delvigne (1989) and Johnson *et al.* (1993) experiments, *critical accumulation* seems to be the dominant failure mode for high viscosity oils that are found in actual slicks.

Critical accumulation results from the interplay of the following physical processes and parameters (see Fig. 1.2),

- the relative *oil-water velocity* U, which controls the magnitude of interfacial friction forces and triggers and sustains KH instability;

- the fluid *density difference*, $\Delta\rho_{ow} = \rho_w - \rho_o$ (or, $1 - s$, with $s = \rho_o/\rho_w$), which affects both slick thickness and spreading forces;

- $\Delta\rho_{ow}$ and the *surface tension* at the oil water interface, σ_{ow}, which both affect the growth of interfacial KH waves;

- the interfacial *friction coefficient*, C_f, which controls the magnitude of interfacial friction forces and thus affects oil slick thickness, and is a function of interfacial shape (including irregularities due to KH waves);

- *oil viscosity*, ν_o, which damps out short interfacial waves and limits the strength of internal circulation cells within the oil slick (hence justifying a quasi-hydrostatic assumption for highly viscous oil slicks).

Other parameters of lesser importance are : σ_{aw} and σ_{oa}, the air-water and oil-air surface tension, respectively.

As far as the KH instability at the interface, increasing U or C_f reinforces the instability whereas increasing σ_{ow} or $\Delta\rho_{ow}$ (i.e., buoyancy) reduces the instability.

Overall, a steady-sate slick shape can be achieved for $U < U_{cr}$, when stabilizing forces (i.e., spreading forces and circulation in the slick) can balance interfacial friction forces. For $U > U_{cr}$, however, increased friction forces at the interface can no longer be compensated by counteracting forces, particularly for high viscosity oils for which circulation in the slick is very limited. Hence, slick length must decrease to balance friction forces and, as a result, interfacial waves grow even larger (see Fig. 1.3), which increases friction forces even more. This leads to the unstable reduction in slick length and total loss of oil by drainage under the boom that characterize *critical accumulation*. Delvigne points out that, at the onset of critical accumulation, strong deformations of interfacial waves, headwave, or both are observed. [This is confirmed by Johnson *et al.*.] He also notes that, for lower viscosity oils, a similar unstable growth of interfacial waves would probably lead to oil being torn off the wave crests and, therefore, to droplet entrainment.

Hence, it appears that modeling KH instability and resulting interfacial waves in the context of oil containment by a boom is the key to both understanding and predicting *critical accumulation*. In proposing this project and anticipating the high degree of complexity of physical mechanisms involved, we initially suggested an "incremental" modeling approach where the initial model would only be a first step towards a more comprehensive model of oil containment that could eventually provide practically useful results. In view of the better overall understanding of critical accumulation that resulted from the extensive literature review conducted as part of this project, we can now more clearly identify a hierarchy of modeling strategies aimed at "incrementally" addressing the problem. This hierarchy will correspond to phases in model development with successive improvements of the level of

	OIL	O - W INTERFACE	WATER
	Modeling techniques used in literature		
	Quasi-hydrostatic Viscous (NS)	Vortex Sheet (no S.T) Viscous (NS)	Inviscid Fluid Viscous (NS)
	Proposed modeling strategies for the project		
Phase I	Quasi-hydrostatic	Inviscid Vortex Sheet with surface tension	Inviscid Fluid
Phase II	Quasi-hydrostatic	Viscous Vortex Sheet with surface tension	Inviscid Fluid
Phase III	Viscous (NS)	Viscous Vortex Sheet with surface tension	Inviscid Fluid

Figure 1.5: Table of existing and proposed modeling strategies. Phase I model was developed under the FY94 project reported on here and Phase II model is currently being developed as part of the FY95 project. NS : Navier-Stokes equations; S.T : surface tension.

physics modeled and, hence, also of increased modeling accuracy. This will be detailed in the following.

Modeling the problem sketched in Fig. 1.2 involves solving for the unsteady motion of a two fluid system in the presence of fixed obstacles (bottom, boom). This system has both free surfaces (air-oil, air-water) and an interface (oil-water) for which viscous and turbulent effects may be important. Apart from the region very close to the oil-water interface, water behaves as an almost perfect *inviscid fluid*, due to the large Reynolds number of the underlying flow (e.g., Batchelor, 1967). From the literature review, it is apparent that *dynamic effects* dominate along the oil–water interface as far as development of KH instabilities and interfacial waves (e.g., Wilkinson, 1972). Besides dynamic effects, both slick thickness $q(x)$ and shape also depend, but to a lesser extent, on *viscous/turbulent effects* at both the oil-water interface and within the oil slick (slow viscous circulation occurs within the oil slick; Milgram and Van Houten, 1978). *Surface tension* at the interface also plays an important role in the development of KH waves (Di Pietro and Cox, 1980; Rangel and Sirignano, 1988).

Figure 1.5 gives a summary of modeling techniques, discussed in Section 1.2.4, that were proposed in the literature for representing the motion of the oil slick, the oil–water interface, and the underlying water, in the oil containment problem. Among the few existing models, it seems that only the older work by Zalosh (1974) included the important parameters identified above as affecting interfacial instability phenomena responsible for

the *critical accumulation* failure of oil slicks. In particular, this was the only model where unsteadiness of KH shear instability and detailed shapes of interfaces were accounted for. This work was based on using inviscid Vortex Sheets (VS) to represent interfacial geometry and vorticity as a function of time. Several unrealistic simplifications and mistakes in the model equations, however, prevented this model from providing quantitatively realistic results for a sufficiently long time (see further discussion of this in Chapters 2 and 3). Two other models (Bai and Kim, 1992; Clavelle and Rowe, 1993) concentrated on representing fluid behavior in the bulk of the oil and water domains and ignored surface tension and KH waves on the oil–water interface. Because domain-discretization-type methods were used in the latter models (i.e., Finite Difference Method, Finite Volume Method), they also lacked sufficient resolution for the discretization of the interface geometry. These, however, are the regions of the flow where accuracy is most needed in order to correctly model and predict oil containment failure by critical accumulation.

It will be shown in Chapter 2 that, for an inviscid fluid in which (shear-induced) vorticity is concentrated along interfaces and solid boundaries, vorticity is well represented by vortex sheets (VS). The analysis of the VS dynamics shows that induced velocities can be expressed by Biot-Savart's law (e.g., Lamb, 1947; Batchelor, 1967), which employs a boundary integral formulation. This allows for the development of Boundary Integral Equation (BIE) models which, when combined with higher-order Boundary Element Methods (BEM) for the spatial discretization, have proved to be very efficient and accurate for solving unstable free surface flow and gravity wave problems (e.g., Grilli and Subramanya, 1995, 1996). More specifically, in BIE/BEM models, discretization of the solution is limited to boundaries (i.e., to interfaces in the present case) whereas the representation of the solution inside the fluid domain is exact. Hence, model grids are very much reduced in size compared to domain-discretization-type methods and high resolution can thus be achieved along the boundaries. Furthermore, for moving boundary problems like the present one, time updating of both the discretization and the boundary conditions along boundaries is a much more efficiently and accurately implemented in BEM models than in domain-discretization-type models where the whole spatial grid has to be recreated at each time step.

It was thus decided, in the present study, to adopt the *inviscid VS* approach to represent the shear layer (interface) between oil and water in a first model of oil containment instabilities. This model is hereafter referred to as the *Phase I model* and the present report concentrates on describing the development and the implementation of this model. The Phase I model assumes that viscous circulation is neglected in the oil slick, i.e., a *quasi-hydrostatic* hypothesis. This is acceptable in view of the experimental results discussed in the literature review, particularly for high viscosity oils, which are those found in many slicks. The VS approach exactly accounts for the vorticity generated by the velocity jump at the oil-water interface but not for the viscous or turbulent diffusion of vorticity that may occur at the interface [5]. The Phase I model also assumes that the underlying water behaves

[5]Note that the vorticity along the VS's will induce a slow non-viscous rotational motion in the oil slick, but with likely minimal vertical accelerations; this is consistent with the assumption that pressure in the oil is close to hydrostatic. Accounting for a slow circulation in the slick would only provide small additional

as an incompressible *inviscid fluid* (i.e., ideal fluid). The main features.for the Phase I model are summarized in Fig. 1.5.

The Phase I model was developed and validated as part of Task (ii) of this project. As stated in our original objectives, it is anticipated that this model will "provide a firm foundation with which to perform more sophisticated analyses that are more closely representative of at sea- and full-scale laboratory conditions". Such analyses will imply extending the Phase I model to include a more accurate physical representation of interfacial instability and will be the object of continuations of this project (see Section 4.4). In particular, *interfacial friction* was identified as one of the important factors for critical accumulation. In the Phase I model, however, no explicit friction term was included in the dynamics of inviscid VS's. Hence, it is proposed, in an extension to the present study, to model viscous and turbulent effects within a small boundary layer close to the oil-water interface and thus to include friction forces in the analysis. This approach, globally referred to as *viscous VS*, will be implemented as part of the Phase II model, as a continuation of this project. Finally, modeling of the slow *viscous circulation* in the oil slick will be proposed as the last extension to the present model, referred to as the Phase III model. This modeling will be done through solving Stokes flow equations within the oil slick. The main characteristics for the Phase II and III models are summarized in Fig. 1.5.

In the Phase I model, VS's will be discretized by *piecewise-constant elements* of vorticity. This represents an improvement over most existing VS models which use less accurate point vortices to discretize vortex sheets (e.g., Zalosh, 1974, 1976; Zalosh and Jensen, 1975; Rangel and Sirignano, 1988). [In the Phase II model, however, we are planning on using higher-order elements to represent VS's and thus providing better accuracy for the representation of interfacial waves.] *Time evolution* of the vortex sheets at the oil-water interface will be computed using an equation that accounts for both the oil-water density difference and interfacial tension effects (Zaroodny and Greenberg, 1973; Fink and Soh, 1974; Zalosh, 1974, 1976; Zalosh and Jensen, 1975; Rangel and Sirignano, 1988). Details of the Phase I model equations, and numerical algorithms and implementation are given in Chapter 2 and 3, respectively.

---

stabilizing forces reducing interfacial waves. Hence, the present model is likely to slightly overpredict the growth of interfacial instabilities.

Chapter 2

General equations for the dynamics of vortex sheets

2.1 Velocity-vorticity equations for a vortex sheet

For inviscid, incompressible, uniform fluids in two-dimensional motion in the plane (x, y) (e.g., Fig. 1.2), with vorticity, $\boldsymbol{\omega}(x, y) = \omega(x, y)\nabla z$, the velocity, $\boldsymbol{u} = (u, v)$, can be calculated for points (x, y) according to the Biot-Savart law (Batchelor, 1967, p84) as,

$$\begin{aligned} u(x,y) &= -\frac{1}{2\pi}\int\int \frac{y-y'}{r^2}\,\omega(x',y')\,dx'\,dy' \\ v(x,y) &= \frac{1}{2\pi}\int\int \frac{x-x'}{r^2}\,\omega(x',y')\,dx'\,dy' \end{aligned} \tag{2.1}$$

with

$$r(x,y,x',y') = \{(x-x')^2 + (y-y')^2\}^{1/2} \tag{2.2}$$

When vorticity is concentrated within *vortex sheets* or within *point vortices* aligned as a sheet, equations (2.1) transform into (Batchelor, 1967, p527),

$$\begin{aligned} u(x,y) &= \frac{1}{2\pi}\int \frac{y-y'}{r^2}\,\gamma(s)\,ds \\ v(x,y) &= -\frac{1}{2\pi}\int \frac{x-x'}{r^2}\,\gamma(s)\,ds \end{aligned} \tag{2.3}$$

where, $\gamma(s) = -\omega(x', y')$, is the *clockwise* vortex sheet strength and $s(x', y')$ is the curvilinear abscissa along the sheet.

When points, $\boldsymbol{x} = (x, y)$, do not belong to the sheet, integrals in (2.3) are non-singular. For points (x, y) within the sheet, integrals in (2.3) are singular for vanishing r and must thus be calculated in a Cauchy Principal Value (CPV) sense. In this case, (2.3) also takes the form of a Boundary Integral Equation (BIE) for $\boldsymbol{u}(x, y)$ on the sheet.

In the numerical model that will be developed to track the motion of vortex sheets representing interfaces between fluids (see Chapter 3), various discretized expressions of

(2.3) will be used to calculate the sheet position as a function of time, according to the Lagrangian definition of velocities,

$$\frac{d\boldsymbol{x}}{dt}(t) = \boldsymbol{u}(x, y) \tag{2.4}$$

where the time derivative follows the motion of the sheet (see below for detail).

2.2 Piecewise constant vorticity and point vortices

A standard simplifying assumption in modeling studies using Biot-Savart law is to assume that the vorticity in vortex sheets is either *piecewise constant* or is concentrated at *point vortices*. Despite their similarity—and sometimes their confusion in the literature—, these two representations differ in the sense that point vortices do not have a self-induced velocity contribution to Eqs. (2.3) whereas piecewise constant distributions of vortices do have self-induced velocity at the center of each interval, due to CPV integral contributions in (2.3) (Fink and Soh, 1974; Van de Vooren, 1980; Rangel and Sirignano, 1988). Finally, point vortices essentially specify an isotropic flow around their center whereas, for vortex sheets (even with piecewise-constant vorticity distribution), the flow is essentially inhomogeneous for the directions tangent and perpendicular to the sheet.

Differences and similarities between these approaches have been somewhat controversial in the literature and will be detailed in the following.

2.2.1 Point vortices

For point vortices, the vortex sheet is replaced by a series of N equal length segments containing a point vortex of strength (i.e., circulation) Γ_i at the mid-point of each segment.

Since there is no self-induced velocity for point vortices (e.g., Batchelor, 1967, p530), equations (2.3) reduce to,

$$\begin{aligned} u(x_i, y_i) \equiv u_i &= \frac{1}{2\pi} \sum_{j \neq i} \frac{y_i - y_j}{r_{ij}^2} \Gamma_j \\ v(x_i, y_i) \equiv v_i &= -\frac{1}{2\pi} \sum_{j \neq i} \frac{x_i - x_j}{r_{ij}^2} \Gamma_j \end{aligned} \tag{2.5}$$

for $(i, j = 1, ..., N)$, and,

$$r_{ij} = \{(x_i - x_j)^2 + (y_i - y_j)^2\}^{1/2} \tag{2.6}$$

These are essentially the equations used in Zalosh (1974,1976).

2.2.2 Piecewise constant vortices

As pointed out by several authors (Fink and Soh, 1974; Van de Vooren, 1980; Rangel and Sirignano, 1988), point vortices are a poor representation for a continuous vortex sheet—for instance representing the interface between two fluids—and usually quickly lead to inaccurate or even to unstable results, when used to calculate the dynamics of vortex sheets as a function of time. This seems unless point vortices are continuously regridded to equal arc-length distance on the sheet (Fink and Soh, 1974). The reason for this will be clear from the following.

Vortex sheets in fact represent a continuous (line) vorticity variation which can be well represented by a piecewise polynomial distribution of vorticity, similar to Boundary Elements used in continuum mechanics (e.g. Brebbia, 1978). The simplest possible representation is made of N piecewise-constant elements of vorticity density, $\gamma(s_i) = \gamma_i$.

Doing so, (2.3) transforms into,

$$\begin{aligned} u_i &= \frac{1}{2\pi}\sum_{j=1}^{N}\gamma_j \int_{s_j-\Delta s_j/2}^{s_j+\Delta s_j/2} \frac{y_i - y}{r_i^2}\, ds \\ v_i &= -\frac{1}{2\pi}\sum_{j=1}^{N}\gamma_j \int_{s_j-\Delta s_j/2}^{s_j+\Delta s_j/2} \frac{x_i - x}{r_i^2}\, ds \end{aligned} \tag{2.7}$$

for $(i = 1, ..., N)$, and,

$$r_i = \{(x - x_i)^2 + (y - y_i)^2\}^{1/2} \tag{2.8}$$

When assuming that the geometry within each vortex element is smoothly varying and can thus be approximated by values at mid-point s_i of each element, and denoting by, $\Gamma_i = \gamma_i \Delta s_i$, the circulation attributed to each element i (see geometric explanation of this in Section 2.3), (2.7) reduces to (2.5) for $j \neq i$.

For cases with, $j = i$, however, integrals in (2.7) are singular and CPV's must be calculated. This is easily done using either polar coordinates or complex notations and one finds (e.g., Fink and Soh, 1974),

$$\begin{aligned} u_i &= \frac{1}{2\pi}\sum_{j\neq i}\frac{y_i - y_j}{r_{ij}^2}\Gamma_j - \frac{1}{2\pi}\frac{\Gamma_i}{\Delta s_i}\sin\theta_i \log\frac{r_{i+1/2}}{r_{i-1/2}} \\ v_i &= -\frac{1}{2\pi}\sum_{j\neq i}\frac{x_i - x_j}{r_{ij}^2}\Gamma_j + \frac{1}{2\pi}\frac{\Gamma_i}{\Delta s_i}\cos\theta_i \log\frac{r_{i+1/2}}{r_{i-1/2}} \end{aligned} \tag{2.9}$$

for $(i = 1, ..., N)$; where θ_i is the angle between the x-axis and segment i, and $[r_{i-1/2}, r_{i+1/2}]$ denote distances from both extremities to the mid-point of segment i. Terms with logarithmic variations in (2.9) represent CPV's contributions to velocity (u_i, v_i). It is easy to see in Eq. (2.9) that these contributions disappear when vortex elements are regridded to equal arclength distance[1] so that, $r_{i-1/2} = r_{i+1/2}$.

[1]This was the method used by Rangel and Sirignano (1988) to avoid calculating CPV integrals.

Thus, when regridding is used or when vortex elements do not change length too much as a function of time (actually over one time step in numerical calculations; see Chapter 3), Eqs. (2.5) and (2.7) are essentially identical and the discrete vortex method provides the same results as the piecewise constant vortex elements. When, either regridding is not used or when the length of vortex elements significantly changes with time, CPV's terms provide significant contributions in (2.9) and the assumption of discrete vortices is unacceptable [2]. This is the likely reason why Zalosh (1974,1976), who used discrete vortices and no regridding was unable to pursue computations for a long time without experiencing numerical instability whereas Rangel and Sirignano (1988), who also used discrete vortices but performed regridding at each time step, were able to calculate the development of Kelvin-Helmholtz instability and rolling-up of vortex sheets at an interface, for a fairly long time (see Fink and Soh, 1974; and Van de Vooren, 1980, for discussions of this and other related problems).

As we will see in Chapter 3, with a piecewise-constant representation of vortex sheets, it is not possible to satisfy all dynamic equilibrium equations of vortex sheets when performing regridding of the discretization to equal arc-length distance. Therefore, in the present model, it will be necessary to accurately calculate CPV integrals representing self-induced velocity contributions.

2.3 Vorticity dynamics equations for a vortex sheet

2.3.1 Circulation on a vortex sheet

Along a material contour $[0, s]$, circulation is defined as (Batchelor, 1967),

$$\Gamma(s) \equiv \int_o^s d\Gamma = \int_o^s \boldsymbol{u} \cdot d\boldsymbol{s}' \tag{2.10}$$

where s denotes the curvilinear abscissa and $d\boldsymbol{s}'$ is the tangential vector element along the contour.

For a vortex sheet representing the interface between two fluids, following Zalosh (1974, 1976), Van de Vooren (1980), and Rangel and Sirignano (1988), the elementary circulation $d\Gamma$ can be calculated by isolating an element of interface of small but finite thickness and considering a contour crossing the interface, as,

$$d\Gamma \equiv \gamma(s)\, ds = \Delta\boldsymbol{u} \cdot d\boldsymbol{s} = \Delta u_s\, ds \tag{2.11}$$

in which $\Delta\boldsymbol{u}$ and Δu_s denote jumps of fluid velocity and tangential fluid velocity across the interface, respectively.

[2] One would see, for instance, that if elements (i.e., boundary segments) are very much stretched or become very small, CPV terms in (2.9) provide almost singular (i.e., very large) contributions, whereas discrete vortices approaching each other would not exhibit this behavior in (2.5).

Equation (2.11) implies that, for a vortex sheet at the *interface between two fluids* moving with velocity $\boldsymbol{u}_o$ and $\boldsymbol{u}_1$, respectively, the vortex sheet strength is given by,

$$\gamma(s) = \Delta u_s = u_{os} - u_{1s} \tag{2.12}$$

in which,

$$u_{os} = \boldsymbol{u}_o \cdot \boldsymbol{s} \quad ; \quad u_{1s} = \boldsymbol{u}_1 \cdot \boldsymbol{s} \quad ; \quad \boldsymbol{s} = [\cos\beta, \sin\beta] \tag{2.13}$$

where $\boldsymbol{s}$ is the tangential vector along the sheet and $\beta(s)$ is the angle between the tangent to the sheet and the x-axis [3].

If we now calculate the circulation associated with a small vortex element i of length Δs_i, over which we can assume constant velocity and smoothly varying geometry, (2.10)-(2.12) transform into,

$$\Gamma(s_i) \equiv \Gamma_i = \int_{s_i-\Delta s_i/2}^{s_i+\Delta s_i/2} (\, u_{os} - u_{1s}\,)\, ds \simeq (\, u_{os} - u_{1s}\,)_i\, \Delta s_i = \gamma_i \Delta s_i \tag{2.14}$$

2.3.2 Rate of change of circulation for a vortex sheet

For a uniform, incompressible, inviscid fluid with conservative forces, Kelvin's theorem states that the rate of change of circulation around a closed material contour moving with the fluid is zero (e.g., Batchelor, 1967),

$$\frac{D\Gamma}{Dt} = 0 \qquad \text{with} \qquad \frac{D}{Dt} \equiv \frac{\partial}{\partial t} + \boldsymbol{u} \cdot \boldsymbol{\nabla} \tag{2.15}$$

where D/Dt denotes the material derivative.

For a vortex sheet at the interface between two regions of different velocity within the same fluid (e.g., jet, shear current), however, Van de Vooren (1980) clearly showed that a contour crossing the interface and moving with the fluid does not remain closed. Hence, Kelvin's theorem as stated in (2.15) is not applicable. Kelvin's theorem may only be applied for a contour moving with the reference velocity, $\boldsymbol{u} = \frac{1}{2}(\boldsymbol{u}_o + \boldsymbol{u}_1)$, equal to the mean between velocities on both sides of the sheet. This reference velocity will be referred to as the *sheet velocity* and will be used whenever calculating material time derivatives with respect to the sheet motion, referred to as d/dt.

For the interface between two different fluids with density ρ_o and ρ_1, and non-zero interfacial tension σ_{o1}, the fluid is non-uniform and forces are non-conservatives. Hence the rate of change of circulation around a material contour crossing the interface is non-zero and an evolution equation must be developed for it. Zaroodny and Greenberg (1973) first derived an equation for the rate of change of circulation for a continuous vortex sheet without surface tension. Zalosh (1974,1976) developed a similar equation, including surface tension effects, for a sheet discretized with discrete vortices but made an error when he failed to

[3]Note that β and θ, introduced earlier, have different definitions but that, for calculations of self-induced velocity of piecewise constant vortex sheet elements, these angles have the same value.

consider the difference mentioned above between time derivatives, D/Dt, following fluid particles on either side of the sheet and those, d/dt, following the sheet motion. This was pointed out in a discussion by Rottman and Olfe (1977). Rangel and Sirignano (1988) derived the correct evolution equation but without including gravity effects.

The following is a derivation of the rate of change of circulation, including both gravity and surface tension effects at the interface between two fluids, for a vortex sheet with piecewise constant vorticity elements. Taking the material time derivative of the circulation equation (2.10), we get,

$$\frac{D\Gamma}{Dt}(s) = \int_o^s \frac{D\boldsymbol{u}}{Dt} \cdot d\boldsymbol{s}' + \int_o^s \boldsymbol{u}(s') \cdot d(\frac{D\boldsymbol{s}'}{Dt}) \tag{2.16}$$

Because the material derivative follows the fluid particles, we have, by the Lagrangian definition of velocity, $D\boldsymbol{s}'/Dt = \boldsymbol{u}(s')$, and the dot product in the second integral is zero. Hence, using (2.11),(2.12),(2.13),

$$\frac{D\Gamma}{Dt}(s) = \int_o^s (\frac{Du_{os}}{Dt} - \frac{Du_{1s}}{Dt})\, ds \tag{2.17}$$

As done in equation (2.14) for the circulation, we can now use (2.17) to calculate the rate of change of circulation associated with a small vortex element i of length Δs_i, over which we can assume constant velocity and smoothly varying geometry,

$$\frac{D\Gamma}{Dt}(s_i) \equiv \frac{D\Gamma_i}{Dt} = \int_{s_i-\Delta s_i/2}^{s_i+\Delta s_i/2} (\frac{Du_{os}}{Dt} - \frac{Du_{1s}}{Dt})\, ds \simeq (\frac{Du_{os}}{Dt} - \frac{Du_{1s}}{Dt})_i \Delta s_i \tag{2.18}$$

Tangential accelerations in (2.18) can be expressed for both fluids using Euler's equations,

$$\frac{D\boldsymbol{u}_{o,1}}{Dt} = -\frac{1}{\rho_{o,1}} \nabla p_{o,1} - g\nabla y \tag{2.19}$$

in which subscripts denote fluid 0 or 1, p is the fluid pressure (discontinuous across the interface due to surface tension) and g is the acceleration of gravity (vertical pointing in the downward y direction). Taking the dot product of (2.19) with the tangential vector $\boldsymbol{s}$, we get,

$$\frac{Du_{os,1s}}{Dt} = -\frac{1}{\rho_{o,1}} \frac{\partial p_{o,1}}{\partial s} - g \sin\beta \tag{2.20}$$

Replacing tangential accelerations from (2.20) in (2.18), we get,

$$\frac{D\Gamma_i}{Dt} = (\frac{1}{\rho_1}\frac{\partial p_1}{\partial s} - \frac{1}{\rho_o}\frac{\partial p_o}{\partial s})_i \Delta s_i \tag{2.21}$$

From the definition of the *sheet velocity*, $\boldsymbol{u}$, the tangential acceleration following the vortex sheet is obtained as,

$$\frac{du_{si}}{dt} = \frac{1}{2}(\frac{du_{os}}{dt} + \frac{du_{1s}}{dt})_i \tag{2.22}$$

with, according to the definitions of different material derivatives,

$$\frac{d}{dt} = \frac{D}{Dt} \pm \frac{1}{2}(\boldsymbol{u}_o - \boldsymbol{u}_1) \cdot \nabla \tag{2.23}$$

with the plus sign being taken in fluid 1 and the minus sign in fluid 0. Using (2.23) in (2.22), we get,

$$\frac{du_{si}}{dt} = \frac{1}{2}(\frac{D\,u_{os}}{D\,t} + \frac{D\,u_{1s}}{D\,t})_i - \frac{1}{4}(u_{os} - u_{1s})_i(\frac{\partial u_{os}}{\partial s} - \frac{\partial u_{1s}}{\partial s})_i \tag{2.24}$$

Finally, using Euler equations (2.20) for the tangential velocities and equation (2.12) for the vortex sheet strength, we get,

$$\frac{du_{si}}{dt} = -\frac{1}{2}(\frac{1}{\rho_o}\frac{\partial p_o}{\partial s} + \frac{1}{\rho_1}\frac{\partial p_1}{\partial s} + 2g\,\sin\beta)_i - \frac{1}{4}\gamma_i\frac{\partial \gamma_i}{\partial s} \tag{2.25}$$

Due to a confusion between different material derivatives, the last term in equation (2.25) was missing in Zalosh's (1974,1976) equations.

From the expression of surface tension effects at the interface between two fluids (Batchelor, 1967), the pressure jump across the vortex sheet is given by,

$$p_o - p_1 = \sigma_{o1}\frac{1}{\mathcal{R}} \tag{2.26}$$

in which $1/\mathcal{R}(s)$ is the sheet curvature. In curvilinear coordinates, it can easily be shown that the curvature is identical to, $\partial\beta/\partial s$. Hence, taking the tangential derivative of (2.26), we get,

$$\frac{\partial p_o}{\partial s} - \frac{\partial p_1}{\partial s} = \sigma_{o1}\frac{\partial^2\beta}{\partial s^2} \tag{2.27}$$

Eliminating the pressure between equations (2.21),(2.25), and (2.27), we finally get the rate of change of circulation at point s_i of the sheet as,

$$\frac{D\,\Gamma_i}{D\,t} = 2\kappa\,\Delta s_i\left(\frac{du_{si}}{dt} + g\,\sin\beta_i + \frac{1}{4}\gamma_i\frac{\partial\gamma_i}{\partial s}\right) - \frac{2\sigma_{o1}}{\rho_o + \rho_1}\Delta s_i\frac{\partial^2\beta_i}{\partial s^2} \tag{2.28}$$

where $\kappa = (\rho_1 - \rho_o)/(\rho_1 + \rho_o)$, by (2.14), $\gamma_i = \Gamma_i/\Delta s_i$, and by (2.13),

$$\frac{du_{si}}{dt} = \frac{du_i}{dt}\cos\beta_i + \frac{dv_i}{dt}\sin\beta_i \tag{2.29}$$

2.3.3 Acceleration-rate of change of circulation equations for a vortex sheet

Equation (2.28) contains tangential acceleration terms along the vortex sheet, du_{si}/dt proportional to fluid acceleration on the sheet (2.29). In most earlier numerical models of unsteady motion of vortex sheets, accelerations were calculated by backward finite differentiation (Zalosh, 1974, 1976; Zalosh and Jensen, 1975; Rangel and Sirignano, 1988). As

suggested (without detail) by Rangel and Sirignano (1991), however, accelerations can also be calculated by direct time differentiation of Biot-Savart equations (2.3). When carried out under the integral signs following Leibnitz rule, such a differentiation creates terms proportional to both Γ_i and $D\Gamma_i/Dt$. Hence, rates of change of circulation $D\Gamma_i/Dt$ can be iteratively calculated using (2.28) and this expression of accelerations (see Section 3.1.3). Note that limits of integrations, say $s_a(t)$ and $s_b(t)$, have to be set in (2.3) for the variable $s(t)$ before carrying out time differentiation.

In their time differentiation of (2.3), however, it is not clear whether Rangel and Sirignano (1991) accounted for various CPV integrals. In fact, since they altogether avoided calculating such terms for the velocities in (2.9) by using a regridding method (see discussion in previous Section), we believe that they simply calculated accelerations by time differentiating the equivalent [4] of (2.5),(2.6).

In the following, accelerations are calculated by time differentiation of (2.3), assuming a vortex sheet with a piecewise-constant distribution of N vortex elements along curve, $[s_a(t), s_b(t)] = \sum_{j=1}^{N} \Delta s_j(t)$, and taking into account CPV integrals resulting from self-induced velocities. In the numerical model, accelerations will be explicitly replaced in (2.28), as a function of Γ_i and $D\Gamma_i/Dt$, and rates of change of circulation $D\Gamma_i/Dt$ will be explicitly calculated.

Thus, by (absolute) time differentiation (2.3) following the motion of point, $\boldsymbol{x} = (x, y)$ on the vortex sheet as well as changes along the sheet at points $\boldsymbol{x}' = (x', y')$, and with (2.11), we obtain for, $i = 1, ..., N$,

$$\begin{aligned}
\frac{du_i}{dt} &= \frac{1}{2\pi}\sum_{j=1}^{N}\frac{d}{dt}\Big\{\int_{\Delta s_j}\frac{y_i - y'}{r_i^2}\gamma\, ds'\Big\} \\
\frac{dv_i}{dt} &= -\frac{1}{2\pi}\sum_{j=1}^{N}\frac{d}{dt}\Big\{\int_{\Delta s_j}\frac{x_i - x'}{r_i^2}\gamma\, ds'\Big\}
\end{aligned} \tag{2.30}$$

which, by applying Leibnitz rule and isolating CPV integrals (last terms), reads,

$$\begin{aligned}
\frac{du_i}{dt} &= \frac{1}{2\pi}\Big\{\sum_{j\neq i}\frac{d}{dt}[\frac{y_i - y_j}{r_{ij}^2}]\Gamma_j + \sum_{j\neq i}\frac{y_i - y_j}{r_{ij}^2}\frac{d\Gamma_j}{dt} + \sum_{j\neq i}\gamma_j \\
&\quad [\frac{y_i - y_{j+1/2}}{r_{i,j+1/2}^2}\frac{ds_{j+1/2}}{dt} - \frac{y_i - y_{j-1/2}}{r_{i,j-1/2}^2}\frac{ds_{j-1/2}}{dt}] + \frac{d}{dt}\Big(\int_{\Delta s_i}\frac{y_i - y'}{r_i^2}\gamma\, ds'\Big)\Big\} \\
\frac{dv_i}{dt} &= -\frac{1}{2\pi}\Big\{\sum_{j\neq i}\frac{d}{dt}\frac{x_i - x_j}{r_{ij}^2}\Gamma_j + \sum_{j\neq i}\frac{x_i - x_j}{r_{ij}^2}\frac{d\Gamma_j}{dt} + \sum_{j\neq i}\gamma_j \\
&\quad [\frac{x_i - x_{j+1/2}}{r_{i,j+1/2}^2}\frac{ds_{j+1/2}}{dt} - \frac{x_i - x_{j-1/2}}{r_{i,j-1/2}^2}\frac{ds_{j-1/2}}{dt}] + \frac{d}{dt}\Big(\int_{\Delta s_i}\frac{x_i - x'}{r_i^2}\gamma\, ds'\Big)\Big\}
\end{aligned} \tag{2.31}$$

[4]Note that in Zalosh (1976), Van de Vooren (1980), and Rangel and Sirignano (1988,1991), periodic problems were solved for which (2.5) was replaced by a different expression assuming a spatial periodicity λ, for the interface shape.

where r is given by (2.2), r_i by (2.8), r_{ij} by (2.6), and $(d\gamma_j/dt)\,\Delta s_j = d\Gamma_j/dt$.

Last terms in Eq. (2.31), for both components of the acceleration, represent CPV integrals that can be calculated following the procedure used for the CPV integrals for the velocity components (see Eq. (2.9)). We get,

$$\begin{aligned}
\frac{d\tilde{u}_i}{dt} &= \frac{1}{2\pi}\frac{d}{dt}\Big\{\int_{\Delta s_i}\frac{y_i - y'}{r_i^2}\,\gamma\,ds'\Big\} = \frac{1}{2\pi}\frac{d}{dt}\Big\{\frac{\Gamma_i}{\Delta s_i}\,\sin\theta_i\,\log\frac{r_{i+1/2}}{r_{i-1/2}}\Big\} \\
\frac{d\tilde{v}_i}{dt} &= -\frac{1}{2\pi}\frac{d}{dt}\Big\{\int_{\Delta s_i}\frac{x_i - x'}{r_i^2}\,\gamma\,ds'\Big\} = -\frac{1}{2\pi}\frac{d}{dt}\Big\{\frac{\Gamma_i}{\Delta s_i}\,\cos\theta_i\,\log\frac{r_{i+1/2}}{r_{i-1/2}}\Big\}
\end{aligned} \tag{2.32}$$

where $[r_{i-1/2}, r_{i+1/2}]$ denote distances from both extremities to the mid-point of segment i.

In the first terms of Eq. (2.31) we have, for both components of the acceleration,

$$\begin{aligned}
\frac{dr_{ij}}{dt} &= \frac{(u_i - u_j)(x_i - x_j) + (v_i - v_j)(y_i - y_j)}{r_{ij}} \\
&= -(u_i - u_j)\cos\theta_{ij} - (v_i - v_j)\sin\theta_{ij}
\end{aligned} \tag{2.33}$$

where Eq. (2.4) has been used and θ_{ij} denotes the angle between the vector from point i to j and the x-axis. Hence, using (2.33), we get,

$$\begin{aligned}
\frac{d}{dt}\Big[\frac{x_i - x_j}{r_{ij}^2}\Big] &= -\frac{(u_i - u_j)\,[(x_i - x_j)^2 - (y_i - y_j)^2] + 2(v_i - v_j)(x_i - x_j)(y_i - y_j)}{r_{ij}^4} \\
&= -\frac{1}{r_{ij}^2}\{(u_i - u_j)\cos 2\theta_{ij} + (v_i - v_j)\sin 2\theta_{ij}\} \\
\frac{d}{dt}\Big[\frac{y_i - y_j}{r_{ij}^2}\Big] &= \frac{(v_i - v_j)\,[(x_i - x_j)^2 - (y_i - y_j)^2] - 2(u_i - u_j)(x_i - x_j)(y_i - y_j)}{r_{ij}^4} \\
&= \frac{1}{r_{ij}^2}\{(v_i - v_j)\cos 2\theta_{ij} - (u_i - u_j)\sin 2\theta_{ij}\}
\end{aligned} \tag{2.34}$$

Terms involving time derivatives of $(s_{j+1/2}, s_{j-1/2})$ in Eq. (2.31) represent contributions to the acceleration obtained by applying Leibnitz's rule in Eq. (2.30). For piecewise constant vortex elements, as usual, we can assume that the geometry is approximated by values at the center point of the elements. Hence, third summations in (2.31) can be simplified as,

$$\begin{aligned}
\sum_{j\neq i}\gamma_j\Big[\frac{y_i - y_{j+1/2}}{r_{i,j+1/2}^2}\frac{ds_{j+1/2}}{dt} - \frac{y_i - y_{j-1/2}}{r_{i,j-1/2}^2}\frac{ds_{j-1/2}}{dt}\Big] &\simeq \sum_{j\neq i}\gamma_j\frac{y_i - y_j}{r_{ij}^2}\frac{d\Delta s_j}{dt} \\
\sum_{j\neq i}\gamma_j\Big[\frac{x_i - x_{j+1/2}}{r_{i,j+1/2}^2}\frac{ds_{j+1/2}}{dt} - \frac{x_i - x_{j-1/2}}{r_{i,j-1/2}^2}\frac{ds_{j-1/2}}{dt}\Big] &\simeq \sum_{j\neq i}\gamma_j\frac{x_i - x_j}{r_{ij}^2}\frac{d\Delta s_j}{dt}
\end{aligned} \tag{2.35}$$

where $\Delta s_j = s_{j+1/2} - s_{j-1/2}$ is the length of segment j. Furthermore, by definition of $s(x,y)$ and using (2.4) for the velocity, we have,

$$\begin{aligned}
\frac{d\Delta s_j}{dt} &= \frac{ds_{j+1/2}}{dt} - \frac{ds_{j-1/2}}{dt} \\
&= \{u_{j+1/2}\frac{\partial x_{j+1/2}}{\partial s} + v_{j+1/2}\frac{\partial y_{j+1/2}}{\partial s}\} - \{u_{j-1/2}\frac{\partial x_{j-1/2}}{\partial s} + v_{j-1/2}\frac{\partial y_{j-1/2}}{\partial s}\} \\
&= (u_{j+1/2} - u_{j-1/2})\cos\theta_j + (v_{j+1/2} - v_{j-1/2})\sin\theta_j \qquad (2.36)
\end{aligned}$$

where the piecewise-constant segment approximation has been used, with θ_j the angle between the x-axis and segment j. Hence Eq. (2.36) represents effects of differential velocity between extremities of segment j.

Combining Eqs. (2.31)-(2.32), we get,

$$\begin{aligned}
\frac{du_i}{dt} &= \frac{1}{2\pi}\Big\{\sum_{j\neq i}\frac{\Gamma_j}{r_{ij}^2}\{(v_i - v_j)\cos 2\theta_{ij} - (u_i - u_j)\sin 2\theta_{ij}\} \\
&+ \sum_{j\neq i}\frac{y_i - y_j}{r_{ij}^2}\frac{d\Gamma_j}{dt} + \sum_{j\neq i}\frac{y_i - y_j}{r_{ij}^2}\frac{\Gamma_j}{\Delta s_j}\frac{d\Delta s_j}{dt}\Big\} + \frac{d\tilde{u}_i}{dt} \\
\frac{dv_i}{dt} &= \frac{1}{2\pi}\Big\{\sum_{j\neq i}\frac{\Gamma_j}{r_{ij}^2}\{(u_i - u_j)\cos 2\theta_{ij} + (v_i - v_j)\sin 2\theta_{ij}\} \\
&- \sum_{j\neq i}\frac{x_i - x_j}{r_{ij}^2}\frac{d\Gamma_j}{dt} - \sum_{j\neq i}\frac{x_i - x_j}{r_{ij}^2}\frac{\Gamma_j}{\Delta s_j}\frac{d\Delta s_j}{dt}\Big\} + \frac{d\tilde{v}_i}{dt} \qquad (2.37)
\end{aligned}$$

in which $d\Delta s_j/dt$ is given by Eq. (2.36).

The CPV integrals in Eq. (2.37) can be calculated using Eq. (2.32) and applying Leibnitz's theorem. After some algebrá, we get,

$$\begin{aligned}
\frac{d\tilde{u}_i}{dt} &= \frac{1}{2\pi}\frac{d\Gamma_i}{dt}\frac{\sin\theta_i}{\Delta s_i}\log\frac{r_{i+1/2}}{r_{i-1/2}} + \frac{1}{2\pi}\frac{\Gamma_i}{\Delta s_i}\Big\{\frac{1}{\Delta s_i}\log\frac{r_{i+1/2}}{r_{i-1/2}} \\
&\{(v_{i+1/2} - v_{i-1/2})\cos 2\theta_i - (u_{i+1/2} - u_{i-1/2})\sin 2\theta_i\} + \\
&\sin\theta_i\{\cos\theta_i(\frac{u_{i+1/2} - u_i}{r_{i+1/2}} - \frac{u_i - u_{i-1/2}}{r_{i-1/2}}) + \sin\theta_i(\frac{v_{i+1/2} - v_i}{r_{i+1/2}} - \frac{v_i - v_{i-1/2}}{r_{i-1/2}})\}\Big\} \\
\frac{d\tilde{v}_i}{dt} &= -\frac{1}{2\pi}\frac{d\Gamma_i}{dt}\frac{\cos\theta_i}{\Delta s_i}\log\frac{r_{i+1/2}}{r_{i-1/2}} + \frac{1}{2\pi}\frac{\Gamma_i}{\Delta s_i}\Big\{\frac{1}{\Delta s_i}\log\frac{r_{i+1/2}}{r_{i-1/2}} \\
&\{(v_{i+1/2} - v_{i-1/2})\sin 2\theta_i + (u_{i+1/2} - u_{i-1/2})\cos 2\theta_i\} - \\
&\cos\theta_i\{\cos\theta_i(\frac{u_{i+1/2} - u_i}{r_{i+1/2}} - \frac{u_i - u_{i-1/2}}{r_{i-1/2}}) + \sin\theta_i(\frac{v_{i+1/2} - v_i}{r_{i+1/2}} - \frac{v_i - v_{i-1/2}}{r_{i-1/2}})\}\Big\}
\end{aligned}$$

(2.38)

2.3.4 Semi-infinite vortex sheets

As in Zalosh (1974), horizontal semi-infinite vortex sheets will be used in the numerical model in Chapter 3 to represent regions of the water domain with constant uniform horizontal

velocity U. In Fig. 2, this corresponds to free surface and bottom regions both in front of the slick (from $x = -\infty$ to $x = x_\ell$) and behind the boom (from $x = x_r$ to $x = +\infty$).

Assuming no air velocity and no flow in the bottom, these semi-infinite sheets have a tangential velocity jump, $\Delta u_s = \pm U$ (with the negative sign being taken on the free surface and the positive sign on the bottom).

When part of the fluid domain is discretized with point vortices or piecewise-constant vortex elements, such semi-infinite vortex sheets provide contributions to the discretized forms, (2.5) or (2.9), of Biot-Savart integrals (2.3) for the sheet velocity and also to equation (2.37), for the sheet acceleration. These contributions are calculated in the following.

Let us first calculate the contribution to the velocity field, $\boldsymbol{u}_\ell$, of a horizontal sheet at depth $y = y_\ell$, with velocity jump, $\Delta u_{s\ell}$, from $x = -\infty$ to $x = x_\ell$,

$$\begin{aligned} u_\ell(x,y) &= +\frac{1}{2\pi}\Delta u_{s\ell}\int_{-\infty}^{x_\ell}\frac{y-y_\ell}{(x-x')^2+(y-y_\ell)^2}\,dx' \\ v_\ell(x,y) &= -\frac{1}{2\pi}\Delta u_{s\ell}\int_{-\infty}^{x_\ell}\frac{x-x'}{(x-x')^2+(y-y_\ell)^2}\,dx' \end{aligned} \tag{2.39}$$

Straightforward integration of these equations yields,

$$\begin{aligned} u_\ell(x,y) &= -\frac{1}{2\pi}\Delta u_{s\ell}\{\arctan(\frac{x-x_\ell}{y-y_\ell}) - \frac{\pi}{2}\operatorname{sign}(y-y_\ell)\} \\ v_\ell(x,y) &= +\frac{1}{4\pi}\Delta u_{s\ell}\{\log[(x-x_\ell)^2+(y-y_\ell)^2] \\ &\quad - \lim_{x'\to-\infty}\log[(x-x')^2+(y-y_\ell)^2]\} \end{aligned} \tag{2.40}$$

in which the indefinite limit will disappear when combined with other sheets (see below).

Similarly, we compute the contribution to the velocity field, $\boldsymbol{u}_r$, of a horizontal sheet at depth $y = y_r$, with velocity jump, Δu_{sr}, from $x = x_r$ to $x = +\infty$, as,

$$\begin{aligned} u_r(x,y) &= +\frac{1}{2\pi}\Delta u_{sr}\{\arctan(\frac{x-x_r}{y-y_r}) + \frac{\pi}{2}\operatorname{sign}(y-y_r)\} \\ v_r(x,y) &= -\frac{1}{4\pi}\Delta u_{sr}\{\log[(x-x_r)^2+(y-y_r)^2] \\ &\quad - \lim_{x'\to+\infty}\log[(x-x')^2+(y-y_r)^2]\} \end{aligned} \tag{2.41}$$

Following the same procedure as for the velocity, we can now calculate contributions of semi-infinite vortex sheets to the acceleration field by time derivation of Eq. (2.39) and of a similar equation for the rightward sheets leading to Eq. (2.41). For stationary vortex sheets with constant strength, $\pm U$, simplifications occur and after integrating from $-\infty$ to x_ℓ, for $d\boldsymbol{u}_\ell/dt$, and from x_r to $+\infty$, for $d\boldsymbol{u}_r/dt$, we get,

$$\begin{aligned} \frac{du_\ell}{dt} &= \frac{1}{2\pi}\frac{\Delta u_{s\ell}}{r_\ell^2}\{v(x-x_\ell) - u(y-y_\ell)\} \\ \frac{dv_\ell}{dt} &= \frac{1}{2\pi}\frac{\Delta u_{s\ell}}{r_\ell^2}\{u(x-x_\ell) + v(y-y_\ell)\} \end{aligned} \tag{2.42}$$

and,

$$\begin{aligned}
\frac{du_r}{dt} &= -\frac{1}{2\pi}\frac{\Delta u_{sr}}{r_r^2}\{v(x-x_r) - u(y-y_r)\} \\
\frac{dv_r}{dt} &= -\frac{1}{2\pi}\frac{\Delta u_{sr}}{r_r^2}\{u(x-x_r) + v(y-y_r)\}
\end{aligned} \tag{2.43}$$

with,

$$\begin{aligned}
r_\ell &= \{(x-x_\ell)^2 + (y-y_\ell)^2\}^{1/2} \\
r_r &= \{(x-x_r)^2 + (y-y_r)^2\}^{1/2}
\end{aligned} \tag{2.44}$$

As mentioned above, in the numerical model in Chapter 3, semi-infinite vortex sheets will be used to model parts of the free surface and parts of the bottom. Assuming that the unperturbed free surface is at, $y = 0$ and the horizontal bottom is at, $y = -h$, we can calculate the total contribution to both the velocity and the acceleration field, of four vortex sheets located at $(x_\ell, 0)$ and $(x_r, 0)$, with strength $-U$, and at $(x_\ell, -h)$ and $(x_r, -h)$, with strength $+U$.

First, for the velocity, using (2.40) and (2.41), we get,

$$\begin{aligned}
u_{\ell r} &= \frac{U}{2\pi}\{2\pi + \arctan(\frac{x-x_\ell}{y}) - \arctan(\frac{x-x_\ell}{y+h}) - \arctan(\frac{x-x_r}{y}) + \arctan(\frac{x-x_r}{y+h})\} \\
v_{\ell r} &= \frac{U}{4\pi}\log\frac{[(x-x_r)^2+y^2]\,[(x-x_\ell)^2+(y+h)^2]}{[(x-x_\ell)^2+y^2]\,[(x-x_r)^2+(y+h)^2]}
\end{aligned} \tag{2.45}$$

where, as expected, indefinite limits have cancelled each other. Note that, as a verification, if we take, $x_\ell = x_r$, thus assuming a uniform flow represented by two infinite vortex sheets, we can see that (2.45) indeed reduces to, $u_{\ell r} = U$ and $v_{\ell r} = 0$.

Finally, for the acceleration, it can be seen that all contributions from the four sheets cancel each other and we get, $du_{\ell r}/dt = dv_{\ell r}/dt = 0$.

Chapter 3

Equations for numerical model

3.1 General model equations

3.1.1 Principle of computations

Figure 3.1 gives a sketch of a typical computational domain used in the model, with definition of various parameters.

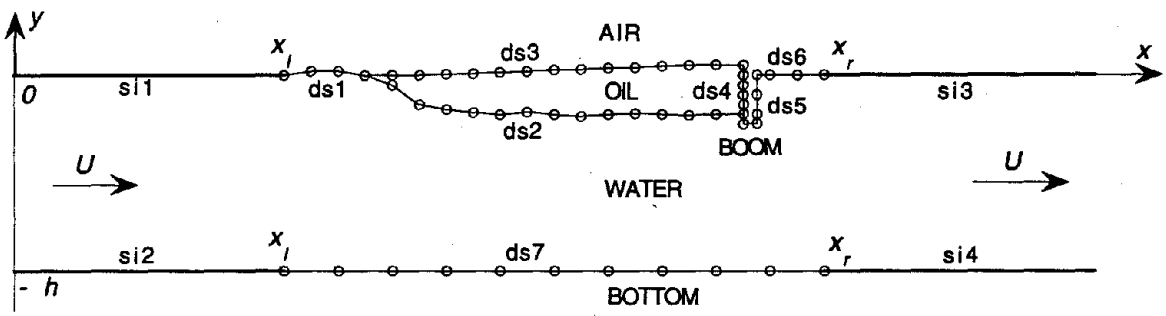

Figure 3.1: Sketch of computational domain with definition of main parameters : U = flow velocity; si1-si4 = semi-infinite vortex sheets; ds1-ds7 = piecewise-constant discretized vortex sheets; o = centers of discretized vortex elements.

In the model, the geometry of boundaries and interfaces is represented using both discretized vortex sheets (ds) with piecewise-constant vorticity distribution and continuous semi-infinite horizontal vortex sheets (si), representing regions of the water domain with constant uniform horizontal velocity U. Vortex sheet dynamics equations for both of these cases have been detailed in Chapter 2.

Contributions of semi-infinite sheets to various integrals presented in Chapter 2 are exactly accounted for in the model, whereas contributions of sheets with piecewise-constant vorticity are discretized using values of both geometry $[(x_i, y_i), \Delta s_i, \theta_i, \beta_i, \partial^2\beta_i/\partial s^2]$ and field variables $[\Gamma_i, d\Gamma_i/dt, (u_i, v_i), (du_i/dt, dv_i/dt)]$ at mid-points ($i = 1, ..., N$) of each constant vortex sheet element (boundary element).

Assuming that both discretized geometry and field variables are known at time t, the numerical model is used to compute these quantities at time $(t + \Delta t)$ (with Δt being a small time step). This can be done by simultaneously integrating vortex sheet dynamics equations in discretized form, (2.9), (2.14), (2.28), (2.29), and (2.37), together with contributions of semi-infinite vortex sheets of the form (2.40)-(2.45). Computation of an initial steady state solution is discussed in Section 3.2.

In earlier models proposed in the literature for solving vortex sheet dynamics equations, implicit iterative methods were used for the integration of equations of the form (2.4), (2.5) (or equivalent for periodic problems; see Chapter 4) and (2.28) (or equivalent), together with iterative or backward finite difference approximations of accelerations (Zalosh, 1974, 1976; Rangel and Sirignano, 1988, 1991). These models, however, often exhibited sawtooth instability of the solution which required smoothing of the geometry after each time step (e.g., Zalosh, 1974). Such instabilities, we believe, are partly due to the non-representation of self-induced velocities of vortex elements and to the implicit iterative scheme used in the models. In the present study, CPV integrals are exactly accounted for and, hence, self-induced velocity contributions are included in the equations and an explicit time stepping method is developed to hopefully improve both the stability and the accuracy of computations.

The explicit time stepping method is based on truncated Taylor series expansions expressed in Lagrangian form for the position and the vorticity value of individual vortex elements (Grilli and Subramanya, 1995). In the present case, second-order Taylor series are used for time updating of both the sheet geometry and circulation as,

$$\begin{aligned}
x_i(t+\Delta t) &= x_i(t)\ \Delta t \frac{dx_i}{dt}(t) + \frac{(\Delta t)^2}{2}\frac{d^2x_i}{dt^2}(t) + \mathcal{O}[(\Delta t)^3] \\
y_i(t+\Delta t) &= y_i(t)\ \Delta t \frac{dy_i}{dt}(t) + \frac{(\Delta t)^2}{2}\frac{d^2y_i}{dt^2}(t) + \mathcal{O}[(\Delta t)^3] \\
\Gamma_i(t+\Delta t) &= \Gamma_i(t)\ \Delta t \frac{d\Gamma_i}{dt}(t) + \frac{(\Delta t)^2}{2}\frac{d^2\Gamma_i}{dt^2}(t) + \mathcal{O}[(\Delta t)^3]
\end{aligned} \tag{3.1}$$

with, using the Lagrangian definition of velocities (2.4),

$$\begin{aligned}
\frac{dx_i}{dt} &= u_i \quad ; \quad \frac{dy_i}{dt} = v_i \\
\frac{d^2x_i}{dt^2} &= \frac{du_i}{dt} \quad ; \quad \frac{d^2y_i}{dt^2} = \frac{dv_i}{dt}
\end{aligned} \tag{3.2}$$

where velocities (u_i, v_i) are given by (2.9), accelerations $(du_i/dt, dv_i/dt)$ are given by (2.37) (with (2.36) and (2.38)), and rates of change of circulation, $d\Gamma_i/dt$, are given by (2.28),(2.29), with contributions of semi-infinite vortex sheets being added to the equations for the velocity and the acceleration as detailed in Chapter 2.

As pointed out before, equations for $(du_i/dt, dv_i/dt)$ and $d\Gamma_i/dt$ are coupled and therefore first must be solved, simultaneously at time t, before accelerations and rates of change of circulation can be used for time stepping of the vortex sheet geometry and circulation to

time $(t + \Delta t)$ using Eqs. (3.1),(3.2). This is discussed in Section 3.1.3 for the explicit time stepping scheme. Also note that second derivatives of circulation needed in Eq. (3.1) are calculated based on backward finite differences as,

$$\frac{d^2\Gamma_i}{dt^2} \simeq \frac{1}{\Delta t}\{\frac{d\Gamma_i}{dt}(t) - \frac{d\Gamma_i}{dt}(t - \Delta t)\} \tag{3.3}$$

For sake of comparison with earlier models in the literature, an implicit time stepping scheme has also been implemented in the present model, in which equations for the velocities and the rate of change of vorticity are integrated in time using a standard 4th-order Runge-Kutta scheme. This scheme is based on equations listed in Section 3.1.2 in non-dimensional form, Eqs. (3.9) and (3.13),(3.15). Both explicit and implicit schemes have been used in the applications presented in Chapter 4.

Following a similar approach as in Grilli and Subramanya (1995, 1996), the time step Δt used in the model is adaptively calculated at each time step based on a constant mesh Courant number C_o such that,

$$\Delta t = C_o \frac{\text{Min}(\Delta s_i)}{\text{Max}(|\, u_i \,|)} \tag{3.4}$$

where the numerator represents the minimum length and the denominator represents the maximum velocity of vortex elements at the current time t. A value $C_o \simeq 0.5$ was found to ensure good accuracy and stability of computations in most cases.

In the following subsections, model equations are first put in a non-dimensional form better suited to accurate numerical calculations. The computation of acceleration terms is then presented. This is followed by a discussion of the representation of the geometry using "sliding-elements" for calculating vortex sheet geometry and $\partial/\partial s$ derivatives. A description of the node regridding method used in some applications of the model is given. Finally, the computation of initial slick shape is discussed.

3.1.2 Non-dimensional model equations

In computations, a characteristic length scale is defined as λ and a characteristic time scale as $\lambda/\Delta U$, in which ΔU denotes a characteristic velocity jump at the interface. The non-dimensional time is thus, $\tau = t\Delta U/\lambda$.

Based on these, the following non-dimensional variables are introduced for coordinates of vortex element centers and their arc-length,

$$\xi_i = \frac{x_i}{\lambda} \quad ; \quad \eta_i = \frac{y_i}{\lambda} \quad ; \quad \Delta s_i = \frac{\Delta s_i}{\lambda} \tag{3.5}$$

for the curvature at vortex element centers,

$$c_i = \lambda \frac{\partial \beta}{\partial s} \tag{3.6}$$

for velocities at vortex elements centers,

$$\mathrm{u}_i = \frac{u_i}{\Delta U} \qquad ; \quad \mathrm{v}_i = \frac{v_i}{\Delta U} \tag{3.7}$$

for the vorticity of vortex elements,

$$\mathrm{g}_i = \frac{\Gamma_i}{\lambda \Delta U} \tag{3.8}$$

Using variables (3.5)-(3.8), the rate of change of vorticity of vortex elements, Eq. (2.28), is transformed into ($i = 1, ..., N$),

$$\frac{d\,\mathrm{g}_i}{d\tau} = 2\kappa\,\Delta\mathrm{s}_i \left(\frac{d\,\mathrm{u}_{is}}{d\tau} + \frac{\mathrm{g}_i}{4(\Delta\mathrm{s}_i)^2} \frac{\partial \mathrm{g}_i}{\partial \mathrm{s}} \right) + 2\Delta\mathrm{s}_i \mathbf{Fr}^{-2} \sin\beta_i - 2\Delta\mathrm{s}_i \mathbf{We}^{-1} \frac{\partial \mathrm{c}_i}{\partial \mathrm{s}} \tag{3.9}$$

where **Fr** denotes the Froude number,

$$\mathbf{Fr} = \frac{\Delta U}{\sqrt{g\kappa\lambda}} \tag{3.10}$$

and **We** denotes the Weber number,

$$\mathbf{We} = \frac{\rho_w \lambda (1+s)(\Delta U)^2}{\sigma_{o1}} \tag{3.11}$$

The non-dimensional tangential acceleration at the interface in (3.9) is found using (2.13) and variables (3.5)-(3.8) as ($i = 1, ..., N$),

$$\frac{d\,\mathrm{u}_{is}}{d\tau} = \frac{d\,\mathrm{u}_i}{d\tau} \cos\beta_i + \frac{d\,\mathrm{v}_i}{d\tau} \sin\beta_i \tag{3.12}$$

Velocity components are calculated by Biot-Savart law, using Eqs. (2.9) which, with non-dimensional variables, read ($i = 1, ..., N$),

$$\begin{aligned} \mathrm{u}_i &= \frac{d\xi_i}{d\tau} = \frac{1}{2\pi} \sum_{j \neq i} \frac{\eta_i - \eta_j}{\mathrm{r}_{ij}^2} \mathrm{g}_j - \frac{1}{2\pi} \frac{\mathrm{g}_i}{\Delta\mathrm{s}_i} \sin\theta_i \log \frac{\mathrm{r}_{i+1/2}}{\mathrm{r}_{i-1/2}} + \mathrm{u}_{\ell r} \\ \mathrm{v}_i &= \frac{d\eta_i}{d\tau} = -\frac{1}{2\pi} \sum_{j \neq i} \frac{\xi_i - \xi_j}{\mathrm{r}_{ij}^2} \mathrm{g}_j + \frac{1}{2\pi} \frac{\mathrm{g}_i}{\Delta\mathrm{s}_i} \cos\theta_i \log \frac{\mathrm{r}_{i+1/2}}{\mathrm{r}_{i-1/2}} + \mathrm{v}_{\ell r} \end{aligned} \tag{3.13}$$

with by (2.6),

$$\mathrm{r}_{ij} = \{(\xi_i - \xi_j)^2 + (\eta_i - \eta_j)^2\}^{1/2} \tag{3.14}$$

Contributions $(\mathrm{u}_{\ell r}, \mathrm{v}_{\ell r})$ of semi-infinite vortex sheets have been added to velocities in Eq. (3.13). If 4 semi-infinite sheets are used in the model as shown in Fig. 3.1, we obtain, using Eq. (2.45) in non-dimensional form,

$$\begin{aligned} \mathrm{u}_{\ell r} &= 1 + \frac{1}{2\pi}\{\arctan(\frac{\xi - \xi_\ell}{\eta}) - \arctan(\frac{\xi - \xi_\ell}{\eta + \mathrm{h}}) - \arctan(\frac{\xi - \xi_r}{\eta}) + \arctan(\frac{\xi - \xi_r}{\eta + \mathrm{h}})\} \\ \mathrm{v}_{\ell r} &= \frac{1}{4\pi} \log \frac{[(\xi - \xi_r)^2 + \eta^2]\,[(\xi - \xi_\ell)^2 + (\eta + \mathrm{h})^2]}{[(\xi - \xi_\ell)^2 + \eta^2]\,[(\xi - \xi_r)^2 + (\eta + \mathrm{h})^2]} \end{aligned} \tag{3.15}$$

where $\mathrm{h} = h/\lambda$.

Accelerations $(d\,\mathrm{u}_i/d\tau,\, d\,\mathrm{v}_i/d\tau)$ are calculated for the implicit time stepping scheme using simple backward finite differences. For the explicit scheme, accelerations are calculated using Eq. (2.37) put in non-dimensional form,

$$
\begin{aligned}
\frac{d\,\mathrm{u}_i}{d\tau} &= \frac{1}{2\pi}\Big\{\sum_{j\neq i}\frac{\mathrm{g}_j}{\mathrm{r}_{ij}^2}\{(\mathrm{v}_i-\mathrm{v}_j)\cos 2\theta_{ij} - (\mathrm{u}_i-\mathrm{u}_j)\sin 2\theta_{ij}\} + \sum_{j\neq i}\frac{\eta_i-\eta_j}{\mathrm{r}_{ij}^2}\frac{d\,\mathrm{g}_j}{d\tau} \\
&+ \sum_{j\neq i}\frac{\eta_i-\eta_j}{\mathrm{r}_{ij}^2}\frac{\mathrm{g}_j}{\Delta \mathrm{s}_j}\{(\mathrm{u}_{j+1/2}-\mathrm{u}_{j-1/2})\cos\theta_j + (\mathrm{v}_{j+1/2}-\mathrm{v}_{j-1/2})\sin\theta_j\} \\
&+ \frac{d\,\mathrm{g}_i}{d\tau}\frac{\sin\theta_i}{\Delta \mathrm{s}_i}\log\frac{\mathrm{r}_{i+1/2}}{\mathrm{r}_{i-1/2}} + \frac{\mathrm{g}_i}{\Delta \mathrm{s}_i}\Big\{\frac{1}{\Delta \mathrm{s}_i}\log\frac{\mathrm{r}_{i+1/2}}{\mathrm{r}_{i-1/2}} \\
&\{(\mathrm{v}_{i+1/2}-\mathrm{v}_{i-1/2})\cos 2\theta_i - (\mathrm{u}_{i+1/2}-\mathrm{u}_{i-1/2})\sin 2\theta_i\} + \sin\theta_i \\
&\{\cos\theta_i(\frac{\mathrm{u}_{i+1/2}-\mathrm{u}_i}{\mathrm{r}_{i+1/2}} - \frac{\mathrm{u}_i-\mathrm{u}_{i-1/2}}{\mathrm{r}_{i-1/2}}) + \sin\theta_i(\frac{\mathrm{v}_{i+1/2}-\mathrm{v}_i}{\mathrm{r}_{i+1/2}} - \frac{\mathrm{v}_i-\mathrm{v}_{i-1/2}}{\mathrm{r}_{i-1/2}})\}\Big\}\Big\} \\
\frac{d\,\mathrm{v}_i}{d\tau} &= \frac{1}{2\pi}\Big\{\sum_{j\neq i}\frac{\mathrm{g}_j}{\mathrm{r}_{ij}^2}\{(\mathrm{u}_i-\mathrm{u}_j)\cos 2\theta_{ij} + (\mathrm{v}_i-\mathrm{v}_j)\sin 2\theta_{ij}\} - \sum_{j\neq i}\frac{\xi_i-\xi_j}{\mathrm{r}_{ij}^2}\frac{d\,\mathrm{g}_j}{d\tau} \\
&- \sum_{j\neq i}\frac{\xi_i-\xi_j}{\mathrm{r}_{ij}^2}\frac{\mathrm{g}_j}{\Delta \mathrm{s}_j}\{(\mathrm{u}_{j+1/2}-\mathrm{u}_{j-1/2})\cos\theta_j + (\mathrm{v}_{j+1/2}-\mathrm{v}_{j-1/2})\sin\theta_j\} \\
&- \frac{d\,\mathrm{g}_i}{d\tau}\frac{\cos\theta_i}{\Delta \mathrm{s}_i}\log\frac{\mathrm{r}_{i+1/2}}{\mathrm{r}_{i-1/2}} + \frac{\mathrm{g}_i}{\Delta \mathrm{s}_i}\Big\{\frac{1}{\Delta \mathrm{s}_i}\log\frac{\mathrm{r}_{i+1/2}}{\mathrm{r}_{i-1/2}} \\
&\{(\mathrm{v}_{i+1/2}-\mathrm{v}_{i-1/2})\sin 2\theta_i + (\mathrm{u}_{i+1/2}-\mathrm{u}_{i-1/2})\cos 2\theta_i\} - \cos\theta_i \\
&\{\cos\theta_i(\frac{\mathrm{u}_{i+1/2}-\mathrm{u}_i}{\mathrm{r}_{i+1/2}} - \frac{\mathrm{u}_i-\mathrm{u}_{i-1/2}}{\mathrm{r}_{i-1/2}}) + \sin\theta_i(\frac{\mathrm{v}_{i+1/2}-\mathrm{v}_i}{\mathrm{r}_{i+1/2}} - \frac{\mathrm{v}_i-\mathrm{v}_{i-1/2}}{\mathrm{r}_{i-1/2}})\}\Big\}\Big\}
\end{aligned}
\tag{3.16}
$$

3.1.3 Computation of acceleration terms in explicit scheme

At a given time τ, both the geometry of vortex sheets $(\xi_i, \eta_i, \Delta \mathrm{s}_i, \theta_i)$ and the vorticity g_i are fixed and Eq. (3.13) can thus be used to calculate velocities along the sheets, $(\mathrm{u}_i, \mathrm{v}_i)$.

Hence, Eqs. (3.9) and (3.16) reduce to,

$$
\begin{aligned}
\frac{d\,\mathrm{g}_i}{d\tau} &= \mathcal{F}(\frac{d\,\mathrm{u}_i}{d\tau}, \frac{d\,\mathrm{v}_i}{d\tau}) \\
\frac{d\,\mathrm{u}_i}{d\tau} &= \mathcal{G}_1(\frac{d\,\mathrm{g}_i}{d\tau}) \\
\frac{d\,\mathrm{v}_i}{d\tau} &= \mathcal{G}_2(\frac{d\,\mathrm{g}_i}{d\tau})
\end{aligned}
\tag{3.17}
$$

which represents a coupled system of linear algebraic equations for, $d\,\mathrm{g}_i/d\tau$, and for $(d\,\mathrm{u}_i/d\tau,\, d\,\mathrm{v}_i/d\tau)$, at $i = 1, ..., N$, vortex sheet element centers. In the model, this system is solved by iterations at each time step, before the explicit time stepping (3.1)-(3.3) is

used to update the sheets geometry and vorticity to (dimensionless) time, $\tau + \Delta\tau$ (i.e., time $t + \Delta t$).

3.1.4 Computation of geometry and tangential derivatives

In earlier studies (e.g., Zalosh, 1974), simple lower-order finite difference approximations were used to calculate tangential derivatives along interfaces [1]. For the problems solved in the present study, however, due to the intense roll-up of vortex sheets that occurs when instabilities develop along the oil-water interface, even if a low-order (piecewise-constant) representation is satisfactory for the vorticity, it is necessary to use a higher-order representation of the geometry along interfaces. Roll-up indeed leads to a large curvature of the interface and to enhanced surface tension effects (proportional to second-order tangential derivatives of the slope angle; see Eq. (2.28)) which must be accurately accounted for. Hence, the interfacial slope and the curvature must be continuous between vortex elements which requires using a piecewise representation of the geometry of third-order or better.

A higher-order representation of the geometry can be achieved along a segment of an interface either by defining a sliding polynomial interpolation of the geometry on center nodes of vortex elements $(\xi_i, \eta_i; i = 1, ..., N)$ or by using a cubic spline fit on these nodes. In the model, sliding polynomials are 5-node quartic isoparametric boundary elements in which geometric characteristics are calculated for the middle node of the polynomial. Slope angles β_i and tangential derivatives $\partial/\partial s$ are calculated along the vortex sheets by direct differentiation within the polynomials. To calculate characteristics for the next node along the interface, the sliding polynomial element is moved forward by one node. The polynomial is kept identical for the first 3 nodes and for the last 3 nodes on a sheet. With cubic splines, 2-nodes cubic polynomials are defined in such a way as to maintain continuity of the slope from one polynomial to the other. This method, however, requires knowledge of end slopes on the interface to be used as boundary conditions in the spline analysis. Moreover, due to the multiple-valued interface geometry that occurs during roll-up, it is necessary to simultaneously use two parametric spline approximations of the geometry.

Details about both methods can be found in Grilli and Subramanya (1996). In the applications, the sliding and the spline methods are used either individually or in combination. In the latter case, a *hybrid method* is defined which combines the advantages of both methods to achieve optimal accuracy : (i) the *sliding* method is first used to calculate the slope at both extremities of the computational domain representing an interface; and (ii) the *spline* method is then applied to the whole interface, using the slopes computed in (i) as boundary conditions at both extremities.

More specifically, using either one of the interpolation methods, the angle β along the interface can be expressed as a piecewise analytical expression. Following a classical Boundary Element methodology (e.g., Brebbia, 1978), we define the intrinsic coordinate $\mu \in [-1, +1]$ in a piecewise sliding or in a cubic polynomial interpolation. Under this

[1] This is likely another reason why Zalosh could not follow the time development of interfacial instabilities for very long.

representation, $x(\mu), y(\mu)$ and $s(\mu)$ are expressed in closed form within each piecewise polynomial approximation of the geometry of an interface and we get, for the geometric parameters in the model,

$$\cos\beta = \frac{x_\mu}{s_\mu} \quad , \quad \sin\beta = \frac{y_\mu}{s_\mu} \quad , \quad s_\mu = \{x_\mu^2 + y_\mu^2\}^{1/2} \tag{3.18}$$

and, for the curvature and its gradient along s,

$$\begin{aligned} \frac{\partial\beta}{\partial s} &= \frac{x_\mu y_{\mu\mu} - x_{\mu\mu} y_\mu}{s_\mu^3} \\ \frac{\partial^2\beta}{\partial s^2} &= \frac{1}{s_\mu^5}\left\{ s_\mu \left(y_{\mu\mu\mu} x_\mu - x_{\mu\mu\mu} y_\mu\right) - \frac{3}{s_\mu}\left[x_{\mu\mu} y_{\mu\mu}\left(x_\mu^2 - y_\mu^2\right) - x_\mu y_\mu \left(x_{\mu\mu}^2 - y_{\mu\mu}^2\right)\right]\right\} \end{aligned} \tag{3.19}$$

respectively, in which indices denote total derivatives with respect to the intrinsic coordinate. Note that, in the second equation (3.19), third derivatives of the geometry are needed to calculate curvature gradients along interfaces. This justifies using at least cubic polynomials for the representation of the geometry [2].

3.1.5 Node regridding

Regridding of point vortices was used in earlier works (e.g., by Rangel and Sirignano, 1988, in their study of Kelvin-Helmholtz (KH) instability), to prevent vortices from excessively concentrating in roll-up regions of the interface. Due to the increased length of the interface with time, nodes were added prior to regridding to the initial number of nodes used on the interface and were then regridded to equal arc-length distance. A consequence of regridding was also that the need for evaluating CPV integrals was eliminated (see discussion in Chapter 2).

Grilli and Subramanya (1996) developed a node regridding technique to study breaking surface waves based on a combination of sliding and cubic polynomial interpolations similar to those discussed in the previous Section. This technique was modified to apply to a piecewise constant distribution of vortices. More specifically, a node arc length vector, s_l (with $l = 1, ..., N$) is first calculated for the old locations of nodes/centers-of-vortex-elements on the interface, $\boldsymbol{x}_l$, by computing, $\int_0^{s(\mathbf{x}_l)} ds$, over the entire interface as a summation over vortex elements whose geometry is given by the cubic sliding/spline interpolation method. A boundary section is then defined over which regridding is to be performed and the (arbitrary) number of nodes to be added to or removed from this section is used for computing the new arc length increment within the section. Based on this increment, a new arc length vector, s_l^r, is calculated for regridded nodes and mapped node

[2] In fact, in the applications, to improve the accuracy of computed curvature gradients when cubic splines are used, the third derivatives in (3.19) are calculated within a (second) spline approximation directly built on the first-derivatives.

by node onto s_l, to isolate vortex elements k (old nodes $(k, k+1)$) within which new nodes are located. For each such element, an iterative procedure is used to calculate the intrinsic coordinate μ corresponding to a given component of s_l^r and, based on this, nodal coordinates $\boldsymbol{x}_l = \boldsymbol{x}^k(\mu)$ are re-calculated for the new node locations and, similarly, for the vorticity.

This regridding technique was tested in the present model for the KH instability problem. It was thought that the addition of point vortices to selected regions of the interface with high curvature (i.e., roll-up regions) would make results more accurate. Moreover, regridding had proved efficient in the computations by Rangel and Sirignano (1988) who used point vortices. Initial computational results, however, despite a very accurate evaluation of vorticity at regridded nodes, always showed the occurrence of small irregularities in point vortex motions right after regridding, which quickly grew with time. Such a phenomenon was found to occur no matter how many nodes were added and no matter whether regridding was used on the whole interface or only on part of it.

After a more detailed analysis of the vortex sheet dynamics parameters before and after regridding, it was found that regridding violated kinematic conditions of the discretized vortex sheet system. It can be shown, indeed, that the dynamic equilibrium of a vortex sheet system $[s_o, s_N]$ is governed by values of the following three parameters (Batchelor, 1967),

$$\begin{aligned}
\bar{x}_N &= \frac{1}{\Gamma_{TN}} \int_{s_o}^{s_N} x\,\gamma(s)ds \\
\bar{y}_N &= \frac{1}{\Gamma_{TN}} \int_{s_o}^{s_N} y\,\gamma(s)ds \\
\bar{r}_N &= \frac{1}{\Gamma_{TN}} \int_{s_o}^{s_N} \sqrt{x^2+y^2}\,\gamma(s)ds
\end{aligned} \tag{3.20}$$

where,

$$\Gamma_{TN} = \int_{s_o}^{s_N} \gamma(s)ds \tag{3.21}$$

is the total vorticity on the vortex sheet.

For point vortex systems, these parameters take the forms,

$$\begin{aligned}
\bar{x}_N &= \frac{1}{\Gamma_{TN}} \sum_{i=1}^{N} x_i\,\Gamma_i \\
\bar{y}_N &= \frac{1}{\Gamma_{TN}} \sum_{i=1}^{N} y_i\,\Gamma_i \\
\bar{r}_N &= \frac{1}{\Gamma_{TN}} \sum_{i=1}^{N} \sqrt{x_i^2+y_i^2}\,\Gamma_i
\end{aligned} \tag{3.22}$$

where,

$$\Gamma_{TN} = \sum_{i=1}^{N} \Gamma_i \tag{3.23}$$

For a system made of piecewise-constant vortex elements, however, they take the form,

$$
\begin{aligned}
\bar{x}_N &= \frac{1}{\Gamma_{TN}} \sum_{j=1}^{N} x_i \gamma_i \Delta s_i \\
\bar{y}_N &= \frac{1}{\Gamma_{TN}} \sum_{j=1}^{N} y_i \gamma_i \Delta s_i \\
\bar{r}_N &= \frac{1}{\Gamma_{TN}} \sum_{j=1}^{N} \sqrt{x_i^2 + z_i^2}\, \gamma_i \Delta s_i
\end{aligned}
\tag{3.24}
$$

where Γ_{TN} is again given by (3.23) and $\Delta s_i = \Delta s_{i-1/2} + \Delta s_{i+1/2}$.

Assuming that partial regridding is performed for an arbitrary section of an interface made of N piecewise-constant vortex elements, based on the sole condition of conservation of total circulation on the interface (i.e., Γ_{TN} constant), it can be seen that changes in both Δs_i's and γ_i's of vortex elements will cause variations in $\bar{x}_N, \bar{y}_N$, and $\bar{r}_N$, according to Eqs. (3.23),(3.24). On the other hand, when only point vortices are used, the element length does not affect the value of the vortex sheet system dynamic parameters in Eqs. (3.22),(3.23) which can thus be maintained constant. This explains why regridding worked for Rangel and Sirignano's results.

To date, we have not been able to reconcile values of dynamic parameters with regridding for piecewise-constant vortex elements. In Phase II of this study, however, we will introduce higher-order (e.g., cubic) vortex elements with which, we believe, we might be able to use regridding techniques while preserving values of the dynamic parameters of the system.

3.2 Computation of initial steady state slick shape

3.2.1 Principle of initialization

In earlier studies of headwave instability, the initial shape of the oil slick was selected rather arbitrarily. Zalosh (1974) for instance used part of a sine function to define the initial slick shape in his computations (see Section 4.3 for details about this initialization). Based on our analysis of the oil containment problem, we believe that such an arbitrary choice of initial slick shape (and dynamics) in the numerical model may actually induce non-physical (numerical) instabilities of the slick.

An arbitrary geometry selected to represent the interface between oil and water indeed is not likely to satisfy both the kinematic and dynamic boundary conditions along the interface. A violation of these equilibrium conditions is similar to creating an initial perturbation on the interface which, when introduced in a time dependent dynamic model, readily tries to adjust its shape to satisfy the equilibrium conditions. It is likely that such adjustments do not match actual instabilities occurring along an initially stable interface, for which the underlying current velocity is increased beyond the instability threshold.

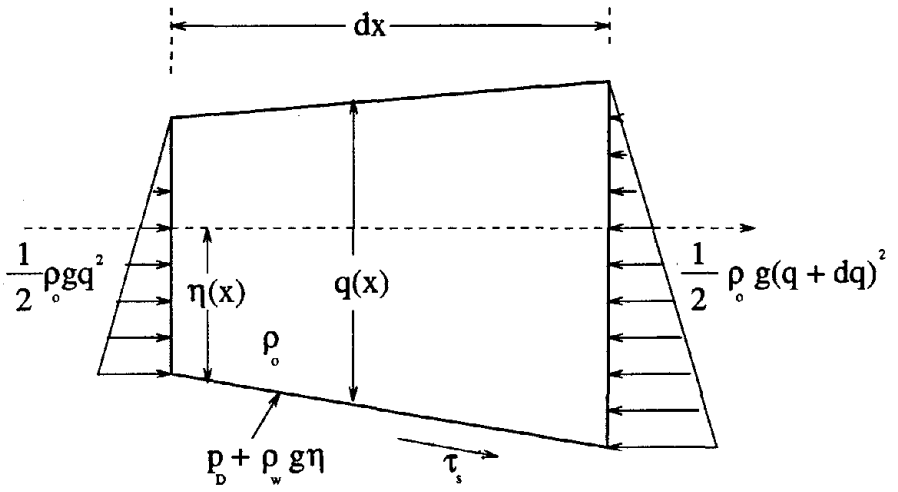

Figure 3.2: Sketch of forces acting on a differential element of length dx of the oil slick as in Milgram and Van Houten's (1978) quasi-hydrostatic model.

In the present Phase I study, only simple cases will be solved in Chapter 4 in order to validate the model equations and numerical procedures (i.e., Kelvin-Helmholtz and headwave instabilities). Hence, the initial shape of interfaces used in the applications will be selected as done in earlier studies.

In the more sophisticated applications of the model to oil containment by a boom that will take place under the ongoing Phase II of this study, however, it will be necessary to calculate an initially stable shape of the oil slick interface, corresponding to an underlying current velocity U below the instability threshold, before interfacial instability is studied. After this initialization stage, current velocity will be increased beyond the instability threshold and development of interfacial waves will be calculated as a function of time using the numerical model developed in this study.

Initialization thus consists in finding the shape of the slick interface $\eta(x)$ (measured from still water level; Fig. 3.2) that satisfies both the dynamic and kinematic conditions on the interface. Following Milgram and Van Houten (1978) quasi-hydrostatic approach within the slick, we express the Bernoulli equation between the front of the slick and any point on the slick interface and get,

$$p_D = \frac{1}{2}\rho_w (U^2 - U_{ws}^2) \tag{3.25}$$

Expressing the horizontal equilibrium along the interface (Fig. 3.2), we get to the first-order,

$$(p_D + \rho_w g\,\eta)\frac{\partial \eta}{\partial x} + \tau_s = \rho_o g\, q \frac{\partial q}{\partial x} \tag{3.26}$$

Expressing the vertical equilibrium along the interface (Fig. 3.2), we get to the first-order,

$$p_D + \rho_w g\,\eta = \rho_o g\, q \tag{3.27}$$

where p_D is the dynamic pressure in the water below the slick, U_{ws} is the tangential flow velocity along the slick, τ_s is the shear stress along the slick, q is the the total slick thickness (i.e., η plus the part above still water level; see Fig. 3.2). The shear stress along the slick can be classically expressed using a simple drag formula (e.g., Batchelor, 1967),

$$\tau_s = \frac{1}{2}\rho_w C_f U_{ws}^2 \tag{3.28}$$

where C_f is a non-dimensional friction coefficient function of flow characteristics and roughness along the interface.

In Milgram and Van Houten's study, the interface shape $\eta(x)$ and slick thickness $q(x)$ were experimentally measured and the tangential velocity of the underlying flow was calculated using ideal flow theory, assuming a uniform velocity U for the incident flow ahead of the slick. The friction coefficient (the only "unknown" left in the equations) was then calculated along the interface using Eqs. (3.25)-(3.28). When carrying out Phase II calculations with the present model, we will use the same approach but in reverse mode : the friction coefficient C_f will be calculated along the interface using boundary layer theory and the quasi-steady slick shape will be predicted. Since C_f is a function of *a priori* unknown flow characteristics (e.g., Reynolds number), an iterative method will be used : (i) a slick shape will be assumed; (ii) the tangential velocity along the interface will be calculated for the external water flow, based on ideal flow theory; (iii) the friction coefficient will be calculated for the external flow calculated in (ii); and (iv) a corrected slick shape will be calculated.

More details are provided in the following Sections for stages (ii) to (iv) of the iterative method. Results from this iterative method will be presented as part of Phase II of this study.

3.2.2 External flow calculation

Using a streamfunction representation in the water (e.g., Batchelor, 1967), continuity equation reads,

$$\nabla^2\psi = 0 \tag{3.29}$$

where ψ is the streamfunction defined such that,

$$u_w = -\frac{\partial\psi}{\partial y} \quad ; \; v_w = \frac{\partial\psi}{\partial x} \quad ; \; U_{ws} = -\frac{\partial\psi}{\partial n} \tag{3.30}$$

where (u_w, v_w) are velocity components in the water and $\boldsymbol{n}$ denotes the normal direction along the slick interface pointing outwards from the water. Eq. (3.29) is solved using a Boundary Integral Equation representation (BIE),

$$\alpha(\boldsymbol{x}_l)\psi(\boldsymbol{x}_l) = \int_{\Gamma(\boldsymbol{x})} [\frac{\partial\psi}{\partial n} G(\boldsymbol{x}, \boldsymbol{x}_l) - \psi \frac{\partial G(\boldsymbol{x}, \boldsymbol{x}_l)}{\partial n}] \, d\Gamma(\boldsymbol{x}) \tag{3.31}$$

with,

$$G(\boldsymbol{x}, \boldsymbol{x}_l) = -(1/2\pi)\log|\,\boldsymbol{x} - \boldsymbol{x}_l\,| \tag{3.32}$$

the free space Green's function, $\boldsymbol{x} = (x, y)$ and $\boldsymbol{x}_l = (x_l, y_l)$ representing position vectors for points on boundary Γ, and $\alpha(\boldsymbol{x}_l)$ a geometric coefficient.

The BIE (3.31) is solved using a higher-order Boundary Element Method (BEM) (Grilli and Subramanya 1995, 1996), together with boundary conditions expressing no-flow on the bottom boundary Γ_b and on the boom, and uniform incoming and outgoing flows on lateral boundaries Γ_l (see, e.g., Fig. 3.1). Along the slick interface Γ_s, we also assume a no-flow conditions for the quasi-steady case. In a streamfunction representation, no-flow conditions correspond to specifying streamlines with ψ =cst (e.g., 0 on Γ_s and $h\,U$ on Γ_b) and uniform flow conditions correspond to specifying a linearly varying streamfunction in the vertical direction, i.e., $\psi = |\,y\,|\,U$.

The solution of (3.31) directly provides, $\partial\psi/\partial n = -U_{ws}$, along the slick interface, to be used in Eq. (3.25). Hence, the ideal flow solution allows one to calculate the dynamic pressure along the slick for any assumed slick shape.

3.2.3 Iterative calculation of slick shape

Non-dimensional variables are introduced in Eqs. (3.25)-(3.28), based on a length scale U^2/g, a velocity scale U, and a stress scale $\rho_w U^2$ (note that for the oil-water interface, $U = \Delta U$). We thus get,

$$x' = \frac{gx}{U^2} \quad ; \quad q' = \frac{gq}{U^2} \quad ; \quad \eta' = \frac{g\eta}{U^2} \tag{3.33}$$

$$p'_D = \frac{p_D}{\rho_w U^2} \quad ; \quad \tau'_s = \frac{\tau_s}{\frac{1}{2}\rho_w U^2} \quad ; \quad C'_f = C_f \frac{U_{ws}^2}{U^2} \tag{3.34}$$

where primes denote non-dimensional variables.

Using definitions (3.33),(3.34), Eqs. (3.25)-(3.28) transform into,

$$p'_D = \frac{1}{2}(1 - U'^2_{ws}) \tag{3.35}$$

where $U'_{ws} = U_{ws}/U$.

$$(p'_D + \eta')\,\eta_{x'} + \frac{1}{2}\tau'_s = s\,q'\,q'_{x'} \tag{3.36}$$

where x' indices denote derivatives with respect to x', and $s = \rho_o/\rho_w$.

$$p'_D + \eta' = s\,q' \tag{3.37}$$

$$\tau'_s = C'_f \tag{3.38}$$

Combining Eqs. (3.36) and (3.38), we further get,

$$(p'_D + \eta')\left((1-s)\eta'_{x'} - p'_{Dx'}\right) = \frac{s}{2}C'_f \tag{3.39}$$

After some algebraic transformations, Eq. (3.39) reads,

$$\begin{aligned}\eta'^2 + \frac{2}{1-s} p'_D \eta' + \frac{1}{1-s} p'_D &= \frac{s}{1-s} \int_0^{x'} \{ C'_f(\xi) + 2 p'_D(\xi) \tan\beta(\xi) \} \, d\xi \\ &= \frac{s}{1-s} F(x') \end{aligned} \tag{3.40}$$

where, $\eta'_{x'} = \tan\beta$, has been used along the interface. The integrand in the right hand side of Eq. (3.40) represents both shear friction effects and, for small β, the horizontal force due to the dynamic pressure along the slick [3].

Eq. (3.40) is a quadratic equation for η' which can be solved as,

$$\begin{aligned}\eta'(x') &= \frac{1}{1-s} p'_D(x') \left\{ \sqrt{s} \{ 1 + (1-s) \frac{F(x')}{p'^2_D(x')} \}^{1/2} - 1 \right\} \\ &= \mathcal{F}(s, F(x'), p'_D(x')) \end{aligned} \tag{3.42}$$

with, from the external flow calculations, using Eq. (3.30) and (3.35),

$$p'_D(x') = \frac{1}{2} (1 - \psi'^2_{n'}(x')) \tag{3.43}$$

where $\psi'_{n'}$ is directly provided along the slick interface by the BEM solution for the underlying flow.

The iterative method for calculating the initial slick shape is obtained based on Eqs. (3.42),(3.43), as,

$$\begin{aligned}\eta'_{k+1}(x') &= \mathcal{F}(s, F_k(x'), \psi'_k(x')) \qquad \text{for } k = 1, \ldots \\ F_k(x') &= \int_0^{x'} \{ C'_{fk}(\xi) + (1 - \psi'^2_{kn'}(\xi)) \tan\beta_k(\xi) \} \, d\xi \end{aligned} \tag{3.44}$$

where k denotes the iteration number. A rough initial shape, say $\eta'_o(x')$, can be assumed for the slick, e.g. as in Zalosh (1974), and a first BEM solution can be calculated for the underlying flow, providing ψ'_o. F_o is then calculated, with $\tan\beta_o = \eta'_{ox'}$ and an improved slick shape η_1 is obtained using (3.44). This process is repeated until convergence is reached.

In applications, the slick is represented by N_{ow} vortex elements along the oil-water interface. Slick geometry is thus defined at the center points of these elements. BEM computations are also carried out in a discretized geometry in which nodes are defined along the boundary. For the slick interface boundary Γ_s, the BEM nodes will be selected at locations identical to the nodes defining vortex elements. For each iteration, Eq. (3.44) is

[3]Note that for small current velocity, the dynamic pressure in (3.40) can be neglected and we get,

$$\eta'(x') = \left\{ \frac{s}{1-s} \int_0^{x'} C'_f(\xi) \, d\xi \right\}^{1/2} \tag{3.41}$$

which directly provides the shape of the slick due to purely frictional effects.

thus applied to the N_{ow} nodes defining the slick interface. To accelerate convergence and limit sawtooth oscillations of the slick shape, after each iteration, the geometry calculated at the nodes using (3.44) will be fitted using a Least Square Method to a smoother "simplified" slick shape, function of only a few parameters, including the slick angle at the leading edge and the slick depth far away from the leading edge.

3.2.4 Friction coefficient calculation

According to the classical laminar Boundary Layer theory (e.g., Batchelor, 1967) applicable to smooth slender bodies, the friction coefficient is a simple function of a Reynolds number **Re** based on the tangential velocity and the (arclength) distance s from the leading edge of the flow,

$$\mathbf{Re} = \frac{U_{ws}\, s}{\nu_w} \tag{3.45}$$

where ν_w denotes the water kinematic viscosity.

We have,

$$C_f = \frac{0.73}{\sqrt{\mathbf{Re}}} = \varepsilon\,(U_{ws}(s)\,s)^{-1/2} \qquad \text{with } \varepsilon = 0.73\sqrt{\nu_w} \simeq 0.00073 \tag{3.46}$$

If one neglects dynamic effects (i.e., $p'_D = 0$ and by (3.35) $U'_{ws} = 1$), the slick shape purely due to friction can be found using Eq. (3.41). With (3.46), assuming $s' \simeq x'$, we get,

$$\eta'(x') = \frac{s}{1-s}\sqrt{2\varepsilon}\, x'^{1/4} \quad \text{and} \quad \eta'_{x'}(x') = \frac{s}{1-s}\sqrt{\frac{\varepsilon}{8}}\, x'^{-3/4} \tag{3.47}$$

Eq. (3.47) predicts a slick shape which is both unbounded for large x' and has a vertical tangent at the leading edge ($x' = 0$). These results are not quite realistic if one compares them to experiments. Furthermore, comparing the general variation of C_f given by Eq. (3.46) when $U'_{ws} = 1$ (i.e. $C_f \propto s^{-1/2}$) to results calculated by Milgram and Van Houten (1978) for actual slicks, one sees that the true variation of C_f is much more complex along the slick, particularly in the headwave region, than predicted by this simplified (purely frictional) equation.

Thus, as concluded by Milgram and Van Houten, dynamic pressure plays an important role in the headwave region in determining slick shape. This also means that U_{ws} in this region exhibits significant variations and so do **Re** and C_f. This justifies using the complete iterative procedure (3.44) to calculate the initial slick shape in the model, together with a representation of C_f similar to Eq. (3.46). Now, for a more accurate prediction of C_f, it will be necessary to introduce a representation of the BL along the slick which includes both laminar and turbulent regimes. This will be done as part of Phase II of this project.

Chapter 4

Model test and validation

4.1 Principle of model validation

Due to the complexity of the oil containment problem, it is difficult at this stage to independently test various numerical aspects of the model, for both accuracy and convergence, on fully realistic test cases. Moreover, there is not, to our knowledge, any detailed experimental data available for oil slick evolution that could be directly compared with model predictions.

To proceed with model validation and testing, it was decided instead to separately assess the accuracy of specific aspects of the numerical model, using simpler test cases having physical features similar to the oil containment problem by a boom, for which both analytical and experimental data are available.

The first test case deals with the periodic shear instability of a two-fluid system, also known as a Kelvin-Helmholtz (KH) instability. Through a detailed analysis of the relevant literature for this problem (e.g., Drazin *et al.*, 1966; Drazin, 1970; Van de Vooren, 1980; Rangel and Sirignano, 1988), it was found that the periodic KH problem produced instability patterns similar to those occurring in the headwave of an oil slick contained by a boom (see Chapter 1). In order to simulate the KH problem, however, the model had to be slightly modified to account for periodic lateral boundary conditions and periodic CPV singularity, while keeping most of its numerical procedures unchanged (e.g., for time updating of geometry and vorticity in the interface). In doing so, a practical tool was constructed to test and validate modeling assumptions and analyze propagation of errors with time. In a following section, we explain how the model was modified to address the periodic KH problem and give results of computations for two selected sets of parameter values corresponding to examples treated by Rangel and Sirignano (1988).

A second test case was selected for the pure headwave instability in deep water of a semi-infinite oil slick over a uniform water flow (i.e., a slick without a boom modeled using 3 si sheets and 2 sd sheets; Fig. 3.1). This case is similar to the one that Zalosh (1974) studied with an equivalent but less accurate model. It was found that the mechanism of roll-up of the vortex sheet in the headwave was very similar to the one occurring for a slick contained by a boom. In a following section, we explain how the model is used to solve the

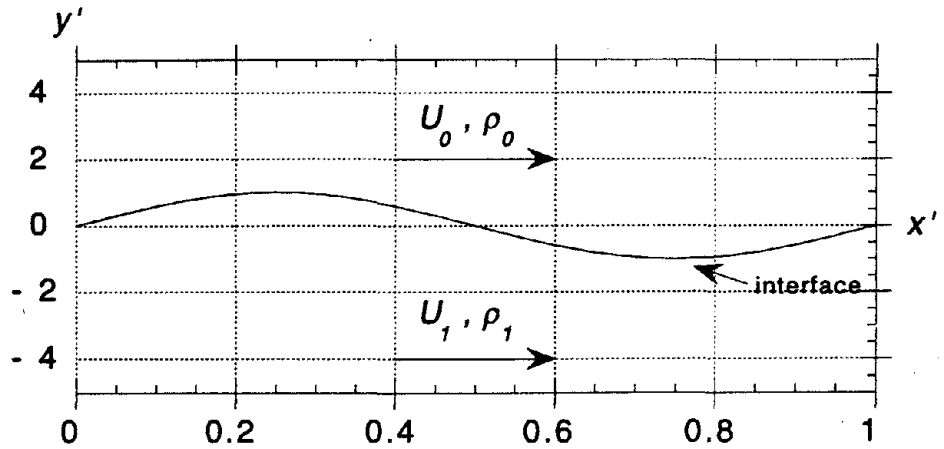

Figure 4.1: Sketch of computational set-up for periodic Kelvin-Helmholtz instability. U_o, U_1 are uniform velocities and ρ_o, ρ_1 are densities of fluid 0 and 1, respectively.

headwave instability problem (particularly the selection of the initial slick shape) and give results for cases corresponding to those modeled by Zalosh (1974).

4.2 Periodic KH instability

New formulations for the Cauchy Principal Values (CPV) integrals for *periodic sinusoidal disturbances* were derived and both the explicit and implicit time updating methods were tested in these applications.

4.2.1 Overview

We consider a two-layer stratified system of infinite extension in the x direction made of homogeneous inviscid fluids with density ρ_o (e.g., the oil) and ρ_1 (e.g., the water) and uniform horizontal velocity U_o and U_1, respectively (Fig. 4.1). An initial sinusoidal disturbance of wavelength λ, $\eta(x) = \varepsilon \sin 2\pi x/\lambda$, is specified on the interface between both fluids, with initial vorticity distribution corresponding to the velocity discontinuity (see Section 4.2.4).

This problem was solved by Lamb (1932) in a linear framework (see p. 373 and p. 461; see also Leibovich, 1976). He found that a periodic disturbance would always be unstable and grow exponentially with time if,

$$\Delta U = | U_o - U_1 | > \frac{1+s}{\sqrt{s}} c_o \tag{4.1}$$

where,

$$c_o = \left(\frac{1}{1+s} \{(1-s)\frac{g}{k} + \sigma_{o1}\frac{k}{\rho_1}\} \right)^{1/2} \tag{4.2}$$

the speed of propagation of interfacial waves, where, $k = 2\pi/\lambda$, is the wavenumber of the interfacial perturbation waves, $s = \rho_o/\rho_1$ and σ_{o1} is the interfacial tension coefficient.

Another way of expressing condition (4.1) is, $W < 1$ with,

$$W = \{(1-s)\frac{g}{k} + \sigma_{o1}\frac{k}{\rho_1}\}\frac{1+s}{s(\Delta U)^2} = \frac{(1+s)^2}{s}\frac{c_o^2}{(\Delta U)^2} \tag{4.3}$$

According to Eq. (4.1), the growth of the instability will be maximum for a minimum value of c_o. Calculating $dc_o/dk = 0$ in Eq. (4.2), we see that the minimum value of c_o is achieved for a wavelength,

$$\lambda_m = 2\pi\left(\frac{\sigma_{o1}}{\rho_1 g(1-s)}\right)^{1/2} \tag{4.4}$$

and takes the value,

$$c_{om} = \left(\frac{2}{1+s}\sqrt{\frac{\sigma_{o1}}{\rho_1}g(1-s)}\right)^{1/2} \tag{4.5}$$

the critical interfacial wave velocity.

If we select $\lambda = \lambda_m$ from (4.4) as the wavelength of the interfacial instability and $W = W_m = 1$ (given by Eq. (4.3) with $c_o = c_{om}$, from Eq. (4.5), and $k = 2\pi/\lambda_m$), we can calculate the critical velocity discontinuity causing instability, ΔU_{cr}, and see whether there is (linear) instability or not for a specified discontinuity ΔU. We get,

$$\Delta U_{cr} = \left(2\frac{1+s}{s}\sqrt{\frac{\sigma_{o1}}{\rho_1}g(1-s)}\right)^{1/2} \tag{4.6}$$

Lamb's solution detailed above assumes that the height of interfacial waves is infinitesimal. This is only an approximation particularly if the instability is free to develop for a long enough time. As a first approximation, however, this solution can be used to predict the threshold velocity ΔU likely to cause initial instability of interfacial waves. Moreover, despite their limitations, Lamb's equations contain the correct physical parameters influencing interfacial instability (i.e., fluid density ratio, interfacial tension and gravity) that will be used in the more exact solution presented hereafter.

4.2.2 Governing equations

Using the present model, no approximation is made on the size of interfacial waves and computations can be pursued up and into the roll-up of vortex sheets representing the interface (e.g., Figs. 4.2., 4.3).

Since a velocity discontinuity exists at the interface (i.e., a shear layer), a vorticity distribution is created along the interface. Hence, for both (ideal) fluids in the system, the velocity potential obeys a Poisson equation (i.e., not the simple Laplace's equation of classical ideal fluid cases). It can be shown that the flow velocity induced in both fluids due to the interfacial vorticity can be calculated using Biot-Savart's law (2.3) (e.g., Batchelor,

1967, pps. 84 and 527). In doing so, it is assumed that the interface is well represented by a vortex sheet.

For a periodic disturbance of wavelength λ on the interface with infinite extension in the s direction, Eq. (2.3) reads, in complex form,

$$u(z) - i\,v(z) = \frac{i}{2\pi} \int_{-\infty}^{+\infty} \gamma(s) \frac{1}{z - z'} ds \tag{4.7}$$

where, $i = \sqrt{-1}$, $z = x + iy$, $z' = x' + iy'$, and $s = s(z')$. Due to periodicity, Eq. (4.7) can be transformed into,

$$u - i\,v = \frac{i}{2\pi} \int_0^{\lambda} \gamma(s) \sum_{n=-\infty}^{\infty} \frac{1}{z - z' + n\lambda} ds \tag{4.8}$$

or, following Van de Vooren (1980), into,

$$u - i\,v = \frac{i}{2\lambda} \int_0^{\lambda} \gamma(s) \cot\left[\frac{\pi}{\lambda}(z - z')\right] ds \tag{4.9}$$

After some algebraic transformations (Van de Vooren, 1980) and introduction of dimensionless variables, $\xi = x/\lambda$, $\eta = y/\lambda$, and $\tau = t\,\Delta U/\lambda$, Eq. (4.9) becomes,

$$\begin{aligned} u &= \Delta U \frac{d\xi}{d\tau} = \frac{1}{2\lambda} \int_0^{\lambda} \frac{\sinh 2\pi(\eta - \eta')}{\cosh 2\pi(\eta - \eta') - \cos 2\pi(\xi - \xi')} \gamma(s)\, ds \\ v &= \Delta U \frac{d\eta}{d\tau} = -\frac{1}{2\lambda} \int_0^{\lambda} \frac{\sin 2\pi(\xi - \xi')}{\cosh 2\pi(\eta - \eta') - \cos 2\pi(\xi - \xi')} \gamma(s)\, ds \end{aligned} \tag{4.10}$$

Eq. (4.10) can be used in this form to time march the geometry of the interface, defined by points (ξ, η), provided integrals on the right hand side of the equation are calculated as a function of time. As described in Chapter 2, this can be done by assuming that the interface (vortex sheet) is made of N segments with piecewise constant vorticity density γ_j. This is similar to the discretization used in Eq. (2.7). The velocity induced at the mid-point of a segment i is thus given by $(i, j = 1, ..., N)$,

$$\begin{aligned} u_i &= \frac{1}{2\lambda} \sum_{j \neq i} \Gamma_j \frac{\sinh 2\pi(\eta_i - \eta_j)}{\cosh 2\pi(\eta_i - \eta_j) - \cos 2\pi(\xi_i - \xi_j)} + \tilde{u}_i \\ v_i &= -\frac{1}{2\lambda} \sum_{j \neq i} \Gamma_j \frac{\sin 2\pi(\xi_i - \xi_j)}{\cosh 2\pi(\eta_i - \eta_j) - \cos 2\pi(\xi_i - \xi_j)} + \tilde{v}_i \end{aligned} \tag{4.11}$$

where $\tilde{u}_i$ and $\tilde{v}_i$ denote CPV integrals resulting from singularities occurring when the source point (x_i, y_i) coincides with the integration point (x_j, y_j) (i.e., self-induced velocity contributions; see Section 2.2.2). These CPV integrals are calculated in the next section.

4.2.3 Calculation of self-induced velocity contributions for piecewise constant element

As pointed out by Van de Vooren (1980), there is a need for accurately evaluating self-induced velocity contributions resulting from singularities in (4.10) when the source point coincides with the integration point. It seems, however, that a number of studies have avoided this problem either by using (less accurate) point vortices (e.g., Zalosh, 1974, 1976), which do not have self-induced velocity (see Section 2.2.1) and/or by regridding discretization points at equal distance in such a way as to (knowingly or unknowingly) cancel self-induced velocity contributions (Rangel and Sirignano, 1988, 1991; see also the discussion in Fink and Soh, 1974, and in Section 2.2.2).

Starting from the complex form (4.9) of the periodic Biot-Savart law, the CPV integrations over segment i of length Δs_i give,

$$\tilde{u}_i - i\,\tilde{v}_i = \frac{i}{2\lambda}\int_{s_{i-1/2}}^{s_{i+1/2}} \gamma_i \cot\left[\frac{\pi}{\lambda}(z_i - z')\right] e^{-i\theta_i} dz' \tag{4.12}$$

where for a straight line segment we have used, $ds = dz' e^{-i\theta_i}$, with θ_i the angle between segment i and the x-axis.

Eq. (4.12) can be readily integrated to yield,

$$\tilde{u}_i - i\,\tilde{v}_i = -\frac{\Gamma_i}{2\pi\Delta s_i}(\sin\theta_i - \cos\theta_i)\,\ln\left|\frac{\sin\left[\pi(z_i - z_{i+1/2})/\lambda\right]}{\sin\left[\pi(z_i - z_{i-1/2})/\lambda\right]}\right| \tag{4.13}$$

where, $\Gamma_i = \gamma_i \Delta s_i$, is the total vorticity of segment i.

Separating real and imaginary parts of (4.13), we obtain,

$$\begin{aligned} \tilde{u}_i &= \frac{\Gamma_i}{2\pi\Delta s_i}\left\{\cos\theta_i \arctan P - \frac{\sin\theta_i}{2}\ln|\,Q\,|\right\} \\ \tilde{v}_i &= -\frac{\Gamma_i}{2\pi\Delta s_i}\left\{\sin\theta_i \arctan P + \frac{\cos\theta_i}{2}\ln|\,Q\,|\right\} \end{aligned} \tag{4.14}$$

with,

$$\begin{aligned} P = \Big(&\{\cot(\pi\Delta s_{i+1/2}\cos\theta_i)\tan(\pi\Delta s_{i+1/2}\sin\theta_i)\} - \\ &\{\cot(\pi\Delta s_{i-1/2}\cos\theta_i)\tan(\pi\Delta s_{i-1/2}\sin\theta_i)\}\Big)/ \\ &\Big(1 + \{\cot(\pi\Delta s_{i+1/2}\cos\theta_i)\tan(\pi\Delta s_{i+1/2}\sin\theta_i)\} \\ &\{\cot(\pi\Delta s_{i-1/2}\cos\theta_i)\tan(\pi\Delta s_{i-1/2}\sin\theta_i)\}\Big) \end{aligned} \tag{4.15}$$

and,

$$Q = \frac{\sin^2(\pi\Delta s_{i+1/2}\cos\theta_i)\cosh(\pi\Delta s_{i+1/2}\cos\theta_i)}{\sin^2(\pi\Delta s_{i-1/2}\cos\theta_i)\cosh(\pi\Delta s_{i-1/2}\cos\theta_i)} \tag{4.16}$$

It can be shown that Eqs. (4.14)-(4.16) for the self-induced velocities generalize the equations derived by Van de Vooren (1980), using a Taylor series expansion method truncated to first-order. Hence, the present method is both more general and more accurate than Van de Vooren's method.

Using Eqs. (4.11) and (4.14)-(4.16), the total velocity induced by a vorticity distribution on the interface can be calculated along the interface and, if needed, in the bulk of both fluids. Selection of the initial vorticity distribution on the interface is discussed in the next section.

4.2.4 Initial vorticity distribution

Using linear theory (Lamb, 1932), the initial distribution of vorticity density is determined on the interface for the KH problem as ($i = 1, ..., N$),

$$\gamma_i = \frac{1}{N\Delta s_i}\left(1 + 2\pi\varepsilon\left\{\kappa\sin(2\pi\xi_i) - 2\frac{\sqrt{s(1-W)}}{(1+s)}\cos(2\pi\xi_i)\right\}\right) \tag{4.17}$$

where κ is the Atwood number defined in Section 2.3.2, ε is the initial amplitude of the interfacial wave, and W (< 1) is given by Eq. (4.3) for the selected values of physical parameters.

Eqs. (4.17) and (4.3) were used by Rangel and Sirignano (1988), with $g = 0$, to specify initial vorticity in their solution of KH instability problems without gravity effects [1].

If the two-fluid system is made of identical fluids with different velocities, we have $s = 1$, $\kappa = 0$, and $W = 0$ and, hence, the initial vorticity distribution is given by,

$$\gamma_i = \frac{1}{N\Delta s_i}\left\{1 - 2\pi\,\varepsilon\,\cos(2\pi\xi_i)\right\} \tag{4.18}$$

Zalosh (1976) used this simpler equation to specify the initial vorticity distribution in his solution of the KH-problem. Since he used two different fluids, however, this led to an incorrect specification of the initial disturbance, which might partly explain why he could not achieve sufficient accuracy and stability in his computations.

4.2.5 Summary of computational techniques

A computational test case for the KH instability problem is defined by selecting values of physical parameters : $\rho_o, \rho_1, \Delta U$, and σ_{o1}. Due to the spatial periodicity of the KH problem, a domain representing only one wave length λ is modeled in the computations and numerical parameters are selected as : (i) the initial number N of piecewise-constant vortex elements

[1] Note that, in this study, computations were carried out using an incorrect coefficient in the equation for time updating of the vorticity (i.e., Eq. similar to (2.28)); this was later corrected by Rangel and Sirignano (1991).

on the interface, of initial length $\Delta s_o = \lambda/N$; and (ii) the initial time step, Δt_o. The latter is found according to Eq. (3.4), in which we assume that the initial sheet velocity is, by definition, the average of fluid 0 and 1 velocities (see Section 2.3.2), i.e., $\Delta U/2$ (for $U_o = 0$ in the present case), and the Courant number $C_o = 0.5$; we thus get, $\Delta t_o = \lambda/(N\Delta U)$.

The initial vorticity distribution on the interface is calculated using Eqs. (4.17) and (4.3) for a two-fluid system (second application below) and Eq. (4.18) for a problem with the same fluid for both layers (first application below). In the present computations, as in Rangel and Sirignano (1988), we use $\varepsilon = 0.025$ to define the initial perturbation on the interface, and the initial shape of the interface is selected as $\eta(x) = \varepsilon \sin 2\pi x/\lambda$.

Due to periodicity, corner points at both extremities of the modeled interface-sheet (i.e., points 1 and N) must always behave similarly in the computations, i.e., have the same y-coordinates, x-coordinates separated by λ, and have identical velocity, acceleration, and vorticity. Lateral boundary conditions are used to "enforce" these requirements in the model. For instance, horizontal coordinates are constrained as,

$$(x_N - x_1) + \Delta s_{1/2} \cos\beta_1 + \Delta s_{N+1/2} \cos\beta_N = \lambda \tag{4.19}$$

The interface evolution is tracked as a function of time by iteratively using the time updating procedure (3.1)-(3.3) (for the explicit time updating scheme). For each time step, the velocity on the interface is calculated using Eqs. (4.11), with (4.14)-(4.16), and the acceleration is calculated using time derivatives of these equations.

Tangential derivatives along the interface are calculated using the cubic sliding polynomial and the spline procedures described in Section 3.1.4. In the present computations, the hybrid method is used in combination with periodicity conditions expressed between nodes $(1+j)$ and $(N-j)$, $(j = 0, ..., 3)$ of the computational domain. This hybrid method was found to eliminate errors and instabilities of the solution that were first observed, particularly at both extremities of the interface, when only one of the above methods was used.

4.2.6 Computational results for interface evolution

Computations were performed using $U_o = 0$ (i.e., a still upper layer) and $U_1 = 0.25$ m/s (which is larger than the critical value for oil/water of about 0.15 m/s; see below), for two cases : (i) $s = \rho_o/\rho_1 = 1$ (water/water interface; same fluid) and no surface tension ($\sigma'_{o1} = 0$); and (ii) $s = 0.90$ (light oil/water interface; two-fluid system) and an average surface tension $\sigma'_{o1} = 0.0237$ N/m (oil/water value). In the present computations, $N = 55$ piecewise-constant vortex elements are first used to discretize the interface for both cases, and the mesh Courant number is set to $C_o = 0.5$, in both cases. Figure 4.2 (a) shows nodes between vortex elements in the discretization after 11 time steps.

In the first case (i), with a water-water system, Eqs. (2.28) or (3.9) would show that $d\Gamma_i/dt = d\mathrm{g}_i/d\tau = 0$, i.e., the vorticity, is constant as a function of time. This case in fact represents a very unstable limiting case of KH instability computations (Rangel and Sirignano, 1988); one for which the instability grows with the same time rate for any wavelength. For this case, due to the absence of surface tension and density difference at

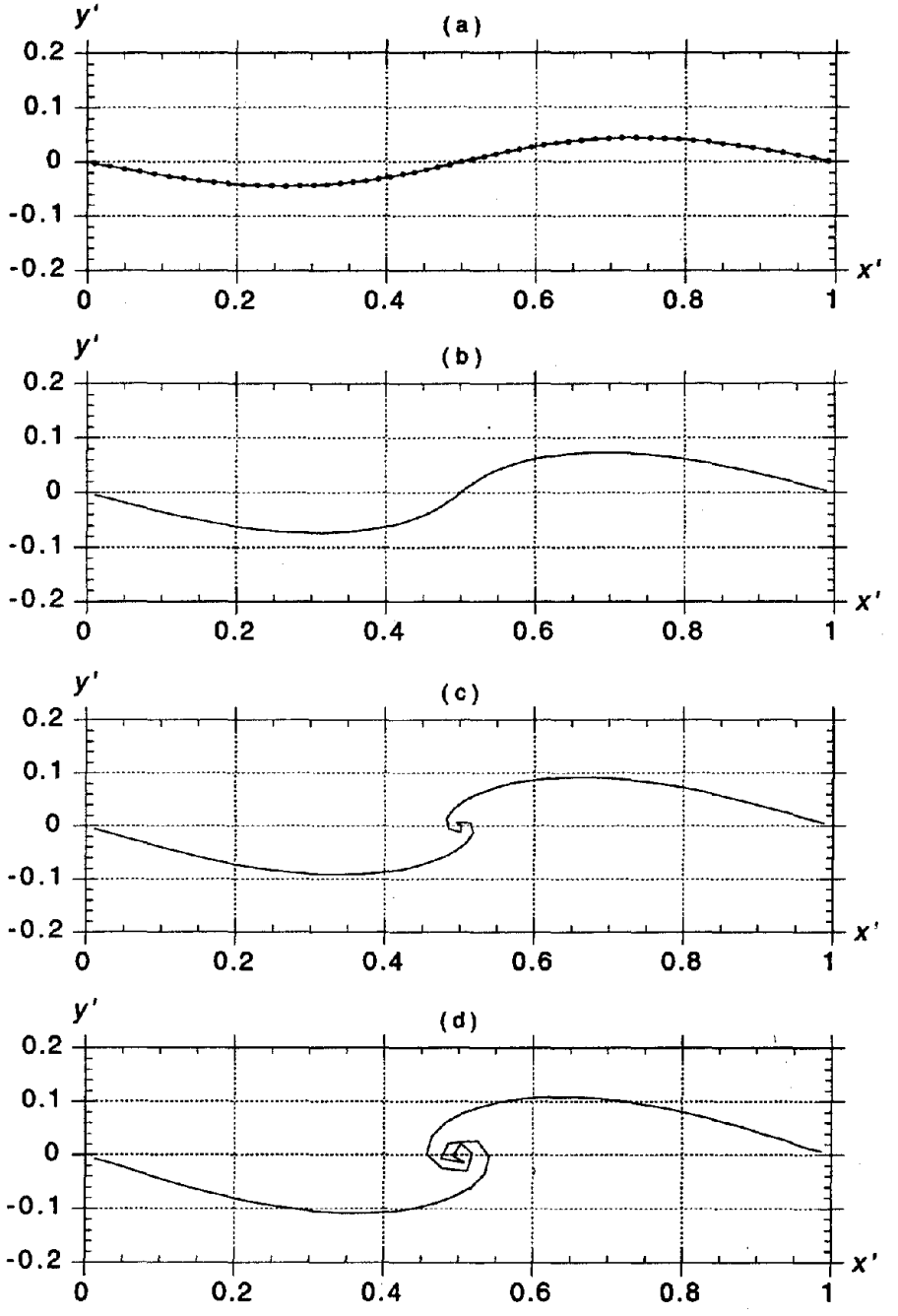

Figure 4.2: Interface shape $x' = x/\lambda$ and $y' = y/\lambda$ for KH instability computations in a set-up similar to Fig. 4.1 with $U_o = 0$ and $U_1 = 0.25$ m/s, $\rho_o/\rho_1 = 1$ (same fluid) and $\lambda = 1$ m and no surface tension. The initial time step is $\Delta t_o = 0.0727$ s and the initial perturbation is a sinusoidal wave with vorticity distribution according to Eq. (4.18), with $\varepsilon = 0.025$. Results are for $t =$ (a) 0.8; (b) 1.53; (c) 1.91; and (d) 2.24 s; corresponding to 11, 21, 31, and 43 varying time steps, respectively. The interface was discretized using $N = 55$ piecewise-constant vorticies and $C_o = 0.5$. (o) in figure (a) denote nodes between vortex elements.

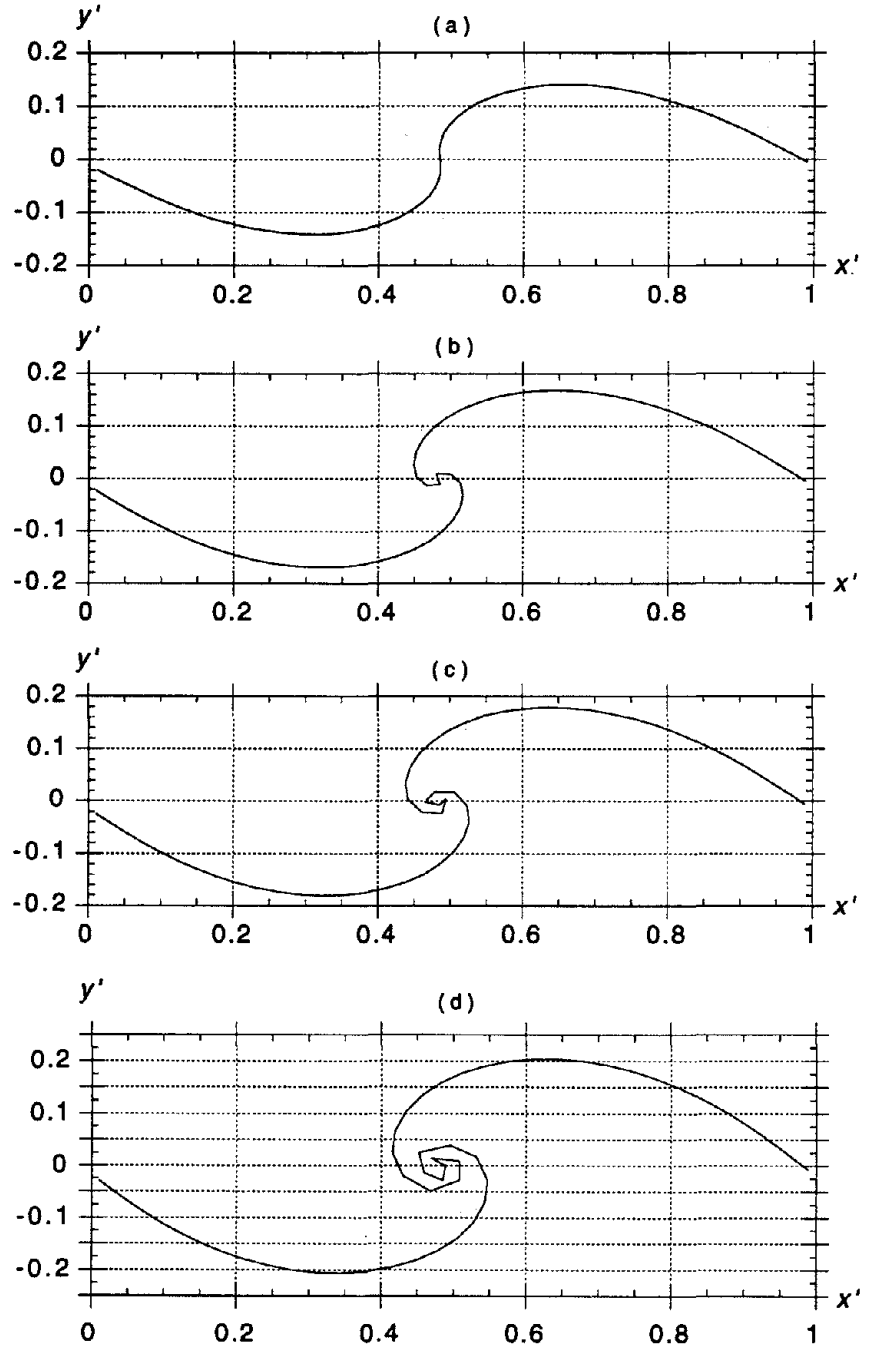

Figure 4.3: Same results as in Fig. 4.2 for $\rho_o/\rho_1 = 0.9$, a surface tension $\sigma_{o1} = 0.0237$ N/m, and $\lambda = 0.031$ m (water-oil; ripple scale). The initial time step is $\Delta t_o = 0.00225$ s and the initial perturbation is as in Fig. 4.2. with the initial vorticity distribution from Eq. (4.17). Results are for $t =$ (a) 1.74; (b) 1.85; (c) 1.89; and (d) 1.98 10^{-2} s; again corresponding to 6, 12, 16, and 22 varying time steps, respectively.

the interface, the analysis of the most unstable wavelength λ_m presented above is irrelevant. Hence, λ can be arbitrarily selected and results for any wavelength should be expected to be self-similar. To confirm this, computations were performed for $\lambda = 0.01$, 0.1, 1, and 5 m and non-dimensional interface profiles were found to be closely identical in all cases, as a function of non-dimensional time. In the following, we present results obtained for case (i) with $\lambda = 1$ m. For this value, the initial time step is $\Delta t_o = 0.0727$ s (or $\Delta \tau_o = 0.01818$; in fact the nondimensional time step does not depend on wavelength).

In the second case (ii), following the linear analysis by Lamb (1932), the wavelength is selected from Eq. (4.4), as $\lambda = \lambda_m$, which provides the maximum growth rate of the (linear) instability, with interfacial wave velocity c_{om} given by (4.5). This gives a value $\lambda = 0.0309$ m and, hence, $\Delta t_o = 0.00225$ s or $\Delta \tau_o = 0.0182$ (note that dimensionless time steps are identical to $1/N$ for both cases (i) and (ii)). This centimetric value of λ corresponds to an instability at the ripple scale (with $c_{om} = 0.0712$ m/s). As a verification of the (linear) instability of the problem for case (ii), we would also get from Eq. (4.3) $W = W_m = 0.325$ and from Eq. (4.6) $\Delta U_{cr} = 0.143$ m/s, i.e., we do have $W < 1$ and $\Delta U > \Delta U_{cr}$.

Results in Figs. 4.2 and 4.3 show the typical KH instability by overturning; intense roll-up of the vortex sheet on the interface, for water/water and oil/water cases, respectively. In the first case, the time step value stays closely equal to its initial value $\Delta \tau_o = 0.01818$ for 23 time steps, up to $t = 1.67$ s (i.e., just slightly beyond the time of Fig. 4.2 (b)). For later time, due to the overturning of the interfacial wave and the resulting shortening of vortex elements length, however, the time step value progressively reduces according to the adaptive time step procedure (3.4), down to $\Delta \tau = 0.00926$ for $t = 2.24$ s (Fig. 4.2 (d)). A similar variation in time step size was observed for the second case. Note that, in earlier works by Zalosh (1976) and Rangel and Sirignano (1988), a constant time step value was used. This prevented adjusting the level of accuracy in their models when interfacial instabilities occurred.

Overall, for both cases, numerical results are smooth and well-behaved, even when vortex sheet elements get very close to each other (see, e.g., Figs. 4.2 and 4.3 (d)). This confirms the correct treatment of CPV singularities in the model.

For both cases in Figs. 4.2 and 4.3, the number of vortex elements on the interface was first decreased to $N = 40$ and then increased to $N = 70$, and the initial time step was adjusted accordingly. Computations were performed for these discretizations. Figure 4.4 (a) shows a comparison of free surface shapes obtained at $t = 2.24$ s for the same case as in Fig. 4.2 and for the three selected discretizations. The agreement between the three results is quite good, except in the small central region where intense roll-up of VS's occurs. Figure 4.4 (b) shows the evolution of the interfacial amplitude as a function of time, for the three discretizations. For both the finer and the coarser discretizations, interfacial amplitudes stay within 2% of the results for $N = 55$. Hence, results are not significantly affected by a slight decrease or an increase in resolution which confirms both the convergence and stability of the numerical model, particularly compared to earlier works by Zalosh (1976) and Rangel and Sirignano (1988) where computed results showed irregular behavior when the size of vortex elements was too small. Finally, note the differences in Fig. 4.4 (b)

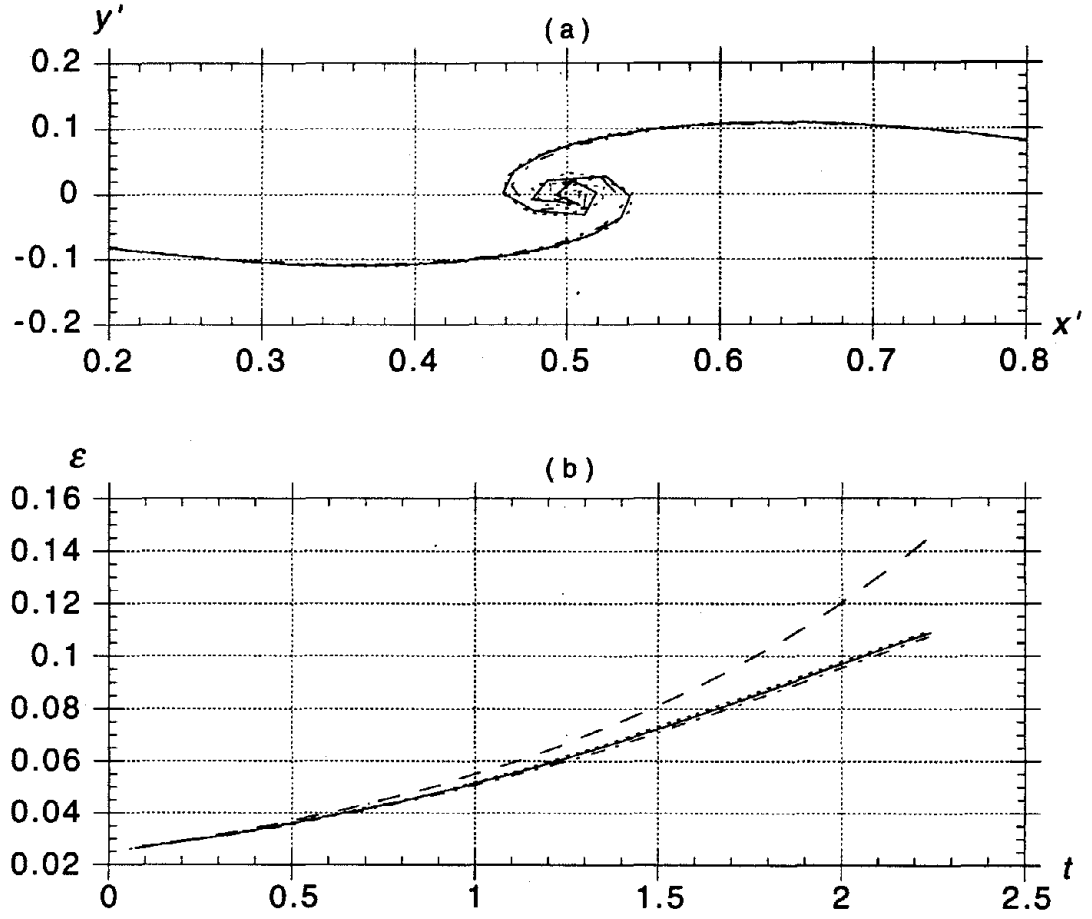

Figure 4.4: Same computations as in Fig. 4.2 for N = (— - —) 40; (——) 55; and (- - - - -) 70, vortex elements on the interface; with : (a) interface shape at $t = 2.24$ s; (b) growth of interfacial amplitude ε as a function of time t compared to (— —), the linear growth rate (Lamb, 1932).

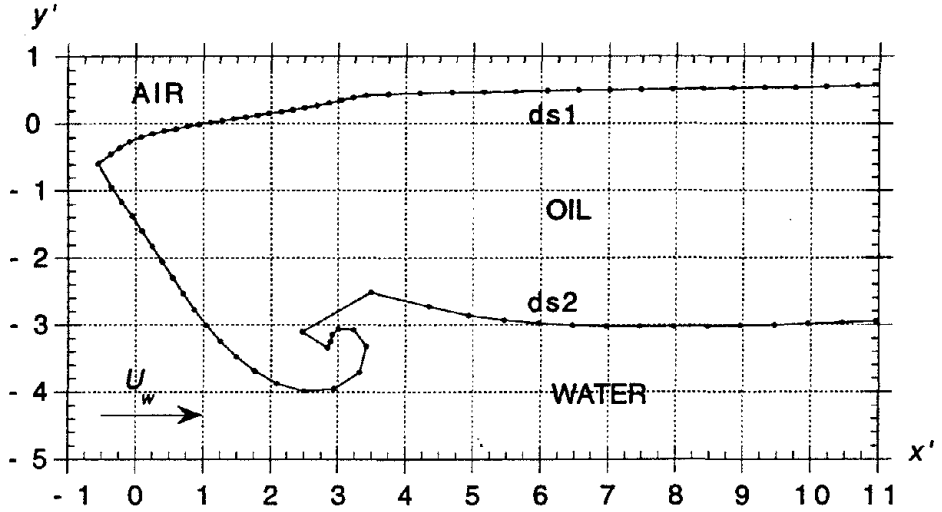

Figure 4.5: Sketch of computational domain for headwave instability of an oil slick, with definition of main parameters : U_w = water velocity with respect to slick ($U_o = 0$); air velocity can be set to U_a and interfacial tensions to σ_{oa} and σ_{ow}; densities are $\rho_a = 0$, ρ_o and ρ_w; si1, si2, si3 (not shown) = three semi-infinite vortex sheets; ds1, ds2 = piecewise-constant discretized vortex sheets; o = centers of discretized vortex elements.

between the amplitude growth rates obtained with the present nonlinear model and the rate predicted by linear theory (Lamb, 1932; in fact simply $\propto \exp(\pi \Delta U t/\lambda)$ in the present case). Clearly, for sufficiently larger time, nonlinearity increases and the instability grows slower in the nonlinear model than predicted by linear theory. This confirms earlier findings that nonlinearity provides stabilizing effects for the KH problem (e.g., Zalosh, 1976; Rangel and Sirignano, 1988).

Comparing both figures 4.2 and 4.3, one can see that the second case, with oil/water and surface tension, leads to a relatively larger scale of instability (in non-dimensional values, i.e., with respect to the selected wavelength) that also develops at a faster (non-dimensional) time rate than in the first case. The interface shape is up/down symmetrical in the first case (Fig. 4.2), where buoyancy does not play a role ($s = 1$), and slightly asymmetrical in the second case (see Fig. 4.3 (d)) due to buoyancy effect ($s = 0.9$). The present results are qualitatively similar to those obtained by Rangel and Sirignano (1988). The latter study, however, did not include gravity and used several incorrect coefficients in the vorticity updating equation. Hence, a direct comparison is not feasible.

4.3 Deep water headwave instability

This case corresponds to the problem solved by Zalosh (1974) and sketched in Fig. 4.5. A semi-infinite oil slick with zero initial velocity $U_o = 0$ is subjected to a water flow velocity

U_w (and an air flow U_a). An instability soon develops in the front part of the slick, and propagates downstream as a headwave which quickly overturns and rolls-up on itself in a way similar to KH instability waves calculated in the previous section.

The computational model used for this case is the original model introduced in Chapters 2 and 3. Errors made by Zalosh in his model for Eq. (2.28) for the interface evolution were corrected and the present, more accurate discretization/updating, method was used. In particular, the sliding/spline method was used to calculate tangential derivatives along the interface and velocities were calculated along the interface using Eq. (2.9). Unlike Zalosh, an exact representation of self-induced velocities of vorticies was used.

Note that, to overcome problems caused by the lack of representation of the self-induced velocities, Zalosh introduced the concept of a viscosity-core, in which contributions of individual point vortices in the discretized Biot-Savart equations (2.5) were multiplied by a term, $[1 - \exp(-r_{ij}^2/R_c^2)]$ (in which R_c is the "core radius"), i.e., providing a very small contribution to the velocity field for point vortices j's very close to point i. Zalosh stated that his numerical model was unstable without the use of this "damping" method. After experimenting with this method, we found that it was not needed for our model to provide both stable and accurate results, except at the three intersections between semi-infinite sheets and the piecewise-constant vortex sheets. This was thought to be due to the local mismatch between the continuous vorticity on the semi-infinite sheets and the piecewise-constant vorticity on the discretized vortex sheets. This problem will likely be eliminated in the Phase II model which will use higher-order vortex elements for the discretization of vortex sheets. For these three points, a core length equal to the distance to the first vortex element center was used.

The *initial slick shape* was selected as in Zalosh (i.e., no BEM initialization was used here; see Fig. 4.6 (o)), based on the observation of various experimental results, as,

$$\begin{aligned} \eta(x) &= D\sin(2\pi\, x/L) && \text{for } 0 \le x \le L/4 \\ \eta(x) &= D && \text{for } L/4 \le x \le L \end{aligned} \tag{4.20}$$

where D and L are the initial depth and length of the slick headwave, respectively. Using Bernoulli's equation between the front and the back of the slick, we get,

$$D = \frac{U_w^2}{2g\,(1-s)} \tag{4.21}$$

Following the work by Von Karman (1940) for density intrusions along solid boundaries, Zalosh assumed a 60° value for the angle of the headwave at the leading edge. With this angle, Eq. (4.20) leads to $L = 3.63D$. As pointed out by Zalosh, experimental results usually show smaller angles at the leading edge, which would lead to increased values of L. In the present case, however, we simply used the same initial shape as Zalosh's to compare our results to those he obtained.

In the computations, three semi-infinite sheets are used and interfaces are discretized using $N_a = 45$ segments with piecewise-constant vorticity between air and oil and $N_w = 85$

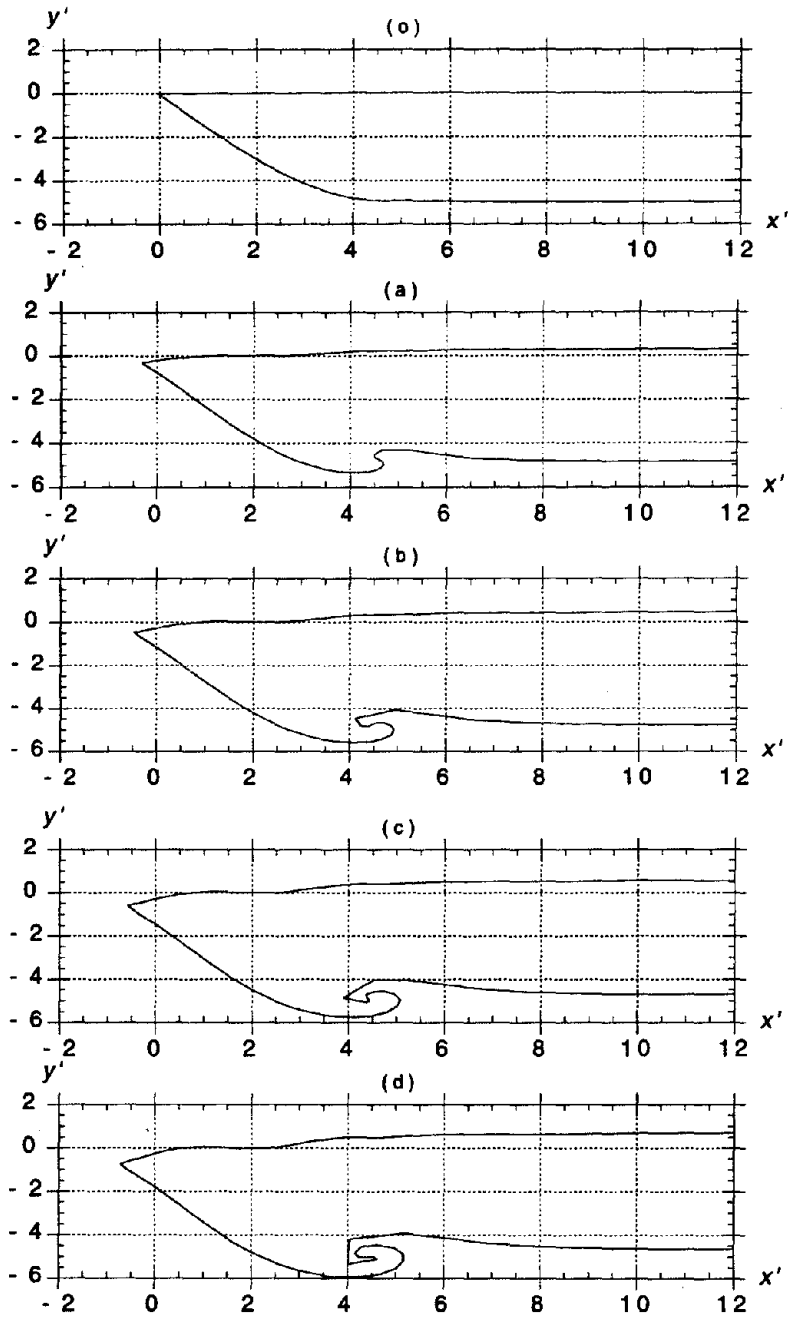

Figure 4.6: Typical results for headwave instability computations as in Zalosh (1974), in a set up similar to Fig. 4.5, with $U_w = 0.25$ m/s, $U_o = 0$, $U_a = 0$ m/s, $s = \rho_o/\rho_w = 0.9$, $\sigma_{ow} = 0.0237$ N/m (water-oil). Results $(D' = 5, L' = 18.15)$: (o) initial shape of the slick after one time step $t = 0.00273$ s; development of instability for $t =$ (a) 1.8; (b) 3.1; (c) 4.1; and (d) 5.2 10^{-2} s; corresponding to 5, 10, 16, and 22 varying time steps, respectively. Three semi-infinite sheets were used and interfaces were discretized with $N_a = 45$ piecewise-constant vorticies between air and oil and $N_w = 85$ between oil and water.

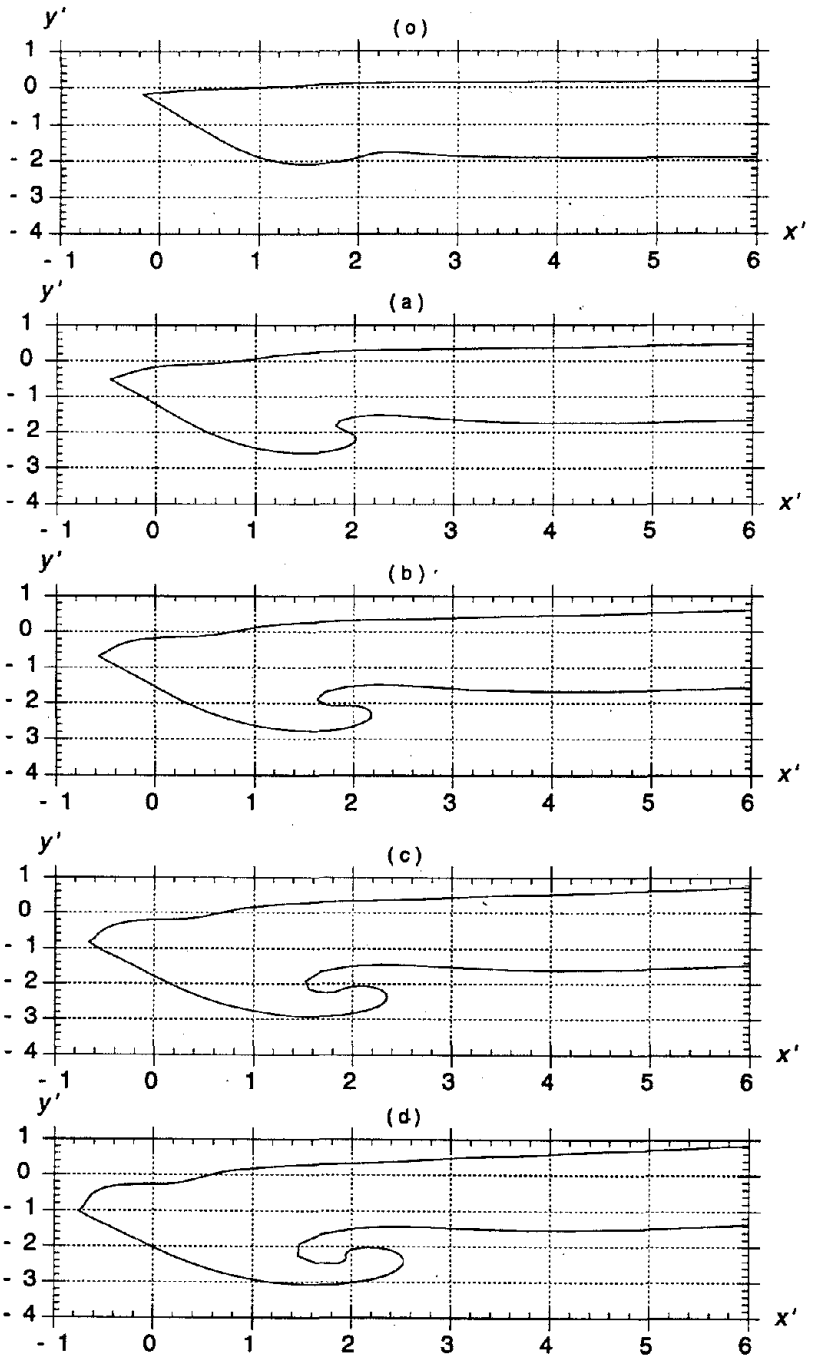

Figure 4.7: Same as in Fig. 4.6 for $\rho_o/\rho_w = 0.75$. Results $(D' = 2, L' = 7.26)$: (o) initial shape of the slick after one time step $t = 0.00109$ s; development of instability for $t =$ (a) 0.59; (b) 0.80; (c) 1.06; and (d) 1.30 10^{-2} s; corresponding to 5, 10, 16, and 22 varying time steps, respectively.

segments between oil and water. For each sheet, in the initial discretization, half the vortices are specified with equal arc-length spacing in the headwave region, i.e., for $0 \leq x \leq L/4$, and the other half are specified with equal arc-length spacing in the rest of the slick, i.e., for $L/4 \leq x \leq L$ (see Fig. 4.5). This provides a finer discretization in the headwave region where the main instability will occur. With this discretization, we have a minimum initial length of vortex elements equal to about $\Delta s_o = L/(2N_w)$ and an initial time step, according to Eq. (3.4), equal to $\Delta t_o = C_o L/(N_w U_w)$ (assuming an initial maximum velocity of the oil-water sheet equal to $U_w/2$).

Two cases are solved for $s = 0.9$ and 0.75, assuming a surface tension $\sigma_{ow} = 0.0237$ N/m. In both cases, the water velocity is set to $U_w = 0.25$ m/s, which is above the critical value for oil and water, and the air velocity is set to $U_a = 0$. A length-scale $\lambda = U_w^2/g = 0.00637$ m is used in the model (defined as in Section 3.2) and the corresponding time scale is $U_w/g = 0.02548$ s. Following Eq. (4.21), the initial slick is specified with depth $D' = D/\lambda = (5, 2)$, and length $L' = L/\lambda = (18.15, 7.26)$, for each test case, respectively. With $C_o = 0.5$, initial time steps $\Delta\tau_o = C_o L'/N_w = 0.107, 0.0427$, for each case, or $\Delta t_o = 0.00273, 0.00109$ s, respectively.

Results obtained in Figs. 4.6 and 4.7 are qualitatively similar to Zalosh's results but are better resolved and the developments of instabilities (roll-up) can be computed for a longer time. Model calculations are found to be both stable and accurate, without need for smoothing the interface or surface geometry or for other transformations of model outputs used in earlier studies (e.g., Zalosh, 1974).

Results of other computations (not reported here) are also found to be improved in both resolution and duration of computations when a larger number of vorticies are used on the interface. This confirms the accuracy of the CPV integrals computed for the self-induced velocities and demonstrates both the stability and the accuracy of the time updating procedures used in the present model.

Chapter 5

Conclusions and future developments

The present report dealt with Phase I model development and testing. To do so, the relevant literature and key physical phenomena relative to oil containment were analyzed. Important parameters were isolated and used to develop a numerical model of interfacial instabilities for a two-phase system consisting of a layer of oil on top of a uniform water stream.

This model relied on well-established *Vortex Sheet* dynamics methods with, however, several significant improvements compared to existing work in the literature. Key improvements included,

- the use of piecewise-constant vortex sheets (instead of point vortices) and the inclusion of self-induced velocity terms along the interfaces (with exact calculation of CPV integrals);
- the use of time updating equations for the sheet vorticity that account for inertial, gravity and surface tension effects;
- the use of a piecewise cubic-continuous representation of the geometry allowing for a more accurate calculation of higher-order tangential derivatives along interfaces, and the use of node regridding techniques;
- the use of a more accurate and stable explicit scheme, with exact calculation of vortex sheet accelerations, for time-updating of both the vorticity and the geometry of the interfaces;
- the use of a self-adaptive, time-stepping method, based on a mesh Courant number.

Applications of Phase I model presented in Chapter 4 mostly concentrated on studying two somewhat "academic" problems aimed at both testing the accuracy of the numerical procedures implemented in the model and better understanding the physics of unstable two-fluid systems; namely, the periodic Kelvin-Helmholtz instability and the semi-infinite headwave instability of a two-fluid system. These two applications showed some of the capabilities and efficiency of the model. They also gave us a solid basis for performing more complex studies including a boom and other solid boundaries like the bottom.

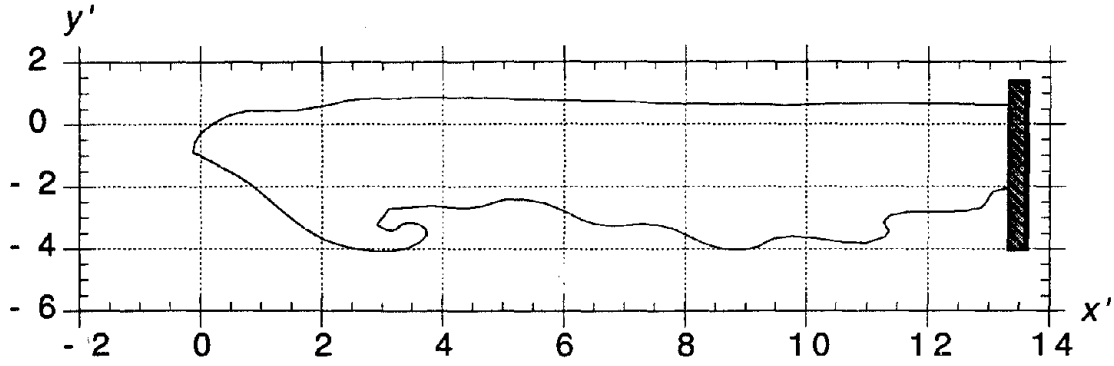

Figure 5.1: Illustration of computations with Phase I model for an oil slick contained by a boom. In this case, both a headwave and interfacial instabilities simultaneously develop.

To carry out the first application (KH problem), model equations had to be re-derived to include the spatial periodicity of the problem. Self-induced velocity terms also had to be expressed for the periodic problem. To our knowledge, such derivations have not been presented in the literature. In the second application to the headwave problem, both for sake of comparison and for simplicity, the initial shape of the oil slick was selected, somewhat arbitrarily, as in the study by Zalosh (1974). This means that the new method, outlined in Section 3.2, for calculating the initial steady-state shape of the slick has not yet been used, nor tested, in this report. It will, however, represent an essential component of the Phase II model which is currently under development and testing.

Future developments for the Phase II model, in particular, will include,

- the study of oil-water-boom systems;
- the initialization of the steady-state oil slick based on the iterative method introduced in Section 3.2;
- a computation of friction along the oil-water interface, both for the initialization of the slick shape and for the time updating of the slick geometry and dynamics; these computations will include both viscous and turbulent diffusion effects within boundary layers close to interfaces;
- using viscous/turbulent vortex sheets combining a local Navier-Stokes solver with turbulent closure models ($k - \varepsilon$ or similar);
- using higher-order vortex elements to provide better accuracy of computations along interfaces (i.e., use of non-constant vortex elements in the BEM);
- performing a broad parametric study of critical accumulation failure modes with validation of computational results by comparison to experimental results; and
- a tentative optimization of boom/barrier systems by varying geometrical and physical parameters of the problem.

To give an idea of future problems addressed in this study, Fig. 5.1 illustrates computations involving a solid boom and an oil slick. These computations had physical parameter values similar to those for the case in Fig. 4.7, with the addition of harmonic "noise", superimposed on the interfacial motion, to represent ocean wave action. Although these computations were performed with the Phase I model, i.e., without both the accurate slick initialization and the numerical improvements planned for the Phase II model, one can see that we obtain quite a realistic picture of interfacial instabilities such as those observed in laboratory experiments (see Chapter 1), namely, the occurrence of both a headwave and interfacial waves propagating along the oil-water interface and reflecting off the boom.

Acknowledgments

This work was supported by the U.S. Department of Transportation Grant No. DTRS-5794-G-00076 under the Oil Pollution Research Grant Program. The able assistance of John Putukian, Volpe National Transportation Systems Center, Boston, Massachusetts, contracting officer's representative, and the enthusiastic support of Ken Bitting, U.S. Coast Guard R&D Center, Groton, Connecticut, are gratefully acknowledged. Andrie Chen, Exxon Production Research, Houston, Texas, served as an industrial technical advisor to the project.

Bibliography

[1] Agrawal, R. K. and Hale, L. A. 'A new criteria for predicting head wave instability of an oil slick by a barrier', *Offshore Technology Conference,* 461-466, 1974.

[2] Bai, K. J. and Kim, J. W. 'A computational model for flow around an oil boom', *Proc. Workshop on Tidal and Oil Spill Modeling,* 5-17, 1993.

[3] Batchelor, G. K. , *An introduction to fluid dynamics* Cambridge University Press, 1967.

[4] Benjamin, T. B. 'Gravity currents and related phenomena', *J. Fluid Mech.* **31** (2), 209-248, 1968.

[5] Brebbia, C. A. , *The Boundary Elements for Engineers* John Wiley and Sons, 1978.

[6] Clavelle, E. J. and Rowe, R. D. 'Numerical simulation of oil–boom failure by critical accumulation', *Arctic Marine Oil Spill Program Technical Seminar,* 409-418, 1993.

[7] Cross, R. H. and Hoult, D. P. 'Oil booms in tidal currents', *Proceedings of 12th Coastal Engineering Conference, ASCE,* 1745-1758, 1970.

[8] Delvigne, G.A.L. 'Barrier failure by critical accumulation of viscous oil', *Proc. Oil Spill Conf.,* USEPA, USCG, and American Petrolium Institute, 143-148, 1989.

[9] Di Pietro, N. D. and Cox, R. G. 'The containment of an oil slick by a boom placed across a uniform stream', *J. Fluid Mech.* **96,** 613-640, 1980.

[10] Drazin, P. G. 'Kelvin-Helmholtz instability of finite amplitude', *J. Fluid Mech.* **42,** 321-335, 1970.

[11] Drazin, P. G. and Howard, L. N. 'Hydrodynamic stability of parallel flow of inviscid fluid', *Advances in Applied Mech.,* **9,** Academic Press, NY, 1966.

[12] Fink, P. T. and Soh, W. K. 'Calculation of vortex sheets in unsteady flow and application in ship hydrodynamics', *Proc. 10th Symp. on Naval Hydrodynamics* (Office of Naval Research, Washington, D.C.), 463-491, 1974.

[13] Grilli, S. and Subramanya, R. 'Recent Advances in the BEM Modelling of Nonlinear Water Waves'. Chapter 4 in *Boundary Element Applications in Fluid Mechanics* (ed. H. Power), pps. 91-122. Advances in Fluid Mechanics Series. Computational Mechanics Publication, Southampton, UK, 1995.

[14] Grilli, S. and Subramanya, R. 'Numerical Modeling of Wave Breaking Induced by Fixed or Moving Boundaries.' *Computational Mechanics* **17** (in press), 1996.

[15] Johnston, A. J., Fitzmaurice, M. R. and Watt, R. G. M. 'Oil spill containment : viscous oils', *Proc. 1993, Oil Spill Conference,* 89-94, 1993.

[16] Jones, W. T. 'Instability at an interface between oil and flowing water', *J. of Basic Engineering.* 874-878, 1972.

[17] Kordyban, E. 'The behavior of the oil-water interface at a planar boom', *J. of Energy Resources Technology.* **112** 90-95, 1990.

[18] Lamb,H. *Hydrodynamics* Cambridge University Press, 6th edition, 1932.

[19] Lau, Y. L. and Moir, J. 'Booms used for oil slick control', *J. Env. Eng., ASCE,* **105** 369-382, 1973.

[20] Lau, Y. L. and Kirchifer, S. A. 'A review of the dynamics of contained oil slicks in flowing water', *J. Hydraulics, ASCE,* 1974.

[21] Leibovich, S. 'Oil slick instability and the entrainment failure of oil containment booms', *J. of Fluids Engineering.* 98-105, 1976.

[22] Milgram, J. H. and Van Houten, R. J. 'Mechanics of a restrained layer of floating oil above a water current', *J. Hydronautics.* **12,** 93-108, 1978.

[23] Moore, D. W. 'A numerical study of the roll-up of a finite vortex sheet', *J. Fluid Mech.* **63** (2), 225-235, 1974.

[24] Rangel, R. H. and Sirignano, W. A. 'Nonlinear growth of Kelvin-Helmholtz instability : Effect of surface tension and density ratio', *Phys. of Fluids.* **31** (7),1845-1855, 1988.

[25] Rangel, R. H. and Sirignano, W. A. 'The linear and nonlinear shear instability of a fluid sheet', *Phys. of Fluids.* **A 3** (10), 2392-2400, 1991.

[26] Robbins, R. J., Hoult, D. and Cross, R. 'Steady state profile for oil barriers', *J. Waterways Harbors and Coastal Engng.,* **97,** 235-238, 1971.

[27] Rottman, J. W. and Olfe, D.B. 'Comment on "discretized simulation of vortex sheet evolution with buoyancy and surface tension effects" ', *J. AIAA* **15**, 1214-1215, 1977.

[28] Song, M., Huh, K. S., Yang, J. Y. and Hyun, B. S. 'Experimental investigation of the evolution of contained oil slick in currents', *Proceedings unknown,* 189–199, 1993.

[29] Subramanya, R. and Grilli, S. 'The state-of-the-art in current-slick interaction' *USCG-FY94, Oil Pollution Research Grant Program* 1st. Quarterly Report, 1994.

[30] Van de Vooren, A. I. 'Numerical investigation of the rolling-up of vortex sheets', *Proc. R. Soc. Lond.* **A 373**, 67-91, 1980.

[31] Von Karman T., *Bull. Am. Math. Soc.* **46**, 615-586, 1940.

[32] Wei, J., Kirby, J.T, Grilli, S.T. and Subramanya, R. 'A Fully Nonlinear Boussinesq Model for Surface Waves. Part1. Highly Nonlinear Unsteady Waves.' *J. Fluid Mech.* **294,** 71-92, 1995.

[33] Wicks, M. 'Fluid dynamics of floating oil containment by mechanical barriers in the presence of water currents', *Proceedings of Joint Conference on Prevention and Control of Oil Spills,* 55-106, 1969.

[34] Wilkinson, D. L. 'Dynamics of contained oil slicks', *J. Hydraulic Division,* **HY6,** 1013-1031, 1972.

[35] Wilkinson, D. L. 'Limitations to length of contained oil slicks', *J. Hydraulic Division,* **HY5,** 701-713, 1973.

[36] Zalosh, R. G. 'A numerical model of droplet entrainment from a contained oil slick', *Report No.* **CG-D-65-75**, DOT/USCG, 1974.

[37] Zalosh, R. G. 'Discretized simulation of vortex sheet evolution with buoyancy and surface tension effects', *J. AIAA* **14**, 1517-1523, 1976.

[38] Zalosh, R. G. and Jensen, D. S. 'A numerical model of droplet entrainment from a contained oil slick', *Proc. Fluid Mech. in Petrolium Industry* ASME, 17-27, 1975.

[39] Zaroodny, S. J. and Greenberg, M. D. 'On a vortex sheet approach to the numerical calculation of water waves', *J. Comp. Phys.* **11**, 440-446, 1973.

DEVELOPMENT OF A RAPID CURRENT CONTAINMENT BOOM: PHASE I

M. Robinson Swift, Barbaros Celikkol, Philip Coyne, University of New Hampshire

I. INTRODUCTION

CONTAINMENT PROBLEM

Conventional oil booms have been an essential tool in major oil spill recovery operations, but they are limited by currents. When the perpendicular component of relative current speed exceeds a critical value, oil entrainment occurs at the head of the restrained oil pool, and the boom fails due to leakage. The critical velocity, for the perpendicular component of current, normally has been found to be 0.6 - 1.0 knots depending on the oil properties.

This limitation poses a serious problem since tidal currents can exceed critical values in the approaches and/or harbors of major ports. Besides difficulty using fixed conventional booms, boom leakage also compromises the use of oil boom in oil boom/skimming operations. The sweeping speed of towed boom used to funnel oil to a skimmer is considerably restricted by leakage.

One approach to circumventing the problem is to angle the boom to the current thus reducing the perpendicular component. The oil is not contained in a pocket, but is instead deflected to a recovery point. This diversion boom approach has, for example, been developed for use in the Piscataqua River/Great Bay system, as described by Swift et al. (1990, 1991, 1992). The logistical problems which arise in deploying long lengths of angled boom, however, become severely limiting. As a practical solution, new oil boom design concepts need to be developed that at least double the critical velocity. This would enable effective response strategies to be developed for nearly all tidal areas as well as many river environments.

This need is addressed in the present study by developing an oil retention system using an operating mechanism different from the standard single barrier concept. The starting point in the development, however, was based on previous research on both standard and new concepts.

PREVIOUS WORK

When floating oil is restrained by a conventional oil boom in the presence of relative current, a "headwave" forms near the leading edge of the slick as described, for example, by Wicks (1969), Agrawal and Hale (1974) and Milgram and van Houton (1978). Though the fluid dynamic processes are still the subject of research, it is known that instabilities and/or turbulence will entrain oil droplets from the headwave thus initiating boom leakage. More recently, Delvigne (1989) has described an unstable reduction of the restrained slick termed "failure by critical accumulation". He has also summarized known laboratory studies which all indicate that boom failure occurs at less than 1 knot.

The current-induced failure mechanisms are avoided by the barrier configuration shown in Fig. 1. In this concept, the oil is not restrained by a single barrier as a pool exposed to the incident current. Instead, the oil moves down the inclined submergence

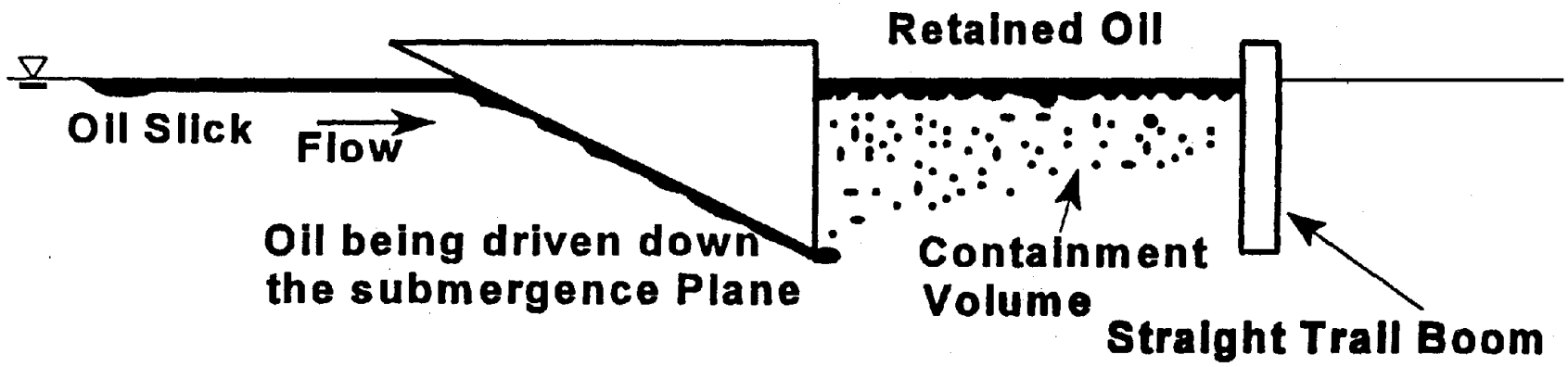

Fig. 1 Initial submergence plane/containment volume concept.

plane and is trapped in a protected containment region. Research by Bianchi and Henry (1973) indicates that the concept will retain oil at relative velocities above 2 knots. This concept has been further developed by JBF Scientific, Inc. and (independently) by LPI Corp. for the purpose of designing oil skimmers. The overall goal of the research program discussed here, on the other hand, is to return to the fundamental idea in order to develop an oil barrier system capable of superior fast current performance.

The concept is consistent with and closely related to observations by Delvigne (1984) and Johnston et al. (1993) regarding closely spaced double booming (two booms deployed parallel to each other with a small separation distance). They noted that oil becomes trapped between the booms (in a slowly rotating back eddy) at incident current speeds that would normally cause leakage. In addition, a similar trapping process can happen when oil flows under ice as described by Cox et al. (1980).

OBJECTIVES

The specific objectives of this study were to:

1. Develop an oil barrier design that offers superior rapid current performance.

2. Obtain an understanding of the fluid dynamic processes associated with the developed configuration.

The starting point was the cross-section shown in Fig. 1. This needed to be evaluated and upgraded to an improved and optimized configuration. The new design was then evaluated, and its fluid dynamics were investigated experimentally with a supporting theoretical effort. The emphasis was on finding the best barrier cross-section, though work on how to implement a fully 3-dimensional system was initiated.

APPROACH

Development of the barrier system was done primarily by means of a sequence of well-ordered laboratory experiments conducted using 2-dimensional physical models in a 40 ft. recirculating flume. Two-dimensional shapes of trial cross-sections were used to minimize scaling effects. With the 2-dimensional approach, the cross-section configurations are about half the size of the expected harbor/estuary design, and the models actually represent full size designs for smaller streams.

The first set of experiments were carries out to evaluate design parameter changes in the initial Fig. 1 configuration. Tests were made using oil substitutes since these exploratory experiments were done for comparison purposes only. The testing addressed questions regarding submergence plane angles, length of the containment region and sensitivity to specific gravity variations. Trials were then conducted to evaluate the effectiveness of various flow control devices. Results were incorporated into the

development of an improved and optimized design concept. This developed concept became the basic configuration which was then subject to further testing.

Retention capability was evaluated in a series of flume experiments using vegetable, synthetic and petroleum oils. The purpose was to determine performance covering the range of specific gravities and viscosities likely to be encountered in practice. The experimental program was supplemented by a theoretical effort in which the basic fluid dynamic equations and non-dimensional parameters were identified. Understanding the fluid dynamics was also addressed by measuring the fluid velocity distribution throughout the configuration using an electro-magnetic sensor and a laser doppler velocimeter. Work on the full, 3-dimensional problem was initiated by constructing and flume testing soft fabric, small-scale physical models having cross-channel curvature in plan view.

FLUME TESTING

Experiments were carried out in the recirculating freshwater flume shown schematically in Fig. 2. The flume design and construction is described by Doane (1994) and was built to be a facility dedicated to oil spill research. The flume is 40 feet long, 4 feet deep and 2 feet wide. The flow is driven by two counter-rotating propellers powered by two variable speed electric motors. The test section on one side is walled by acrylic panels allowing visual observations and access by optical instrumentation.

The 2-dimensional physical models are uniform across the width of the tank thereby representing the barrier cross-section. The oil or oil substitute deployment device was placed upstream from the physical model and mounted on top of the tank. A hopper/spreader was used for deployment of small beads which were employed in preliminary tests and concept development. A reservoir and spreading manifold was mounted for introducing petroleum and non-petroleum liquid oils.

The basic procedure was to first run the flume at the desired current speed until a hydrodynamic steady state was achieved, and then introduce the oil or oil substitute. The substance was deployed at a constant rate and uniformly over the width. Splash plates were used when necessary to minimize penetration and thereby create the desired surface slick.

The physical model barrier was then allowed to operate in a steady state mode until the experiment was terminated. Since quantitative measurement for retention was a principal objective, oil/oil substitute experiments were stopped before any substance could travel past the barrier and be re-introduced a second time.

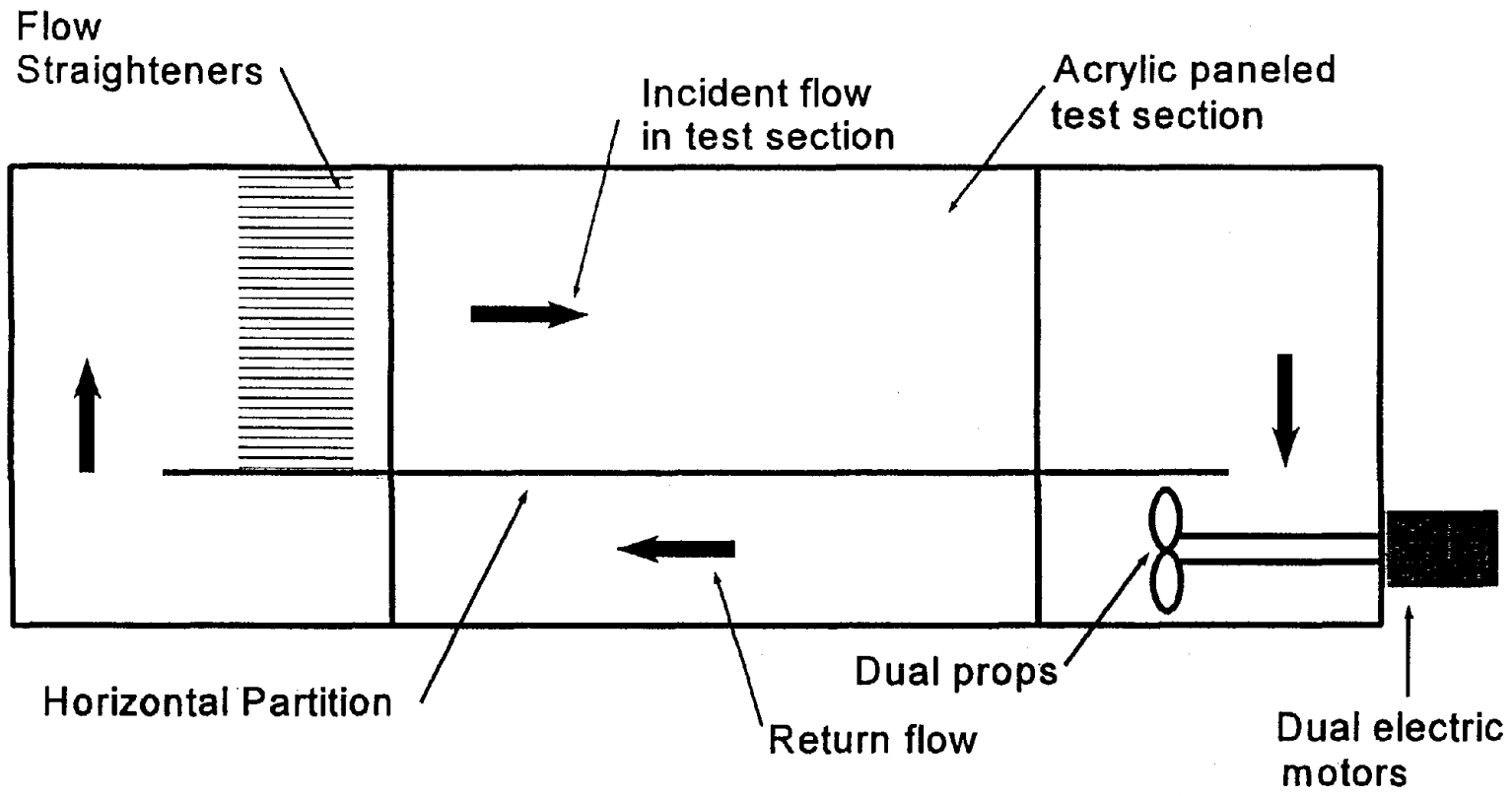

Fig. 2 Schematic of the UNH recirculating flume.

II. CONCEPT DEVELOPMENT

DEVELOPMENT METHODOLOGY

Flume testing began with an evaluation of the initial concept shown in Fig. 1. The first objectives were to observe general flow patterns and to determine the changes in retention ability with variations in submergence plane angle, length of containment region and specific gravity of the substance. Next the use of auxiliary flow control devices was investigated to improve retention.

Most of these development experiments were done using a "slick" of small (1/16 inch) beads. It was assumed that the following characteristics were relatively independent of the use of this substance:

1) Existence of a quiescent zone

2) Advective currents

3) General flow patterns

4) Ranking of physical model performance.

The beads allowed these comparative evaluation tests to be performed expeditiously so that a wide range of design parameter changes could be assessed. Confirmation of bead test conclusions regarding the optimized design concept was done using a liquid vegetable oil similar to a light petroleum product.

INITIAL CONCEPT EVALUATION

The flume testing began with an evaluation of the Fig. 1 initial concept including the effects of varying submergence plane angle, containment region length and substance specific gravity. Experiments were done using 1/16 inch plastic beads using the setup shown in Fig. 3. All experiments were conducted at 1 knot which is above the critical velocity for a simple, single vertical barrier under these experimental conditions. Three sets of experiments were carried out in which:

1) Submergence plane angle only was varied

2) Length of containment region only was varied

3) The specific gravity of the beads only was varied.

Results are summarized on Figs. 4 - 6 which show the percentage of beads retained as a function of the varied parameter. (It should be noted that subsequent tests with real oils indicated that it is more difficult to retain small beads then typical petroleum products.) It is seen that shallow angled submergence planes work best. Retention is improved when the second barrier is far enough from the submergence

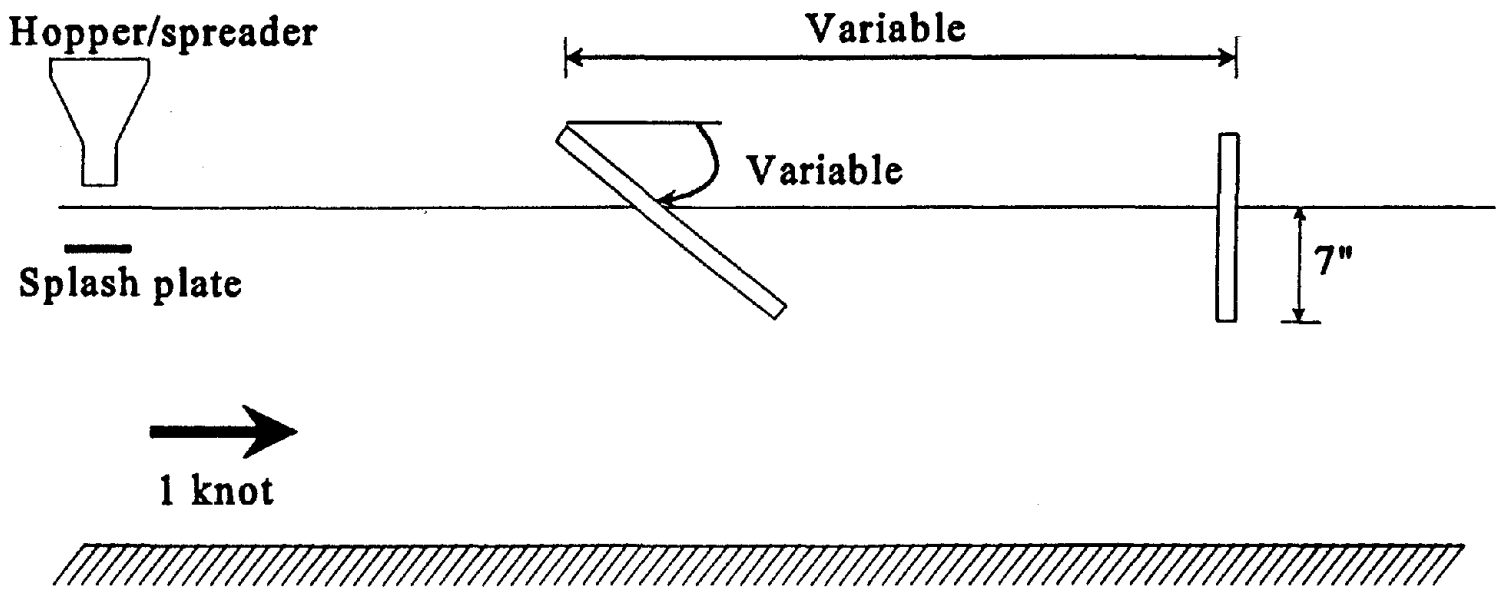

Fig. 3 Experimental setup for the initial development testing using beads.

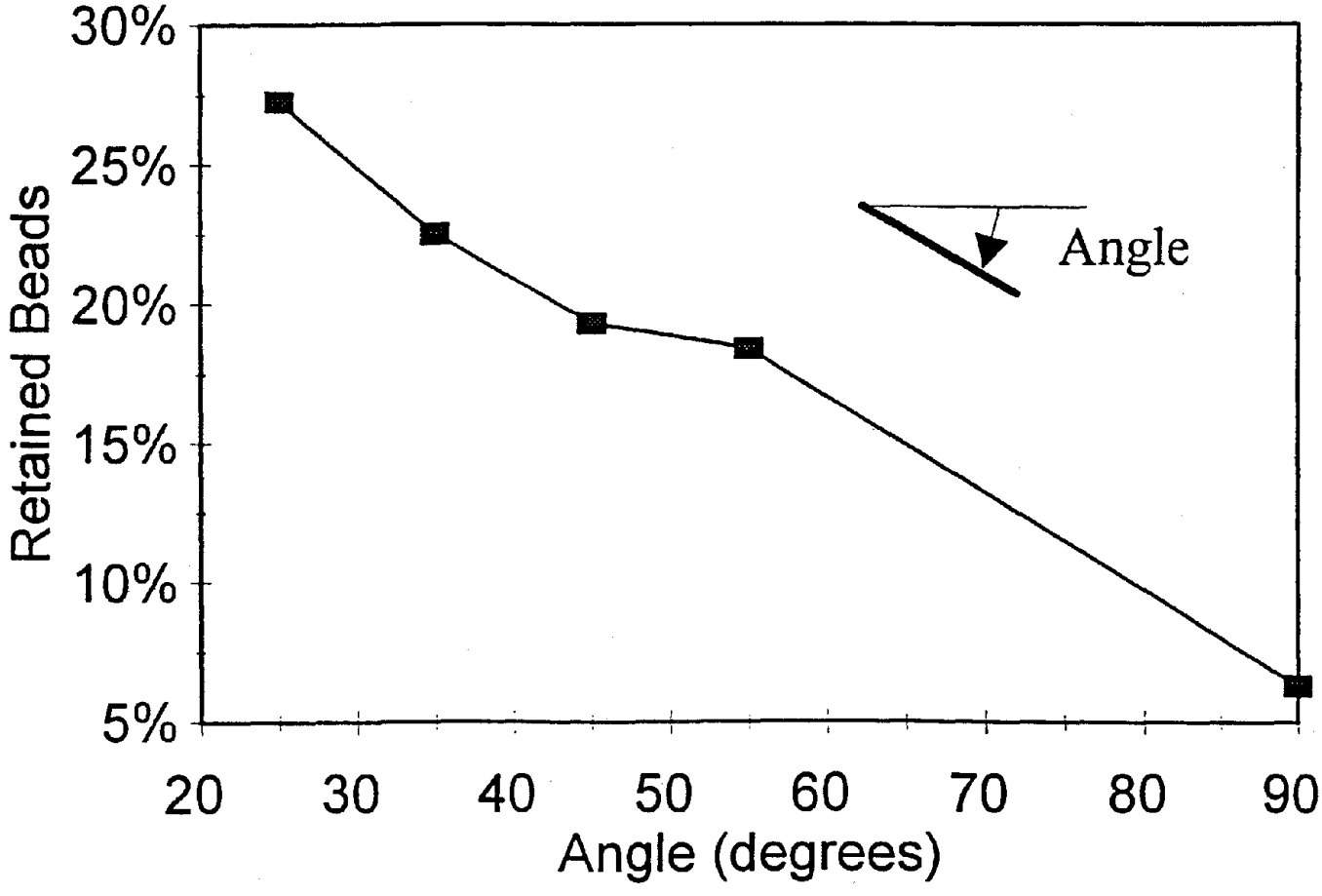

Fig. 4 Bead retention as a function of submergence plane angle with respect to the horizontal. Specific gravity = 0.96; speed = 1 knot.

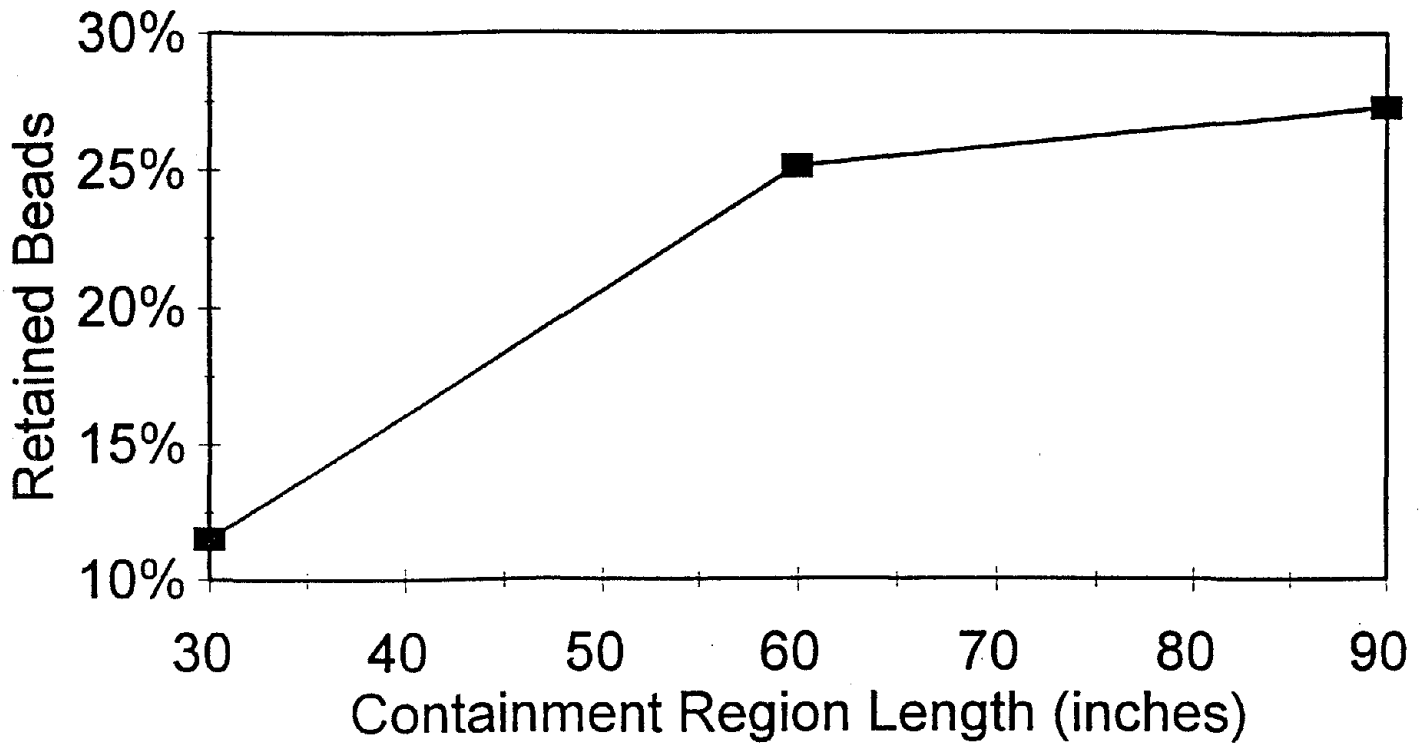

Fig. 5 Bead retention as a function of containment region length. Submergence plane angle = 25 degrees; specific gravity = 0.96; speed = 1 knot.

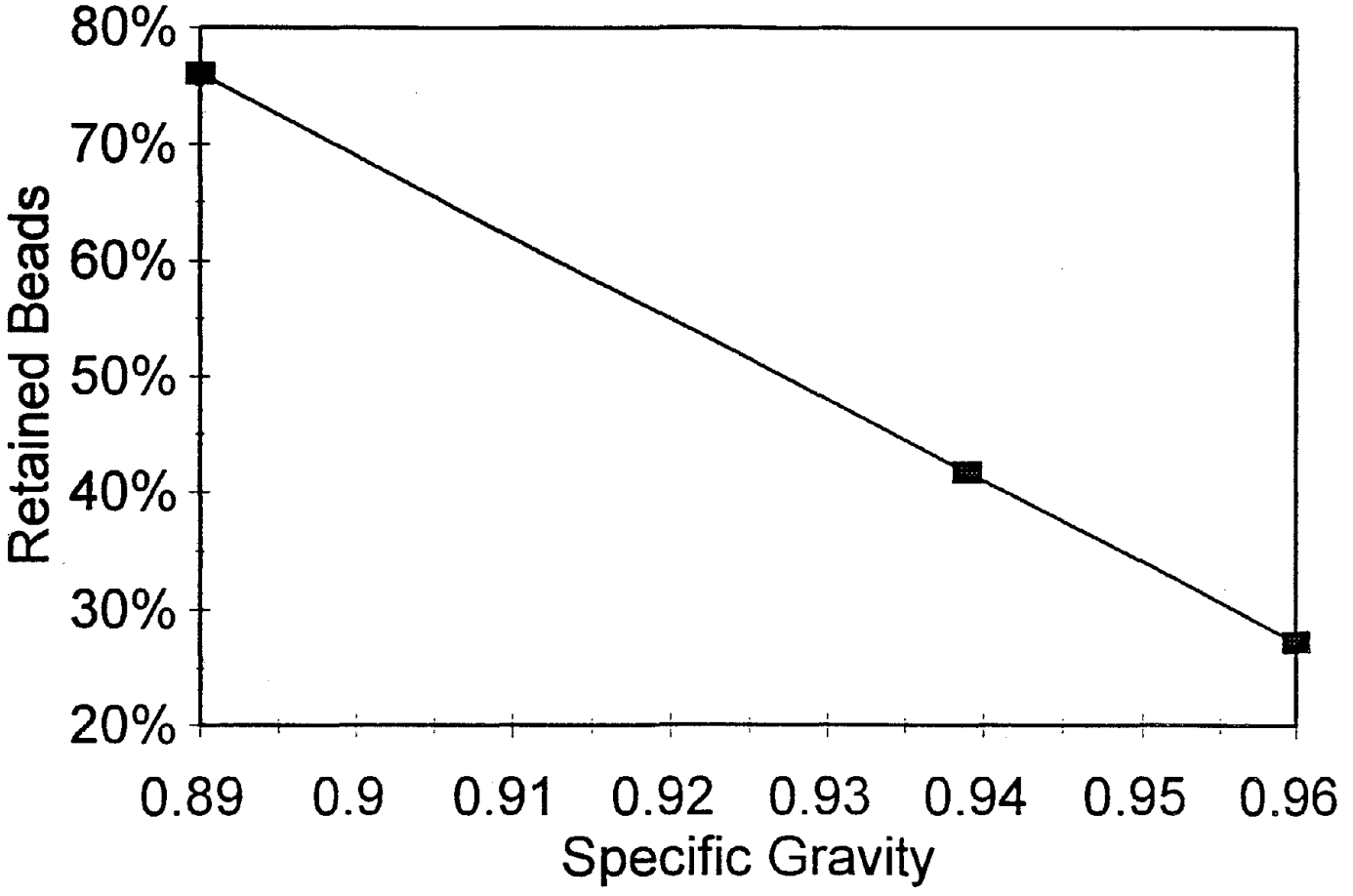

Fig. 6 Bead retention as a function of specific gravity. Submergence plane angle = 25 degrees; speed = 1 knot.

plane that interaction effects are minimized. The concept was found to be very sensitive to the specific gravity of the substance even over the limited range of actual petroleum specific gravities. The principal loss mechanism was observed visually to be entrainment by flow beneath the containment region.

FLOW CONTROL COMPONENTS

Losses were due to part of the retained "slick" in the containment region between the barriers becoming washed out by current below the system. This was the major process limiting retention. Various flow control devices were tried to:

1) Limit volume rate of inflow to the quiescent region

2) Maximize rise time

3) Minimize exit flow speed.

Several configurations tested are shown in Fig. 7 with the corresponding retention rates provided. It is seen that the horizontal barrier works best to separate the containment region from entrainment. In order to test this conclusion, an experiment was conducted using a liquid vegetable (canola) oil using the cross-section configuration shown in Fig. 8. This oil is roughly comparable to #2 fuel oil except that canola's specific gravity is higher (and canola is, therefore, harder to retain). At 1 knot, 90% of the oil was retained thereby supporting the conclusions of the development effort.

Supplementary flow control experiments were also carried out using an active device consisting of a moving submergence plane. No benefit was observed for this barrier application (though helpful when used as a skimmer).

OPTIMIZED DESIGN CONFIGURATION

Further experiments using beads and light viscosity oils at higher speeds indicated that turbulence can mix the incident slick vertically. To be practical, the opening must be large enough to capture the full mixed layer. It was also noted that a larger containment volume with exit flow at the bottom gave more time for the oil to rise to the surface and kept the exit flow low minimizing entrainment. The optimized configuration employing these concepts is shown in Fig. 9. This improved design was then subject to a thorough investigation including retention experiments using a variety of oils and studies of the system's fluid dynamic processes.

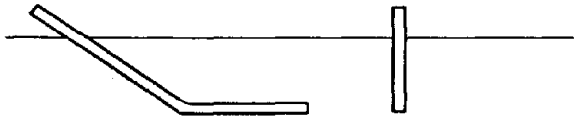

Percent of beads retained	
Test 1	27.3%
Test 2	25.0%
Test 3	23.4%
Ave Test	**25.2%**

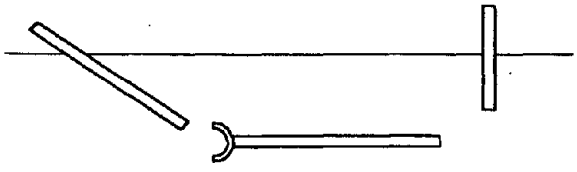

Percent of beads retained	
Test 1	45.8%
Test 2	56.5%
Test 3	56.3%
Ave Test	**52.9%**

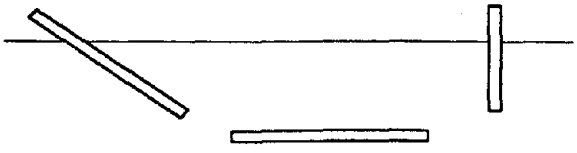

Percent of beads retained	
Test 1	52.2%
Test 2	65.3%
Test 3	65.3%
Ave Test	**60.9%**

Fig. 7 Some of the flow control devices tested and retention results.

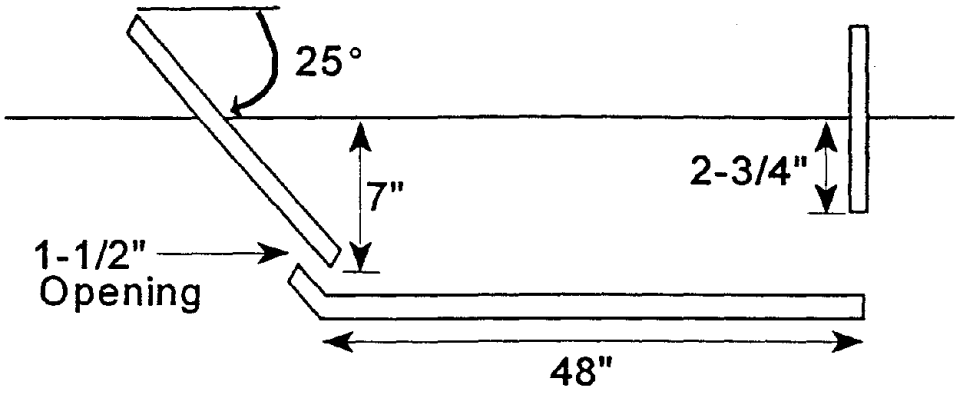

Fig. 8 Configuration used for the first (canola) oil test.

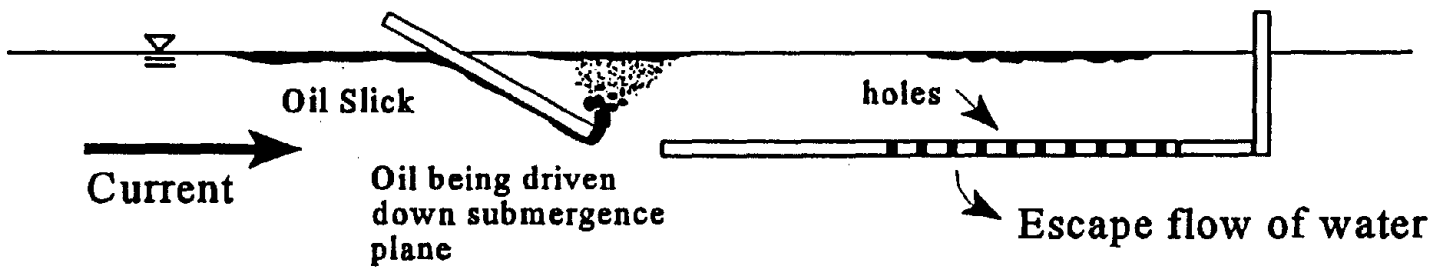

Fig. 9 Optimized design cross-section.

III. OIL CONTAINMENT PERFORMANCE TESTING

METHODS

The developed barrier configuration shown in Fig. 9 was evaluated by conducting oil retention experiments using a variety of oils. The oils, both non-petroleum and petroleum products, were selected to encompass the range of oil properties likely to be encountered in a spill situation. The 2-dimensional configuration was duplicated using marine plywood, sheet aluminum and sheet acrylic plastic and having the dimensions shown in Fig. 10. The model spanned the full width of the tank. The model is a large scale representation and is approximately 1/2 size for an estuarine prototype or may be regarded as full-size for use in small streams.

Before oil release, the flume was brought up to an incident flow speed of 1 1/2 knots. This speed is approximately 3 times the critical velocity for oil loss using a single vertical barrier of the same draft under the same flume conditions. Oil was then released from a reservoir and spread using a manifold/splash plate system. The system then operated under steady state conditions until the experiment was terminated by stopping the oil supply and the flume flow. This was done in time to prevent the possible recycling of oil escaping past the barrier and encountering the system a second time.

All experiments were video taped, and measurements were made of oil retention. Oil and oil/water mixtures were independently recovered from within the containment region, in front of and in back of the barrier system. Each volume was allowed to separate, and the amount of oil in each volume was quantified. These measurements, as well as data on the amount released, allowed the percent of encountered oil retained by the barrier system to be calculated. The retention was computed as the amount retained in the containment region divided by the amount passing the submergence plane. This definition is actually somewhat conservative in that additional oil was stopped in front of the submergence plane and some was trapped in back of the end vertical plane. (These amounts were not counted because their ultimate fate under field conditions is uncertain.) The redundancy in oil measurements enabled internal checks to be made and measurement uncertainty to be minimized.

Information on oil properties was obtained from the literature and from direct measurement. Published values by other researchers and by the product suppliers were collected and used for initial guidance. Actual oil properties for the oils used in this series of experiments were measured directly in the UNH Chemical Engineering Lab. Standard protocols were used to obtain surface tension, interfacial tension, specific gravity and viscosity.

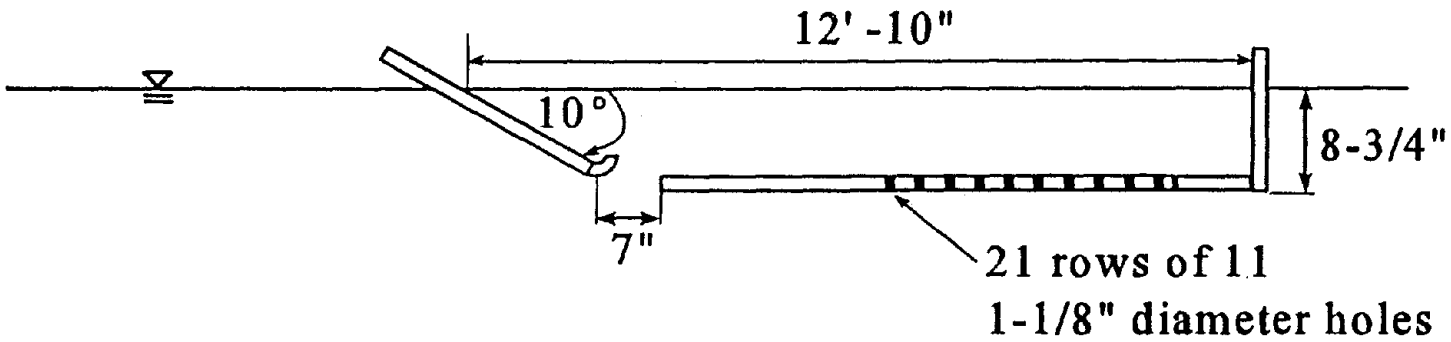

Fig. 10 Two-dimensional physical model dimensions.

Table I. Retention rates and oil properties.

Oils	Density ($^{lb}/ft^3$)	SG	Surface tension ($^{Dynes}/_{cm}$)	Interfacial tension FW ($^{Dynes}/_{cm}$)	Viscosity (centistoke)	Retention Percentage
#2 Oil	51.66	0.8309	30.0	6.7	7.55	88
#4 Oil	54.57	0.8778	30.4	23.9	62.89	85
#5 Oil	58.49	0.9407	34.7	20.9	221.5	80
#6 Oil	62.80	1.010	37.6	17.4	4050.0	Non-floating
Silicone 1,000 cSt	60.35	0.9708	24.6	22.6	993.1	84
Silicone 10,000cSt	60.35	0.9707	25.0	23.0	10,655.0	89
Lube oil 600	55.48	0.8924	36.5	13.0	629.9	86
Lube oil 2000	57.01	0.917	36.2	27.9	2011.0	98
Lube oil 3000	57.23	0.921	28.2	31.5	3280.0	95

Density measurements taken at 30°C with a DA-3000 Density Meter.
Kinematic viscosity measurements taken at 25°C with a Brookfield synchro-electric viscometer
Surface tension and interfacial tension made with a DuNouy Ring Tensiometer

RESULTS AND OBSERVATIONS

Results for retention rates of the oils tested and their corresponding oil properties are summarized in Table I. It is seen that retention is generally very good (above 80 %) to excellent (above 90%) in all cases. The results also indicate that performance is somewhat dependent on oil viscosity and specific gravity.

Visual and video observations were also helpful in understanding how the system works and providing insights into the critical fluid dynamic processes. The slick encountered by the submergence plane was not floating placidly in a layer at the surface but was at least partially mixed in a near surface band. The agitation was due mostly to the inherent turbulence level in the flume and, to a lesser extent, the method of introducing the oil. Because turbulent fluctuations are part of all natural flows, especially in estuaries and rivers, the test program was regarded as being a realistic representation of field conditions.

The mixed layer was concentrated while moving down the submergence plane and most entered the containment region at the entrance gap. One evident loss mechanism, however, was mixing of oil filaments so deep in the water column that the entrance was missed. Oil and water entering the containment region formed a small jet which contributed to further mixing. Most of the oil then separated into surface slicks just above the submergence plane and towards the aft surface of the containment region. These were areas of quiescent fluid, the oil simply rose to the surface and was trapped. A second loss mechanism, however, was the entrainment of small droplets in the exit flow through bottom baffle holes.

Though losses were very small in comparison to the oil retained, attention was focused on the processes of oil escape in order to build a knowledge base for future design development. The two loss mechanisms were strongly influenced by droplet size and specific gravity. Large droplets with low specific gravity have a high rise velocity. Large droplets, therefore, formed a concentrated band going down the submergence plane which favored entering the device. Once inside, large, low density droplets rose quickly and were less influenced by the exit water flow.

In general, it was observed that high viscosity oils formed large droplets, while low viscosity oils were more susceptible to turbulent breakdown into small droplets. Both the incident flow turbulence and turbulence in the entrance jet played a role. These visual observations are consistent with the Table 1 results that retention is enhanced at high viscosities and low specific gravities.

Since the role of viscosity is characterized by the Reynolds number, retention rates are expected to increase with decreasing Reynolds number. In this context, the Reynolds number (Vd/ν) can be computed using incident velocity for V, oil kinematic viscosity for ν, and draft for d. The effects of buoyancy on droplet rise velocity are characterized by the internal Froude number $(V/(\frac{\Delta\rho}{\rho}\ gd)^{1/2})$ in which $1 - \frac{\Delta\rho}{\rho}$ is

equivalent to specific gravity. Retention is expected to improve at low internal Froude numbers which correspond to higher droplet rise velocities (as well as lower incident velocities.) Since both non-dimensional parameters are relevant, retention is plotted in Fig. 11 as a function of Reynolds number for groupings of data points having similar internal Froude numbers. In Fig. 12, retention is plotted as a function of internal Froude number for data points having similar Reynolds numbers. The expected trends are evident.

Overall, retention rates for the improved design configuration are very good to excellent. Visual observations of physical processes provide physical insights which enhance understanding and may, in the future, lead to further design improvements.

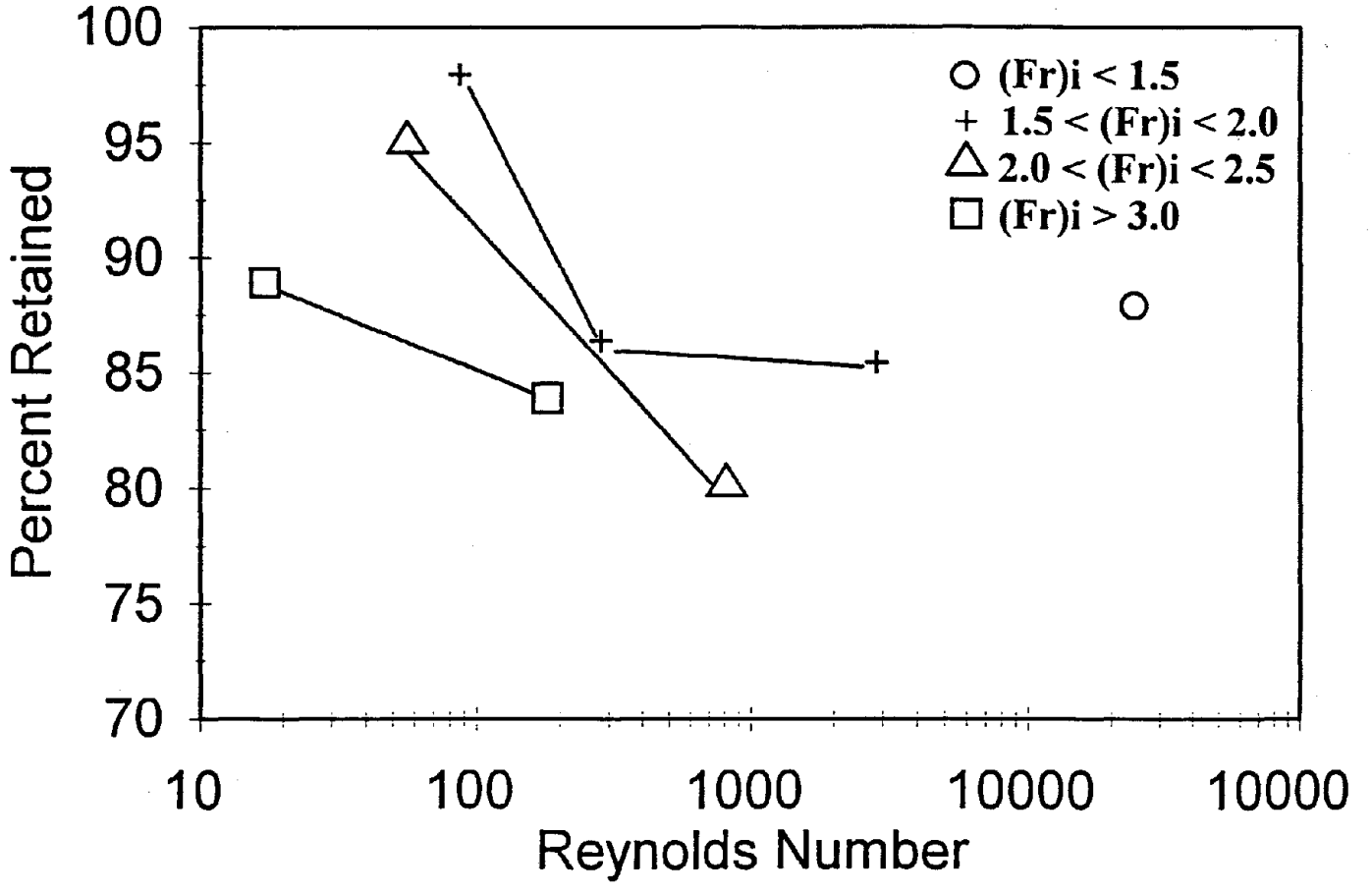

Fig. 11 Oil retention as a function of Reynolds number.

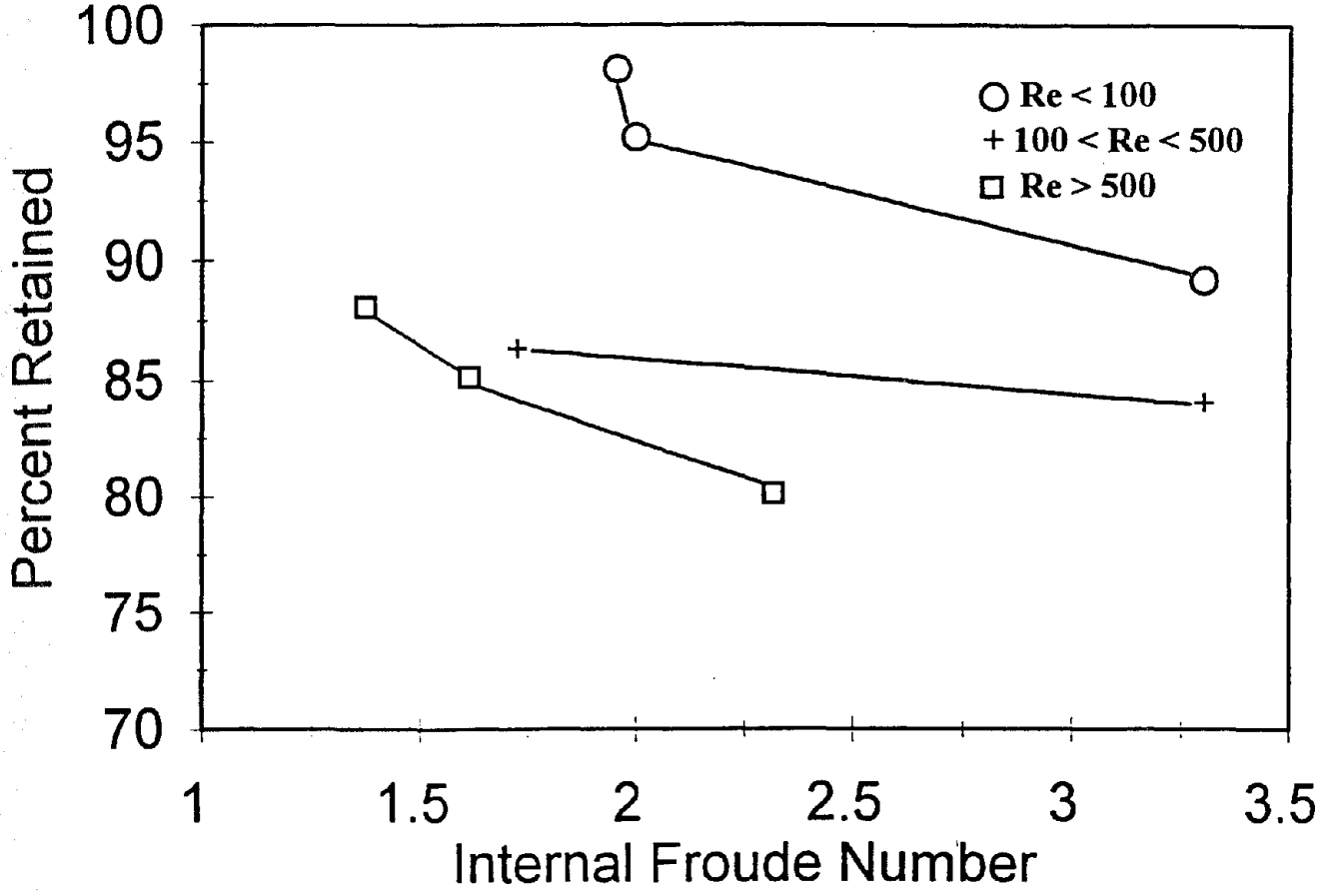

Fig. 12 Oil retention as a function of internal Froude number.

IV. THEORETICAL CONSIDERATIONS

PURPOSE

The experimental program was supplemented by a concurrent study of theoretical aspects. The fundamental field equations which apply in both the oil and water liquids and the associated boundary conditions were reviewed. The purpose was to understand the basic factors governing the flow, to identify critical non-dimensional parameters, and to serve as a guide in interpreting experimental data.

In the next section, the partial differential field equations are presented and nondimensionalized. Equation coefficients yield the relevant nondimensional parameters governing dynamic similarity. Consideration of oil droplet rise velocity provides additional scaling information. Next, a control volume approach is taken in which the "volume" consists of the barrier system. The purpose here is to gain insights into the effects of configuration design changes and to gain a further understanding of trends and processes observed in the experimental program.

FUNDAMENTAL EQUATIONS AND SCALING

Assuming an incompressible, Newtonian, viscous fluid, conservation of mass (continuity) and the equation of motion can be written, respectively, as

$$\nabla \cdot \bar{v} = 0 \tag{1}$$

and

$$\rho \frac{\partial \bar{v}}{\partial t} + \rho \, \bar{v} \cdot \nabla \bar{v} = -\nabla P + \mu \, \nabla^2 \bar{v} - \rho g \hat{k} \tag{2}$$

In the above equations,

$\bar{v}$ = velocity vector
ρ = density
P = pressure
μ = shear viscosity
g = gravitational acceleration
and
$\hat{k}$ = unit vector in the vertical direction. (3)

The governing field equations apply within the oil constituent and within the water portion (with different property values). At solid-liquid boundaries, the no-slip condition must apply and stresses must be equal and opposite over the contact surface. On free surfaces, fluid particles on the boundary must remain on the boundary, and the surface is normally regarded as stress-free. Along an oil-water interface, the velocity field must be continuous, and shear stresses across the interface must be equal and opposite.

Interfacial tension and curvature of the oil-water boundary affect the normal stresses on each side according to

$$\Delta\sigma = \alpha\left(\frac{1}{R_1} + \frac{1}{R_2}\right) \tag{4}$$

in which $\Delta\sigma$= difference in normal stresses, α = interfacial tension and R_1, R_2 are principal radii of curvature.

The equation of motion can be put into nondimensional form using V_s as a velocity scale and L as a length scale. The result is

$$\frac{\partial \bar{v}'}{\partial t'} + \bar{v}' \cdot \nabla' \bar{v}' = -\nabla' P' + \frac{1}{Re} (\nabla')^2 \bar{v}' - \frac{1}{Fr^2} \hat{k} \tag{5}$$

in which primes denote nondimensional variables. The nondimensional coefficients are the Reynolds number,

$$Re = \frac{\rho V_s L}{\mu} \tag{6}$$

and the Froude number,

$$Fr = \frac{V_s}{\sqrt{gL}} \tag{7}$$

Thus for exact dynamic similarity in physical model experiments, both Reynolds number and Froude number scaling is important.

Visual observations of the flume experiments indicated that oil droplet rise velocity strongly influences retention. As a droplet ascends, the principal dynamic balance is between the buoyancy force balancing fluid drag so that

$$\Delta\rho g L^3 \;\alpha\; \rho V_{rise}^2 L^2 \tag{8}$$

in which $\Delta\rho$ is the density difference and V_{rise} = rise velocity. Thus the ratio of rise velocity to incident velocity is proportional to

$$\frac{V_{rise}}{V_s} \;\alpha\; \frac{\sqrt{\frac{\Delta\rho}{\rho} gL}}{V_s} = \frac{1}{(Fr)_{internal}} \tag{9}$$

which is the inverse of the internal Froude number. This implies theoretically that oil barrier system performance should strongly depend on internal Froude number. This result is consistent with the earlier discussion (on physical grounds) and the plotting of retention as a function of internal Froude number on Fig. 12.

CONTROL VOLUME APPROACH

Some important design trade-offs become apparent when considering a control volume around the barrier system as shown in Fig. 13. The system is represented schematically in which V_{in} is the spatially averaged velocity over A_{in}, the gap entrance area, and V_{out} is the spatially averaged velocity over A_{out}, the sum of the exit areas.

From conservation of mass under steady state conditions,

$$V_{in} A_{in} = V_{out} A_{out} \tag{10}$$

Since it is desired to minimize V_{out}, or at least keep V_{out} much less than the rise velocity, A_{out} must be large in comparison with the gap area A_{in}. The entrance area, A_{in}, on the other hand, cannot be reduced too much or losses will occur through oil not entering the system.

For configuration designs in which V_{out} much less than V_{in} has been achieved, another design factor must be considered. In this case, the mechanical kinetic energy being advected out is much less than the kinetic energy being transported in. The difference must be accounted for by dissipation within the control volume according to

$$\text{Dissipation rate} = m \left[\frac{V_{in}^2}{2} - \frac{V_{out}^2}{2} \right] \tag{11}$$

in which $\dot{m}$ is the mass rate of flow through the system. The principal dissipation mechanism is through the turbulence generated in the incoming jet formed at the gap entrance. This has the undesirable effect of breaking the oil up into smaller droplets and can thereby contribute to increased entrainment by exit flow.

Lengthening and deepening the containment region serves to separate the incoming jet from the exit flow consequently enhancing the rise time of droplets so they can reach the surface. The trade-off here is a longer, larger barrier system subject to logistical and other practical limitations.

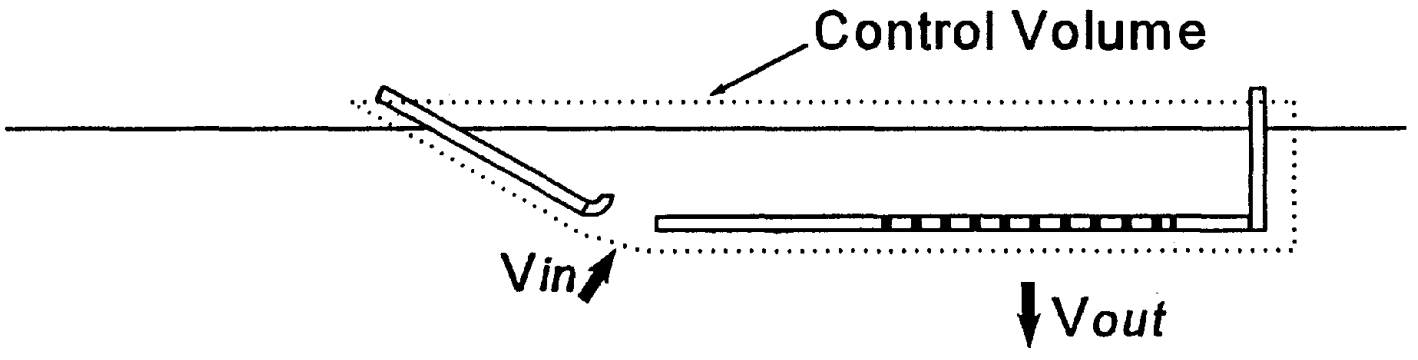

Fig. 13 Control volume used for theoretical considerations.

V. VELOCITY DISTRIBUTION

METHODS

Measurements were made of the fluid velocity field generated by the 2-dimensional design configuration used in the oil retention experiments. The purpose was to obtain a quantitative understanding of the fluid dynamic processes through detailed velocity vector measurements incident to, within and below the barrier system.

Since the primary concern was the velocity field associated with the currents determined by the barrier system geometry, measurements were made without oil. Visual observations of the retention experiments indicate that the oil droplet field is subject to advection by the water velocity field which is, in turn, governed by the configuration geometry. A preliminary set of measurements was made using a small electro-magnetic probe. Then a laser doppler velocimeter (LDV) was used to make more detailed measurements. Because of their greater accuracy and completeness, only the LDV measurements will be presented in this report. The LDV works by sensing the doppler shift in light scattered by small particles passing through the sensing volume. Measurements are mechanically noninvasive and the sensing volume is small (characteristic dimensions are less than 1/2 inch).

Measurements were made at stations on the flume vertical centerline plane spaced to give a greater density of sites at critical areas such as the submergence plane, the entry gap and the exit holes. Off-center measurements were also made at selected stations to measure flow uniformity in the cross-channel direction.

The nominal incident velocity was maintained at 1 1/2 knots (which is the speed used in the retention experiments). Other speeds were used in addition at selected stations to check the proportionality of the flow regime to incident current.

RESULTS

Results are shown on Figs. 14-16 as synoptic velocity vector plots normalized by the incident flow speed. Features such as the submergence plane concentration, the entry gap jet, the quiescent regions and the exit velocity distribution are clearly evident. The incident flow speed variation tests indicate that the current vector magnitudes are proportional to incident speed in the range 0.5 - 1.5 knots. The off-center measurements show that cross-channel uniformity is maintained throughout most of the configuration. The exceptions are the aft corners of the containment region where small, intermittent vertices form which introduce a local downward component. This is a tank "wall-effect" phenomenon which would not be present in prototype barriers long in the width direction. Retention performance results are consequently somewhat conservative with respect to an ideal 2-dimensional situation.

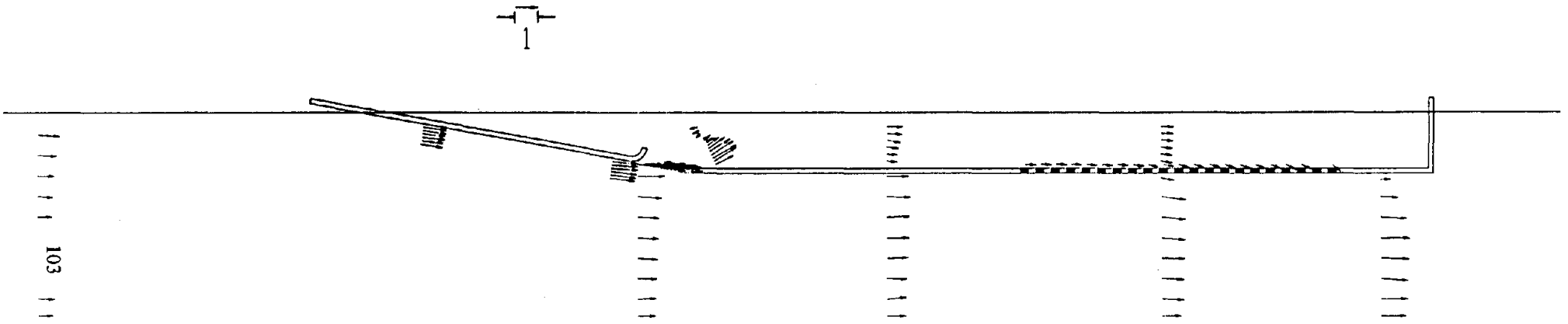

Fig. 14 Velocity field measured using the LDV. Vector magnitudes (speeds) are referenced to the incident current speed.

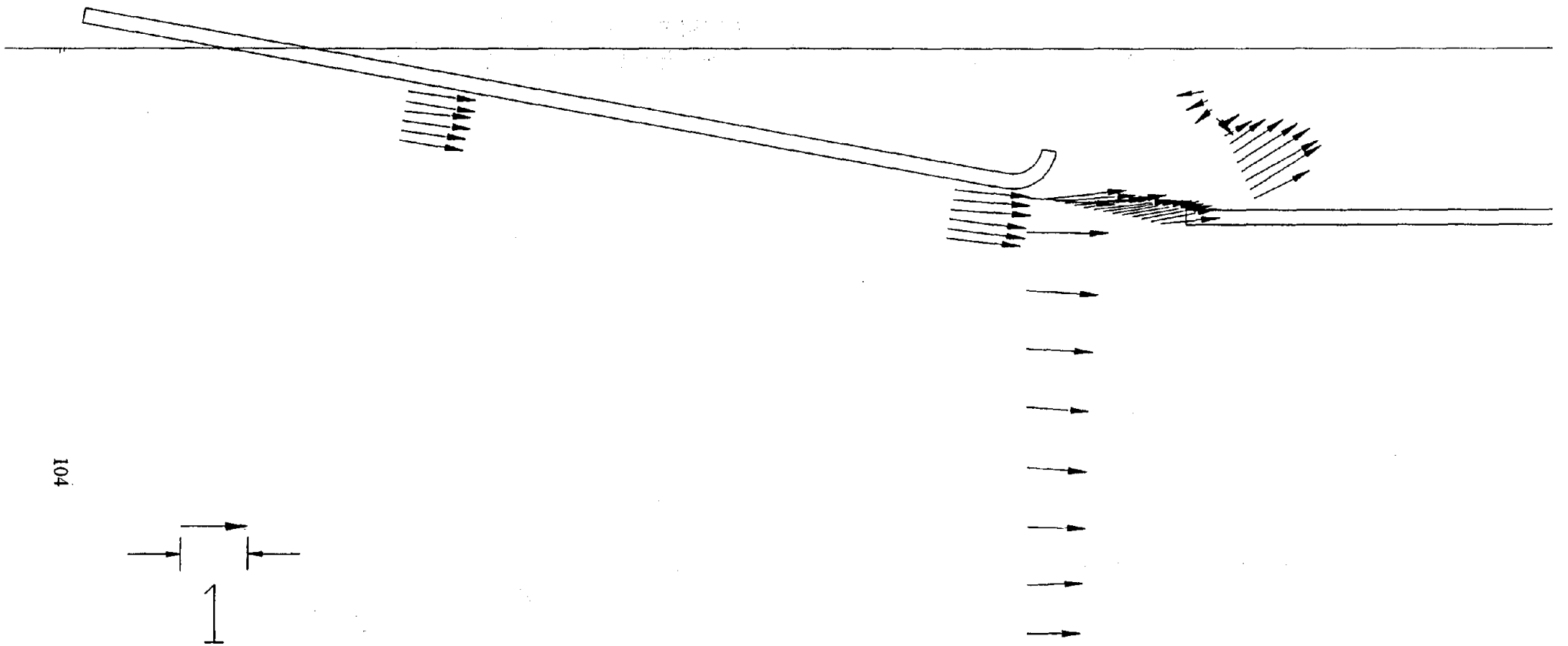

Fig. 15 Closeup of the submergence plane and gap flow.

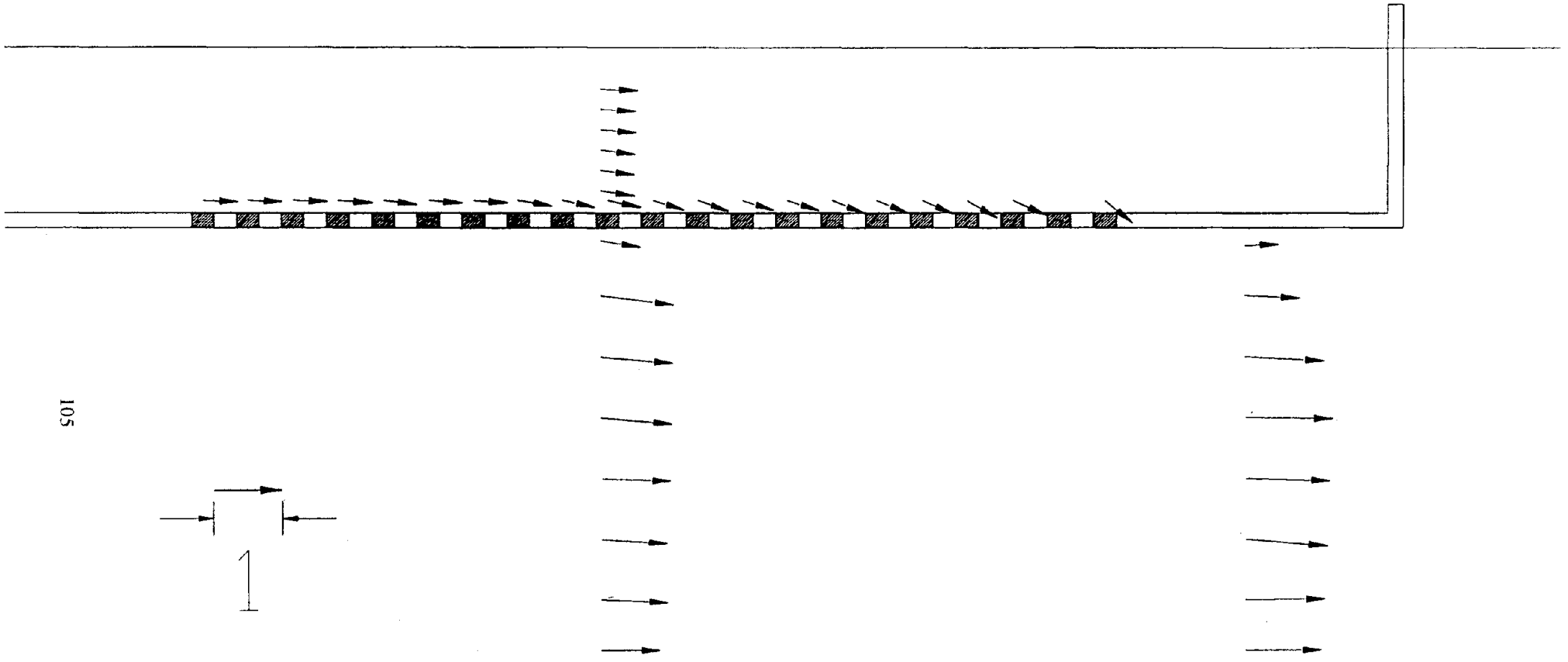

Fig. 16 Closeup of the containment volume/exit flow.

VI. FLEXIBLE 3-DIMENSIONAL PHYSICAL MODELS

APPROACH

The purpose of the flexible small scale physical model experiments was to develop, in 3-dimensions, design concepts which reproduce the 2-dimensional cross-section tested in the oil retention experiments. The models incorporate flexibility and were free floating as in standard oil booms. The small scale, flexible 3-dimensional physical models represent a first step in developing full-size practical barrier systems based on the 2-dimensional, rigid configuration developed and tested in this study. Larger models and full-scale prototypes are to be developed in Phase II of the Rapid Current Barrier program.

The developmental approach was to add flexibility to physical model designs in an orderly, gradual manner. Each model was designed to duplicate the desired cross-section shape, then constructed and flume tested. The first model was a semi-rigid system but completely free-floating. Based on this experience, a fully flexible, 3-dimensional physical model was made having curvature in the cross-channel direction.

The physical models developed here were tested solely for their shape rendering capability. At 1/12 of the scale used in the 2-dimensional oil retention tests, they were too small scale for experiments with oil. Since the purpose of these tests was to evaluate model shape, position and orientation while running at speed on the surface, Froude scaling was used. The primary physical model tests were run at the 2-dimensional oil retention test speed (1 1/2 knot) Froude scaled which is 0.43 knots (= $(1/12)^{1/2}$ times 1.5). Of course while in the flume, visual observations were made at actual speeds ranging from still water to 1 knot (3 1/2 knots at the 2-dimensional model scale).

SEMI-RIGID PHYSICAL MODEL

The objective of this design was to introduce a free-floating capability and to allow for flexibility in the horizontal, bottom baffle which is the largest of the 2-dimensional components. As seen in the cross-section design drawing, Fig. 17, floatation and ballast are positioned to maximize stability. The intention was to use drag of the aft vertical barrier to keep the horizontal barrier taut.

In the flume, the system floated at the designed waterline in still water and "towed" at the proper orientation at 0.43 knots (1 1/2 knots at the 2-dimensional model scale) as shown in the Fig. 18 photograph. The horizontal baffle, however, did not remain taut and billowed downward aft due to exit flow drag. It could be argued that this is acceptable since entrainment by current below the barrier is not increased and the containment volume is in fact larger. Since the objective of this study was to duplicate the 2-dimensional cross-section shape, on the other hand, horizontal baffle tautness was addressed in the next physical model design.

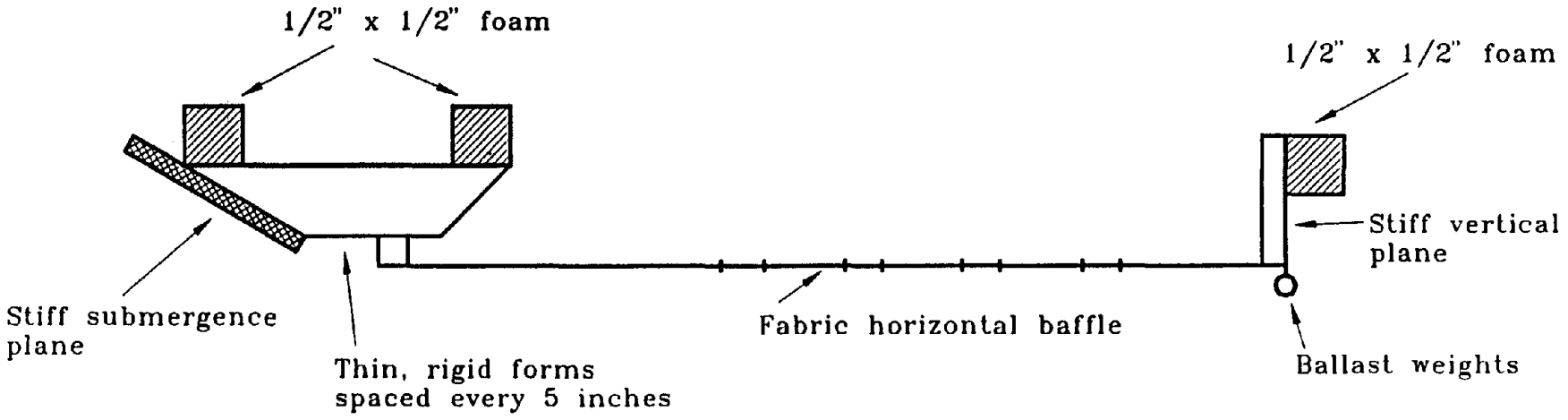

Fig. 17 Design cross-section of the semi-rigid physical model.

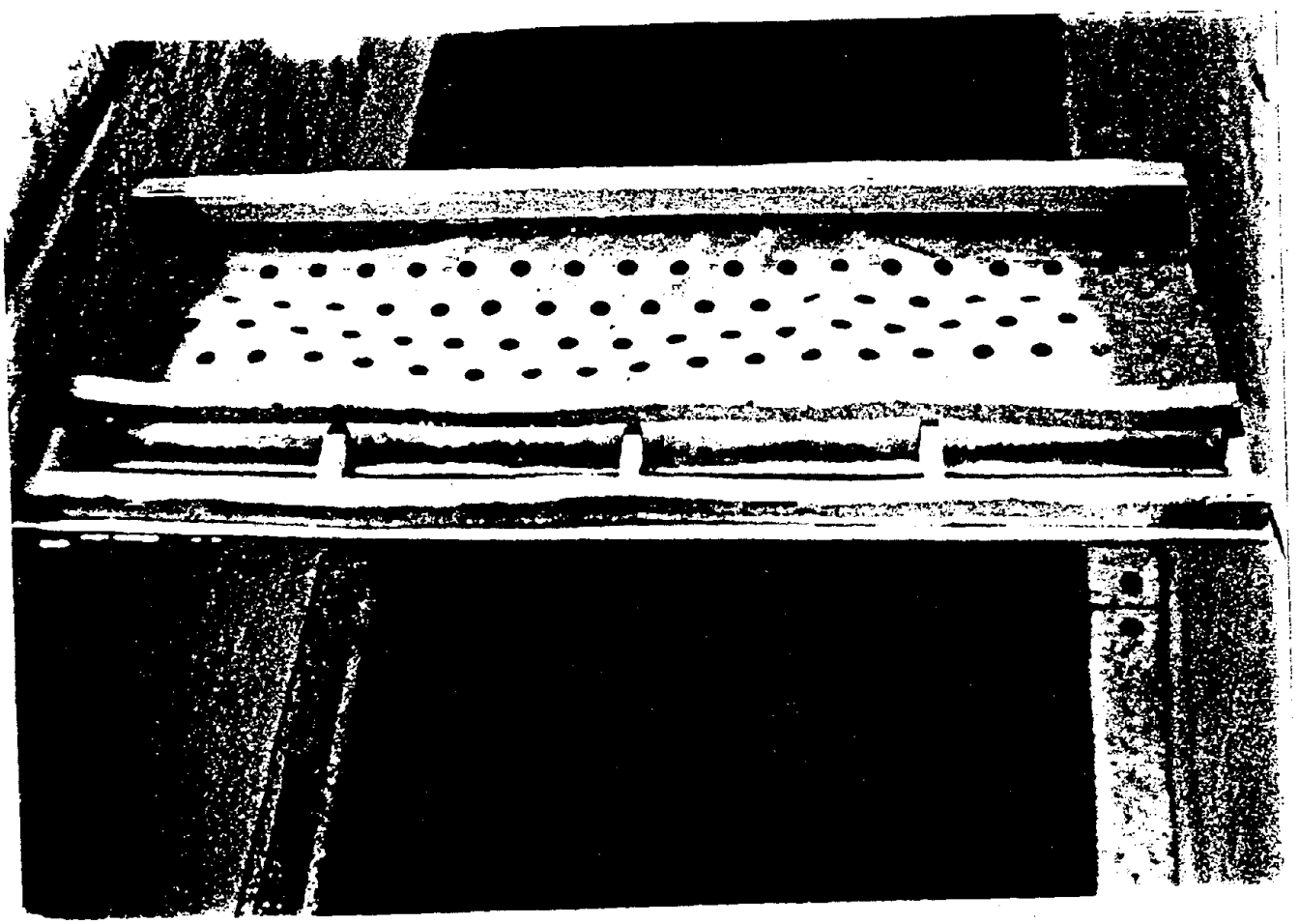

Fig. 18 Semi-rigid model at 1 1/2 knots (Froude scaled) in the flume.

FLEXIBLE COMPONENTS PHYSICAL MODEL

In this model, flexibility is incorporated into the submergence plane and the trailing vertical plane (as well as the horizontal baffle). These are constructed of foam as shown in the Fig. 19 design cross-section. The model is designed to bend in plan view (in the cross-current direction), so it can assume the usual catenary curve associated with standard oil booms. To maintain tautness in the horizontal baffle, light weight longitudinal spars are used. They are spaced at regular intervals in the cross-current direction. Stability is achieved by placing the foam buoyancy sources at the leading and trailing edges.

In the flume, the system floated at the proper waterline in still water and maintained the desired position and orientation when "towed". As seen in the Fig. 20 photograph, cross-current curvature was obtained.

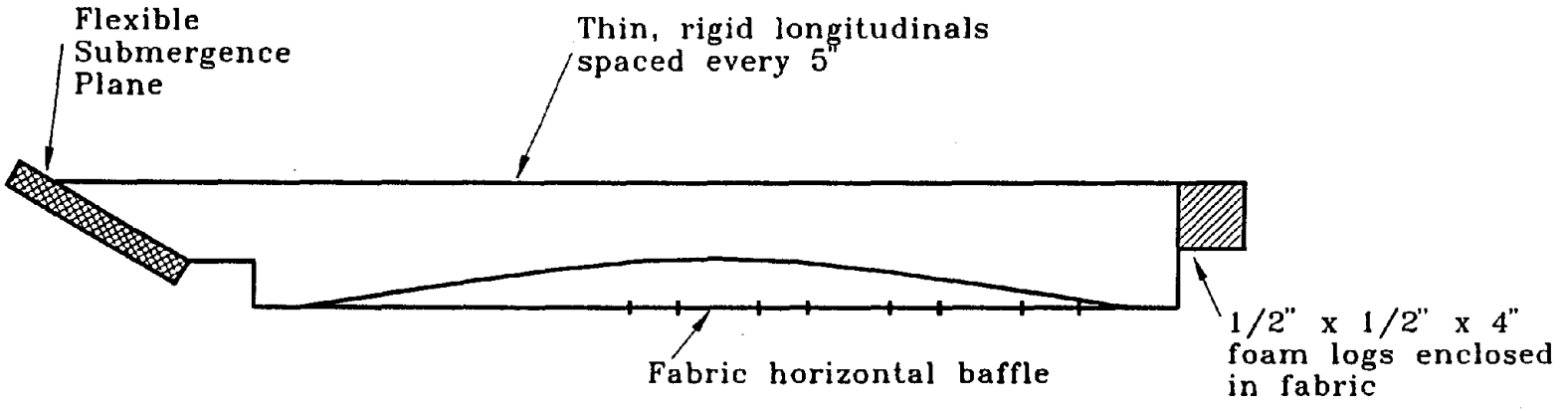

Fig. 19 Design cross-section of the flexible, 3-dimensional physical model.

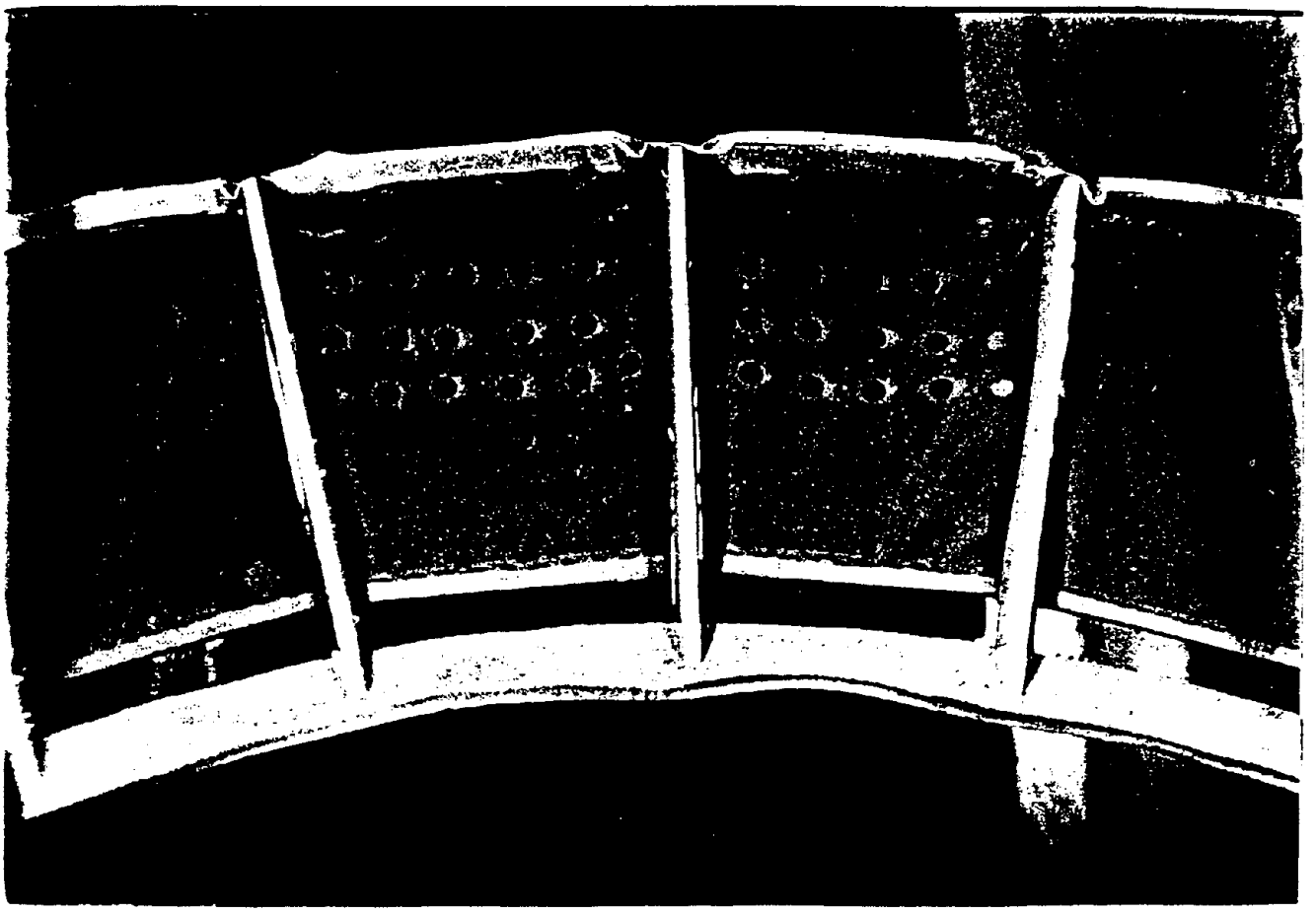

Fig. 20 Flexible 3-dimensional model at 1 1/2 knots (Froude scaled) in the flume.

VII. SUMMARY AND CONCLUSIONS

The main result of this study has been the development of a barrier system configuration that, in its 2-dimensional form, has been shown effective in retaining oil in rapid currents. The final cross-section configuration was developed from the initial Fig. 1 starting point by optimizing angles and dimensions and by the addition of a horizontal baffle. Flume experiments showed very good to excellent oil retention at speeds up to 3 times the critical leakage current for a plane, vertical barrier under the same flume conditions. Oils tested had fluid properties covering the range of values associated with petroleum liquids likely to be spilled and for which floating barriers are appropriate. A supplementary theoretical study and measurements of the velocity distribution provided insights to the important fluid mechanical processes and design trade-offs. Initial 3-dimensional designs incorporating soft materials were tested using small scale physical models. Flume observations indicate that it is technically feasible to build practical, flexible 3-dimensional systems which have the desired cross-section configuration.

These encouraging results lead to the conclusion that the cross-section design investigated in this study under laboratory conditions should be developed further. Larger models and full scale prototypes should be designed based on the knowledge acquired in this study, then built and tested. Continuation of basic research on fluid dynamic processes and the effects of design parameter variations would also be significant to the development of both oil barrier systems and other devices, such as skimmers, utilizing submergence planes and containment volumes.

VIII. REFERENCES

Agrawal, R.K. and L.A. Hale (1974) "A New Criterion for Predicting Headwave Instability of an Oil Slick Retained by a Barrier", Proc. of the Offshore Technology Conference.

Bianchi, R.A. and G. Henry (1973) "The Development and Demonstration of an Underwater Oil Harvester Technique", Report submitted to the EPA, EPA-R2-73-205.

Cox, J.C., L.A. Schultz, R.P. Johnson and R.A. Shelsby (1980) "The Transport and Behavior of Oil Spilled In and Under Sea Ice", ARCTEC, Inc., Columbia, MD.

Delvigne, G.A.L. (1989) "Barrier Failure by Critical Accumulation of Viscous Oil", Proceedings of the 1989 Oil Spill Conference, American Petroleum Institute, Washington, DC, 143-148.

Delvigne, G.A.L. (1984) "Laboratory Experiments on Oil Spill Protection of a Water Intake", in Oil in Freshwater, Vandermeulen and Hrudy (eds), Pergamon Press, Elmsford, New York, 446-458.

Doane, C.W. (1994) "An Open-Channel Flume for the Study of Two-Dimensional Oil Containment Boom Models in Fast Current," M.S. Thesis, Ocean Engineering, University of New Hampshire, Durham, NH.

Johnston, A.J., M.R. Fitzmaurice and R.G.M. Watt (1993) "Oil Spill Containment: Viscous Oils", in the Proceedings of the 1993 International Oil Spill Conference, American Petroleum Institute, Washington, DC, 89-94.

Milgram, J.H. and R. Van Houghton (1978) "Mechanics of a Restrained Layer of Floating Oil above a Water Current", J. Hydronautics, Vol. 12, No. 3, 93 - 108.

Swift, M.R., B. Celikkol and G. Savage (1990) "Diversion Booms in the Piscataqua River, NH", in Oil Spill Management and Legislative Implications, M.I. Spaulding and M. Reed (eds.) ASCE, New York, 528-540.

Swift, M.R., B. Celikkol, C.E. Goodwin, R. Carrier, S.P. McDonald and J. Chadwick (1991) "Oil Spill Response Engineering and Planning", Final Report submitted to the NH Water Resources Research Center, UNH, Durham, NH.

Swift, M.R., B. Celikkol, G. LeCompagnon and C.E. Goodwin (1992) "Diversion Booms in Current", Journal of Waterway, Port, Coastal and Ocean Engineering, Vol. 118, No. 6, 587-598.

Wicks, M., III (1969) "Fluid Dynamics of Floating Oil Containment by Mechanical Barriers in the Presence of Water Currents", Proceedings API/FWPCA Joint Conference on Prevention and Control of Oil Spills, 55-106.

SOURCE IDENTIFICATION OF OIL SPILLS BASED ON THE ISOTOPIC COMPOSITION OF INDIVIDUAL COMPONENTS IN WEATHERED OIL SAMPLES

R. Paul Philp, University of Oklahoma

SUMMARY

The determination of the source of oils spilt into the environment is an extremely difficult task, complicated by the fact that the composition of the oil will change as a result of weathering effects such as evaporation and biodegradation. Traditionally determination of the source of the spilt oils or fuels involves fractionation of the recovered oil followed by gas chromatography (GC) and/or gas chromatography-mass spectrometry(GCMS) and correlation of the resulting fingerprints.

In the first year of this project, supported by the US Coast Guard through the Dept. of Transportation, the use of a relatively novel approach for the correlation of degraded and non-degraded oil samples in the environment has been investigated. The technique of gas chromatography-isotope ratio mass spectrometry(GCIRMS), permits the determination of the carbon isotopic composition of individual components in very complex mixtures. Even if the sample is weathered the isotopic composition of resolvable individual compounds can be measured. The isotopic compositions of individual compounds in the original and weathered sample should be virtually identical even if weathering has occurred making it possible to undertake correlations based on the isotopic composition of selected components in the samples. In the first part of this project a considerable amount of time was spent on method development. The remainder of the time was devoted to the characterization of a variety of samples both unweathered and weathered, and where appropriate correlations were attempted between these pairs of samples.

In summary the results discussed in this report, demonstrate the potential of GCIRMS for the correlation of weathered and unweathered oil samples spilt into the environment. It is important to emphasize that this technique will not replace the more conventional correlation techniques of GC and GCMS. Rather it is suggested that GCIRMS will compliment these techniques and has the potential to provide answers where possibly GC or GCMS may not be successful because of extensive weathering or biodegradation of the samples.

INTRODUCTION

The project has been concerned with crude oils and refined hydrocarbon products spilt into the environment and the development of a relatively novel analytical approach which can be used, in conjunction with other techniques, to undertake correlations with sources thought to be responsible for the spills. From the moment an oil, or refined hydrocarbon product, is spilt changes will start to occur. Initially the changes will be dominated by evaporation and water washing, both of which tend to remove the lighter hydrocarbon components in the oil(PALMER et al., 1993). Within a relatively short period of time, biodegradation will become dominant and then not only will the residual light components be removed, but progressively heavier components are also removed in a fairly specific and predictable manner(PETERS and MOLDOWAN, 1993). Ultimately all of the saturate hydrocarbons will be removed leaving an unresolved complex mixture of components that are very resistant to biodegradation. With this scenario in mind it becomes extremely difficult to undertake correlations between unweathered and weathered samples. Traditionally, techniques such as gas chromatography(GC) or gas chromatography-mass spectrometry(GCMS), have been used to obtain fingerprints for correlation purposes. Two samples coming from the same source, or genetically related to each other, may be expected to have the same fingerprint but once the fingerprint has been altered as result of weathering it becomes difficult to undertake correlations with any degree of confidence.

Recent developments have lead to the development of a novel

analytical technique, namely combined gas chromatograph-isotope ratio mass spectrometry (GCIRMS), which appears to be a potentially powerful correlation tool(FREEMAN et al., 1990; HAYES et al., 1990; BRENNA et al., 1994; MURRAY et al., 1994). GCIRMS in effect provides the ability to determine the isotopic composition of individual components present in complex mixtures which are resolvable by gas chromatography. Prior to this development, determination of carbon isotopic composition was limited to the bulk isotopic values for unfractionated samples or individual fractions such as total saturate, aromatic, or polar fractions of crude oils (KVENVOLDEN et al., 1993 a and b). There are of course limitations to the GCIRMS approach and in particular these limitations are related to the fact that in order to get good reproducible and reliable data one needs to have good GC resolution. In other words if two components are co-eluting with each other, it will be difficult to obtain reliable isotopic values for either of these components. With well resolved components, reliable isotopic data will be obtained for the individual components.

The purpose of this project has been to demonstrate, that GCIRMS has a potential role to play in the correlation of hydrocarbons, present as contaminants in the environment, with their suspected sources. The basic premise of this approach is that as long as the components can be detected in the weathered samples, the isotopic composition of individual components in unweathered and weathered samples will be virtually identical. In other words

if we are looking at a crude oil sample and comparing the isotopic composition of the individual n-alkanes in the C_{15}-C_{25} range, the isotopic composition of each of these components would be virtually identical in the original crude oil sample and in a sample of the same crude oil left to weather in the environment.

In the following discussion, examples resulting from the application of this technique to the correlation of several weathered and unweathered samples will be described. It is important to emphasize that this approach will not completely replace the more conventional techniques of GC and GCMS. Instead GCIRMS should be used in conjunction with those techniques to provide supporting evidence, and in many cases additional evidence, for any correlations that are being made between samples.

EXPERIMENTAL

Samples

For the purposes of this preliminary study samples of crude oils, fuel oils, gasoline samples and tar balls were obtained from a variety of sources. Specific locations of samples will not be given since they are not necessary for the discussion. Samples were obtained in both unweathered and weathered condition. In some cases the samples were weathered naturally and in other cases the samples were weathered artificially in the laboratory.

Gas Chromatography

Prior to analyses by GCIRMS the samples were analysed by gas chromatography. For the most part the samples were typically analysed, without any fractionation, using a DB-1 fused silica capillary column (0.25mm i.d.; 1.0 um film thickness) and temperature programmed from 40 to 300°C at 4°C/min.

Gas Chromatography-Mass Spectrometry

Where necessary samples were analysed by GCMS using a Finnigan TSQ 70 combined with a Varian 3400 GC. Temperature condition were the same as described above and the system was normally used in the

GCMS mode monitoring commonly used biomarker ions such as m/z 191 and m/z 217 for determination of terpane and steranes respectively.

Gas Chromatography-Isotope Ratio Mass Spectrometry

GCIRMS was performed using a Finnigan MAT 252 Isotope Ratio Mass Spectrometer coupled with a Varian 3400 gas chromatograph. GC conditions were as described above.

RESULTS AND DISCUSSION

As part of the development and application of any new technique or approach, it is necessary to undertake a certain amount of method development. In the next few paragraphs, a brief discussion will be given to illustrate some of the work that has been undertaken to demonstrate the reliability of GCIRMS as a technique for the correlation of weathered and unweathered oil, or oil-derived samples. More details of this are also available from the quarterly reports submitted for this project. Initially one oil sample was analysed several times to demonstrate the reproducibility of the technique. Results from this part of the work are shown in Fig. 1a. The data shown in this figure are obtained from the GCIRMS of the oil following which the major peaks in the chromatogram were selected and then the isotopic values for each of these components calculated and plotted onto the spread sheet as shown in this figure. The slight discrepancies that can be observed for the isotopic compositions of the higher carbon numbered alkanes result from the very low concentration of these compounds in the original sample.

Crude oils are very complex mixtures of a wide variety of

compound classes, including saturate, aromatic, and various polar compounds. Oils can be fractionated into the compound classes by a variety of chromatographic techniques, such as HPLC, column chromatography, or thin layer chromatography. In certain situations sample size may preclude our ability to reliably fractionate samples into individual fractions making it necessary to analyse unfractionated samples directly by GCIRMS. Hence following the reproducibility checks, it was necessary to determine whether or not there was any isotopic fractionation during the separation of a crude oil into saturate and aromatic fractions by HPLC. If not and if the situation arose, a comparison could be made for example between the isotopic composition of n-alkanes present in whole oils vs. the corresponding values for the n-alkanes in the associated saturate fractions. Results of such a comparison are shown in Figure 1b which shows the isotopic composition of individual components present from a whole oil and the corresponding values for the same components in the saturate fraction separated by HPLC prior to analysis by GCIRMS. As can be seen from this plot there is virtually no difference between the whole oil and the values for the saturate hydrocarbon fraction. It should also be noted in Fig. 1 that there are various standard components included in the results of the study. It is essential that such standard components be included during the analysis of any samples. These standards, which are totally deuterated n-alkanes with carbon numbers of 24, 32, and 36, are of known isotopic composition and most importantly do not coelute with any of the undeuterated components. The

isotopic compositions of these standards have been determined individually using the batch inlet system of a separate isotope ratio mass spectrometer. Hence their values are known and if these values are not achieved during the GCIRMS analysis of a sample, then the complete set of GCIRMS data will be discarded and the sample re-run. In other words, these components serve as internal quality control components and their values should be obtained reproducibly to within +/- 0.3‰

From the data shown above, and other more extensive laboratory studies, it has been clearly established that the GCIRMS technique GCIRMS is reproducible and that with the addition of internal standards of known isotopic composition, the effects of weathering on crude oils and hydrocarbon products can be investigated. In this project, a number of crude oil samples and refined hydrocarbon products, weathered and unweathered, have been examined by GC, GCMS and GCIRMS. The first example makes use of an oil from the Middle East which has been weathered by evaporation and which is compared with its unweathered counterpart. The gas chromatograms of the two samples are shown in Fig. 2 from which it can be seen that the evaporation has removed the more volatile components. Analyses of these two samples by GCIRMS to determine the isotopic compositions of the individual n-alkanes resulted in the data shown in Fig. 3. It is clear from these data that little change has occurred to the isotopic composition of the n-alkanes as a result of the evaporation process.

Similar results and conclusions can be drawn from samples of

fuel oils, and other hydrocarbon products, that have been weathered naturally and compared with their unweathered counterparts. Gas chromatograms and the corresponding isotopic data for three additional sets of weathered and unweathered samples are shown in Fig. 4-6. The major conclusion to be drawn from these sets of data is that, in general, the effects of weathering do not appear to have a significant effect on the isotopic composition of the major individual components. This in turn reinforces the notion that the GCIRMS has the potential to be a very useful tool for correlation purposes, particularly if used in conjunction with GC and GCIRMS to determine the source of crude oils and refined hydrocarbon products that have been spilt into the environment.

Crude oil samples which are heavily weathered and subjected to biodegradation initially lose their lower molecular weight n-alkanes and then, with time, increasingly higher carbon number alkanes will be removed. This can lead to a relative concentration effect whereby at a certain stage of the biodegradation process, higher carbon number components may appear to be present in relatively high concentrations. For example, in Fig. 7a and b, hydrocarbons from two heavily weathered tar balls, have been characterized by high temperature gas chromatography(HTGC). HTGC in itself is a relatively new technique and permits one to readily determine the distribution of hydrocarbons in carbon number ranges (i.e. $>C_{35}$) that are not normally detected by conventional gas chromatography(PHILP, 1994). This is an important development particularly for characterization of weathered oil samples where

such concentration effects may be expected to occur. Results from the analyses of these two samples by GCIRMS produced the data shown in Fig. 8a. The strong similarity between the isotopic composition of these two samples leads to the proposal that these two tar ball samples are derived from the same source, probably in this case the same tanker, or two tankers carrying oil from the same source. Confirmation of this conclusion comes from GCMS analysis of the same samples and determination of the distribution of the commonly used biomarkers-steranes and terpanes (Fig. 9a and b and Fig. 10a and b). The similarity between these biomarker distributions for the two samples, supports the conclusions based on the isotope distributions.

Gas chromatograms of the hydrocarbons from a second set of weathered crude oil samples are shown in Fig. 7c and d. These samples, whilst not as weathered as the samples shown in Fig. 7a and b, clearly have been weathered to the extent where the low molecular weight hydrocarbons have been removed and the initial stages of biodegradation have commenced. GCIRMS data shown in Fig. 8b for these two samples suggests that these samples are not directly related to each other as seen from the significant differences in their isotopic compositions, which are far greater than the differences that may be expected from experimental errors or non-reproducibility of the technique. Sterane and terpane biomarker data for these two samples (Figs. 9c and d and Figs 10c and d) shows that whilst there are a number of basic similarities in these samples, one sample contains abundant proportions of the

biomarker called 18α(H)-oleanane, characteristic of a contribution from angiosperm-derived organic matter. Again the isotopic composition combined with the biomarker data clearly support the idea that in this case these two samples are not derived from the same source and that the differences between the samples do not result from biodegradation or weathering but differences in origin.

A slightly different example demonstrates the application of GCIRMS to the characterization of the more volatile gasoline samples. Although not directly related to the current project is does serve to demonstrate the wider applicability of this technique. Two gasoline samples collected from local service stations on opposite corners of an intersection were analysed initially by gas chromatography resulting in chromatograms with virtually no difference between the distribution of individual components within these samples, either qualitatively or quantitatively, when characterized by gas chromatography. However analyses of the same two samples by GCIRMS provided the data shown in Fig. 11 where the isotopic composition of a selected number of components are presented in the same format as above. The components used to construct this diagram have not been identified since for the purpose of this example it is only necessary to ensure that the same components are being monitored for each sample and this can be done on the basis of retention time data. Despite the very close similarity of the GC data it can be seen from Fig. 11 that there are indeed a number of differences between the two samples, particularly the two components with retention times of

921 and 1873sec. Based on the isotopic data alone it is possible to distinguish these two gasoline samples which were virtually identical on the basis of gas chromatography. This example illustrates the potential of GCIRMS for determination of the source of samples responsible for problems associated with leaking underground storage tanks.

The results described in this report have mainly been concerned with the characterization of whole oils or their corresponding saturate hydrocarbon fractions. In many cases the hydrocarbons may be extensively altered by weathering to the extent that virtually all the saturate hydrocarbons have been removed making it impossible to use them for correlation purposes. In such a situation it may be necessary to utilize the more resistant aromatic hydrocarbons for correlation purposes. The aromatic fractions can be isolated by HPLC and then analysed by GCIRMS in the manner as described above. It should be emphasized that a potential problem is the complexity of the aromatic fraction as shown in Fig. 12. There are many co-eluting or closely eluting components in these fractions and, ideally, complete resolution is required to get the most reliable isotopic data. However there are still certain components such as naphthalenes and phenanthrenes, that may be useful for correlation purposes. In order to partially eliminate the problems concerned with coelution, the two major pairs of phenanthrene isomers can be considered as one peak in each case and a combined isotope value obtained for these two components. This is satisfactory, since if the two isomers coelute

in one sample they will coelute in the sample that is being correlated, therefore carbon isotope values are not necessarily required for the individual components in this situation. The values obtained for these phenanthrene isomers plus various naphthalene isomers are shown in Table I. It can be seen that there is a reasonably good correlation between samples that are known to be related. The discrepancies observed here are simply related to the complexity of the mixture and the errors associated with removing the large isotopic contribution from the underlying unresolved complex mixture of components in the sample.

CONCLUSIONS

This report has presented results from the first year of study to evaluate the use of GIRMS as a potential monitoring and correlation tool for use in a variety of environmental problems. The examples used in this particular study are related to environmental problems caused by contamination from crude oils or refined hydrocarbon products. It is proposed that ultimately the technique can be used for other environmental problems. It is not suggested that GCIRMS should be used as a stand-alone technique. Rather it raises the degree of confidence to which correlations are made to a higher level than those simply based on GC and GCMS data. This is particularly important when the samples being examined are weathered or heavily biodegraded. The successful use of GCIRMS depends on the premise that with weathering and biodegradation, the isotopic composition of individual components in a mixture will not be greatly affected. Hence as long as individual components remain

in the weathered sample then isotopic compositions can be determined and used for correlation purposes.

With very heavily weathered samples, the aromatic fractions may be utilized for correlation purposes since these components are more resistant to biodegradation. However a potential problem with the aromatic fractions is their great complexity and the need for good resolution of individual components in order to obtain reliable isotopic data. This problem can be rectified to a large extent by additional fractionation of the aromatic fraction since it is already known that such fractionation will not affect the isotopic compositions of the individual components.

In brief GCIRMS has the potential to become a very powerful correlation tool to be of use in environmental problems. It will be of most use when used in conjunction with other analytical techniques such as GC or GCMS. It will be of greatest additional value in the cases of samples that are heavily biodegraded to the extent where changes have started to occur to the biomarker distributions making correlations difficult or impossible by conventional techniques.

Additional studies need to be undertaken to determine the extent of the applicability of the technique from the examination of a wider range of sample types. In addition it will also be necessary to examine in greater detail the effects of weathering processes such as evaporation, biodegradation and water washing to ensure that the extent of changes in isotopic composition of individual components is negligible.

REFERENCES

ABRAJANO, T., O'MALLEY, V., EAKIN, P., and HELLOU, J., (1993). Compound specific carbon isotope analysis of polycyclic aromatic hydrocarbons in estuarine environments. In: Organic Geochemistry-Poster Session Volume, (Ed. K. Oygard), F. Hurtigtrykk, Oslo, Norway. pp. 664-667.

BRENNA, J.T., 1994. High precision gas isotope ratio mass spectrometry: recent advances in instrumentation and biomedical applications. Acc. Chem. Res., **27**, 340-346.

CONNAN, J., 1984. Biodegradation of crude oils in reservoirs. In: Advances in petroleum Geochemistry, Vol. 1 (Eds. J. Brooks and D. Welte), Academic Press, London, pp. 300-330.
Freeman, K.H., Hayes, J.M., Trendel, J.M., and Albrecht, P.A., (1990). Evidence from carbon isotope measurements for diverse origins of sedimentary hydrocarbons. Nature, **343**, 254- 256.

HAYES, J.M., FREEMAN, K.H., POPP, B.N., and HOHAM, C.H., (1990). Compound specific isotope analyses: A novel tool for reconstruction of ancient biogeochemical processes. Organic Geochemistry, **16**, 1115-1128.

KVENVOLDEN, K., HOSTETTLER, F.D., RAPP, J.B., and CARLSON, P.R. (1993). Hydrocarbons in oil residues of Prince William Sound, Alaska. Marine Pollution Bulletin, **26**, 24-29.

KVENVOLDEN, K., THRELKELD, C.N., WARDEN, A., and CARLSON, P.R., (1993). Forensic geochemistry-carbon isotopic identification of two sources of oil residues in Prince William Sound Alaska. In :Organic Geochemistry-Poster Session Volume, (Ed. K. Oygard), F. Hurtigtrykk, Oslo, Norway. pp. 735-738.

MURRAY, A.P. SUMMONS, R.E., BOREHAM, C.J. and DOWLING, L.M., (1994). Biomarker and n-alkane isotope profiles for Tertiary oils: relationship to source rock depositional setting. Org. Geochem., 22(3-5), 521-542.

PALMER, S.(1993). Effect of biodegradation and water washing on crude oil composition. In: Organic Geochemistry-Principles and Applications (eds. M. Engel and S.A. Macko). Plenum Press, New York. pp 511-534.

PETERS,K.E. and MOLDOWAN, J.M.,(1993). The Biomarker Guide. Prentice Hall, New Jersey. 363p.

PHILP, R.P. (1993). Oil-oil and oil-source rock correlations: Techniques. In:Organic Geochemistry (Eds. M.H. Engel and S.A. Macko), Plenum Press, New York, pp.445-460.

PHILP, R.P. (1994). High temperature gas chromatography for the analysis of fossil fuels. In: The Uses of Chromatography for

Analysis of Synthetic and Fossil Fuels. J. High Res. Chromatography, 17(6), 398-406.

RUBLE, T., BAKEL, A., PHILP, R.P. (1994). Stable Isotopic Compositions of Individual Biomarkers from Unita Basin Bitumens. In: "Compound Specific Isotope Analysis in Biogeochemistry and Petroleum Research" (Eds. M. Schoell and J.M. Hayes) Org. Geochem., 21(6/7), 661-671.

SAMPLE	AlkylNapth.	AlkylNapth.	MePhen.	MePhen.
Australia (Cooper)	-23.7	-24.07	-21.6	-22.8
Australia (Gippsland)	nd	nd	-20.8	-22.4
Mid. East	-24.5	-24.9	-26.9	-27.9
Mid. East (Weathered)	-23.99	-25.7	-27.8	-27.0

Table I. $\delta^{13}C$ Values for selected aromatic compounds from the aromatic fractions of four oils. These data clearly show differences for the values of these compounds in oils from different geographical regions. However comparison between the weathered and unweathered oil from the Middle East shows certainly similarities between these two sets of data. The differences that are observed result from the large number of coeluting compounds in these chromatograms and the large background of unresolved components.

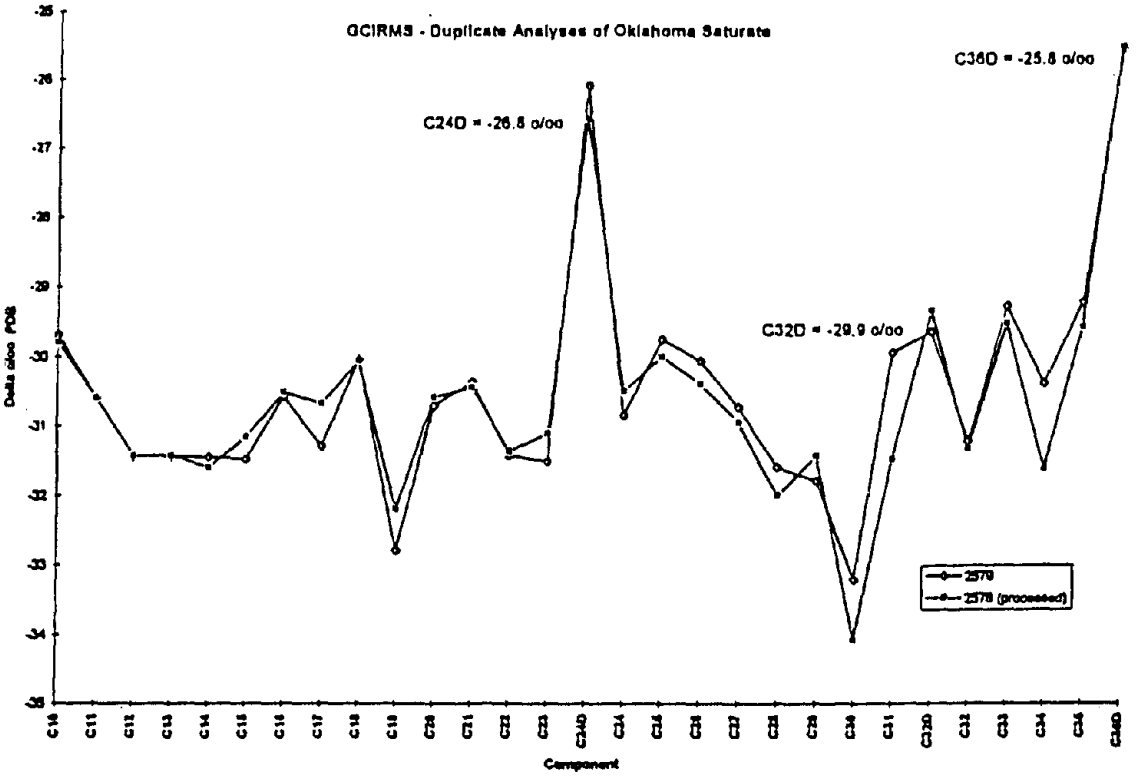

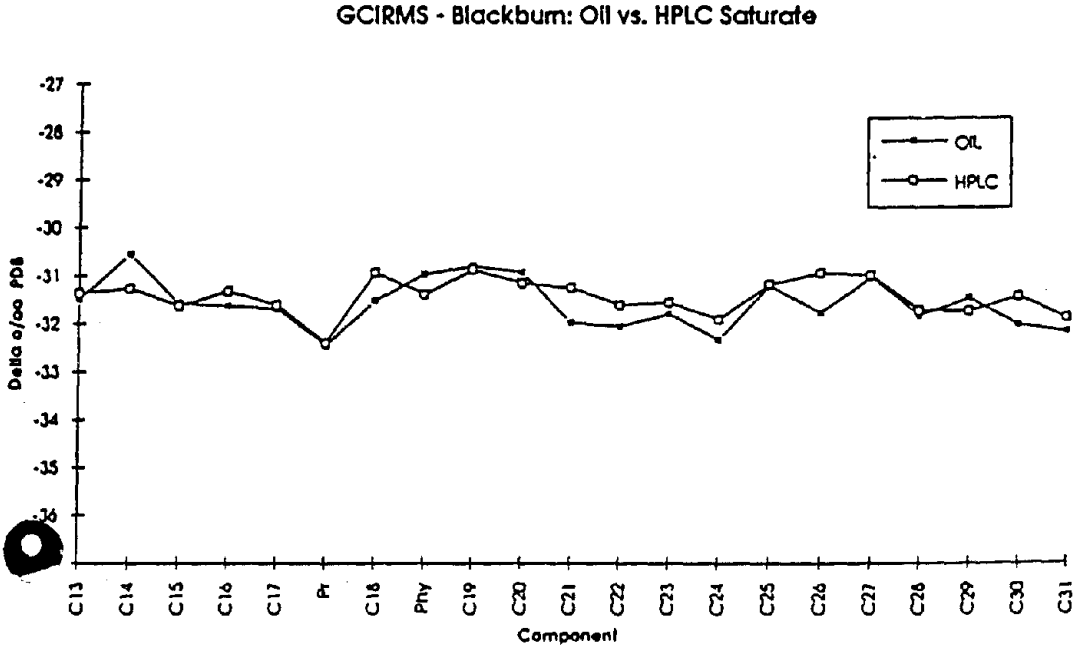

Fig.1. Examples showing (a) the reproducibility of the GCIRMS technique and (b) the fact that there is little or no isotopic fractionation occurring as a result of HPLC separation of the oil into saturate and aromatic fractions.

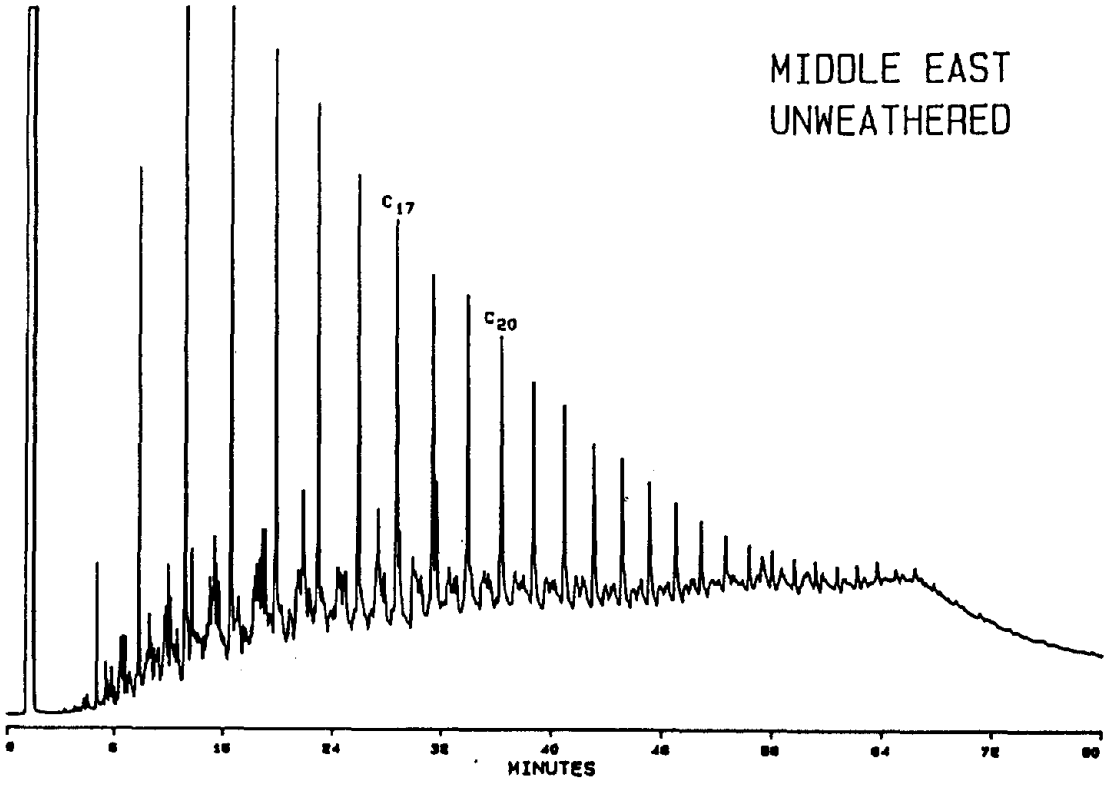

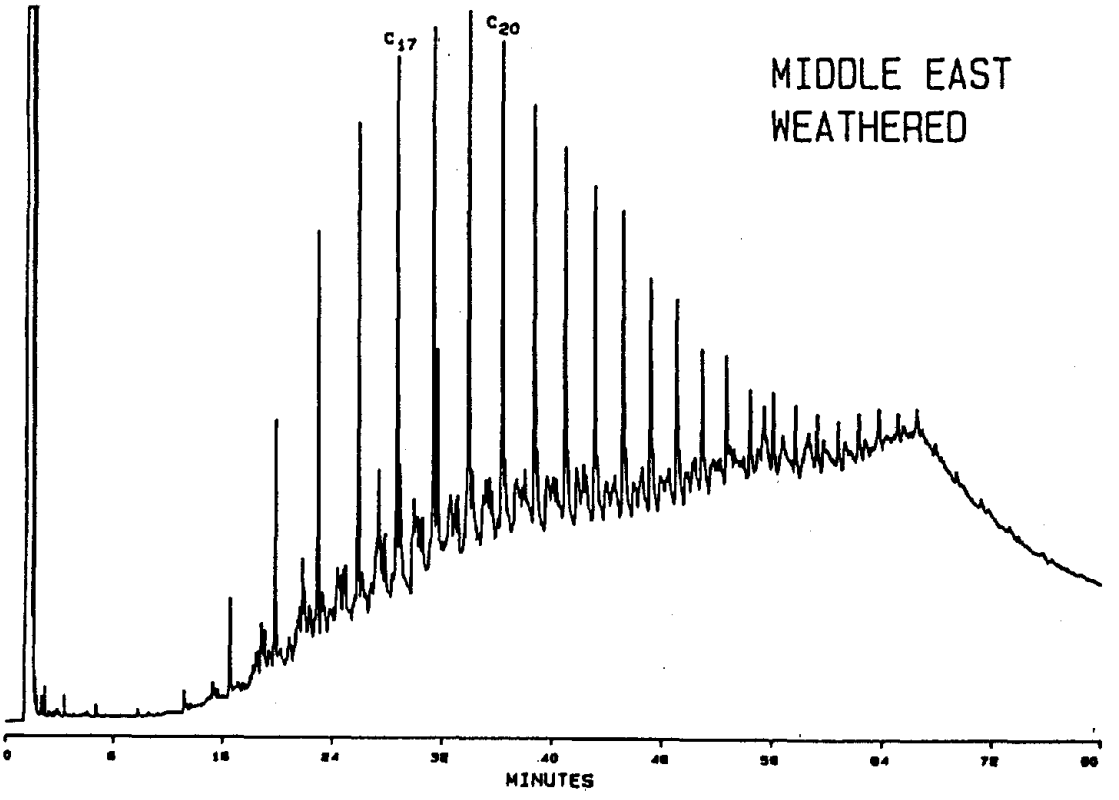

Fig. 2. Gas chromatograms for unweathered and weathered samples of Middle East Crude oils.

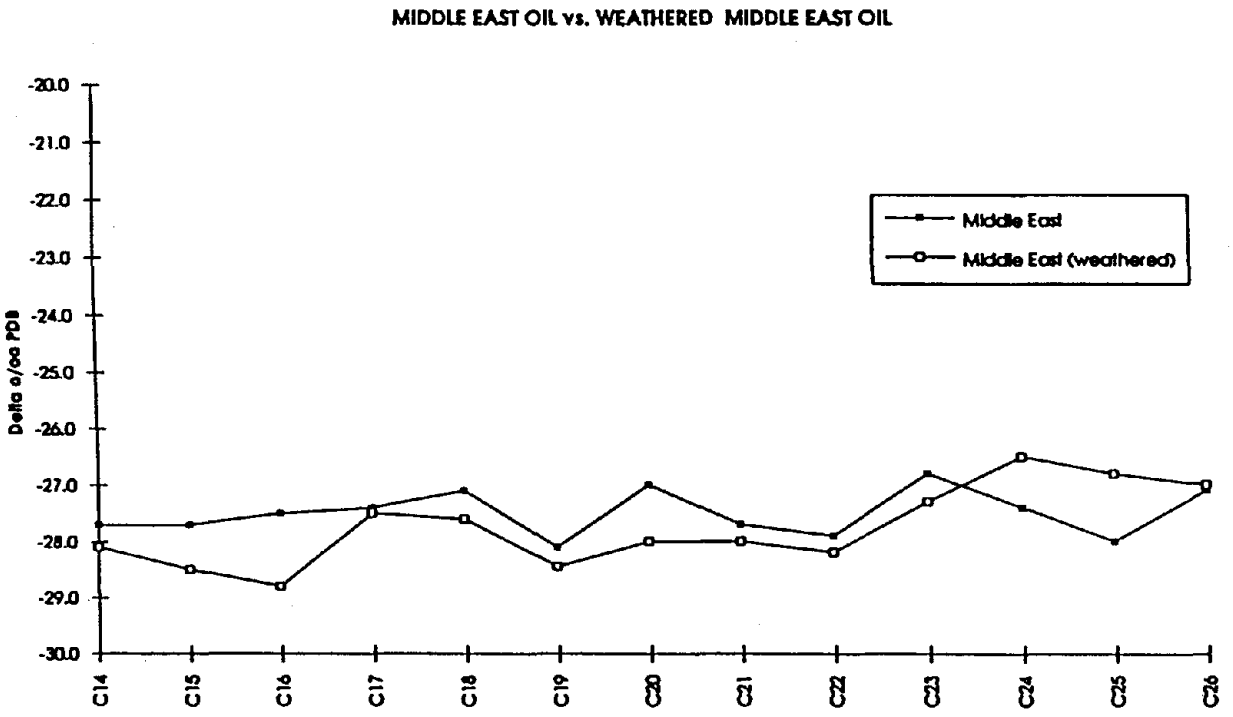

Fig. 3. Comparison between the isotopic data for the individual n-alkanes in the unweathered and weathered samples shown in Fig.2.

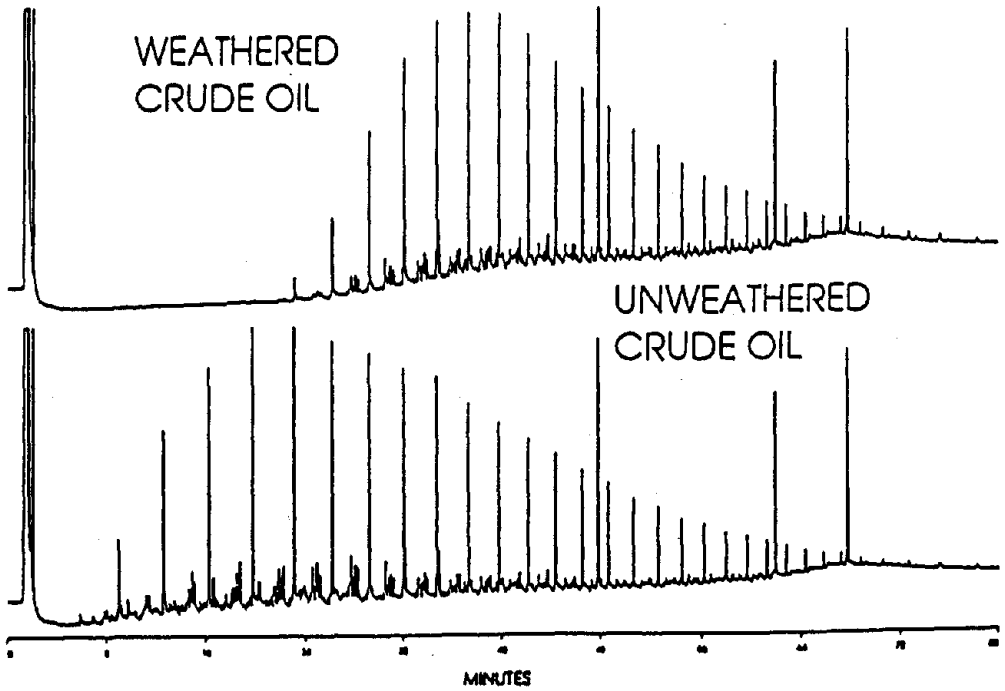

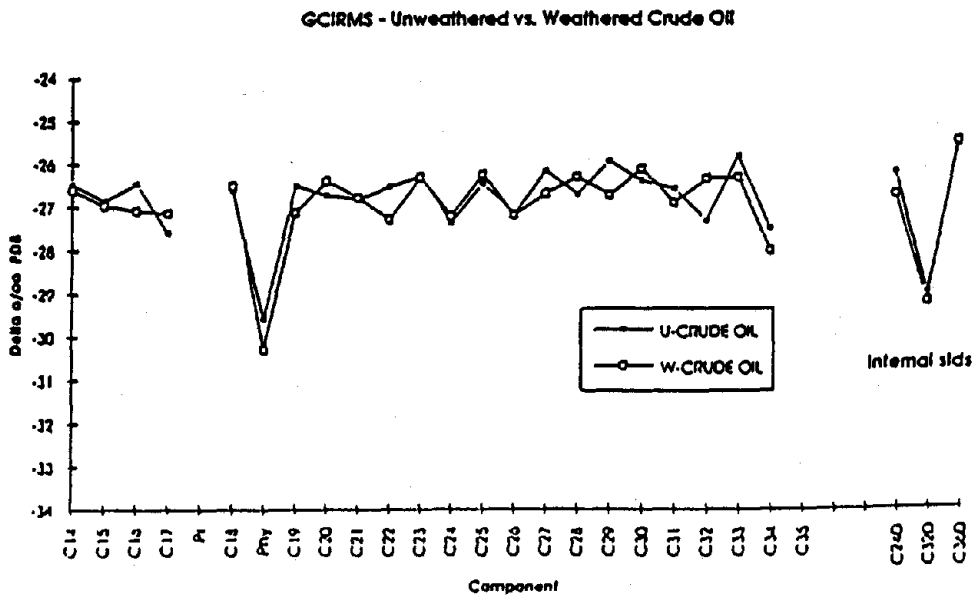

Fig. 4. Gas chromatograms and GCIRMS data for an unweathered crude oil and the same sample after several days of weathering.

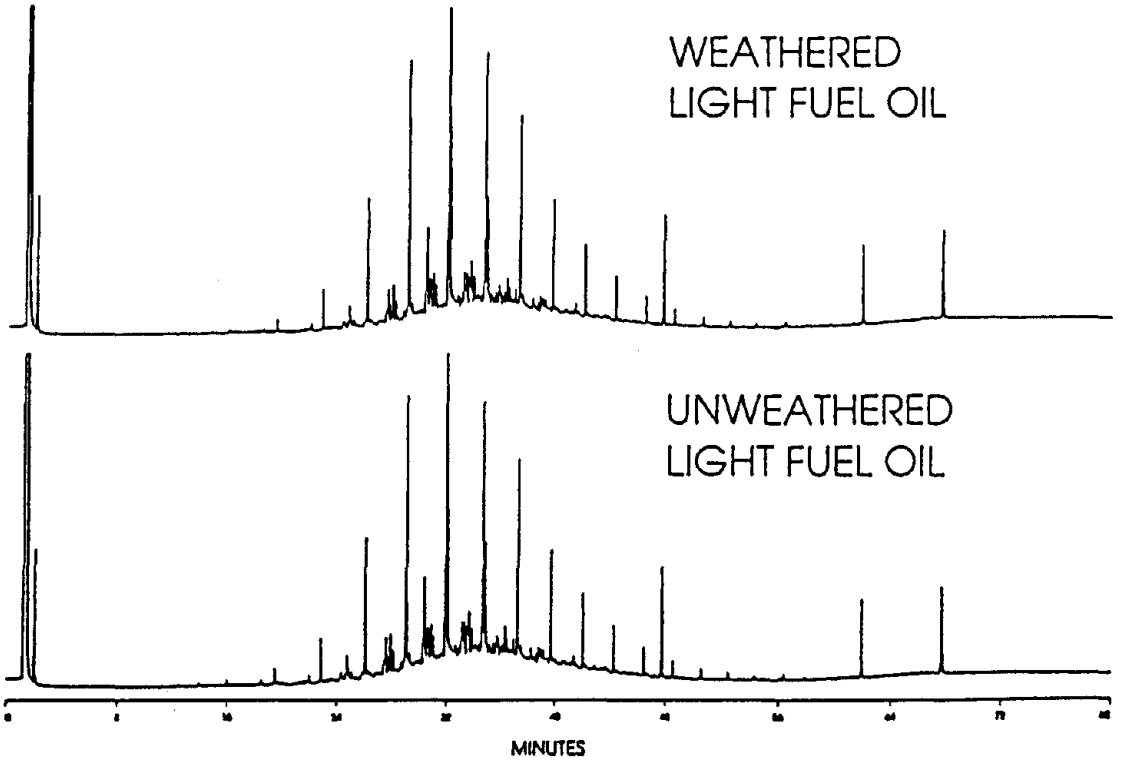

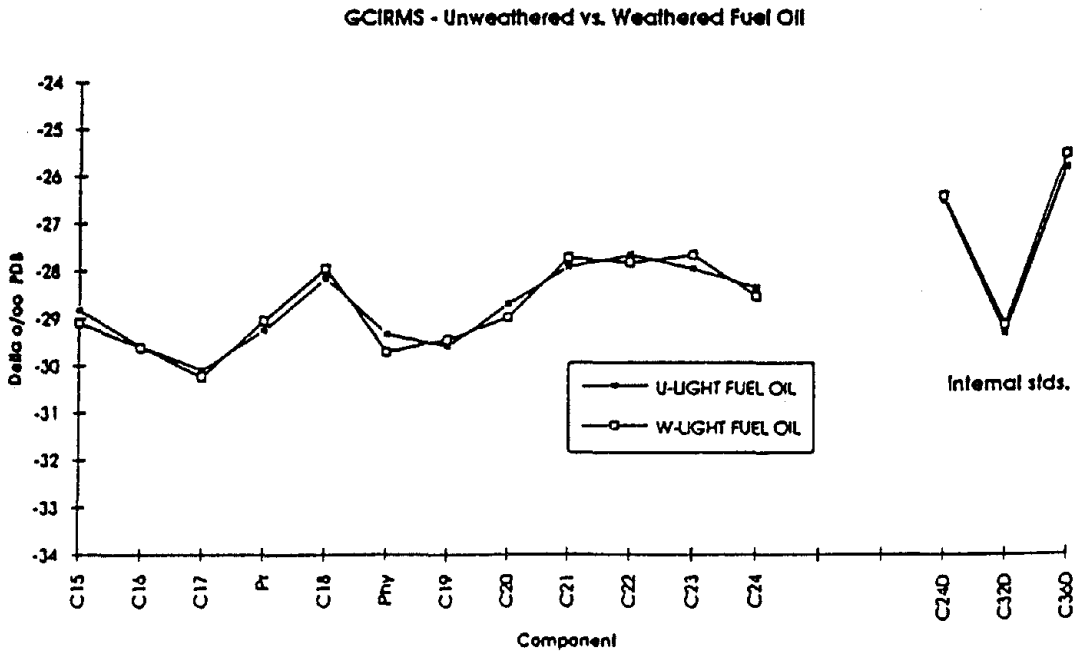

Fig. 5. Gas chromatograms and GCIRMS data for an unweathered light fuel oil and the same sample after several days of weathering.

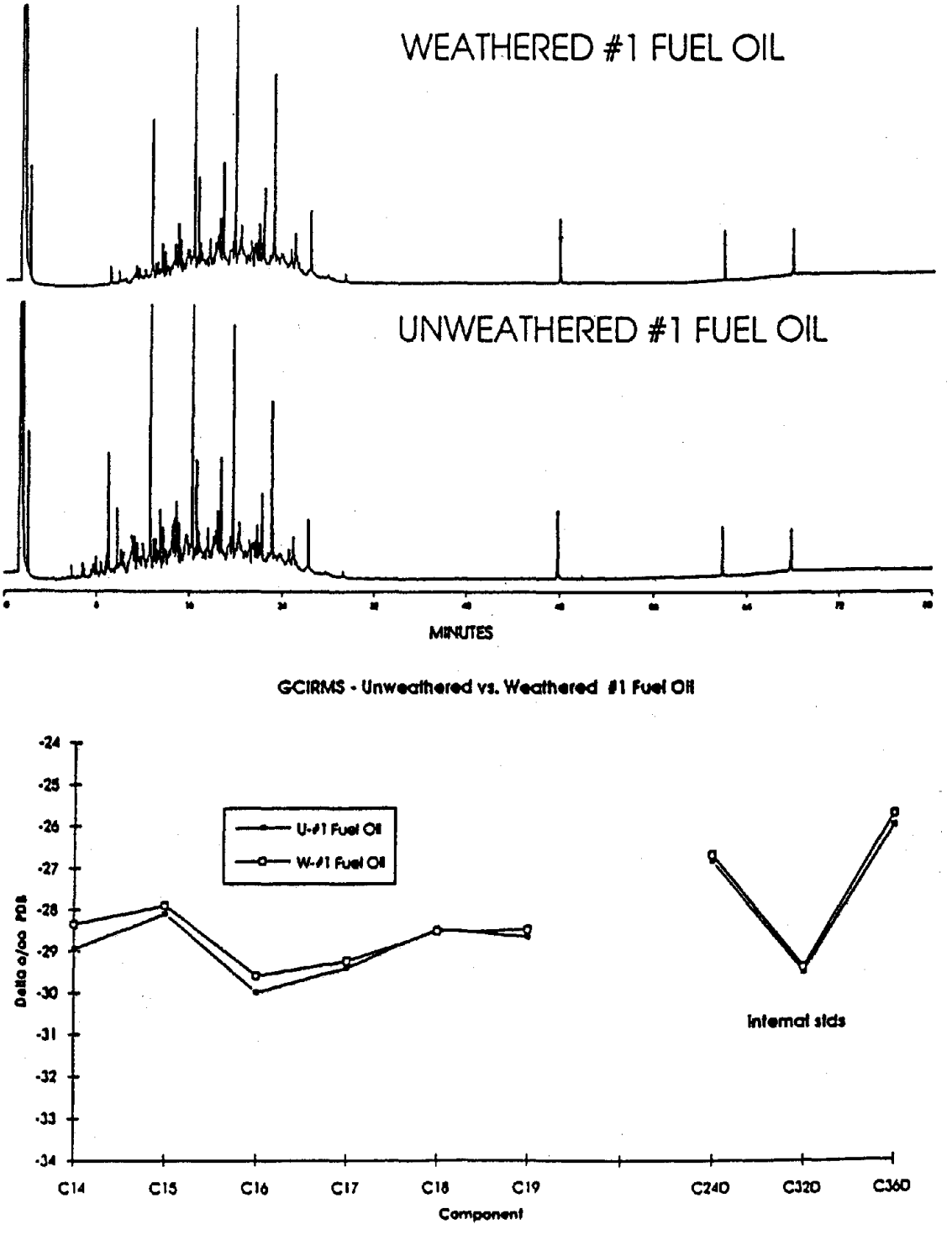

Fig. 6. Gas chromatograms and GCIRMS data for an unweathered #1 fuel oil and the same sample after several days of weathering.

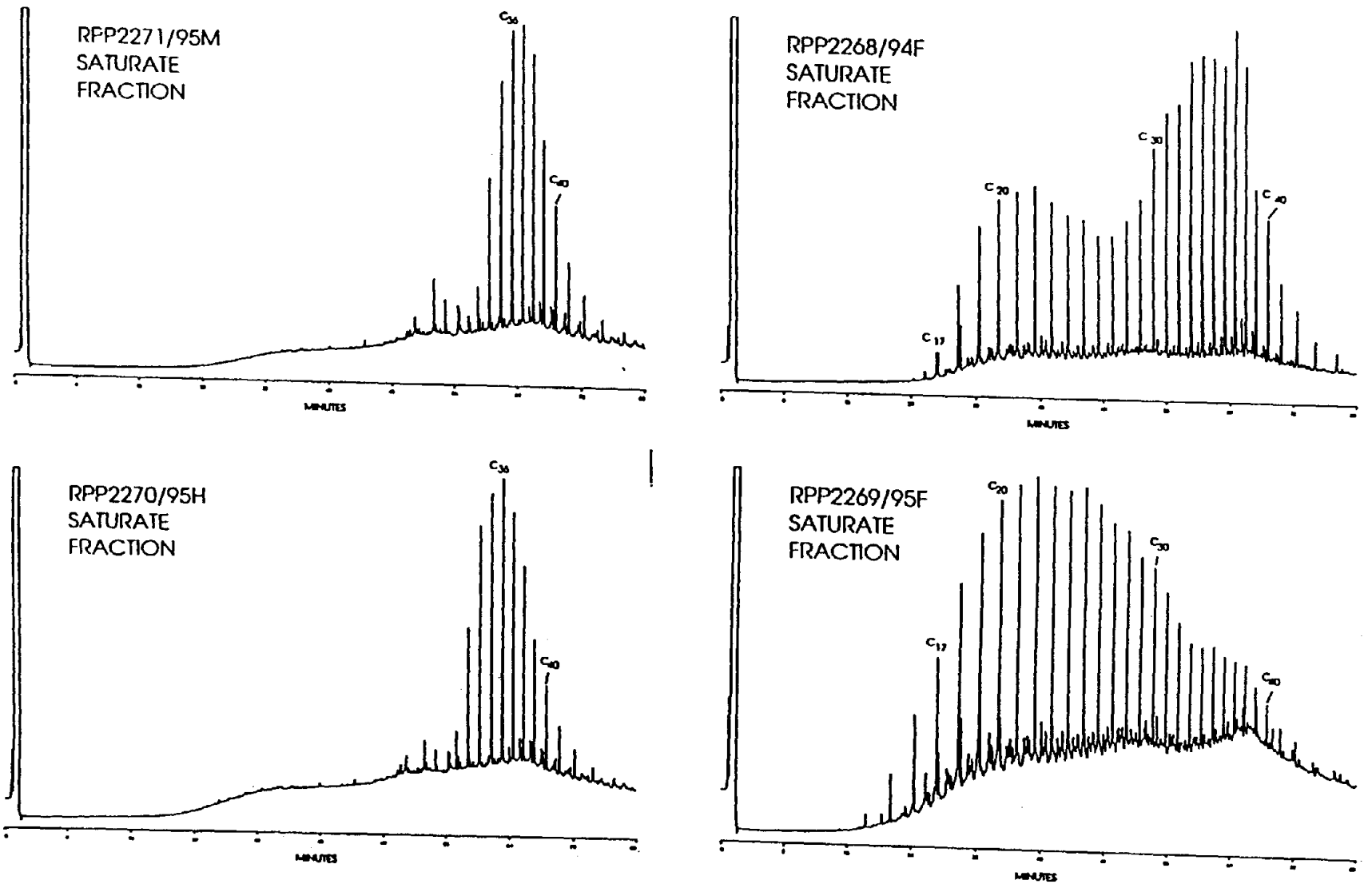

Fig. 7a-d. Gas chromatograms showing the hydrocarbon distributions of tar samples that have been weathered to varying degrees.

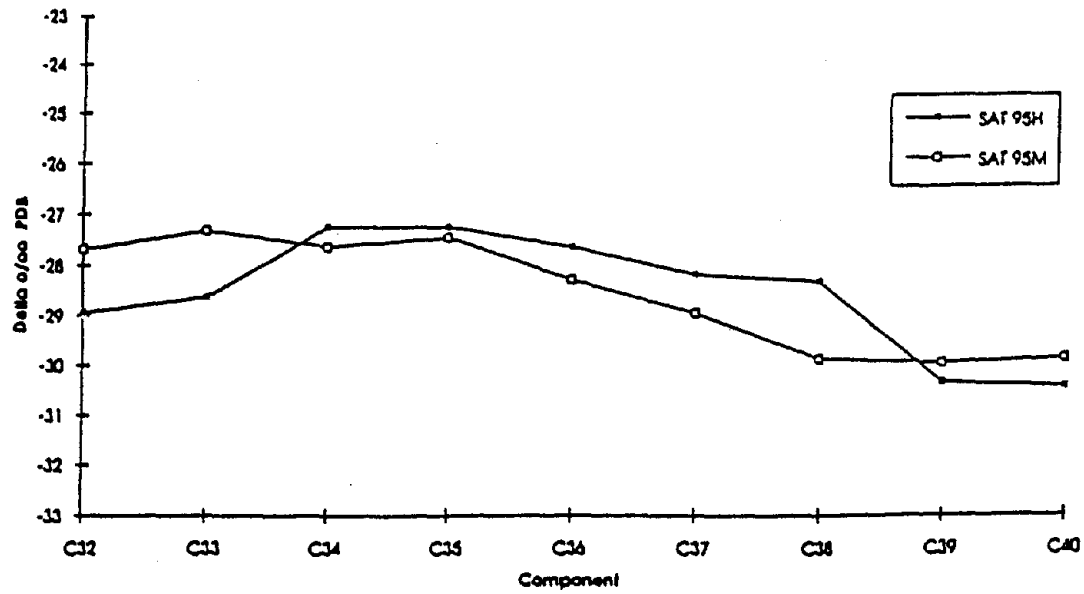

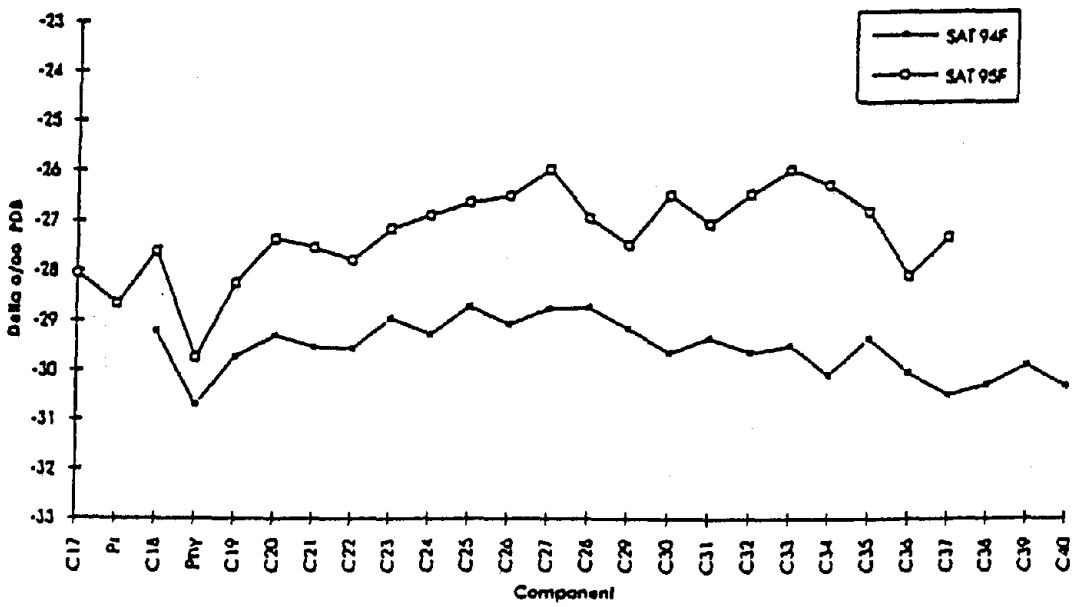

Fig. 8a and b. The carbon isotope distributions for the individual n-alkanes in the two sets of tar ball samples.

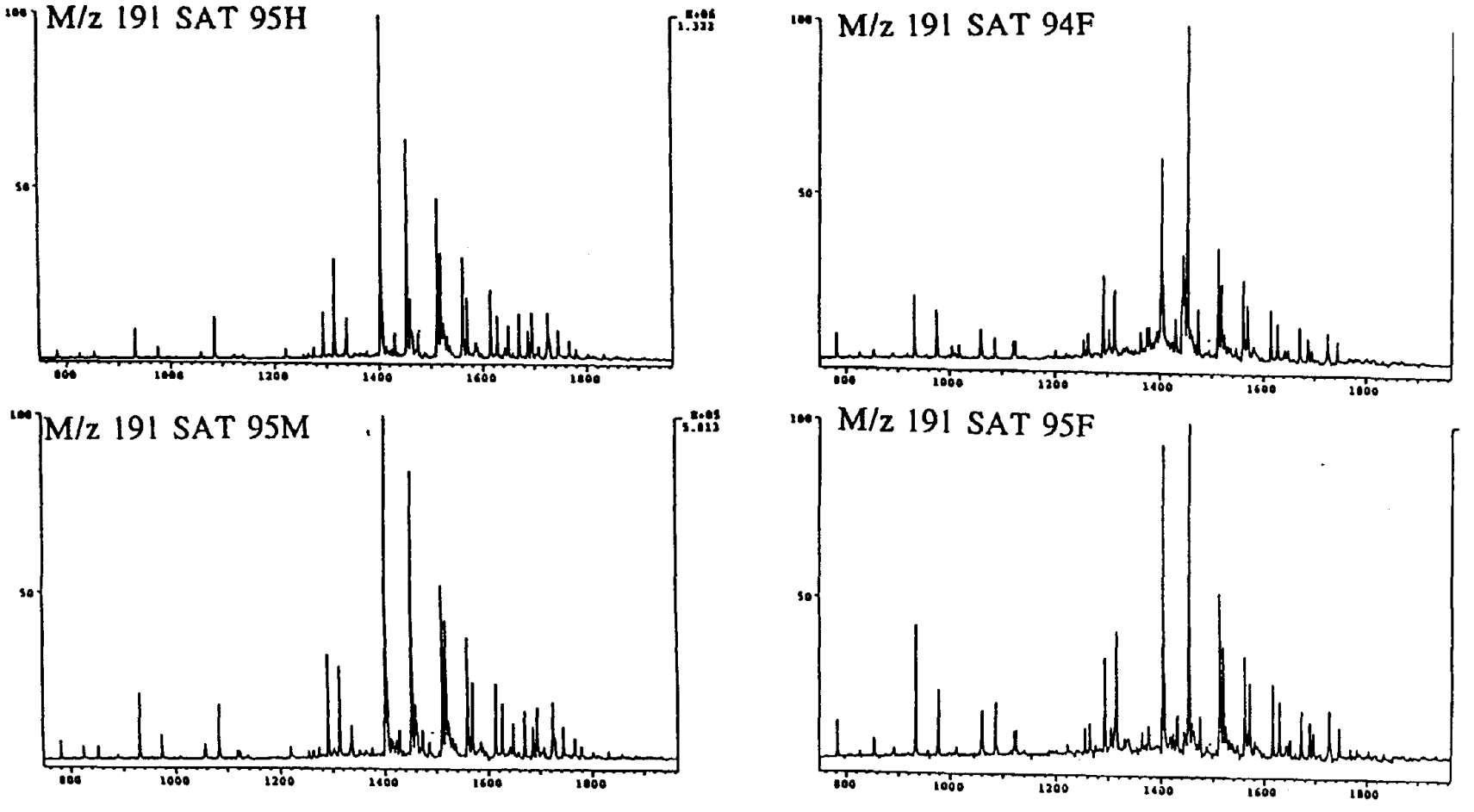

Fig. 9a-d. GCMS data showing the m/z 191 chromatograms for the two sets of tar ball samples shown in Fig. 7a-d.

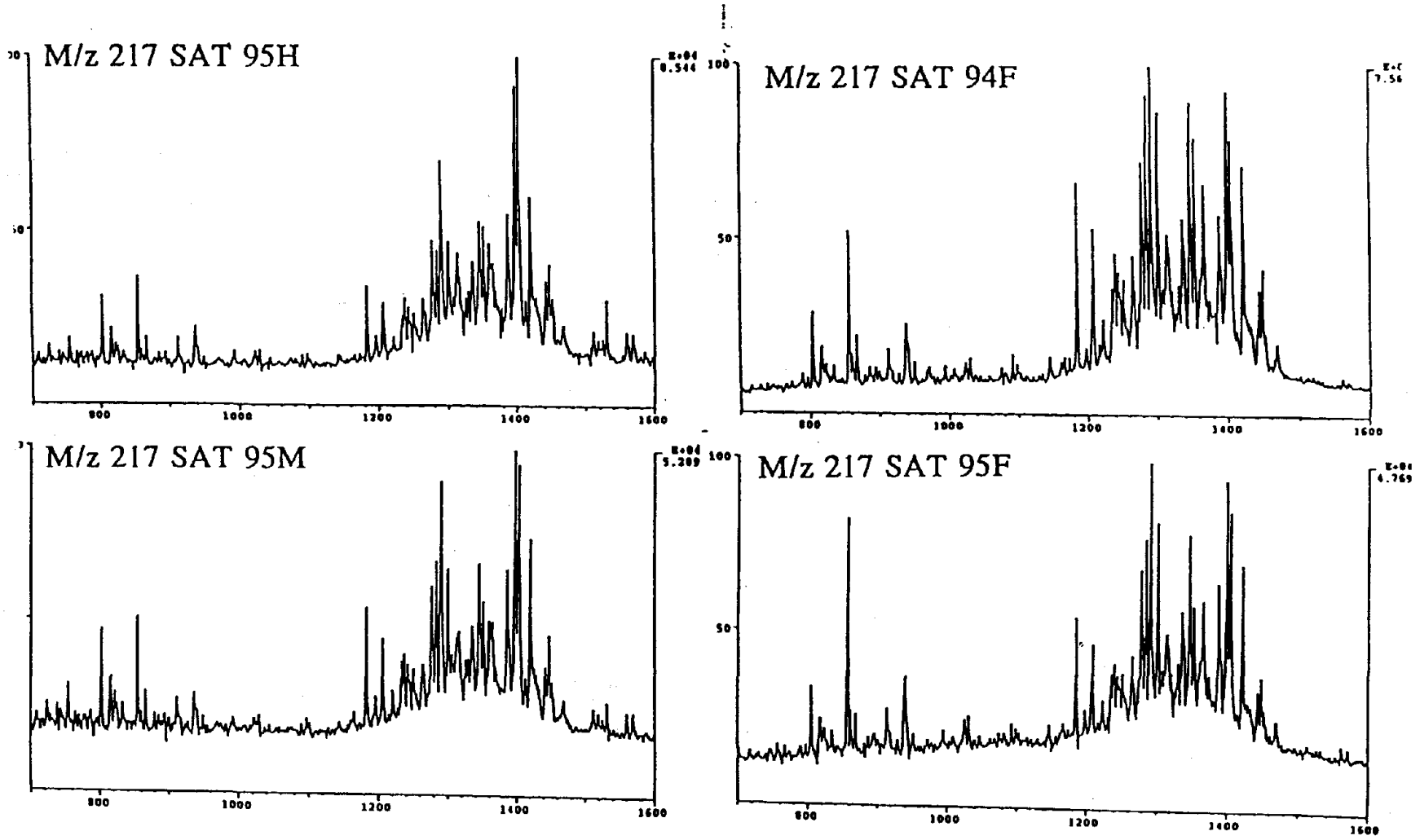

Fig. 10a-d. GCMS data showing the m/z 217 chromatograms for the two sets of tar ball samples shown in Fig. 7a-d.

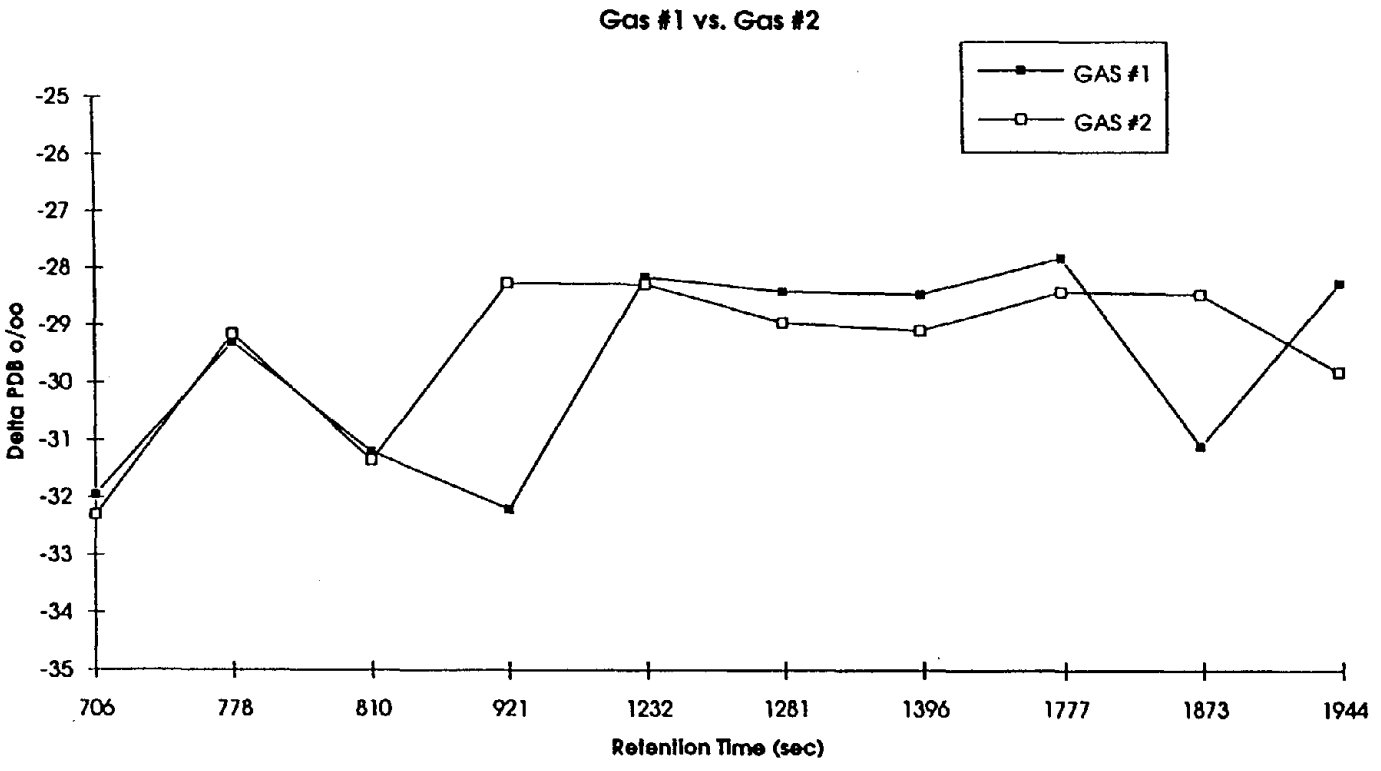

Fig. 11. Carbon isotope data for the major components of the two gasoline samples showing differences in the carbon isotope composition of certain components between the two samples. The two gasoline samples were collected from gas stations on opposite corners of an intersection and were from different suppliers.

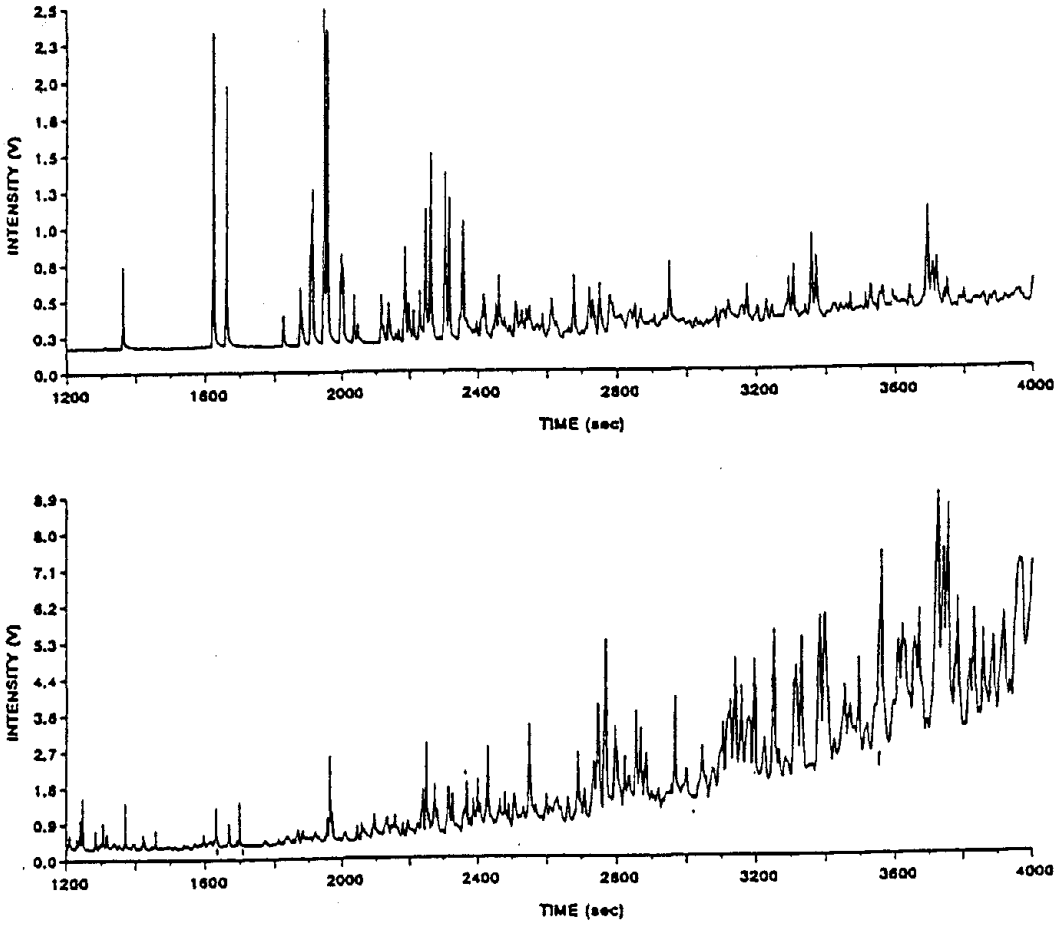

Fig. 12. GCIRMS chromatogram to illustrate the complexity of the aromatic fractions present in crude oils and the problems associated with the determination of the isotopic compositions for the individual components.

PREVENTING OIL SPILLS BY EVALUATING, MONITORING, AND MANAGING PORT AND WATERWAY RISK

John R. Harrald, The Louisiana State University National Ports and Waterways Institute

I. INTRODUCTION

The National Ports of Waterways Institute was funded by the Volpe National Transportation Systems Center to (1) develop risk assessment tools that can be used to evaluate risk on any port an waterway, and (2) to develop a prototype risk monitoring an management system using computer based simulation tools. This Volpe grant enabled the NPWI to extend and to generalize work funded by the State of Washington Office of Marine Safety and the State of Louisiana New Orleans Port Authority. The focus of the Washington State OMS project was to evaluate the risk of oil spills from vessels in Washington State waters. The objective of the New Orleans project was to assess the risk of vessel casualties in the Lower Mississippi River that could involve high capacity passenger vessels. The combined projects (Washington State, New Orleans, and Volpe) allowed the examination of three distinct waterways and multiple port areas: Puget Sound (Ports of Seattle, Tacoma, Port Angeles), Columbia River (Ports of Portland and Vancouver) and the lower Mississippi (Ports of New Orleans and Baton Rouge). The methodology developed in this study is being used as the basis for a major risk assessment project in Prince William Sound, Alaska.

This report has three sections. The first section describes the conceptual framework of the NWPI approach to risk assessment. The second provides a step by step description of the methodology. The third section, Appendix I, is a complete report of the methodologies application to the Port of New Orleans. The NWPI approach to risk assessment is based on three fundamental assumptions:

- Risk is a property of the local port and waterway system and is determined by local characteristics.
- National data bases do not contain the complete and accurate information required to support a port or waterway specific risk assessment.
- The experts that work in and have deep knowledge of a waterway system are a critical resource and their knowledge and judgement is the basis of a port or waterway specific risk assessment.

II. RISK AND "ACCEPTABLE RISK"

The U.S. Coast Guard Captain of the Port (COTP) is tasked by the Ports and Waterways Safety Act of 1972 and the USCG Marine Safety Manual to maintain an acceptable level of risk in the ports and waterways in his or her area of responsibility. An operational understanding of the concepts of risk and acceptable risk is required in order to achieve this goal.

Risk of an accident may be defined as the product of the probability of occurrence of the accident and the consequences or impact of that accident. An ACCIDENT is an event that has adverse consequences (e.g. injury, loss of life, economic loss, environmental damage). A primary objective of risk analysis is to determine the base level of risk in a complex system, the variation in risk level, and the causes of increased risk. Risk management implies that measures are taken to reduce either or both the impact or frequency of accidents, particularly those with potentially high impacts.

The determination of risk acceptability is essentially a sociological and political process that can be aided by analysis, but cannot be delegated to the analyst. Acceptability implies a subject (who is asked to accept the risk?) as well as an object (what risk should be accepted?). It is difficult, if not impossible, to determine an acceptable level of risk without considering the availability and cost of risk reduction measures. The identification and quantification of potential risk reduction measures is, therefore, an essential part of risk analysis. Acceptable risk in a system is defined by the degree to which system improvements can be identified, accepted, and implemented. The determination of acceptable risk is a product of risk analysis, not an a priori assumption.

III. RISK SCENARIOS AND SYSTEM STATES

Risk scenarios are unique sets of ordered events that result in an incident of interest and the consequences of that incident. An INCIDENT is an error or failure that creates an unsafe

condition that may result in and accident The sequences are composed of an initiating event (fault or failure) and all the subsequent equipment and/or human failures that are part of an accident chain. The sequence of events in the causal chain are typically represented by a fault tree; the events that follow the occurrance of an incident or an accident are represented by an event tree. A fault tree can be evaluated when the probability of occurrence of all the events in the causal chain can be estimated. In some closed systems, all possible fault trees can be identified and evaluated using historical data and expert judgment. Risk reduction measures are then evaluated by measuring their ability to interrupt or reduce the probabilities and/or consequences described in the causal chain.

It is difficult in a complex system such as a major port or waterway to identify even a small portion of the potential causal chains that could occur. Since the historical data required to identify and to evaluate fault tree elements is typically not available, evaluating fault trees for a waterway risk analysis can be cumbersome and difficult. This is particularly true when the port operations profile is changed by new usages of the waterway (e.g. high capacity passenger vessels, new toxic cargoes). However, historical data can be used to determine dominant accident types (groundings, allisions, collisions), and case records can be reviewed to determine dominant primary causal factors for a small set of incidents (e.g. power or steering failures, navigational error). This very rough analysis will provide the basis for a first cut risk analysis and will help determine the need for and the scope of a more detailed analysis. The dominant incident types will vary from port to port and depend upon the port configuration, vessel traffic, and weather conditions. Identifying risk reduction measures that will reduce the probability of the dominant causal factors and incident types is a typical product of this first cut risk assessment. A more complete and systematic risk assessment is possible even when a system is complex and critical data is missing. Three key steps are required:

- View risk as a state of the system, not as the study of isolated events.
- Use the knowledge of local experts to help define the system and to evaluate risk.
- Use available local data to determine the frequency of risk states and to calibrate and augment expert knowledge.

The unique risk states are defined by values of variables that make up the system environment. Each risk state may be viewed as an opportunity for an accident, but the probability that an accident will occur varies significantly among risk states. For example, an inexperienced pilot trying to land a single engine plane in a violent thunderstorm is in a "riskier" state than a commercial pilot flying at altitude in a four engine commercial jet. A system state for any local waterway system can be defined by the values of a set of variables. The unique risk states are defined by values of system variables such as wind, visibility, location, waterway configuration, and vessel traffic.

The probability of an accident in this view is composed of the probability of occurrence of a system state times the probability of an accident occurring in that system state. The risk assessment process requires the identification of system states, the estimation of the frequency of occurrence of system states, and the estimation of the probability of an accident occurring given the state of the system. The resulting view is that risk is a dynamic system property, as shown in figure 1.

Risk management initiatives dampen the amplitude of risk spikes and decrease their frequency by identifying the states in which they occur and by implementing appropriate risk reduction measures. Reducing the expected number of accidents means that the system states that produce the highest number of accidents must be identified. These states are not necessarily the system states with the greatest probability that an accident will occur. Figure 2 (a) orders risk states of a system by relative probability of accident occurrence, 2 (b) shows the frequency of the risk states and 2 (c) the product of probability of occurrence times frequency. This illustrates that the greatest number of accidents are produced by system states of moderate risk and moderate frequency. High risk states occur infrequently; the professional mariners in the system and waterways managers ensure that such states are avoided. An important implication of Figure 2 is that worst case scenarios, a valuable tool for response planning, should not be used as the basis for risk management. Focusing exclusively on extremely low frequency, high risk scenarios will not significantly reduce the expected number and consequences of accidents in a waterway.

A PROCESS CONTROL APPROACH TO RISK MANAGEMENT

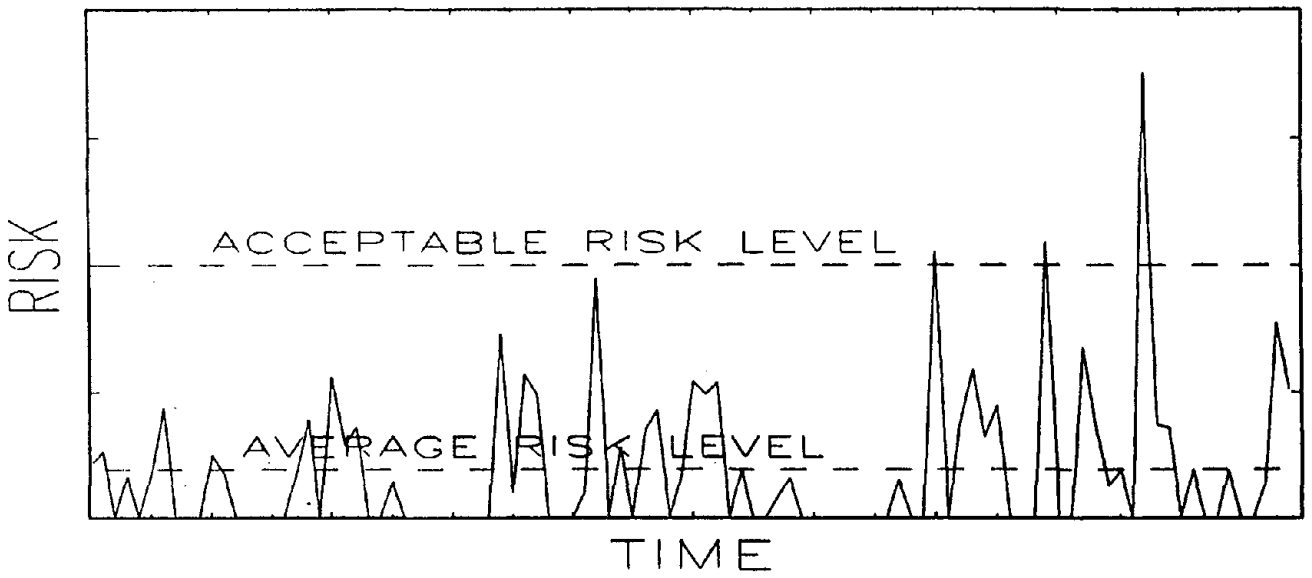

- QUANTIFY RISK
- INVESTIGATE CURRENT RISK PROFILE FOR PEAKS AND AVERAGE
- FORECAST RISK PROFILE FOR SUGGESTED POLICY CHANGES
- MONITOR RISK PROFILE OVER TIME

RELATIVE INCIDENT PROBABILITY ·

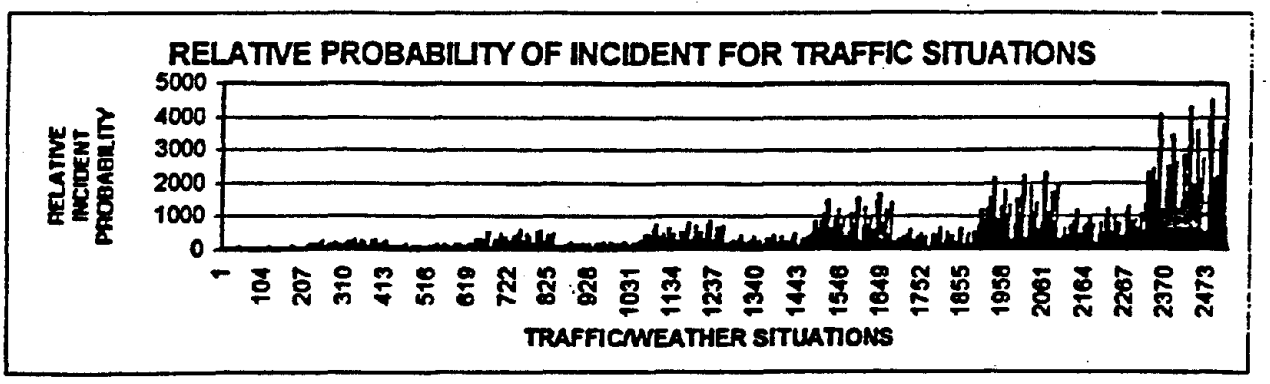

EXPECTED NUMBER OF OCCURRENCES (EXPOSURE)

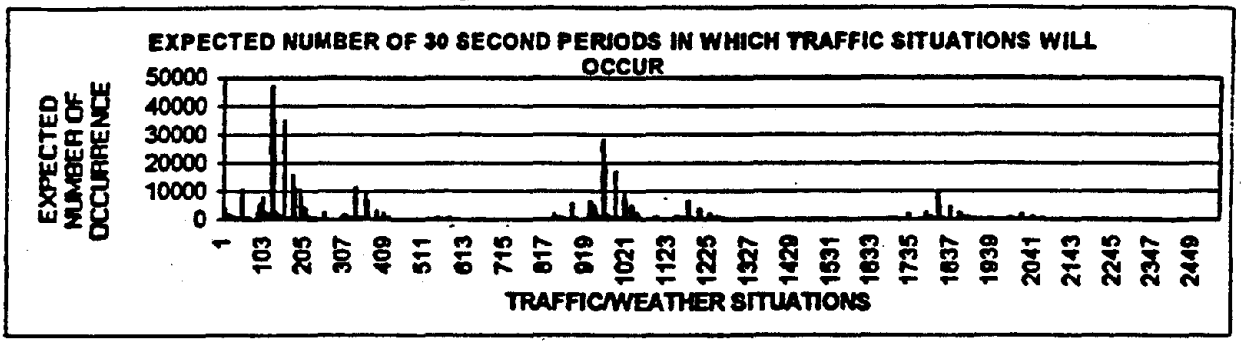

EXPECTED NUMBER OF INCIDENT IS THE PRODUCT

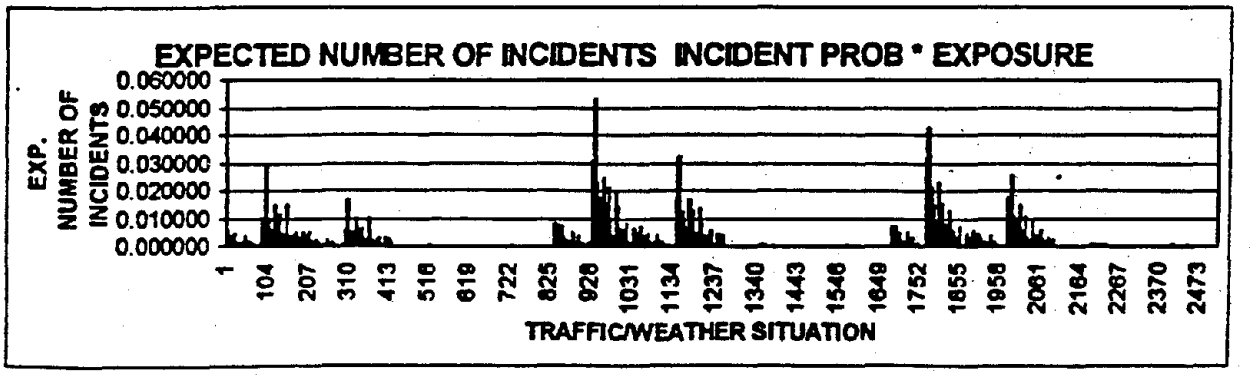

The probability of a vessel casualty is influenced by factors internal to the vessel (e.g. the experience and competence of the pilot, the mechanical condition of the vessel) and by factors in the external environment (e.g. weather, visibility, traffic, sea state, location). Bad things can happen to good vessels in adverse situations. Similarly, the impact of a vessel accident is also dependent upon both vessel and situational variables (and the value placed on the consequences of the accident, e.g. environmental damage, loss of life).. A collision between two vessels has a very different impact if (a) both vessels are coal barges, (2) one vessel is a high capacity passenger vessel and the other vessel is a barge carrying a toxic chemical. The outcome of a collision involving a passenger vessel may depend on the ability to render assistance after the event, which will depend on the availability of response and rescue resources and the environmental conditions. Similarly, the impact of a grounding involving a tanker is dependent upon the pollution response potential and the resources at risk.

IV. A SYSTEM BASED RISK ASSESSMENT METHODOLOGY

Based on the results of the State of Washington and Lower Mississippi risk projects, the National Ports and Waterways has developed a generalize port and waterway risk assessment methodology that incorporates a simplified scenario based analysis into a systems based approach. This methodology for the consistent and valid risk assessments of major ports and waterways is illustrated in fiigure 3. The description that follows is keyed to the steps shown in figure 3.

GATHERING INFORMATION: STEPS 1 THROUGH 3

The first and most critical steps required in the methodology are to define the local waterway system, identify local experts and stakeholders, and identify local and national data sources. The use of expert judgment requires a method of validating and scaling what the experts say. Risk analysts are comfortable in crunching numbers from easily obtainable data bases such as the Coast Guard marine safety data and the Corps of Engineers Waterborne Commerce. They are often less

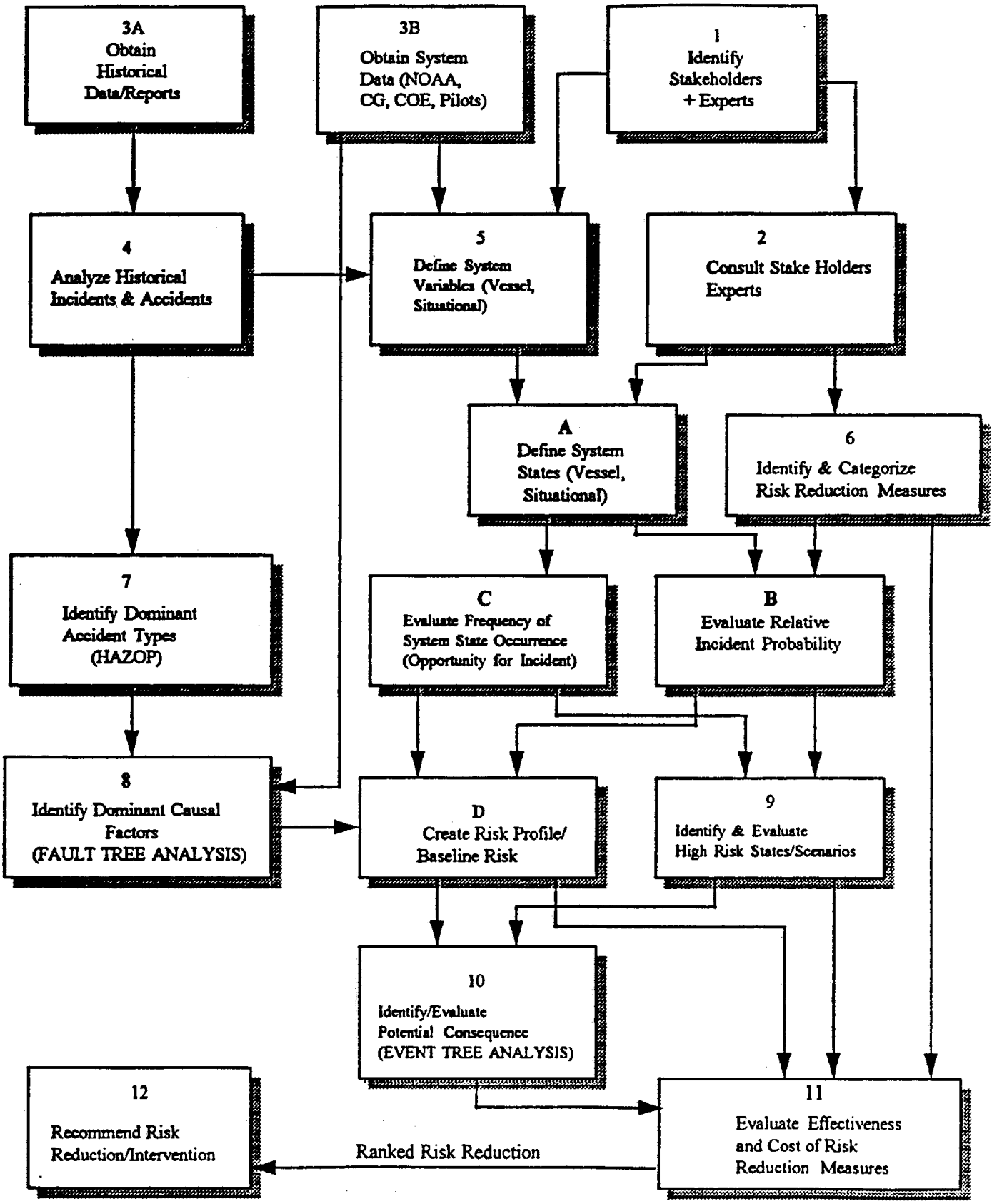

Flow Chart: Formal Risk Assessment

comfortable about seeking local data sources and may not wish to interview local experts. They must do both, otherwise their product will not be acceptable to many stakeholders.

Step 1: Identify stakeholders and experts

Stakeholder means, literally, a person or an organization that has a stake in the outcome. When a new or expanded use of the waterway such as the introduction of a chemical waterfront facility or high capacity passenger vessels operations is proposed, stakeholders will include the users, state and federal regulators, and other interest groups. Table 1 provides a listing of typical stakeholders that should be involved in any waterway risk project. Since the ultimate objective of a risk assessment is the acceptance of rules, procedures and investments shown to be effective in managing risk, the early involvement of stakeholders is essential. *Experts* are individuals such as state pilots, mariners, port authorities, tow boat operators, and Coast Guard marine safety and aids to navigation personnel who have a deep knowledge of the local waterway system. Most experts are also stakeholders (e.g. pilots), but some are not (e.g. retired mariners, local researchers).

Step 2: Consult with stakeholders and experts

Discussions with the stakeholders and experts should provide the answers to three important questions:

1. How will the proposed risk analysis and proposed new uses of the port or waterway affect each stakeholder and what is their perception of the effect of the change on the current level of risk?
2. What are the most significant hazards (e.g collisions at traffic convergence points, groundings on exposed reefs) and situational risk factors (conditions that significantly increase the risk of the system such as low visibility, high river stage) in the waterway?

3. What risk reduction measures are in place that are unique to the port or waterway (e.g. COTP Orders, Notice to Mariners, escort procedures, industry practices) and what measures have been proposed?

TABLE 1

PORT AND WATERWAY STAKEHOLDERS

	STAKEHOLDER /EXPERT GROUP
1.	STATE PILOTS ASSOCIATION
2.	FEDERAL PILOTS ASSOCIATION
3.	USCG PORT SAFETY PERSONNEL
4.	USCG VESSEL TRAFFIC SYSTEM WATCHSTANDERS
5	USCG AIDS TO NAVIGATION TEAMS
6.	SHIPPING AGENTS
7.	TOW BOAT OPERATORS
8.	EXCURSION BOAT OPERATORS
9.	FERRY BOAT OPERATORS
10.	MARINE EXCHANGE
11.	PORT AUTHORITY
12.	MAJOR DEEP DRAFT VESSEL OPERATORS AND AGENTS
13.	MAJOR TERMINAL OPERATORS
14.	COMMERCIAL FISHING ASSOCIATIONS
15.	RECREATIONAL BOATING ASSOCIATIONS

Each stakeholder has an interest in any changes that may result from the risk assessment. Identifying these interests is essential for ensuring stakeholder acceptance of the risk assessment process and the results. Eliciting the stakeholder's perception of the current risk level and of changes in risk due to the proposed new uses is a critical activity. Many non experts have difficulty in estimating the risk of low probability, high consequence events. Risk communication

and risk education are an important activities in any risk analysis and their incororation early in the project, facilitates the acceptance of the results by stakeholders. Stakeholders are also the primary source for potential risk reduction measures (Step 6 below). Experts are also sources of potential risk reduction measures. More importantly, experts can provide invaluable local data on incidents, accidents, and near misses (step 3) and can help define what attributes of the port, waterway, and calling fleet contribute the most to the current risk level (step 5). Experts are capable of identifying the high risk system states (step 10). The dialogue between the analyst and the stakeholders and experts should continue throughout the risk analysis effort.

Step 3: Obtain historical data/reports and system data

Detailed data and investigative reports should be gathered for all significant accidents, incidents, and near misses that have happened in the area of interest. Data is also required to determine the types of vessels and situations that have caused problems, and the profile of the vessel traffic that uses the waterway. Table 2 provides a listing of national and potential local data sources. Coast Guard marine safety data systems are a good source of accident and incident data and the Army Corps of Engineers Waterborne Commerce statistics furnish traffic and cargo data. However, local data source will probably provide the most useful information. The CG WAMS reports contain significant information on all reported incidents keyed to waterway location. WAMS also contains a description of waterways hazards that will help define system variables (Step 5). Other valuable sources of local information a Vessel Traffic System (traffic records, near miss and incident descriptions), state pilots (traffic and near miss information), and port authorities and marine exchanges (traffic data). Anecdotal accounts from experts should be used to augment and interpret the available local data.

TABLE 2

PORT AND WATERWAY INFORMATION SOURCES

	SOURCE	DESCRIPTION	FORMAT
1	USCG MARINE SAFETY DATA	ACCIDENT DATA VIOLATION DATA VESSEL DESC. DATA	ELECTRONIC
2.	US ARMY CORPS OF ENG.	WATERBORNE COMM. RIVER STAGE	ELECTRONIC/ PAPER
3.	N.O.A.A.	WEATHER DATA CURRENT DATA	ELECTRONIC
4.	USCG MSO	INCIDENT DATA VIOLATION DATA	ELECTRONIC/ PAPER
5.	USCG VTS	INCIDENT DATA/ "NEAR MISS" DATA TRAFFIC DATA	ELECTRONIC/ PAPER
6.	PORT AUTHORITY	TRANSIT DATA ALLISION DATA	ELECTRONIC/ PAPER
7.	MARINE EXCHANGE	VESSEL DESC DATA TRANSIT DATA CARGO DATA	PAPER ELECTRONIC
8.	PILOT ASSOCIATION	VESSEL DATA TRANSIT DATA	ELECTRONIC PAPER
9.	USCG AIDS TO NAVIGATION	WAMS REPORTS (INCIDENT/HAZARDS)	PAPER

Note that data sources 4 through 9 are local data sources.

FRAMING THE RISK ASSESSMENT: STEPS 4, 5, 6

Step 4: Analyze historical incidents and accidents

A full causal analysis should be conducted for all relevant historical accidents in the area of interest (Step 3). Dominant accident types, incident types and primary causes should be identified.

Step 5: Define System Variables and States

Tables 3 and 4 in give suggested vessel description variables and waterway system variables. Each table provide suggested categories for these variables. Note that the categories are arranged in order of increasing risk. The number of allowable system states in your model is determined by the number of system variables and the number of categories defined for each variable. A system oriented risk assessment will calculate the following system parameters based on these data:

1. A vessel type profile of the deep draft calling fleet, shallow draft transit fleet and shallow draft local fleet using US Army COE statistics and local data.
2. A vessel risk profile of the calling fleet based on risk models and the identification of high risk vessels.
3. A risk state profile of the water and the identification of the amount of time high risk states occur.

TABLE 3

SUGGESTED VESSEL DESCRIPTION PARAMETERS

	VESSEL DESCRIPTION VARIABLES	TYPICAL VALUES
1.	VESSEL TYPE	Deep Draft Calling Fleet Passenger Vessels Tank Vessels Container Vessels Bulk Cargo Vessels Special Purpose Vessels Other Shallow Draft Transit Fleet Tugs with tows Line Haul tows Fishing Vessels River/inland passenger vessels Other Shallow Draft Local Fleet Ferries Excursion boats Gambling boats Other
2.	VESSEL AGE	0-15 years 15-25 >25
3.	CLASSIFICATION SOCIETY	IACS Member IACS Associate Member Not classed by recognized classification society
4.	PILOT	Pilot on board More than one pilot on board No pilot on board
5.	FLAG	US/Canadian/Traditional Maritime Flag of Convenience Targeted Flag
6.	MANAGEMENT CHANGES	No Changes in owner, flag, or class society within 3 years Change in either owner, flag or class society within 3 years Targeted Flag
7.	VESSEL VIOLATION/INCIDENT HISTORY	No violations or casualties within 3 years Minor violation or incidents within 3 years Repeated minor or recent major incident or v

TABLE 4
SUGGESTED SITUATIONAL RISK PREDICTORS

	SYSTEM VARIABLE	ALLOWABLE VALUES
1.	WATERWAY CONFIGURATION	Open (fairway with good water on both sides) Restricted (shallow water or hazard near the marked channel) Converging (multiple channels that meet or cross)
2.	VISIBILITY	restricted adequate good
3.	WIND	light bothersome difficult
4	CURRENT	none low high
5.	TRAFFIC SITUATION	single vessel simple situation (meeting, overtaking) complex situation (multiple vessels crossing/passing)
6	TRAFFIC DENSITY	no vessel within 0.5 miles one vessel within 0.5 miles multiple vessels with 0.5 miles

Step 6: Identify and Categorize Risk Reduction Measures

A risk assessment provides a quantitative measure of the current or baseline risk in a system; identifies potential failures, and estimates the probability of occurrence and the potential consequences of these failures. The reason for performing a risk assessment is, however, to determine how to make the system safer. Determining what can and should be done are the critical aspects of risk management. Risk reduction measures achieve one or more of the following objectives:

- prevent errors or failures that can cause an accident (e.g. inspections, training programs, quality programs)
- avoid high risk system states where errors or failures have a high probability of resulting in an accident (e.g. port closures, traffic restrictions)
- prevent an accident given that failures have occurred (e.g vessel traffic control, escort vessels)
- lessen the effects of an accident once it occur (e.g. hydrostatic loading)
- minimize the consequences of an accident (e.g. firefighting, pollution response, search and rescue)

A large number of suggested improvements to most local systems have already been identified by prior studies, state and federal agency proposals, and proposals by maritime associations. Consultations with experts and stakeholders will identify others. The purpose of this step is to provide some structure to this listing of concepts that will help you link your risk analysis not only to potential problems, but to potential solutions. A two dimensional categorization of risk reduction measures is useful. The first dimension is determined by where the proposed action intervenes in the causal chain. The second dimension describes the type of intervention. Suggested intervention types are: Waterway Management and Traffic Control, Vessel Personnel and Pilotage, Vessel Equipment and Design, Inspection and Enforcement, and Emergency Equipment and Procedures.

THE EVALUATION OF RISK: STEPS 5A, B, C, D, 7,8, 9 AND 10

The vessel traffic data and environmental data obtained in step 3 are the basis for a quantitative risk assessment, the types of risk reduction measures identified in step 6 provide guidance in the development of system models. The definition of vessel and situational variables in step 5 allows the construction of system based risk models and a system based risk simulation:

Step 5A:	Define possible system states in terms of vessel and situation attributes
Step 5B:	Estimate the relative probability of an accident for each system state based on historical data analysis or expert judgment.
Step 5C:	Evaluate the frequency of occurrence of system states. This evaluation of risk exposure will require a statistical analysis of historical data or a simulation.
Step 5D:	Evaluate the baseline risk of the system and create a risk profile. This baseline risk will be used to evaluate all potential changes and for comparison to risk levels in other ports and in other activities.

Step 7: Identify Dominant Accident Types

Examination of the historical record and discussions with experts will reveal a relatively small number of dominant accident types. These types will vary among ports. River ports may find that collisions and allisions (with docks, moored vessels, and bridges) are the most frequent incident types. Ports in bays or sounds will probably see fewer allisions, but many more groundings. Congested ports with complex traffic patterns and river ports will see more collisions.

Step 8: Identify Dominant Causal Factors

This is the most difficult task in a risk assessment and in a full risk assessment will require either a fault tree analysis, a probabalistic risk analysis, or a statistical analysis of available data..

Step 9: Identify *and evaluate* high risk states and scenarios.

This activity requires that the frequency of high risk states and scenarios is quantitatively evaluated. This step requires the integration of all the information obtained in steps 5, 5A, 5B, 5C, 5D, 7 and 8. High risk states are those involving a high risk vessel and/or a high risk situation as identified in worksheets 2 and 3. High risk states indicate conditions in which a small error or failure is likely to develop into a significant event. In a detailed risk assessment detailed traffic, weather, wind, and current data will be required to determine how often these risk states actually occur using sophisticated simulation or statistical models. High risk scenarios are the causal chains identified is steps 7 and 8. High risk scenarios that occur during high risk system states are the primary concern.

Step 10: Identify and evaluate potential consequences.

Risk is a product of probability of occurrence times the impact or consequence of the event. A detailed risk analysis should contain an event tree analysis or some other analytic method of determining the potential consequences of accidents. The quantitative evaluation of consequences is a difficult task. The value of a human life is not easily determined nor are the values to be attributed to natural resources damaged by pollution. A preliminary risk assessment, however, should be restricted to a description of potential consequences (e.g. significant loss of life, major oil spill, toxic release) for a reasonably selected set of risk scenario/risk state combinations. It is important to include the risk state in this exercise, since the state of the system (location, weather, etc) will determine both the availability and the effectiveness of response resources.

RISK REDUCTION EVALUATION–THE FIRST STEP IN RISK MANAGEMENT: STEPS 11 AND 12

Step 11: Evaluate Effectiveness of Risk Reduction Measures

The reason for the risk assessment is to provide a basis for determining how to make the system safer. Deciding what can and should be done are the critical aspects of risk management. In step 6 you identified and categorized proposed risk reduction measures. In steps 5A, B, C, and D a systems simulation was created and calibrated using data from steps 7, 8, and 9. This simulation is used to measure the potential impact of the proposed risk reduction measures. This evaluation should answer the following questions:

1. Will the proposed measure interrupt the causal chain of the risk scenario or prevent a risk state from occurring? If it does not or if it increases the probability that a risk scenario or risk state will occur, no further evaluation is required.
2. Where in the causal chain does the measure intervene? Does it prevent errors or failures, or prevent accidents even if these errors or failure occur? Does it minimize consequences once an accident happens?
3. What is the relative cost of the intervention measure?
4. How technically, politically, and organizationally feasible is it to implement?

Step 12: RECOMMEND RISK REDUCTION MEASURES

Recommended risk reduction measures must make the system safer. You may find that some proposed measures have no effect or even make the system worse. The set of risk reduction measures that should be recommended are those that are cost effective as shown in figure 4. The measures in the upper left quadrant (low cost, high risk reductions) are clearly your first priority,

assuming that they have passed the feasibility test implied by question 4 above. The measures in the lower right quadrant (high cost, low risk reduction) should not be considered further. Measures in the other two quadrants should be examined if the low cost, high risk reduction measures do not achieve the desired level of risk. You may wish to make those measures that intervene early in the causal chain your top priorities since they will undoubtedly be the cheapest and are often the most effective measures. This is a good time, however, to review stakeholder expectations since those measures that intervene late in the chain (double hulls, escort tugs, external controls, response equipment) are often preferred. They are highly visible and easily verified when compared to the more global measures that attempt to improve organizational and human performance.

CONCLUSIONS

The evaluation of port and waterway risk can be effectively based on local data and the knowledge of local experts. A standard methodology has been developed and applied to several ports by researchers at the National Ports and Waterways Institute. In order to successfully execute this methodology, however, difficult analytical problems must be solved. The risk analysts must develop (1) a valid method for the elicitation of expert judgement, (2) risk models that consider and eliminate expert bias, (2) an method of calibrating the relative risk levels obtained through expert judgment in order to produce absolute values for risk levels.

Appendix I is a case study showing how these problems were solved by NPWI analysts in their assessment of risk in the Lower Mississippi River.

PHASE II: COST VERSUS EFFECTIVENESS

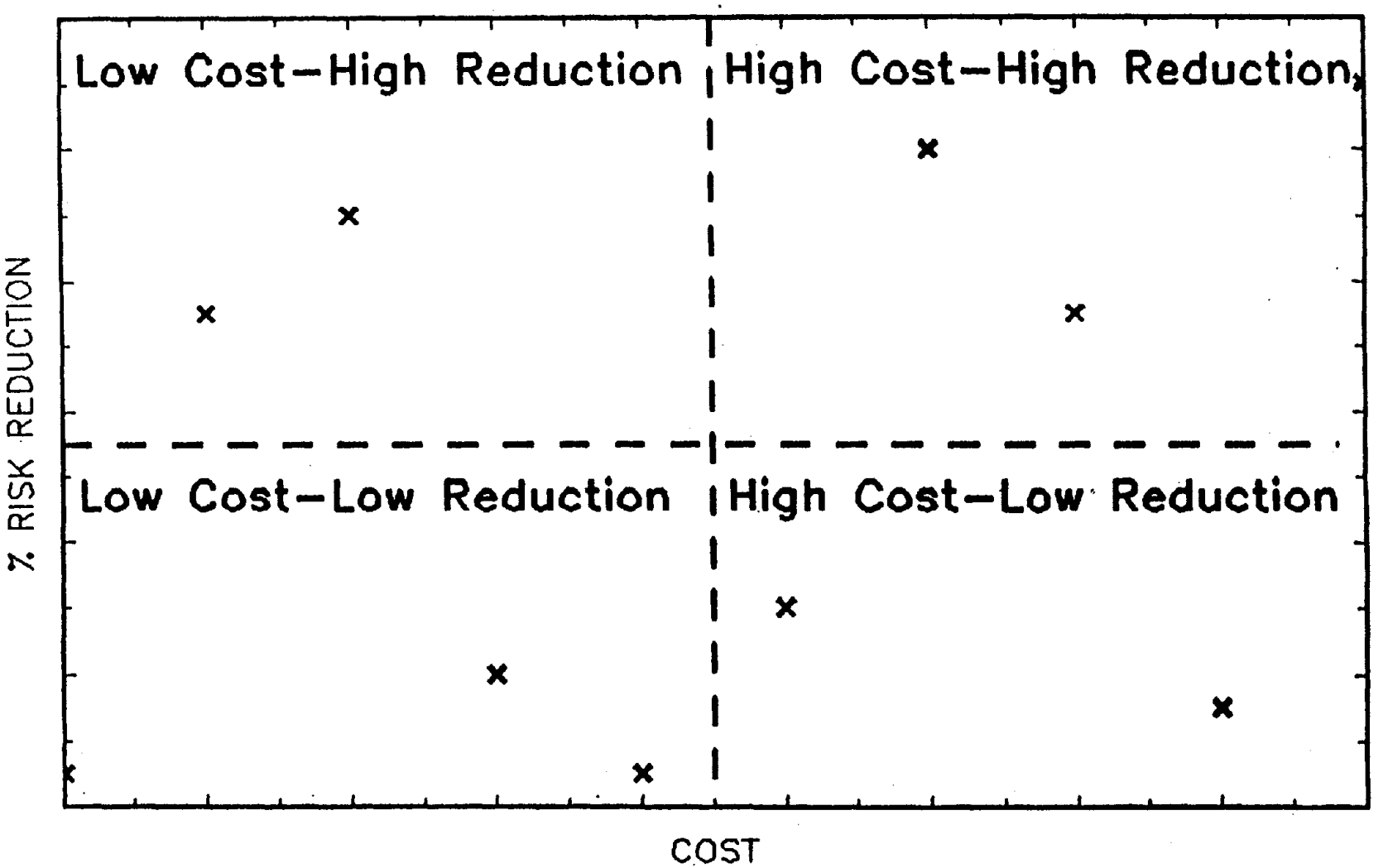

APPENDIX I

EVALUATING AND MONITORING WATERWAY RISK IN THE PORT OF NEW ORLEANS: PHASE II

1. INTRODUCTION

The National Ports and Waterways Institute has completed a two phase analysis of the waterway risk in the Mississippi River in the port of New Orleans. The introduction of river boat gaming vessels with a capacity of thousands of passengers into this busy port provided the motivation for this two phase effort. The Port of New Orleans, the U.S. Coast Guard, and the State of Louisiana are concerned that this new economic activity is managed with an acceptable level of risk. Risk consists of two components: the probability of occurrence of an incident and the potential impact of the incident. Risk management implies the ability to measure and to evaluate both of these elements as well as the ability to quantify the benefits of risk reduction activities.

The Phase I report, delivered in July 1994, described a framework for a system oriented risk analysis of the port. This framework, based on the judgment of experts and a preliminary analysis of available data, allowed the calculation of relative probabilities of vessel collisions associated with the traffic and environmental conditions experienced in the Port of New Orleans. Three risk models were developed for the Port of New Orleans in the Phase I analysis:

The **situational model** is an innovative application of regression analysis and describes how the interaction between the attributes of the waterway, visibility, and weather affect the probability of a vessel collision. The model ranks the relative probability of collision given various situations and may be used to develop vessel traffic management procedures and risk interventions.

The **vessel casualty model** is a hierarchical multi-attribute model that describes the attributes of a vessel that effect its propensity to be involved in a casualty. The results of this model can be used to evaluate the relative risk of proposed new vessels in the port and could be used, in conjunction with data on the types of vessels that transit the Lower Mississippi, to develop a vessel related risk profile of the waterway.

The **impact model** is a hierarchical multi-attribute model that describes the factors that influence the human safety and environmental impact of a vessel casualty. This model may be used to assess the relative impact of various casualty scenarios.

The focus of this Phase II report is on the use of the situational model.

The Phase I study showed that the risk of loss of life and injury to passengers is primarily a function of the external situational risk variables captured in the situational model. These variables are VISIBILITY, WIND, RIVER LOCATION, TRAFFIC SITUATION, and RIVER STAGE. Over 2,500 situational states of the river were defined by the value of these variables. The relative collision probabilities given these states were calculated by the Phase I situational model and ranged from a base level, assigned a value of 1.0, to a maximum value of 4,492. This analysis identified which situations created a higher probability of a vessel collision in the Port of New Orleans. Situations which were more than a thousand times more probable to result in a collision than a normal or base situation were identified as were high impact vessel incidents (allisions or collisions). Phase I did not, however, answer several questions critical to waterways managers:

- How often do high risk situations occur?
- How can high risk situations be prevented from occurring?
- What is the risk level of the port in absolute terms?
- How can the risk reduction resulting from proposed system improvements be measured?

The objective of the Phase II study was to develop methods which would more precisely quantify the risk. This would include determination of absolute probability of vessel incidents given the risk states and the evaluation of the probability of occurrence of each risk state. The effectiveness of mitigation measures identified in Phase I could then be evaluated. The goal was to use these procedures to develop a computer based risk monitoring and mitigation decision aid for the Port of New Orleans.

In Phase II, a simulation of the port was developed and used in conjunction with the situational model of Phase I to establish a risk profile of the Port of New Orleans. This risk profile enables the determination of the frequency of occurrence of high risk states and provides the ability to transform the relative measures developed in Phase I to an absolute scale. A methodology for determining the risk reduction impacts of system interventions was also developed using both simulation and the techniques of Quality Functional Deployment and is described in Section II.

Many risk mitigation measures for the Lower Mississippi River have been proposed by various sources. No prior attempt had been made, however, to evaluate the effectiveness of these measures. The techniques described in Section II provide a unique capability for evaluating the proposed interventions. Candidate risk reduction measures were identified using the following six sources:

1. The Governor's task force on Maritime Industry
2. The Maritime Safety Association (MNSA)
3. The Port of New Orleans Safety Workshop sponsored by the Port of New Orleans and the US Coast Guard
4. The US Coast Guards Operation Safe River Operation Plan
5. Testimony by RADM James Card, Commander Eighth Coast Guard District at field hearings sponsored by Congressman Tauzin.
6. The National Ports and Waterways Institute's risk management recommendations developed for the State of Washington, Office of Marine Safety.

The result was a listing of fifty risk interventions that were grouped into four general areas:

1. Traffic and waterway management improvements (10 proposals)
2. Development and enforcement of vessel material and operational standards (9 proposals)
3. Development and enforcement of personnel standards (4 proposals)
4. Improving communications and information management (7 proposals)

5. Restrictions on gaming boat operation, management, and crewing (9 proposals)
6. Enhanced emergency response (11 proposals)

Using these proposals, a questionnaire was developed with the objective of selecting the most promising proposals for detailed evaluation. This survey was administered to maritime experts from the USCG, the excursion industry, river pilots, and the towboat industry. Twenty interventions were selected for further investigation. These interventions, the method used to evaluate them, and the results of the evaluation are described in Section II.

Four conclusions and six recommendations contained in the Phase I report were examined in detail using the simulation during the Phase II study. The Phase I conclusions were:

1. The addition of gaming boats to the busy Mississippi River increases both the probability of a maritime casualty and the potential impact of such a casualty.
2. Restricting the conditions under which gaming boats may cruise the river or requiring that gaming boats be permanently moored will reduce, but not eliminate, the risk.
3. The impact of a casualty involving a gaming vessel would be significantly greater than that of a casualty involving other types of vessels.
4. The risk of a casualty resulting in loss of life and injury to passengers on board the gaming vessels is primarily a function of the operating environment (situational risk) not the individual vessel (vessel risk).

The Phase I recommendations that were re-examined were:

1. Gaming vessels should be moored in the area of the lowest historical allision rate (Poydras street to First Street)
2. Gaming vessels should remain moored during periods of low visibility, high winds, or high river stage.
3. The potential for protecting the moored gaming vessels by allowing their berths to silt in should be investigated
4. Contingency and disaster management plans should be developed and routine preparedness drills should be held.
5. The issue of providing emergency egress from passenger vessels, to other vessels, to a dock, or to a river bank should be investigated.

2. ANALYSIS

In Phase I, a situational risk model was developed for describing the probability of occurrence of a vessel collision as a function of external factors. The model was formulated as a result of several rounds of discussion with maritime experts. It was concluded that the probability of any vessel incident (allision or collision) was a function of mainly five variables: VISIBILITY, WIND, RIVER LOCATION, RIVER STAGE and TRAFFIC SITUATION. The significant ranges for the first four variables were obtained from experts and are given in Table 1. The variable TRAFFIC SITUATIONS was described by 28 dual vessel situations plus the possible presence of a crossing vessel, where the vessels are operating within 1/2 miles of one another.

Vessels were grouped into classes consisting of Shallow Draft Passenger Vessel (SDPAS), Tug with Tows (TWTOW) or tugs with 6 or less barges, Deep Draft Vessels (DDRFT), Line Haul Tows (LINHL) or tugs with more than 6 barges, In addition, vessel directions of traveling up river (UP) or down river (DOWN) were included in the TRAFFIC SITUATIONS variable.

TABLE 1
SITUATIONAL RISK VARIABLES AND THEIR BREAK POINT VALUES OBTAINED FROM EXPERT ELICITATIONS.

VARIABLE NAME	SIGNIFICANT RANGES		
VISIBILITY	>.5 mile	<.5mile	
WIND	< 25 mph	> 25 mph	
RIVER STAGE	< 8 ft.	8 - 14 ft.	> 14 ft.
RIVER POSITION	80 - 92	92 - 97	97 - 106

. A collection of these individual variable values was termed an

***Opportunity for Incident* (OFI) – a collection of river stage, visibility, wind conditions, and vessel traffic situations that can lead to the occurrence of a reportable incident.**

A log-linear regression model was assumed for relating accident probabilities to the described external variables. This model is similar to that postulated by Roeleven (1992) in the study of the risk of inland waterway transportation in The Netherlands. The parameters of the model were estimated using expert responses on questionnaires. On the questionnaires, experts were required to compare the relative probability of a collision for different pairs of OFI's. Details of the Phase I model and questionnaire are provided in Appendix A. The results of the regression are given in the Phase I report.

The estimated regression model allowed for the calculation of a

***Relative Incident Probability* (RIP) – the relative probability of a reportable incident in the next thirty seconds given that a particular OFI occurs.**

As the RIP are relative probabilities, all RIPs were scaled so that the smallest RIP would equal 1. Using the collection of external variable values, all OFIs were defined and their associated RIPs were obtained using the estimated Phase I model. The Phase I model allowed for the calculation of the RIP for every possible OFI, not just the OFI's for which the experts provided comparative information. Using the estimated Phase I model, the OFI's could be ranked with respect to their "riskiness". However, because the experts were asked to provide only comparative information rather than actual probabilities of collision, one of the model parameters could not be directly

estimated and thus only relative (or comparative) probabilities were obtainable. The actual probability of vessel incident both in general and under each OFI, could not be directly calculated.

In Phase II, the model was extended to include single vessel accidents (allisions) and the calibration of the expert judgment. In addition, the last model parameter was estimated, allowing for absolute probabilities to be calculated. Details of the Phase II extensions to the model are provided in Appendix B.

Given a mechanism for obtaining the relative probabilities of vessel incidents given various external variable values or OFI's, the estimation of the probability of vessel incident reduces to the estimation of the frequency of individual OFI's. At this stage, a considerable amount of data was gathered to determine the frequency of the states of the individual variables VISIBILITY, WIND, and RIVER STAGE. The frequency of TRAFFIC SITUATION and RIVER LOCATION were more difficult to obtain. These would require a tally of each type of traffic situation on the river and no existing data could provide such an estimate. As a result, it was necessary to develop a simulation model of the port area based on the visibility, wind, river stage, and available vessel traffic and vessel characteristic data and allow the program to do the tallying.

The simulation model was the focus of Phase II effort. The basic approach for Phase II is provided in Figure 1 At the start, initial data gathering led to models for weather, visibility, river stage and traffic flow models. These are described in Appendix C and were used to build a simulation model that was close to the actual port operations. After the simulation was built, the modified Phase I model (Appendix B) was used to calculate relative accident probabilities. Historical collision and allision data were then used to tune the modified situational risk model so that the simulation would reasonably replicate the past.

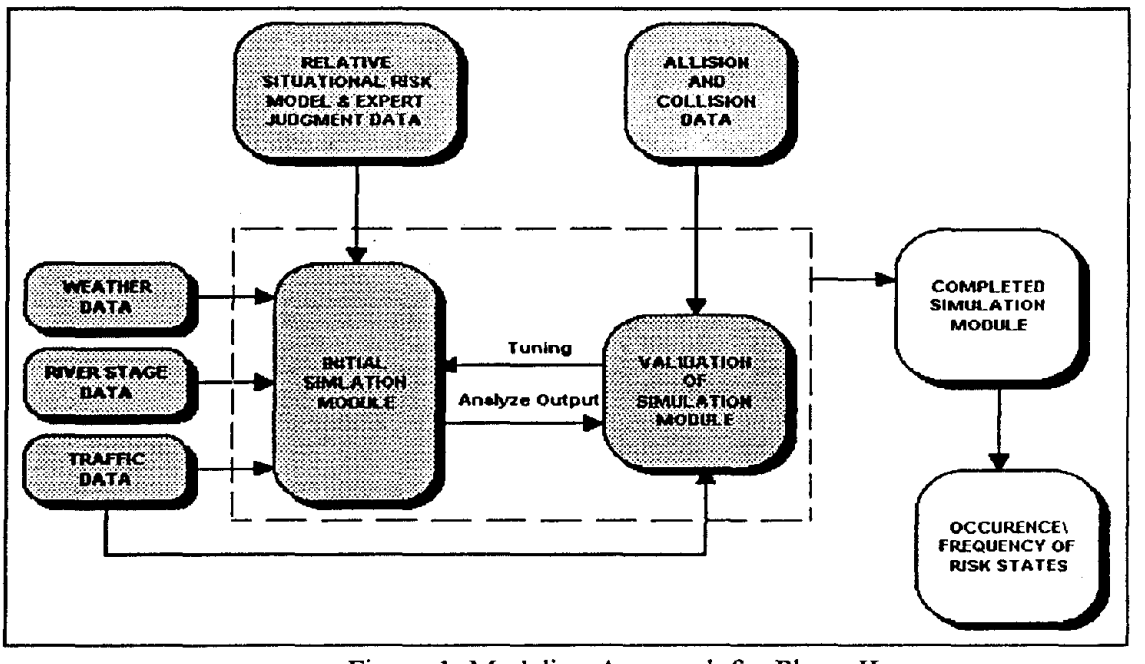

Figure 1. Modeling Approach for Phase II

2.1 INITIAL DATA ANALYSIS

The focus of the initial data analyses was to obtain insight in the characteristics of the port and validate the situational risk model developed in Phase 1. These characteristics include traffic behavior, river stage, visibility, vessel incidents in and around the port and any relation between these attributes that can be established from the data. In addition, the collected data was used to estimate relevant parameters for the simulation tool to be developed.

Data concerning the Port of New Orleans was obtained from the following institutions: Crescent Pilots, New Orleans Board of Trade, US ARMY District Corps of Engineers, US ARMY Corps of Engineers, National Oceanographic Atmospheric Administration (N.O.A.A.), the USCG Marine Safety Office New Orleans, USCG Vessel Casualty (CASMAIN) data base. Table 2 contains an overview of the collected data split up in three sections; *casualty data*, *traffic data* and *weather & river stage data*. In addition, Table 2 gives a short description of the data and the format.

2.1.1 Analysis of Weather Data

Wind and visibility data were purchased from NOAA and compiled for use in the simulation model. It should be noted that these values represent measurements at the New Orleans International Airport but were the best available source for this data. The original questionnaire that was used to elicit expert judgment presented states with visibility above and below 1/2 a mile. In order to coincide with available traffic data, the average visibility data for 1994 was used. A spread sheet was used to calculate the percentage of hours with visibility below 1/2 mile for every hour in every month. There was some variation between months, but the variation was not large and thus a general pattern was estimated. Visibility tends to run in streaks and it was determined from inspection that an assessment of visibility for four hour periods would be appropriate for modeling purposes. The average percentage of hours with visibility less than 1/2 mile was calculated as 0-4 hrs. = 23%, 4-8 hrs. = 45%, 8-12 hrs. = 26%, 12-16 hrs. = 12%. 16-20hrs. = 11%, 20-24 hrs. = 12%.

In addition to these estimates, the traffic logs from the Governor Nicholls light tower were analyzed to determine at what value of visibility the traffic actually came to a halt. This value was determined to be about 400 meters or 1/4 mile. The visibility data was then reanalyzed to determine the percentage of hours with visibility below 1/4 mile and the four hour percentages with visibility less than 1/4 mile are 0-4 hrs. = 4%, 4-8 hrs. = 7%, 8-12 hrs. = 5%, 12-16 hrs. = 2%. 16-20hrs. = 2%, 20-24 hrs. = 2%.

In analyzing the effect of wind, it was noted that the original questionnaire did not have an exact definition for a "25 mile an hour wind", therefore some operational definition had to be developed using the maritime experts. On subsequent trips to New Orleans, the mariners were asked how they interpreted wind above 25 mph and most felt it was average gusts over 25 mph. The data NOAA supplied was in terms of average wind speed over the hour. The wind data was tabulated for percentage of hours over 25 mph for each month in the following manner. The percentage of hours with wind "over 25 mph" was calculated using average wind speeds of more than 20 mph. It was assumed that changes of at least 5 mph must have taken place. This is a conservative assumption as an average wind speed of 15 mph can easily produce gusts of 25 mph.

TABLE 2
DATA SOURCES AND DESCRIPTION OF DATA

SOURCE	DESCRIPTION	FORMAT
	VESSEL CASUALTY DATA	
USCG: CASMAIN data base	Casualty Data; Detailed description of situation at the time of accident, Number of Casualties in each accident	Paper Electronic
USCG: Marine Safety Office	Casualty Data; Port Analysis of Loss of power/steering incident, Barge grounding/ breakaways, Barge/Vessel Collisions	Electronic Electronic
USCG: Marine Safety Office	Daily Reports on Spills and Vessel Casualties. Sept. '93, Febr.'94 - Oct. '94	Paper
Port of New Orleans	Allision Data; '81-'92, Ship name Date, Vessel Number, Dock	Electronic
	TRAFFIC DATA	
Cresent Pilots New Orl. Board of Trade	Deep draft transits per Day per Location Deep draft transits per Month per Location	Paper Electronic
US ARMY: Corps of Engineers	Transits per Vessel Type per River Section per Day, Lock Data	Electronic
USCG: Marine Safety Office	Daily Logs from Governor Nichols and Gretna Lights: 24 Nov. '93 - 31 Dec. '93; 30 Jan.'95 - 8 July '94 ;	Paper Paper
Port of New Orleans	Sailing schedules and routes for passenger ferries, excursion boats and gaming boats in New Orleans Perish	Paper
	WEATHER DATA & STAGE DATA	
US ARMY:	Daily River Stage Data; '82 - '91 District Corps of Engineers	Electronic
N.O.A.A.	Date, Dew point, Dry Bulb Temperature, Visibility, Wind and Wind Direction ; 34 years, '61-'94.	Electronic

The summary statistics for average wind speed exhibit little variation for 1994 and with the exception of June. For this reason the yearly average of .008 probability that the winds exceed "25 mph" for an hour was used for modeling purposes.

2.1.2 Analysis of River Stage Data

Daily river stage measurements at the Carrollton Gage for the years 1981 to 1993. were obtained from the US Army District Corps of Engineers. In the initial data analysis, it was determined that from the data that the daily river stage was in high river stage (> 14 ft.) eight percent of the time, in medium river stage (8 -14 ft.) thirty three percent of the time, and in low river stage (< 8 ft). fifty nine percent of the time. The river rises and falls very slowly, however, and it is rather common place to have two or three months with every day below 8ft. river stage. Therefore, the following analysis was performed to ensure a realistic transition of the stage values. For all 13 years of data, the first day in the year was inspected and it was determined if that day was at low, medium or high river stage. Then the river stage four days (96hrs.) later was inspected and it was again determined whether the river was at high, medium or low river stage. Data was tabulated for each of the stage levels over all years and estimates of transition probabilities from each river stage state to the other was estimated and is presented in Table 3.

TABLE 3
FOUR DAY INTERVAL STAGE TRANSITION PROBABILITIES

TRANSITION MATRIX	Stage 1	Stage 2	Stage 3
Stage 1	95%	5%	0%
Stage 2	8%	88%	3%
Stage 3	0%	13%	88%

2.1.3 Analysis of Traffic Data

The first two data sources mentioned in Table 2 with respect to traffic data, only contain traffic data concerning deep draft vessels.. Through both expert interviews and personal observation, however, it was concluded that shallow draft operation (tows, barge fleeting, passenger vessels) in the Port of New Orleans was one of the main traffic contributors. The third and fourth data source support this hypothesis. The fourth data source was considered to be the most complete and reliable of all the data sources and was used as the main data source to obtain insight into traffic in the Port of New Orleans. Only Deep Draft Vessel, Tug with Tow combinations and Line Haul Tow combination are required to make contact with the lights. However, this does not impose any restriction on using the daily logs as a data source as the fifth data source in Table 2 provides detailed schedule information for the sailing times of Passenger Vessels in and around the Port of New Orleans. This data source, the daily logs of the Governor Nichols light and Gretna light, was in paper format. To be able to analyze the data, a PC-BASED vessel logging program, VLS2000, was developed. Figure 2 contains a sample screen taken from the program.

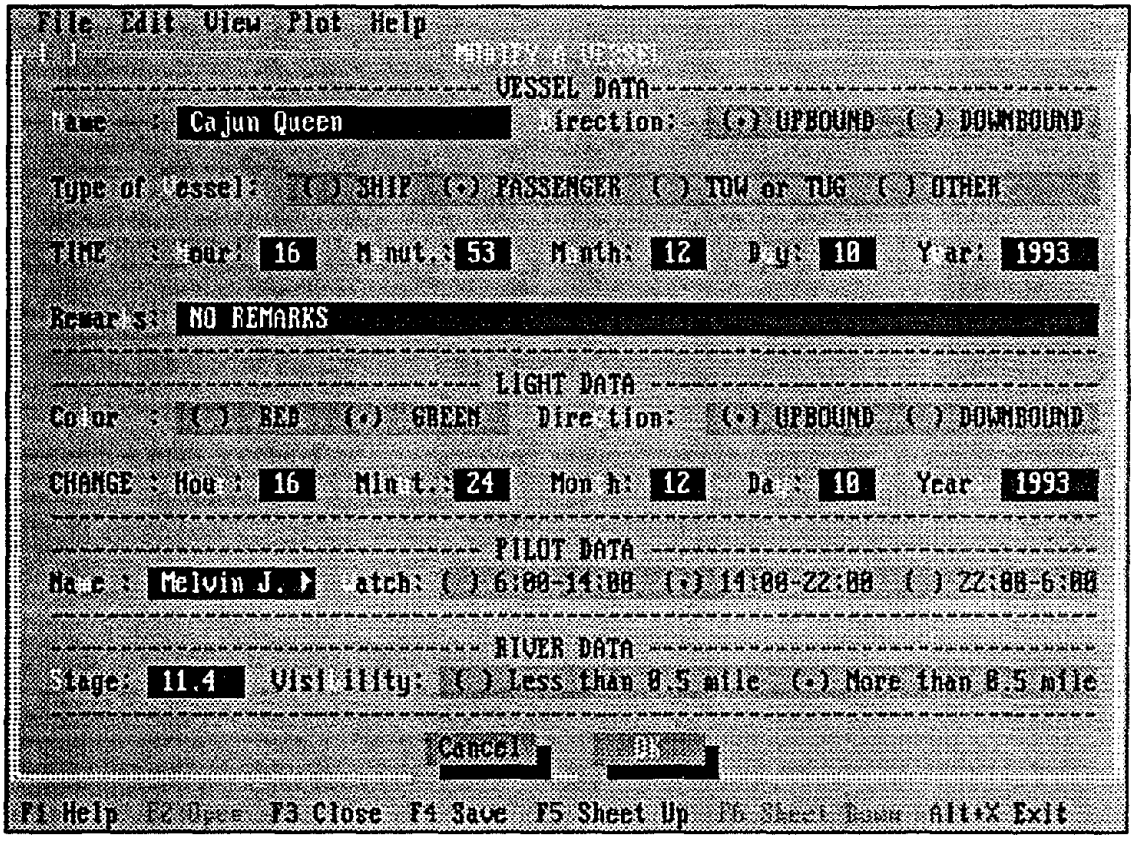

Figure 2. Sample Screen of the Vessel Logging System 2000 (VLS2000).

The effort to manually enter the entire logs would have been too cumbersome and too time consuming and therefore samples of three months worth of data were entered and analyzed. In total, 18 days of December 1993, 9 days from March 1994, and 9 days from June 1994 were entered in the vessel logging program for analysis. December 1993 was an intermediate river stage month (approximately 11 feet). March 1994 was a high river stage month (approximately 15 feet). June 1994 was a low river stage month (approximately 6 feet). In addition, December 1993 overlaps the time period of deep draft vessel data from the first two data sources. This overlap of time for these data sources allowed for cross validation between data sources with respect to consistency.

The result of the analysis is given in Figure 3 which gives the average number of vessel arrivals going up and down river for six four hour periods. For comparison purposes, the second and third plots in Figure 3 are updated using the Passenger Vessel schedules. While, it would be desirable to obtain data for periods with even shorter duration, for accuracy of the estimated arrival rates, it was decided that the minimum length of a period should be four hours. Figure 4 and Figure 5 give the proportion of the arrivals of different vessel type for the four hour periods for up river and down river direction respectively. For comparison purposes, the first column in these figures gives the average proportions over the entire day.

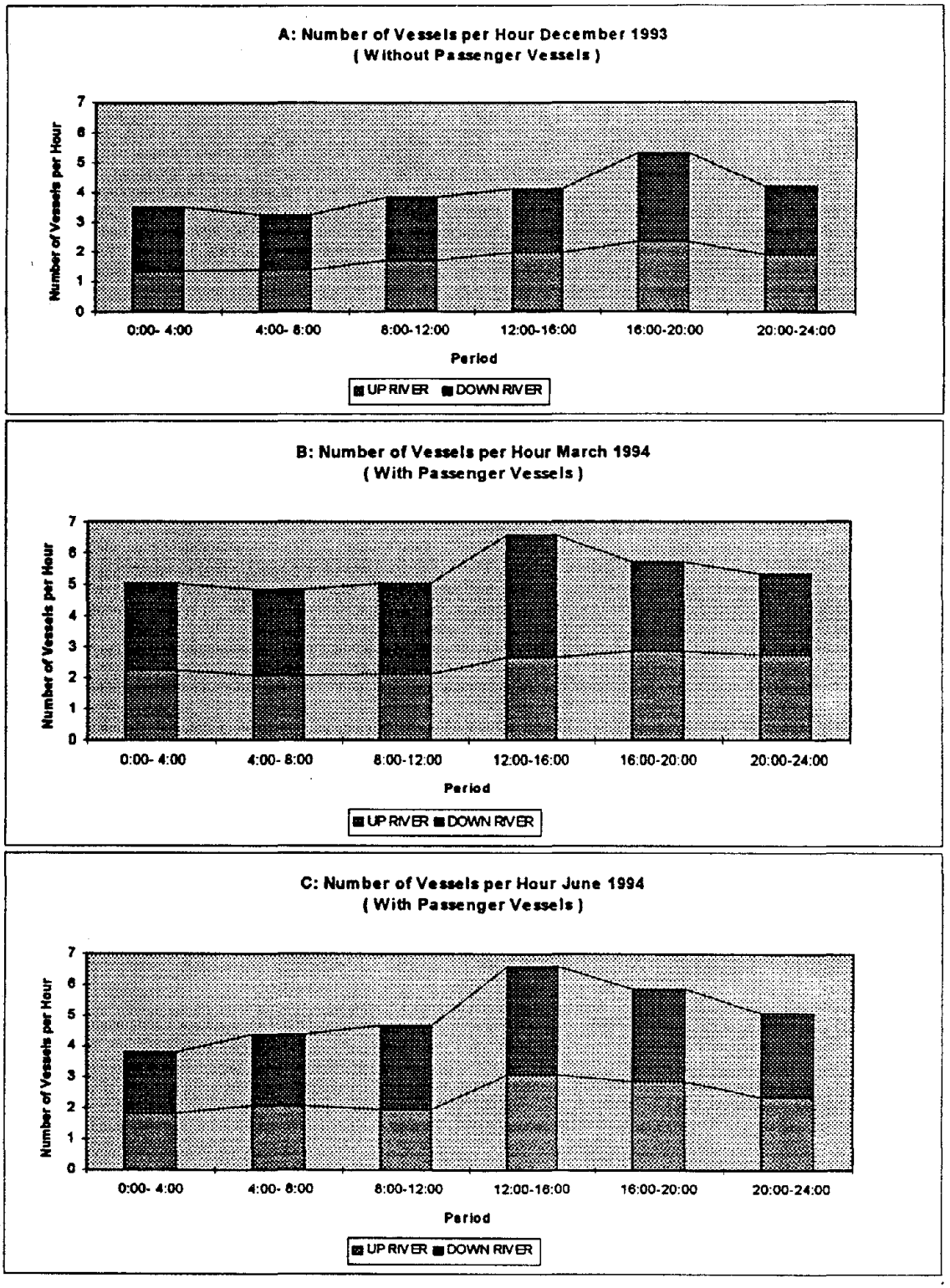

Figure 3. Vessel Arrival Rates per Period for December 1993 , March 1994 and June 1994

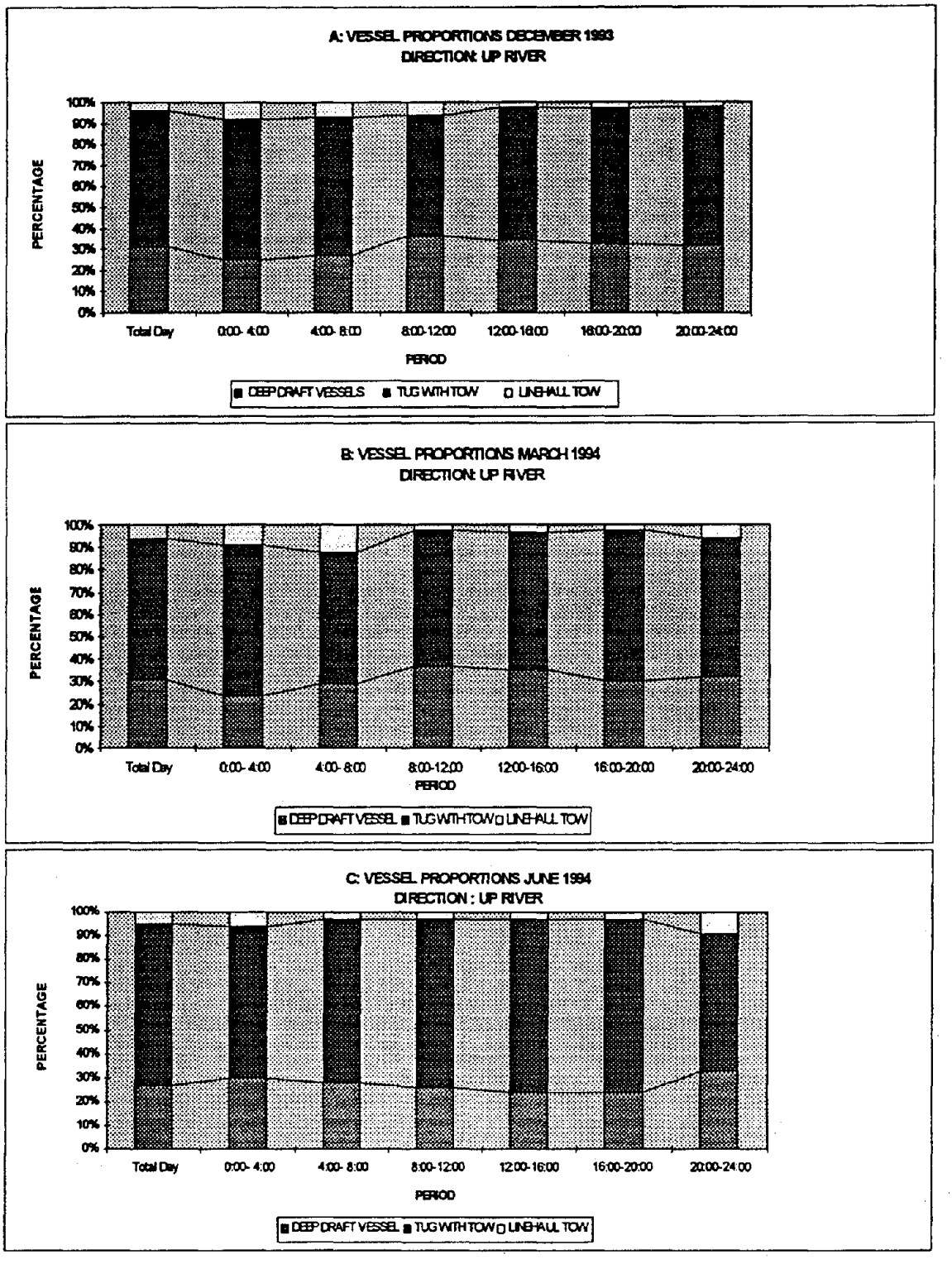

Figure 4. Proportions Per Vessel Type Per Period for December 1993, March 1994 and June 1994 for the UP RIVER direction

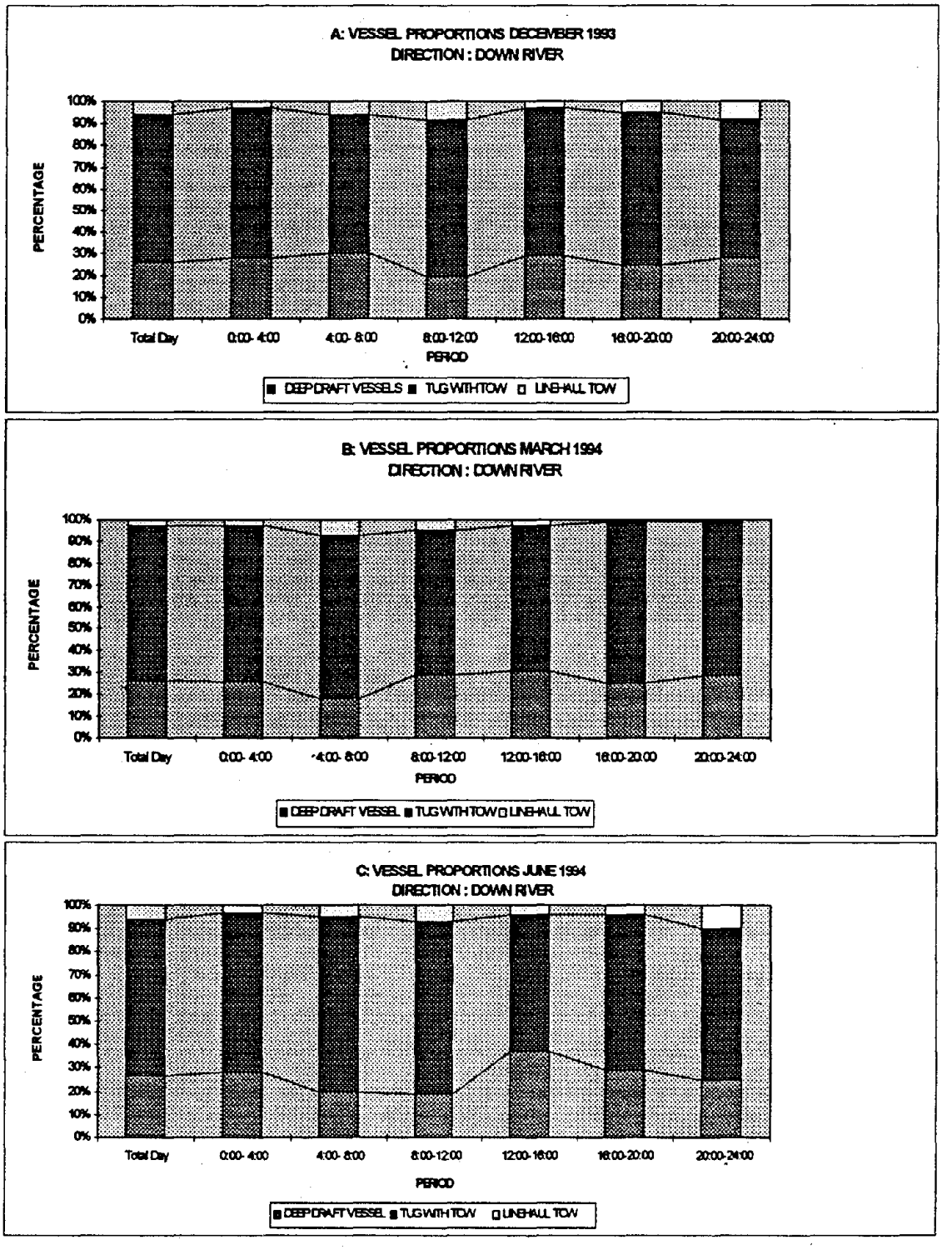

Figure 5. Proportions per Vessel Type per period for December 1993, March 1994 and June 1994 for the DOWN RIVER direction

Three conclusions can be drawn from Figures 3 through 5. First, the *rhythm of the Port* seems apparent. Typically, the period from 8:00 to 12:00 seem to be the period with lowest traffic intensity, whereas the periods 12:00 to 16:00 and 16:00 to 20:00 seem to be competing for the period with the highest traffic intensity. Note that this *rhythm* would be more pronounced in Figure 3A if passenger vessels would have been included as it can be concluded from the schedules that passengers vessels mainly sail over the period from 12:00 to 24:00. Second, it may be concluded from Figure 4 and Figure 5 that the proportion per vessel type seem to be fairly constant over the months. Considering all three figures, a third conclusion is that during periods of high river stage, approximately 5% more tug with tows are going down river than going up river. This was explained by noting that during high river stage, tug with tows avoid fighting the current in the Mississippi River by traveling upbound through the Intercoastal Water Way.

In addition to the above analysis, the Army Corps of Engineers Intercostal Waterway and lock data was also analyzed for arrival patterns. Thus total picture of the vessel flow rate was from many sources and is depicted in Figure 6.

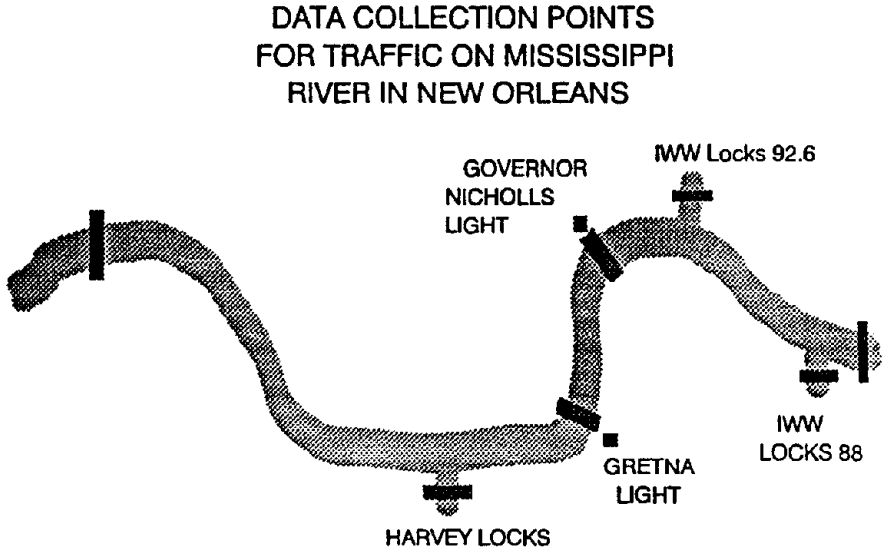

Figure 6. Data Collection Points for Traffic Patterns on the Mississippi River in the New Orleans Port Area.

2.1.4 Analysis of Casualty Data

To obtain insight in the frequency of occurrence of vessel incidents, the casualty data from the USCG and allision data from the Port of New Orleans was analyzed. The USCG New Orleans Marine Safety office and the eighth Coast Guard district maintained a local database for reported vessel collisions. It was concluded that this database was the most reliable source of data with respect to vessel casualties and incidents pertaining to the Port of New Orleans. Figure 7, is a plot of the total number of vessels collisions per location (given by river mile) over the years 1982 - 1991. The river miles of interest for the risk analysis are river miles 80-106. From Figure 7 it

follows that the average number of collisions per year from river mile 80 to river mile 106 over 1982-1991 equals 15.6 collisions per year.

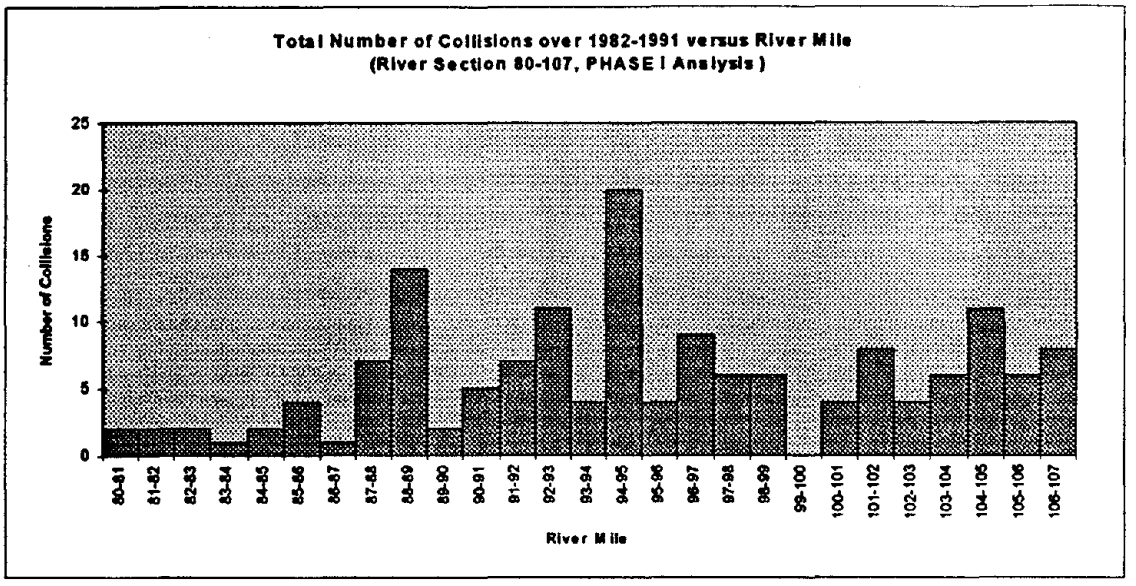

Figure 7. Total Number of Vessel Collisions over 1982 - 1991 versus River Location;

Using the database on river stage, it is possible to link the number of incidents per month over the years 1982-1991 to a particular river stage, in that month. Using these numbers, the average number of reportable incidents were calculated per river stage. The result is given in Figure 8. It follows from the figure that the average number of incidents is relatively constant up to 10 ft (with minor fluctuations) and equals approximately 5 incidents per month. The number of incidents, however, increases with a jump of 5 incidents per month from 10 ft to 11 ft., increases

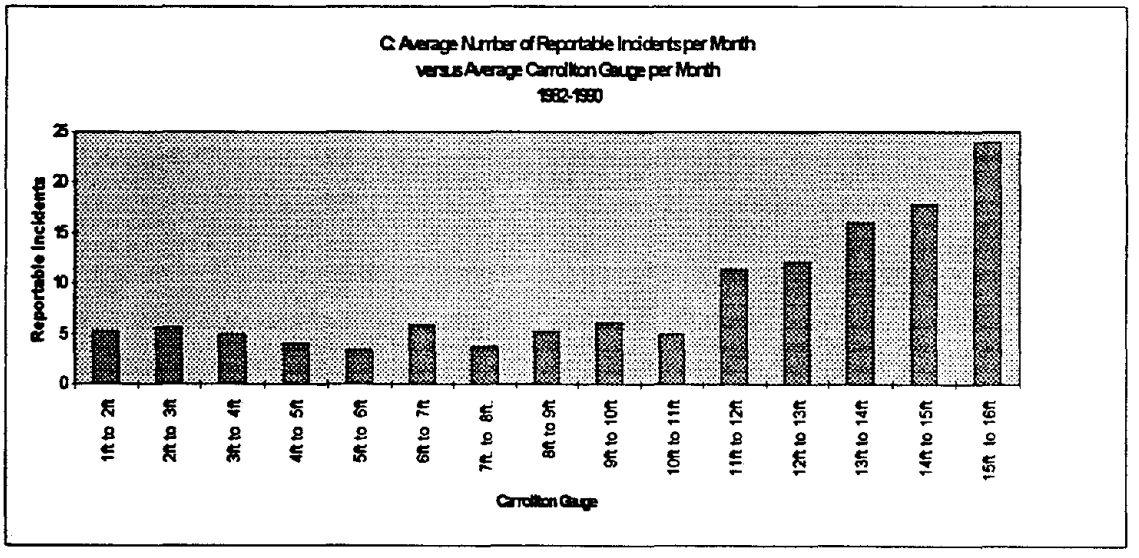

Figure 8. Reportable Incidents Versus River Stage for the years 1982-1991 and River Mile 0-235

with a jump of an additional 5 incidents from 12 ft to 13 ft and increases with a jump of an additional 8 incidents from 14 ft to 15 ft. Clearly, it follows from Figure 8 that high river stage is a dominating factor in determining the riskiness of an OFI.

In addition to the information on vessel collisions, the allision files of The Port of New Orleans were analyzed to obtain the total number of allisions per year per location (given by river mile) over the years 1983-1993. This is typically of interest in making decisions on the location of gaming vessels when they are not underway. The allision data were "filtered" by the Port of New Orleans to remove all allisions of vessels working and maneuvering at the docks. The result of the number of allisions after *filtering* is given in Figure 9. From this figure the more safe locations for docking vessels is clear and the average number of allisions per year from river mile 91 to river mile 101 can be estimated as 4.54.

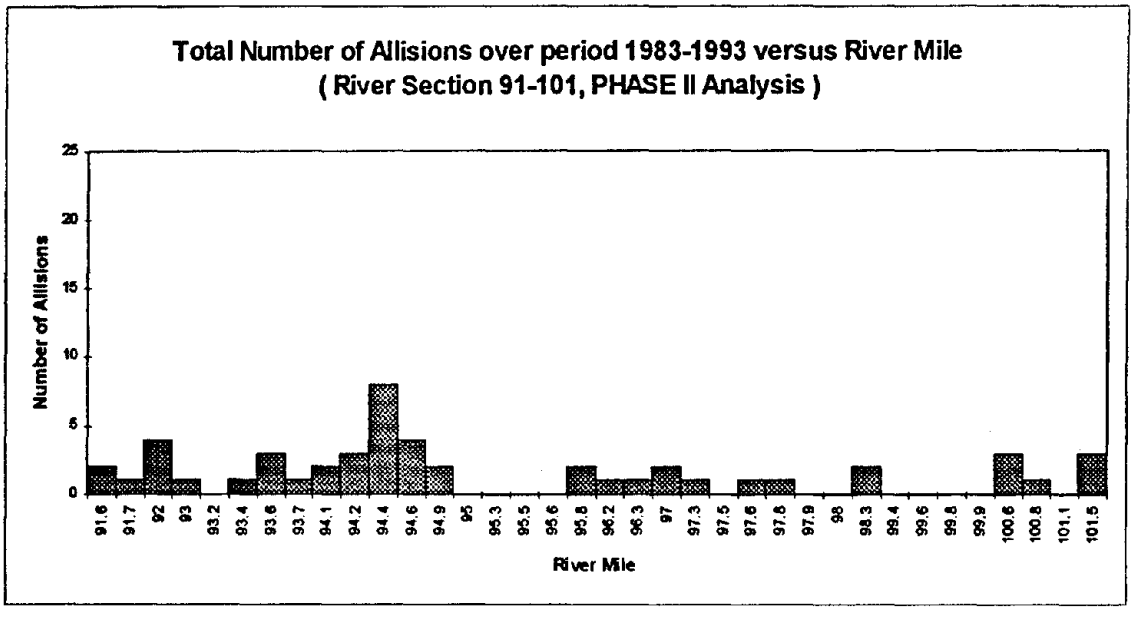

Figure 9. Total Number of Vessel Allisions over 1983 - 1993 versus River Location.

2.2 THE USE OF SIMULATION

The initial data analysis provided the basis for describing the dynamic environment of the Port. The Phase I analysis provided the definition of the environmental factors or OFI's which could lead to an incident and a means for estimating the RIP's for each OFI. The function of the simulation is to provide a means for integrating all available information.

Using the information obtained in the initial data analysis various modules for the simulation were developed for modeling the dynamic environment of the Port. These are presented in detail in Appendix C. Using these modules, the simulation emulates the dynamic environment of the Port with respect to weather and river stage conditions and traffic throughput. However, the single most important function of the simulation is to track and count OFI's. This is done in the following manner

A day is broken up into 30 second periods. At the start of a thirty second period, the simulation first checks the wind, visibility, and river stage situational variables to set them to the proper value. These values only change once in a great while but are part of an OFI definition and therefore included in the risk calculations at each thirty second interval. Next, the simulation checks for new vessel arrivals at each possible arrival point in the port area and introduces the new arrivals to the waterway at the proper position. The simulation then updates the position of each vessel in the river based on their old position, direction, and velocity. If a vessel moves out of the waterway either through one of the Inter Coastal Waterway canals or passes mile 80 or 106 on the Mississippi River, it is removed from the river and no longer considered in further calculations. When all the positions have been updated, the simulation classifies each type of OFI present and calculates the RIP for the Port area. Both the counts of the muber of times each OFI occurs and the Port RIP are saved.

There are 2520 OFI's, denoted OFI_i i = 1,2,3,...,2520. In the simmulation, OFI's are characterized by a nine-dimensional vector whose elements indicate variable values according to Table 4. The OFI's index indicates its rank of in terms of RIP. The lowest RIP value for all of the OFI's, indexed OFI_1, is characterized by the vector (1,1,1,1,1,5,1,1,1). The indices can be read from the chart above by indexing the following states; river under 8ft., low wind (< 25knts.), good visibility ($\geq$ .5mile), a shallow draft passenger vessel going up river, not within a half a mile of another vessel (VESSEL 2 CLASS = NONE), with no crossing vessel in the zone, and in between mile 80 and 92. The relative probability of an incident given that opportunity for incident 1 occurs is 1.000. All RIP's are obtained using the model presented in Appendix B. The RIP's have a wide range of values from 1 to 4492. Thus, the riskiest situation is almost 4492 times more risky than that of OFI_1.

TABLE 4
MATRIX of OPPORTUNITY FOR INCIDENTS

FACTOR	1	2	3	4	5
RIVER STAGE	< 8ft.	8-14ft.	$\geq$ 14ft.		
WIND	< 25knts.	$\geq$ 25knts.			
VISIBILITY	$\geq$ .5mile	< .5mile			
VESSEL 1 CLASS	SDPAD	TWTOW	DDRFT	LLTOW	
VESSEL 1 DIRECTION	UP	DOWN			
VESSEL 2 CLASS	SDPAS	TWTOW	DDRFT	LLTOW	NONE
VESSEL 2 DIRECTION	UP	DOWN			
CROSSING VESSEL	NOT PRES.	PRESENT			
ZONE	80-92	92-97	97-106		

2.2.1 Description of the Simulation OFI Counting

As an illustration of the simulation's counting of OFIs, Figure 10 provides a pictorial presentation of a section of the river changing over four time periods and the associated OFI's added to the count vector. The small vessel is a shallow draft passenger vessel headed down river. The first large vessel headed up river is a tug with tow followed by a deep draft vessel. Notice that each vessel has a 1/2 mile domain defined from the tip of it's bow. The two up river vessels are always within 1/2 mile so the state TWTOW UP , DDRFT UP is in all four time periods. Notice how the SDPAS vessel goes from being within 1/2 a mile of one vessel, to within 1/2 a mile of two vessels, back to within 1/2 a mile of one vessel, and in the last time period, the SDPAS is not within a 1/2 mile of any vessel. Thus in this last time period, the SDPAS vessel forms a situational traffic state by itself as opposed to with another vessel in a dual vessel state. Also notice that in time period 1 : 00 : 30 three vessels are very close to each other so there are three dual vessel cases. All combinations of vessels within 1/2 a mile are made and added to the risk equation. Great care was taken in the simulation to ensure that situations were not counted twice.

The relative positions of the vessel do not change much in thirty seconds, however, the movements of the vessel were exaggerated in this example to demonstrate in general how the states change. It actually takes about 6 to 12 time periods for oncoming vessels to clear each others ± 1/2 mile domains.

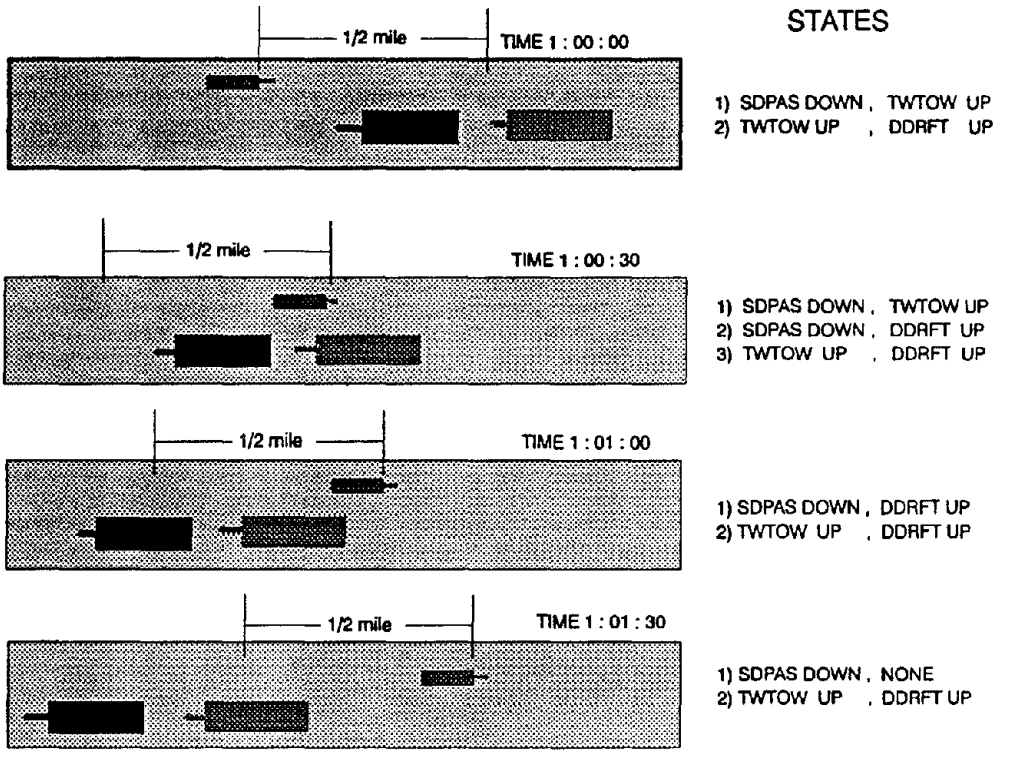

Figure 10. Pictorial Representation of Vessel State Changes Over Time.

It is important to note that the experts judgment provided information on only a snap shot in time of the river and then only on a comparative basis. The simulation assumes the role of stringing these snap shots together in a time continuum thus creating a realistic portrayal of the risk of the river over time.

2.2.2 Use of the Simulation OFI Counting

Let N_i denote the number of OFI_is in some defined time frame (for example one month) and define the following value

$$p_1 = \Pr(\text{Reportable Incident} | N_1 = 1)$$

That is, p_1 is the (absolute) probability of a reportable incident given a single occurrence of the least risk OFI. If p_1 is known, then using the relative probabilities, it is possible to calculate the probability P_i that OFI_i will result in a reportable incident using

$$P_i = \Pr(\text{Reportable Incident} | N_i = 1) = p_1 RIP_i$$

Assuming that the probability of a reportable incident occurring is independent of the number of OFI's of any type and of past OFI's and incidents, the number of reportable incidents occurring due to the occurrence of OFI_i, say INC_i, is given by the Binomial distribution

$$\Pr(INC_i = x_i | N_i) = \binom{N_i}{x_i} P_i^{x_i} (1-P_i)^{N_i - x_i}$$

and accoringly

$$E[INC_i | N_i = n_i] = n_i P_i$$

The assumption of independence of N_i to the other N_j's is not entirely reasonable since the N_i's are dependent on the condition of the river. This assumption is required for probabilistic calculations. The dependence affects are reduced by increasing the length of simulation runs.

The expected value of N_i for all values of i, can be calculated via taking the average N_i from repeated simulations. These results can be used to estimate p_1 via the following methodology. The total number of incidents on the river in a given time period can be written

$$INC = \sum_{i=1}^{2520} INC_i$$

and it follows using the above definitions that

$$E[INC] = \sum_{i=1}^{2520} E[INC_i] = \sum_{i=1}^{2520} E[N_i] P_i = p_1 \sum_{i=1}^{2520} E[N_i] RIP_i$$

The simulation can be run to estimate the $E[N_i]$ and then historical data on the number of accidents can be used to obtain a point estimate for p_1 with the following equation:

$$p_1 = \frac{I_t}{\sum_{i=1}^{2520} E[N_i]\, RIP_i}$$

where I_t is the actual average incidents per desired time unit.

Given the estimate for p_1 and thus the definition for all P_i's, the distribution of the number of accidents that may take place over a given time period may also be estimated via simulation. It is possible to run the simulation hundreds of times and generate hundreds of vectors $\underset{\sim}{N}_j = (N_{1,j}, \ldots, N_{2520,j})$ representing the number of times the different OFI's occur in simulation j. Recalling that INC_i is a binomial random variable with parameters N_i and P_i, then for each $\underset{\sim}{N}_j$ vector, it is possible to generate, $n_{i,j}$ a value for the binomial random variable representing the number of incidents occurring in simulation j due to OFI_i. Then within a given simulation run j, the number of incidents is simulated as $INC_{\bullet j} = \sum_{i=1}^{2520} n_{i,j}$. If the simulation is run many times, the $INC_{\bullet j}$s form a distribution which will be comparable to the distribution of reportable incidents actually seen on the river. The distribution will contain a great deal more information than a simple point estimate.

2.2.3 Baseline Simulation Results

The first baseline simulation ran for 180 months with the river stage being updated as per the Markov Chain method described in Appendix C. The distribution of the number of incidents that can be expected is estimated and given in Figure 11. This plot can be compared that number to actual data. If the distributions are comparable then the historic data would support the simulation models ability to accurately predict the risk state of the river The average number of incidents per month in the Port area (mile 80 to mile 106) in this baseline run was 3.2. The

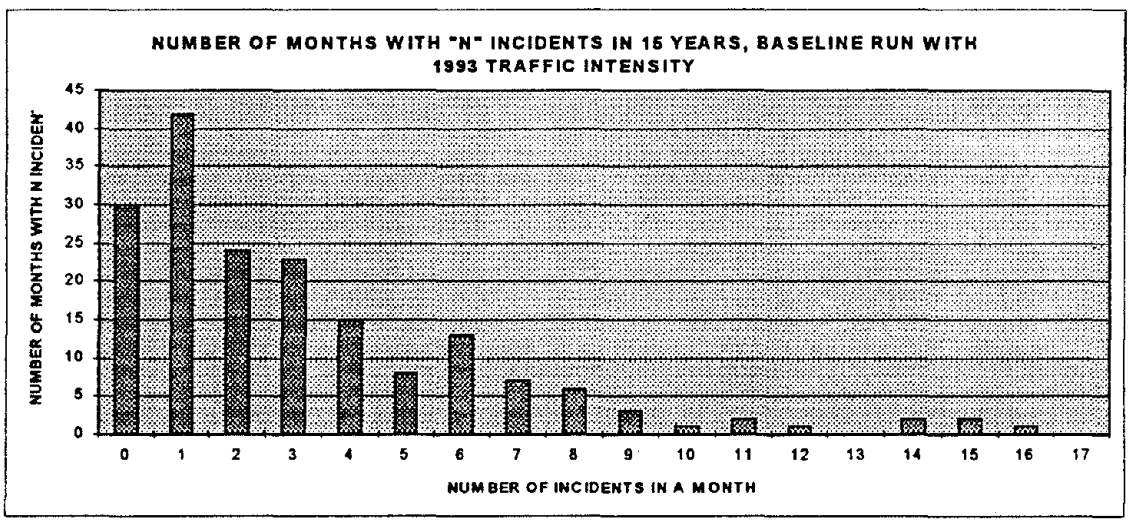

Figure 11. Simulated Distribution of Incidents for 15 Years of Simulated River Activity

average should have been (based on historical data) 2.3 so it is likely that the simulation got caught in a long streak of high stage condition. This can happen in a typical 15 year period. Letting the simulation run long enough to wash out the effect of the slow stage change is not practical. Thus, the baseline run that was used to generate the required information was 30 months long with river stage changes performed by picking from the historic probabilities of high, medium and low stage every 96hrs. (4days). These results were used to estimate the average number of times each OFI occurs in a given month and then to calculate the most common OFIs. The base rate probability was also calculated and the baseline run was used for comparison for the affect of each external variable.

If the OFI's are sorted by decreasing RIP values, it becomes evident that the most risky OFIs rarely happen. In fact in 30 months of simulated traffic the top twenty riskiest OFI's never occurred (see for example Table 5). It is also possible to sort by expected number of incidents due to the occurrences of the OFI's as in Table 6. Recall that this value is the product of the probability of an incident occurring in a thirty second time period times the number of times the OFI occurred in a month. As can be seen in Table 6, the OFI's contributing most to risk have relatively low RIP values. It should be noted from this table that the expected number of incidents for each OFI is small as it is to be multplied by 10^{-6}. Thus for example, the expected number of collisions due to the first OFI of Table 6 is $52718.9 \times 10^{-6} = .0527189$.

The maximum RIP value is 4492 and the minimum RIP value is 1 by definition. It has just been shown that OFI's with high RIP's seldom occur but it may also be surprising to recognize that the mean RIP is 238 and the median RIP is 104. These values point to a distribution skewed to the left with a long right tail. When weighting the RIP's by the number of times the associated OFI's occur the weighted average RIP value is 12.6. This is due in part to the large percentage of single vessel situations but also because the professionals operating on the river are acting as a risk avoiding system as a rule. An example of this phenomena is that most mariners stop moving in dense fog.

TABLE 5
OFI's WITH THE HIGHEST PROBABILITY OF CAUSING A INCIDENT IN THIRTY SECONDS

RIVER STAGE	WIND VELOCITY (MPH)	VISIBILITY (MILES)	VESSEL 1	DIRECTION 1	VESSEL 2	DIRECTION 2	CROSSING VESSEL	RIVER ZONE	RELATIVE PROBABILITY OF INCIDENT	EXPECTED NUMBER OF OFI'S/ MONTH	NUMBER OF EXPECTED COLLISIONS PER/MONTH * 10^6
>14'	>25kts	<.5m	DDRFT	up	LINHL	down	yes x	92-97	4492.230	0.0	0.0
>14'	>25kts	<.5m	TWTOW	up	LINHL	down	yes x	92-97	4295.809	0.0	0.0
>14'	>25kts	<.5m	SDPAS	up	LINHL	down	yes x	92-97	4107.977	0.0	0.0
>14'	>25kts	<.5m	DDRFT	up	DDRFT	down	yes x	92-97	3928.357	0.0	0.0
>14'	>25kts	<.5m	LINHL	down	LINHL	down	yes x	92-97	3756.592	0.0	0.0
>14'	>25kts	<.5m	TWTOW	down	DDRFT	up	yes x	92-97	3592.336	0.0	0.0
>14'	>25kts	<.5m	SDPAS	down	DDRFT	up	yes x	92-97	3435.264	0.0	0.0
>14'	>25kts	<.5m	DDRFT	down	LINHL	down	yes x	92-97	3285.058	0.0	0.0
>14'	>25kts	<.5m	TWTOW	up	DDRFT	down	yes x	92-97	3141.420	0.0	0.0
>14'	>25kts	<.5m	DDRFT	up	LINHL	down	yes x	80-92	3049.910	0.0	0.0
>14'	>25kts	<.5m	SDPAS	up	DDRFT	down	yes x	92-97	3004.063	0.0	0.0
>14'	>25kts	<.5m	TWTOW	up	LINHL	down	yes x	80-92	2916.554	0.0	0.0
>14'	>25kts	<.5m	TWTOW	up	TWTOW	down	yes x	92-97	2872.712	0.0	0.0
>14'	>25kts	<.5m	SDPAS	up	LINHL	down	yes x	80-92	2789.029	0.0	0.0
>14'	>25kts	<.5m	TWTOW	down	LINHL	down	yes x	92-97	2747.104	0.0	0.0
>14'	>25kts	<.5m	DDRFT	up	DDRFT	down	yes x	80-92	2667.080	0.0	0.0
>14'	>25kts	<.5m	SDPAS	down	LINHL	down	yes x	92-97	2626.988	0.0	0.0
>14'	>25kts	<.5m	LINHL	down	LINHL	down	yes x	80-92	2550.463	0.0	0.0
>14'	>25kts	<.5m	SDPAS	down	TWTOW	up	yes x	92-97	2512.124	0.0	0.0
>14'	>25kts	<.5m	TWTOW	down	DDRFT	up	yes x	80-92	2438.945	0.0	0.0

TABLE 6
OFI's WITH THE HIGHEST EXPECTED NUMBER OF INCIDENTS IN A MONTH

RIVER STAGE	WIND VELOCITY (MPH)	VISIBILITY (MILES)	VESSEL 1	DIRECTION 1	VESSEL 2	DIRECTION 2	CROSSING VESSEL	RIVER ZONE	RELATIVE PROBABILITY OF INCIDENT	EXPECTED NUMBER OF OFI'S/ MONTH	NUMBER OF EXPECTED COLLISIONS PER/MONTH * 10^6
8-14	<25kts	>.5m	TWTOW	up	TWTOW	down	no x	80-92	41.359	5249.0	52718.9
>14'	<25kts	>.5m	TWTOW	up	TWTOW	down	no x	80-92	113.223	1548.0	42561.6
8-14	<25kts	<.5m	TWTOW	up	TWTOW	down	no x	80-92	119.658	1111.8	32307.7
>14'	<25kts	>.5m	TWTOW	up	TWTOW	up	no x	80-92	57.900	2225.2	31287.0
8-14	<25kts	>.5m	TWTOW	up	TWTOW	up	no x	80-92	21.150	5975.1	30689.2
<8'	<25kts	>.5m	TWTOW	up	TWTOW	down	no x	80-92	15.108	7951.9	29174.4
>14'	<25kts	<.5m	TWTOW	up	TWTOW	down	no x	80-92	327.572	322.4	25649.0
8-14	<25kts	>.5m	TWTOW	up	NONE	up	no x	80-92	3.633	28054.3	24751.8
8-14	<25kts	>.5m	TWTOW	up	TWTOW	down	no x	97-106	34.079	2891.4	23928.1
>14'	<25kts	>.5m	TWTOW	up	NONE	up	no x	80-92	9.946	9607.9	23206.0
8-14	<25kts	>.5m	TWTOW	up	DDRFT	up	no x	80-92	24.186	3797.7	22305.4
>14'	<25kts	>.5m	TWTOW	up	DDRFT	up	no x	80-92	66.211	1315.6	21153.2
8-14	<25kts	>.5m	TWTOW	down	DDRFT	up	no x	80-92	51.720	1677.7	21071.7
8-14	<25kts	>.5m	TWTOW	down	NONE	down	no x	80-92	4.751	16772.4	19351.1
<8'	<25kts	>.5m	TWTOW	up	TWTOW	down	no x	97-106	12.449	5979.5	18076.3
>14'	<25kts	<.5m	TWTOW	up	TWTOW	up	no x	80-92	167.514	430.0	17493.5
8-14	<25kts	>.5m	TWTOW	up	DDRFT	down	no x	80-92	45.228	1587.7	17437.6
<8'	<25kts	<.5m	TWTOW	up	TWTOW	down	no x	80-92	43.710	1600.7	16991.1
8-14	<25kts	<.5m	TWTOW	up	TWTOW	up	no x	80-92	61.191	1127.3	16750.9
8-14	<25kts	<.5m	TWTOW	up	NONE	up	no x	80-92	10.511	6512.2	16622.9

One way to validate the simulation is to break the river up into five mile zones and see if the simulation can accurately predict the percentage of incidents in each zone. Table 7 is the summary of simulation output for five mile slices of the river starting at mile 80 and ending at mile 105.

TABLE 7
EXPECTED NUMBER OF INCIDENTS FOR FIVE MILE ZONES OF THE LOWER MISSISSIPPI RIVER

	EXPECTED NUMBER OF INCIDENTS/MONTH	STD. DEV. AVG. INCIDENTS/MONTH
MILE 80-85	0.33	0.10
MILE 85-90	0.50	0.14
MILE 90-95	0.75	0.23
MILE 95-100	0.36	0.10
MILE 100-105	0.27	0.07

Figure 12 compares the expected number of incidents to the actual number of collisions for the five mile slices. The correspondence between simulated and actual data is fairly strong. Some of the differences in the two end zones may be explained by poor assumptions on the direction of traffic coming out of the IWW. Relatively good data existed for the zones around the light tower but the traffic behavior was less well known at mile 80 and 106.

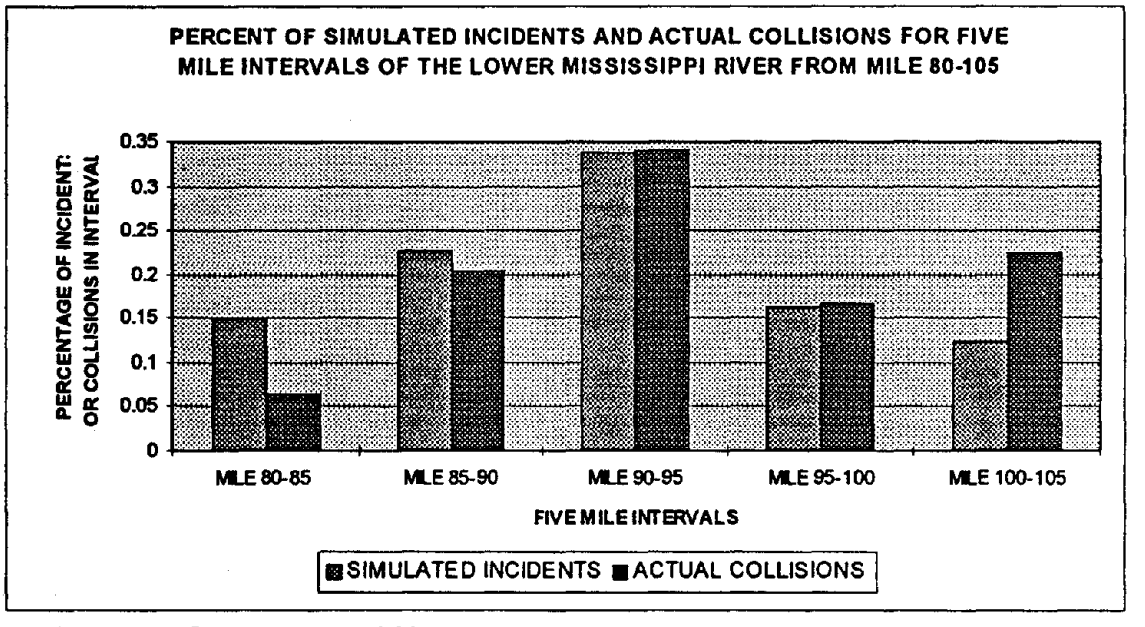

Figure 12. Comparison of Simulated to Actual Incidents for Five Mile Slices of the Lower Mississippi Mile 80 - 105

One of the advantages of a risk management tool is the ability to change the system parameters (like the amount of traffic on the river) and be able to estimate the effect on risk. Traffic congestion is a major factor in the Port of New Orleans. At 1993 traffic levels, approximately 85% of the time a vessel was not within a half mile of another vessel. As traffic increases the percentage of time spent within 1/2 mile of another vessel will increase. The risk when within close proximity to another vessel is much higher so a 1% increase in traffic will tend to increase the number of reportable incidents by more than just 1%. Table 8 and Figure 13 show the effect of traffic increases on the expected number of incidents per month in the Port area .

TABLE 8
EXPECTED NUMBER OF INCIDENTS
AS A FUNCTION OF TRAFFIC INTENSITY

	EXPECTED NUMBER OF INCIDENTS/MONTH	STD. DEV. AVG. INCIDENTS/MONTH
25% 1993 TRAFFIC	0.41	0.13
50% 1993 TRAFFIC	0.93	0.32
75% 1993 TRAFFIC	1.56	0.47
100 % 1993 TRAFFIC	2.27	0.64
125% 1993 TRAFFIC	3.12	0.94

These results are significant in that the economic well being of a large portion of the country depends heavily on affordable transport up and down the Mississippi River. It should be a priority to implement systems that will ensure the continued safe operation of the Lower Mississippi River and provide for increased economic transport as the nations economy grows. The simulation can effectively and quickly help in the evaluation of the effect any traffic increase or traffic management policy.

2.2.4 Analysis of the Impact of Gaming Vessels

One of the findings from the light tower logs and IWW data was that approximately 47,500 vessels with cargo transit the Port of New Orleans annually. This number neglects much of the barge fleeting traffic, the ferry boat traffic, and tugs transiting without loads. The average time that a vessel spends in the river while transiting in the mile 80-106 zone is 1.8 hrs. The number may seem low because many vessels use the IWW system and do not travel the entire 26 miles.

For purposes of this analysis, gaming vessels were assumed to make on average three, two hour trips per day per vessel. This means that each vessel at three trip per day will make approximately 1080 trips per year. Each vessel adds an additional 2.3% traffic to the river between mile marker 80 and 106. It has already been shown that the increase in the expected number of incidents is not directly proportional to the increase in traffic. Rather there appears to be a nonlinear relationship. Furthermore, the additional traffic is concentrated between miles 90 and 95, the most hazardous place in the Port area. From the data analysis, an estimate of 27.2

incidents (allsions and collisions) occurring on the river between mile 80 and 106 per year is obtained. By adding one additional vessel that will add 2.3% to the traffic load, a conservative estimate to the increase in expected number of incidents in the Port area is .6 per year.

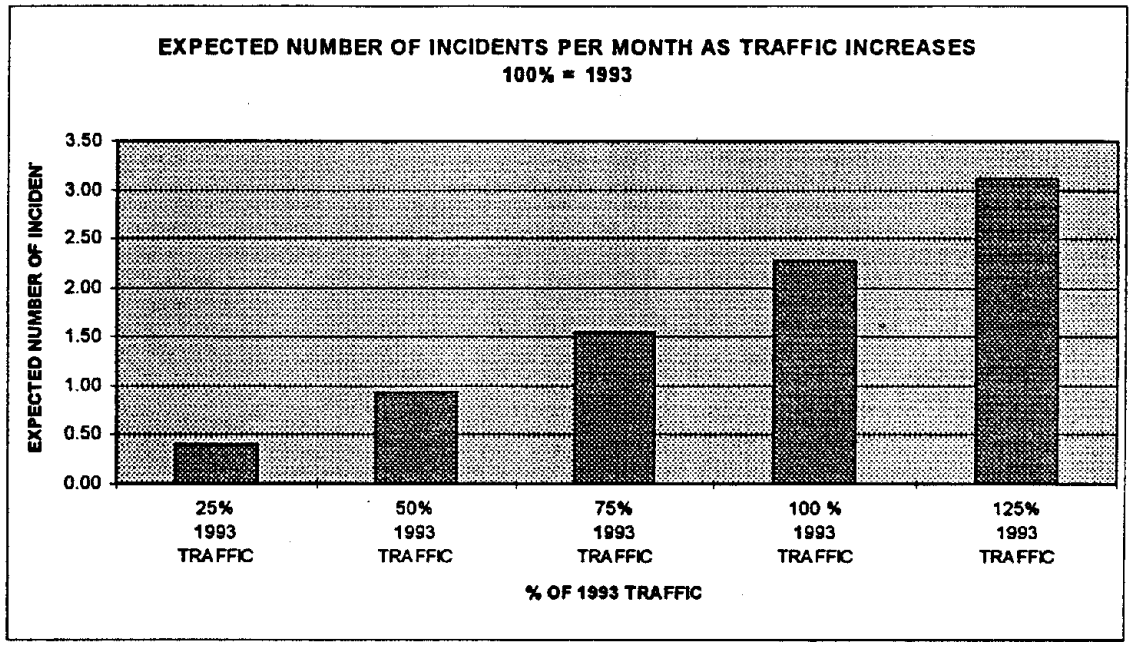

Figure 13. Expected Number of Incidents as a Function of Traffic Intensity.

The simulation can be used to estimate the increased expected number of incidents by adding gaming boats to the river. The data in Table 9 and Figure 14 shows the 1993 baseline data and runs for one gaming vessel (down river), two gaming vessels (one up and one down) and three gaming vessels (one down and two up river). One of the unfortunate aspects of adding gaming vessels to the simulation is that it destroyed the common random number variance reduction enjoyed by most the other runs. Common random numbers is a technique used to reduce the variance of simulation output. In many of the other runs peak periods coincided so even though the variance of the expected number of incidents over many months may be high, high values for individual months across simulations would coincide so relatively minor differences in output were detectable. When extra vessels are added to the simulation and the difference in measures of interest is small the loss of common random number is significant.

In conclusion, the increase in the number of expected reportable incidents in a year due to adding three gaming vessels is 20% or approximately 6.7% per vessel. As expected, the effect appears to be nonlinear in the number of gaming vessels added.

It should be noted that in the above analysis the severity of the incident in terms of expected loss of life is not addressed. However, upper bounds or totals of people at risk could be calculated using the simulation in ccombination with vessel passenger density estimaes.

TABLE 9
THE EFFECT OF ADDING GAMING VESSEL ON THE EXPECTED NUMBER OF INCIDENTS PER MONTH MILE 80 TO 106

	EXPECTED NUMBER OF INCIDENTS/MONTH	STD. DEV. AVG. INCIDENTS/MONTH
NO GAMING VESSELS	2.24	0.63
ONE GAMING VES DOWN	2.27	0.81
TWO GAMING VESSELS	2.31	0.69
THREE GAMING VESSELS	2.69	0.93

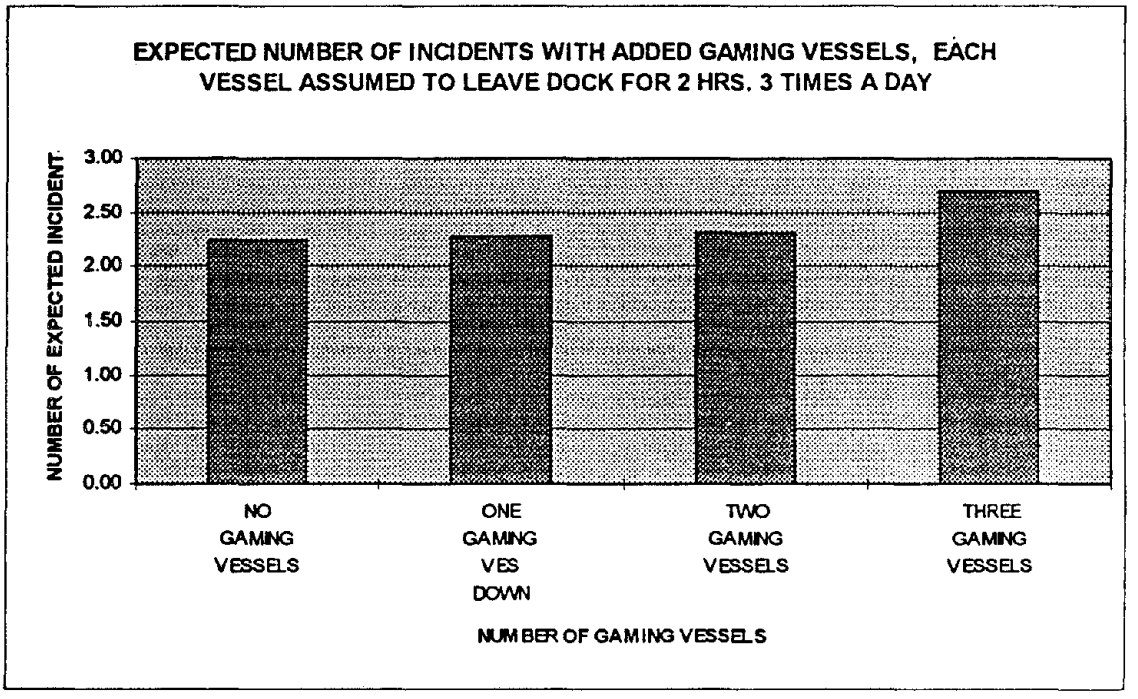

Figure 14. Expected Number of Incidents as a Function Additional Gaming Vessels.

Another question that was addressed was if the gaming vessels were safer dockside or underway. To approach this problem with the simulation, a one mile area around mile marker 93.6 to 94.6 was analyzed. That is, this was the assumed dockside location for the gaming vessel. The OFI's occurring in this mile of the river were counted for six hours per day coinciding with the schedule programmed for the upbound gaming vessels for a period of thirty months. Then the same simulation was run with the gaming vessel going up river except that only OFI's occurring within a half mile of the vessel while on the river (1 mile river length) were tallied. The simulation was run again for the down bound gaming vessel. Table 10 summarizes the results.

TABLE 10
EXPECTED NUMBER OF INCIDENTS PER MONTH WITHIN 1/2 MILE OF GAMING VESSELS UPBOUND, DOWNBOUND, AND DOCKSIDE

VESSEL TYPE	NO. OF INCIDENTS	σ NO. OF INCIDENTS
GAMING VESSEL DOWN	.19	.08
GAMING VESSEL UP	.12	.03
DOCKSIDE VESSEL	.04	.02

The program was written to count only those situations that a gaming vessel was involved in while afloat. While dockside, however, the gaming vessel will only be involved in a small percentage of incidents. Assume that the gaming boat is 500ft. long so it takes up approximately 10% of one mile of one bank. Also assume that any collision will result in a vessel impacting a bank (this is a very conservative assumption). The probability of the gaming vessel being involved in an incident occurring within a half mile is then 1/20 or .05. A conservative estimate for the expected number of incident per month for a gaming vessel kept dockside is .0020/month. It can be concluded from the above that while afloat, it can be expected that a gaming vessel that operates up river from mile 94 will get in 60 times more incidents than if the gaming vessel was kept dockside at mile 94. In addition, it can be expected that while afloat a gaming vessel traveling down river from mile 94 will get in 95 times more incidents than if the gaming vessel was kept dockside at mile 94. It needs to be restated that these are very conservative estimates and that the increased risk while afloat is most likely higher than reported. The above estimates can also be used to say that for an even amount of hours spent on the river, the downbound vessel can expect to be in 58% more incidents than the upbound vessel.

A summary of the effect of changes to the river and the corresponding change in expected number of incidents for a given time period is given in figure 14.

2.2.5 Evaluaton of Mitigation Measures

The purpose of this risk management tool is to quantify risk reductions so improved decisions can be made with respects to the implementation of safety measures on the waterway. The eventual goal will be to optimize the allocation of funds to risk reduction. To consider how risk reductions are entered into the model it will be helpful to recall that risk has two components. The probability of an incident occurring and the impact given that the incident has occurred. Thus, there are three ways to change the expected number of incidents;

1) change the probability of an incident occurring given that an OFI takes place (P_i)

2) change the number of times the OFI's take place in a well defined period of time (N_i)

3) lowering the impact of any incident.

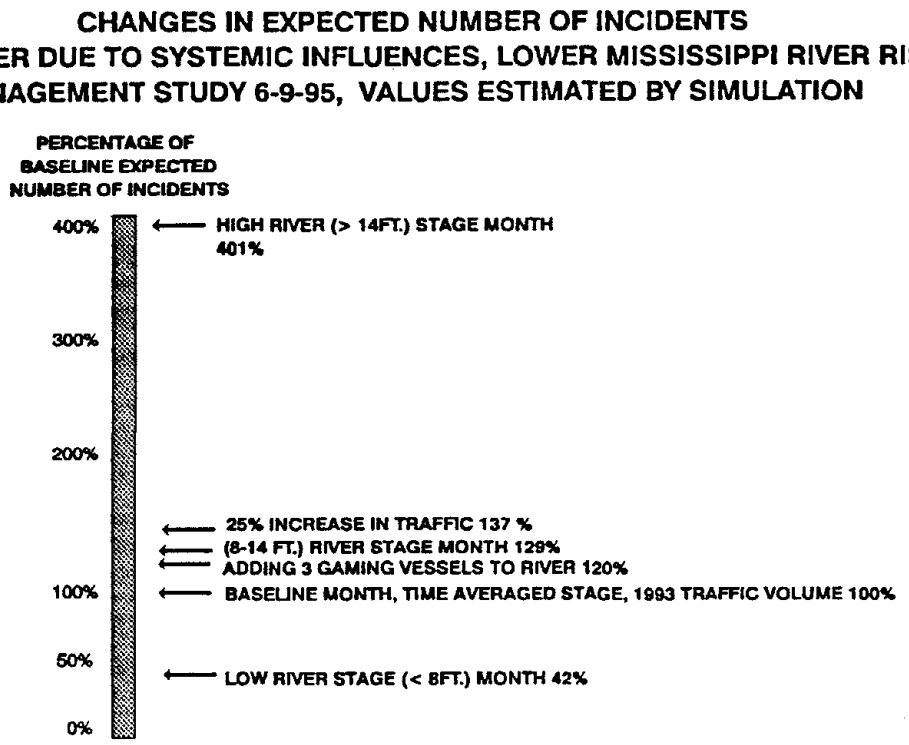

Figure 15. Changes in the Expected Number of Incidents on the River Due to Systemic Influences.

For the first case, where risk is reduced through changing the probability of an incident taking place, the reduction is estimated through another elicitation of expert judgment. The probability values can be used to calculate updated P_i's denoted P_i^*'s and the expected number of incidents can be estimated with the reduced values via

$$E[X^*] = \sum_{i=1}^{2520} E[N_i]P_i^* \ .$$

Estimating the change in the distribution of N_i can be accomplished with the simulation. This type of risk reduction measure would include keeping the Gaming vessels dockside and changing traffic patters or light operations, etc. The final type of risk reduction measure is the reduction of impact. This reduction can again be estimated with expert judgment through an impact model in much the same way the reduction in probability of an incident is calculated.

The risk reduction measures being considered in this study were identified from the following prior studies, reports, and hearings:

The Governor's task force on Maritime Industry
The Maritime Safety Association (MNSA)
The Port of New Orleans Safety Workshop sponsored by the Port of New Orleans and the US Coast Guard
The US Coast Guards Operation Safe River Operation Plan

Testimony by RADM James Card, Commander Eighth Coast Guard District at field hearings sponsored by Congressman Tauzin.

The National Ports and Waterways Institute's risk management recommendations developed for the State of Washington, Office of Marine Safety.

The list of 50 risk reduction measures from these sources had to be reduced to a workable size of twenty or less. A preliminary questionnaire with asking concerned maritime professionals what risk reduction measures are most important to study with respects to the lower Mississippi River was passed out and completed by eleven respondents. Table 11 presents a list of the risk reduction measures considered in Phase II and how the reductions were quantified.

TABLE 11
RISK REDUCTION MEASURES AND RISK RELATIONS

		Year Round Traffic Light Operation	Mandatory VTS	Regulated Navigational area	Minimized Radio Interference	Mariners to Communicate Intentions		Minimize Vessel Waivers	Power displacement Standards	Substandard Ship restrictions	Mandatory Manned engine rooms	Substandard Vessels Denied Entry	Random Drug and Alcohol Testing		High Water Sailing Restrictions	Ensure Experienced Crews	Ensure Gaming Boat Meets Vessel Standards	Sailing Restriction		Assigned Fire Rescue Boat	Conduct Drills
Change distribution of CRFs		X	X												X			X			
Reduce RIPs given an CRI			X	X	X	X		X	X	X	X	X	X			X	X				
Reduce Impact given an incident		X	X		X						X		X		X	X				X	X

A Quality Functional Deployment methodology (QFD) was employed to help elicit expert information concerning changes in the P_i. Developed in Japan in the early 1970's as an approach to designing the Kobe ship yard, the basic premise of QFD is to step by step define important attributes pertaining to a design and to determine what aspects of the next step in the design phase have the biggest effect on the attributes of interest. In this study, 9 vessel operations experts were asked to asked to judge how much an implemented measure would reduce to the risk on the river due to an individual risk factor. The question that was specifically asked was

"If this risk reduction measure were to be implemented by what percent would it reduce the probability for an incident for each factor?" (100% indicates a drop from the highest risk level to the lowest risk level for that factor).

A facilitator guided the experts through each assessment but it was very difficult for the experts to think in terms of individual factors. It was thought at the time that the elicitation went poorly

enough that the data may not be meaningful. After a critical review of the elicited results three responses were eliminated; one due to no variation in response and two others due to an apparent misinterpretation of the questions in the elicitation process. The results of the remaining six questionnaires are shown in Table 11. The results appear reasonable, but were elicited in terms of the factors and not in terms of the probability of a situation causing an incident. An unexpected result of this elicitation method was that the risk reductions were over estimated. At this point of the tool development it will not be possible to calibrate the scale in any way so that reduction measures calculated with the simulation can be compared to reduction measures calculated with the reduction matrix. The values elicited with the matrix however, may still be meaningful with respects to the other reduction measures estimated in the matrix. Figure 15 presents a comparison of the evaluated measures on a relative scale.

TABLE 11
ELICITATION RESULTS FOR RISK REDUCTION MEASURES

		VTS MANDATORY	REGULATED NAVIGATIONAL AREA	MINIMIZE RADIO INTERFEARENCE	MARINERS TO COMMUNICATE INTENTIONS		MINIMIZE VESSEL WAIVERS	POWER/DISPLACEMENT STANDARDS	SUBSTANDARD SHIP RESTRICTIONS	MANNED ENGINE ROOMS REQUIRED	DENY VESSEL ENTRY	DRUG/ALCOHOL TESTING		ENSURE GAMMING BOAT MEETS VESSEL STANDA	ENSURE EXPERIENCED CREWS
Lower risk due to Low Visibility		30%	19%	49%	57%		40%	32%	30%	16%	21%	12%		23%	33%
Lower Risk due to High Wind		28%	19%	28%	40%		29%	39%	24%	16%	13%	10%		23%	27%
Lower Risk due t High River Stage		36%	29%	42%	59%		33%	63%	40%	25%	26%	18%		27%	33%
Lower risk due to River Zones		35%	33%	41%	45%		31%	35%	28%	11%	13%	10%		33%	26%
Lower Risk due to Traffic Configuration		39%	27%	38%	53%		38%	38%	28%	28%	14%	13%		31%	30%
AVERAGE REDUCTION		34%	26%	40%	51%		34%	41%	30%	19%	18%	12%		27%	30%
RANK		4	9	3	1		4	2	6	10	11	12		8	6

To refine the risk reduction measure estimated with the matrix, the baseline distribution of the occurrences of OFI's $\underset{\sim}{N}$ was used to weight the responses by calculating an adjusted relative risk with the mean experts response and then multiplying by the number of expected opportunities for each of the 2520 different opportunities. The average reduction of the causal factors for each reduction measure could have been used but, due to the distribution of the number of OFI's occurring in a month it is possible that reducing the risk due to one causal factor like river stage may be more important than reducing the risk due to another causal factor like maneuvering

vessel. In the example just mentioned, a 25 percent reduction in the risk due to river stage should reduce the risk to the river more than a 25% reduction in the risk due to maneuvering vessels. The final ranking of the reduction measures will be presented on a scale with the most effective measure at the top and the least effective measure at the bottom. The other measures were linearly scaled based on their relative effectiveness.

ESTIMATED RELATIVE EFFECTIVENESS OF RISK REDUCTION MEASURES
LOWER MISSISSIPPI RIVER RISK MANAGEMENT STUDY 6-9-95

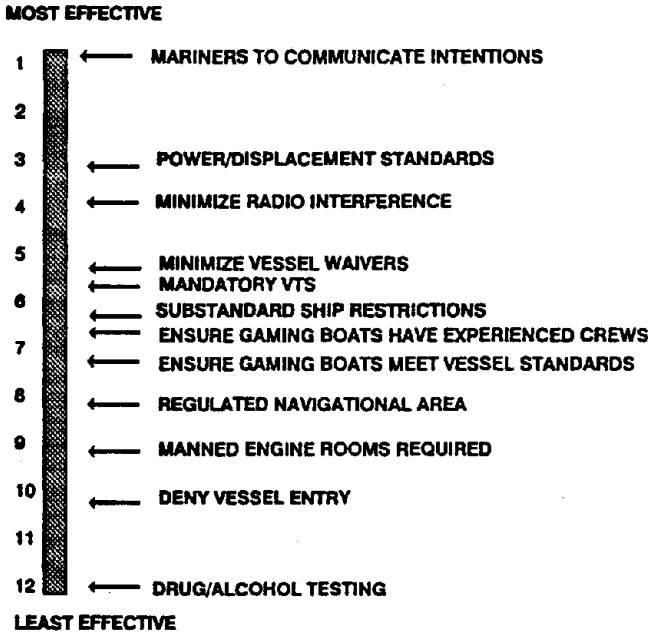

Figure 16. Comparisons of the Effectiveness of Suggested Risk Reduction Measure.

3. CONCLUSIONS AND RECOMMENDATIONS

The Phase II study produced three important results: (1) it creates the ability to quantify the risk of operational scenarios and the effect of risk mitigation interventions, (2) it provides an integrated systems perspective of the factors that affect risk on the river, and (3) it provides a risk profile of the river, showing how often high risk states occur.

The Phase II analysis was guided by the Coast Guard and Port of New Orleans desire to obtain answers to the following specific policy questions:

1. What if any operating restrictions should be imposed on the gaming boats?
    a. Should the boats be required to cruise or should they be held dockside?
    b. Should the number of boats and the excursion routes of the boats be regulated by the Coast Guard for safety purposes?
2. What is the risk of operating during high water conditions?

3. Which proposed waterways management initiatives and system interventions will provide effective risk mitigation?

By manipulating the values of the parameters of the simulation, incident probabilities and risk values may be estimated. The contribution of causal factors to risk states may be demonstrated and the risk reduction that may be achieved by proposed risk mitigation measures may be predicted.

The two most critical risk measurements are the (1) the average incident probability on the river, and (2) the peak incident probability level.. The average risk level on the river is estimated by estimating the probability of an incident per ship transit through the port of New Orleans. This probability is estimated to be approximately 12.6 times the base (or minimum) risk level.. The peak level of risk is determined by the coincidental confluence of risk factors. During a peak period, the probability of incident per ship transit is estimated to be 4,492 times the base rate. This maximum possible risk state is caused by multiple vessels underway between Gretna and Algiers point during high water and low visibility conditions. This state should not occur under current traffic management policies and river piloting procedures. However, risk states with relative values of over 1,000 occur relatively frequently. The distribution of risk states, as described in Section II is sharply peaked (most states are low risk states) with a long, thick tale (the probability of a high risk state occurring is significant). The simulation shows that river traffic is typically in one of the relatively low risk states.

By varying one risk factor while holding the values of the others constant, the contribution of changes in each factor to the overall risk can be measured and predicted. These results obtained from the simulation model apply to the Lower Mississippi river from mile 80 to 106.

- At High River Stage > 14ft. it is expected that 9.39 times more collisions will happen than at 0-8 ft. The river is in this stage only 8% of the time, but 42% of reportable incidents occur when the river stage is > 14'

- At 8-14ft. River Stage it is expected that 3.03 times as many incidents will occur than at 0-8ft.

- An increase of 25% in traffic as compared to 1993 levels will increase the expected number of incidents 37%, from 2.27/month to 3.12 per month in the Port area.

- A gaming vessel leaving the dock and heading eight miles north turning around and heading eight miles south returning to mile 94 can expect to be in 60 times as many incidents as a vessel remaining dockside at mile 94 for the same amount of time.

- A gaming vessel leaving the dock and heading eight miles south turning around and heading eight miles north returning to mile 94 can expect to be in 95 times as many incidents as a vessel remaining dockside at mile 94 for the same amount of time.

- A gaming vessel heading primarily south and returning to mile 94 can expect to get in 58% more incidents than a gaming vessel heading north and returning.

- Adding three gaming vessels to the lower Mississippi river each vessel traveling for two hours three times a day will increase the expected number of incidents 20% from 2.24 incidents/month to 2.69 incidents per month.

Risk mitigation measures were tested using both the simulation and functional deployment methodologies described above. The simulation shows that proposals to keep gaming boats dockside during periods of high water will decrease the level of risk to the boats by a factor of 50 to 100. The proposals to require boats to cruise upriver from Poydras Street rather than downriver was shown to produce a significant level of risk reduction as was the proposal to restrict the number of gaming boats cruising at any time. The simulation shows that existing policies and piloting procedures prevent many high risk states from occurring. For example, river traffic stops during periods of low visibility and the Coast Guard enforces one way traffic during periods of high water. The simulation also shows, however, that the current operating procedures of the traffic lights when the river stage is in the 8-12' range may produce higher risk states than would otherwise occur if two way traffic were allowed. The risk of the additional congested conditions outweighs the risk avoided by minimizing meeting situations under these conditions.

The functional deployment matrix technique was used to evaluate the relative effectiveness of risk reduction interventions that could not be tested using the simulation. The five most effective interventions were determined to be:

Improve communications between vessels to ensure that mariners are communicating their intentions in a timely and accurate manner to the vessels. Traffic congestion sometimes produces situations where mariners are unsure of which vessel is responding to their call and occasionally a mariner will encounter a vessel that does not respond or responds improperly.

Implement vessel displacement/horsepower requirements to prevent under powered tows from becoming hazards to navigation, particularly during high water conditions.

Minimize radio interference from shore based transmitters (e.g. cellular phones, taxi cab radios, etc) by obtaining more frequency bandwidth for maritime use and by vigorously enforcing regulations intended to minimize interference.

Minimizing Coast Guard wavers which may permit vessels with known operational or mechanical deficiencies to enter or leave the port.

Providing mandatory vessel traffic control through a Coast Guard operated Vessel Traffic System.

Although the implementation of a mandatory VTS was not among the top three mitigation measures, it should be noticed the a VTS will provide significant enhanced marine communications capability which addresses two of the top three mitigation measures.. More importantly, a VTS will insure that the high risk states that now occur too frequently are avoided through effective traffic management. The simulation shows for example that proper spacing of vessels and and control of vessel movements during periods of high river stage, can significantly reduce the risk.

Six recommendations for minimizing the risk of high capacity passenger vessel operations in the Port of New Orleans follow from these conclusions:

1. Gaming boats should not be underway during periods of high water. The risk level on the river is greatest during periods of high river stage. The risk starts to significantly increase when the river stage is greater than 10'.

2. The Captain of the Port should control gaming boat sailing schedule and cruising routes in order to minimize traffic congestion. No more than one gaming vessel at a time should cruise the portion of the river between Poydras Street and Algiers point at a time. The gaming boats should be encouraged to cruise upriver from mile 94.

3. The Coast Guard, at both the national and the regional level, should vigorously pursue with the Federal Communications Commission the improvement of maritime radio frequency access and control. Adequate bandwidth should be obtained and vigorous enforcement of violations of existing regulations should be required.

4. Improved vessel traffic management for the port of New Orleans should be supported. For example, procedures for vessel spacing to reduce traffic density should be investigated.

5. The Coast Guard and the Port of New Orleans should ensure that response plans and resources are adequate to deal with a casualty involving a high capacity passenger vessel. Although the probability of an incident involving a high capacity passenger vessel can be minimized, the only way to minimize the potential impact of such an event is to invest in the resources and planning required to effectively respond to such a casualty.

6. Traffic management in the Port of New Orleans should be enhanced in the short term by providing the Governor Nicholls and Gretna Light Towers with better vessel tracking and logging capabilities and additional operational authority and discretion. The operators should, for example, have the ability to slow traffic down to avoid congestion at Algiers point and to allow two-way traffic when, in their opinion, moving vessels is safer than delaying them. In the near term, the USCG and the Port of New Orleans should strongly support the implementation of the Lower Mississippi River Vessel Traffic System.

The results and recommendations of this study are, of course, based on the methodologies employed. The limitations of these methodologies should be considered when interpreting the

results and in the design of any follow on studies or projects. The simulation methodology provides a limited capability of providing confidence intervals to the point estimates made. These confidence intervals, like the results themselves, depend upon the basic assumptions coded into the simulation. The only way of testing the validity of these underlying assumptions is to attempt to replicate historical data with the simulation as was done in this analysis. The elicitation procedure for evaluating risk reduction measures provides only a relative risk reduction metric and is not calibrated against the risk reduction predictions made by the simulation. It is, therefore, difficult to use these relative risk reduction estimates as the basis for a cost benefit study. The results of this study are, however, extensive and unique. They withstand the comparison with historical accident and incident data and the reality check of the maritime experts who participated in the surveys and interviews.

REFERENCES

Camerer, C.F. and H. Kunreuther. 1989 "Decision Processes for Low Probability Events: Policy Implications, Journal of Policy Analysis. pp. 565-592.

Cooke,R.M. 1991. Experts in Uncertainty: Expert Opinion and Subjective Probability in Science, Oxford University Press.

Covello, V.T. 1987. Decision Analysis and Risk Management Decision Making: Issues and Methods. Risk Analysis 7:2, 131-138.

Grabowski, M, J. Harrald and T. Mazzuchi, 1994. Draft Final Report: Vessel Operations Risk Analysis

Harrald, J.R., T. Mazzuchi, and C.M. Stone. 1992. "Risky Business: Should We Believe in Port Risk Assessments?" Proceedings, PORTS 92. The Sixth Special Conference on Ports Sponsored by the American Society of Civil Engineers. Seattle, WA. pp. 657-669.

Harrald, J.R. C. Stone, V. Bagal, and S. Al-Hajj. 1992. Final Report: Second International Marine Safety Workshop. George Washington University Research Report.

Harrald, J.R., B. Muskovitz, R. Salem, V. Bagal, and K. Harrald 1991. Final Report: International Marine Safety Workshop. George Washington University Research Report.

Howard, R.A. " Knowledge Maps" Management Science 35:8. 1989. pp. 903-922.

Hauser, John R.and Clausing, D., "Harvard Business Review", vol. 66, no. 3, May-June 1988 pgs. 63-70

Louisiana State University, 1981. Lower Mississippi River Safety Study. Baton Rouge, LA.

Maio, D., Ricci, R., Rossetti, M., Schwenk, J., and Liu, T., 1991. Port Needs Study--Vessel Traffic Services Benefit. Report No. DOT-VNTSC-CG-91-2.I, DOT-VNTSC-CG-91-2.II, Pt. 1, DOT-VNTSC-CG-91-2.II, Pt. 2, and DOT-VNTSC-91-1.III. Prepared by John A. Volpe National Transportation Systems Center for US Coast Guard (USCG). Washington, DC.

Mitroff, I.I. and T. Pauchant. 1990. We're So Big and Powerful Nothing Bad can happen to us. Birch Lane Press.New York.

National Research Council (NRC). 1990. Crew Size and Maritime Safety. Washington: National Academy Press.

National Research Council. 1981 Commercial Maritime Information: A Critical Appraisal. National Academy Press.

Oliver, R. M. and J. Q. Smith, 1990. Influence Diagrams, Belief Networks, and Decision Analysis, John Wiley and Sons, Chichester,

Perrow, C. 1984. Normal Accidents: Living with High Risk Technologies. New York: Basic Books,

Saaty, Thomas L. 1980. The Analytic Hierarchy Process. New York: McGraw Hill.

Saaty, Thomas L. 1982. Decision Making for Leaders. Belmont CA; Lifetime Learning Publications.

Roeleven, Duko 1992. Modeling the Probability of Accident for Inland Waterway Transport:, Thesis, Delft University of Technology.

U. S. Coast Guard. 1973 Vessel Traffic Systems Analysis of Port Needs. Washington, D.C.

U.S. Coast Guard, Eighth Coast Guard District. 1993. Waterways Analysis and Management Study of the Lower Mississippi River.
New Orleans, LA.

U.S. Coast Guard, Eighth Coast Guard District, 1993. Post Exercise Report, SAREX 94. New Orleans, LA

U.S. Army Corps of Engineers, 1990. The Port of New Orleans. Port Series Number 20

U.S. General Accounting Office, 1992 Coast Guard: Progress in the Marine Safety Network, but Many Uncertainties Remain. GAO/RCED-92-206.

U.S. Congress, Subcommmittee on Coast Guard and Navigation, Field Hearing on USCG "Operation Safe River" and Related navigational Safety Issues on the Lower Mississippi River. Prepared Statements by RADM J.C. Card, and George Duffy.

Van Noortwijk, J.M., R. Dekker, R. M. Cooke, and T. A. Mazzuchi, 1992. "Expert Judgment in Maintenance Optimization", IEEE Transactions on Reliability.

Wenk, Edward, Jr. 1986. Tradeoffs: Imperatives of Choice in a High Tech World. Johns Hopkins University Press, Baltimore, Md.

APPENDIX A
PHASE I SITUATIONAL RISK MODEL

In Phase I, the the relationship between these external risk variables and the probability of a vessel incident was postulated to be described by a loglinear regression equation. A similar model has been used by Roeleven (1992) in a study of the risk on inland waterway transportation in The Netherlands. Due to the scarcity of data, both the model building and the parameter estimation were based on expert judgement.

Based on several rounds of discussion with maritime experts, it was concluded that the probability of a vessel incident was a function of mainly five variables: VISIBILITY, WIND, RIVER LOCATION, RIVER STAGE and TRAFFIC SITUATION. The significant ranges of these variable were obtained from maritime experts and are presented for the first four variables in Table A.1.

TABLE A.1
SITUATIONAL RISK VARIABLES AND THEIR RANGES
OBTAINED FROM EXPERT ELICITATIONS.

		ASSIGNED VALUE		
VARIABLE NAME	VARIABLE	1	2	3
VISIBILITY	X_{vis}	>.5 mile	<.5mile	
WIND	X_{wind}	< 25 mph	> 25 mph	
RIVER STAGE	X_{stage}	< 8 ft.	8 - 14 ft.	> 14 ft.
RIVER POSITION	X_{pos}	80 - 92	92 - 97	97 - 106

The variable TRAFFIC SITUATIONS was described by 28 dual vessel situations and the possible presence of a crossing vessel, where the vessels are operating within 1/2 miles of each other. Vessels were grouped into classes consisting of Shallow Draft Passenger Vessel (SDPAS), Tug with Tows (TWTOW) or tugs with less than 5 barges, Deep Draft Vessels (DDRFT), Line Haul Tows (LINHL) or tugs with more than 5 barges, Vessels were further classified as traveling up river (UP) or down river (DOWN),.. The dual vessel traffic situations considered are given in Table A.2. These situations are presented in rank order from least likely to produce a vessel casualty to most likely to produce a vessel casualty. The assigned values for these traffic situation variable, X_{sit}, for the regression equation were from 0.1 to 2.8. Thus, the traffic situations were considered as one variable with 28 different values of risk. In addition, an indicator variable, X_{man}, was used to denote the presence or absence of a crossing vessel.

TABLE A.2
DUAL VESSEL TRAFFIC SITUATIONS

VESSEL 1	DIRECTION	VESSEL 2	DIRECTION
SDPAS	UP	SDPAS	UP
TWTOW	UP	SDPAS	UP
TWTOW	UP	TWTOW	UP
DDRFT	UP	SDPAS	UP
DDRFT	UP	DDRFT	UP
DDRFT	UP	TWTOW	UP
SDPAS	DOWN	SDPAS	DOWN
TWTOW	DOWN	SDPAS	DOWN
TWTOW	DOWN	TWTOW	DOWN
DDRFT	DOWN	SDPAS	DOWN
DDRFT	DOWN	DDRFT	DOWN
DDRFT	DOWN	TWTOW	DOWN
SDPAS	UP	SDPAS	DOWN
TWTOW	DOWN	SDPAS	UP
TWTOW	UP	SDPAS	DOWN
LINHL	DOWN	SDPAS	DOWN
LINHL	DOWN	TWTOW	DOWN
TWTOW	UP	TWTOW	DOWN
DDRFT	DOWN	SDPAS	UP
DDRFT	DOWN	TWTOW	UP
DDRFT	DOWN	LINHL	DOWN
DDRFT	UP	SDPAS	DOWN
DDRFT	UP	TWTOW	DOWN
LINHL	DOWN	LINHL	DOWN
DDRFT	UP	DDRFT	DOWN
LINHL	DOWN	SDPAS	UP
LINHL	DOWN	TWTOW	UP
DDRFT	UP	LINHL	DOWN

The the relationship between these external risk variables and the probability of a vessel incident was postulated to be described by the equation

$$P(X_{vis},X_{wind},X_{stage},X_{pos},X_{sit},X_{man}) = \delta \cdot p_1 \cdot e^{-\sum_{i=1}^{21} \beta_i \cdot X_i} \qquad (1)$$

where $X_1 \equiv X_{vis}$, ..., $X_6 \equiv X_{man}$, $X_7 \equiv X_{vis}*X_{wind}$, ..., $X_{21} \equiv X_{sit}*X_{man}$, δ indicates random error, and p_1, β_i, $i = 1, ...,21$ are unknown parameters.

The use of expert judgment in parameter estimation was facilitated by noting that the β parameters could be directly estimated via a log regression of expert responses on the relative probability of vessel incidents from sets of comparisons of different situations. Eliciting expert judgments on a relative scale is possible without eliciting the actual probability of a vessel incident due to the fact that the ratio of the probability of vessel incident in the situation explained by the vector $\underset{\sim}{X}$ as compared to the situation described by the vector $\underset{\sim}{X}^*$ is given by

$$\frac{P(X_{vis}, X_{wind}, X_{stage}, X_{pos}, X_{sit}, X_{man})}{P(X^*_{vis}, X^*_{wind}, X^*_{stage}, X^*_{pos}, X^*_{sit}, X^*_{man})} = \frac{\delta}{\delta^*} \cdot e^{-\sum_{i=1}^{21} \beta_i \cdot (X_i - X_i^*)}$$

It follows that, taking the logarithm of both sides of the equation yields

$$\ln\left[\frac{P(X_{vis}, X_{wind}, X_{stage}, X_{pos}, X_{sit}, X_{man})}{P(X^*_{vis}, X^*_{wind}, X^*_{stage}, X^*_{pos}, X^*_{sit}, X^*_{man})}\right] = \ln\left[\frac{\delta}{\delta^*}\right] - \sum_{i=1}^{21} \beta_i \cdot (X_i - X_i^*)$$

which is in the standard form of the linear regression model.

In order to estimate the model parameters, seventy two questions similar to the following were asked of 11 substantive experts with a deep and current knowledge of the Lower Mississippi River.

In the following sets of comparisons, circle one number per comparison on the side of that scenario which you consider to be more likely to result in a vessel collision. If you think that the scenarios are equally likely to produce a collision, then circle 1. Otherwise indicate the relative magnitude or degree of increase in likelihood on the side of the scenario most likely to produce a collision.

visibility	< 0.5		visibility	< 0.5
wind	< 25		wind	< 25
river stage	< 8		river stage	>14
position	80 - 92		position	80 - 92
situation		9 8 7 6 5 4 3 2 1 2 3 4 5 6 7 8 9	situation	
vessel 1	DDRFT		vessel 1	DDRFT
direction	UP		direction	UP
vessel 2	LLINE		vessel 2	LLINE
direction	DOWN		direction	DOWN
manuvering	YES		manuvering	YES

Notice that for the above comparison, only the attribute RIVER STAGE changed from less than eight feet to greater than fourteen feet. In each comparison only a single variable value was changed in an effort to make the comparisons as easy as possible for the experts.

Due to the number of possible permutations of the situational variables it was not possible to ask the experts for every possible comparison. Thus, experimental design techniques had to be used to define a relatively small number of comparisons which could be asked and still allow for the estimation of all unknown parameters. The parameter p_1 is factored out due to taking ratios and had to be estimated using other methods. Because p_1 is more or less a scale factor, only relative probabilities were available in Phase I.

The regression analysis on the expert judgment is reported in Phase I. The analysis concluded that based on the judgments of maritime experts, only 7 of the 21 variables postulated were significant in describing accident probabilities. Once the regression equation parameters were estimated, the relative accident probability for every possible combination of external variables was evaluated and ranked.

APPENDIX B
MODIFICATIONS OF THE PHASE I SITUATIONAL RISK MODULE

Accounting for Single Vessel Incidents

In Phase II it was realized that while proper information had been elicited for all the dual vessel traffic situations, about 80 to 85% of the time vessels are operating on the river without another vessel within a half mile. Thus the model had to be extended to include single vessel accident probabilities or the probability of allsion. Table B.1 describes the seven single vessel traffic situations that were added in Phase II.

TABLE B.1
SINGLE VESSEL TRAFFIC SITUATIONS

VESSEL 1	DIRECTION
SDPAS	UP
TWTOW	UP
DDRFT	UP
SDPAS	DOWN
TWTOW	DOWN
DDRFT	DOWN
LINHL	DOWN

These were accounted for in the traffic situational vector by allowing adding a fifth definition of NONE to the vessel 2 category.

Assigned values for the regression equation for these single vessel situations were estimated using historical collision and allision data. Not only is the total number of incidents known from historical data from mile marker 80 - 106, but the ratio of collisions to allision's is also known. Using this ratio it is possible to balance the risk between the dual and single vessel cases, through a vessel situation factor κ which gets subtracted from the situational variable score in the single vessel cases. Only situational vectors $\underset{\sim}{X}$ that have identical vessel types and directions for vessel 1 and vessel 2 are used to calculate the single vessel RIP's. Index variable I_1 is introduced to the Phase I model to account for single and dual risk states.

Use of Incident Data for Scaling Expert Judgment:

Another problem encountered in the use of expert judgment is the intrduction of scale bias. Experts were asked to give relative differences of probability of a collision given different situations on a fixed scale. Thus an individual may have circled a 2 not only due to his judgment of the probability of getting into a collision but also based on the maximum possible value offered being 9. It is often possible to avoid scale biasing by letting the expert pick his own scale, but this tends to further confuse an already difficult elicitation. This situation can be corrected with historical incident and river stage data by accounting for a scale bias factor γ. In the lower Mississippi there is a significant and measureable difference in the probability of getting in a incident at low medium and high river stage. This statistical information can be used to estimate

γ. Where sufficient data exists it may often be preferable to use the data to adjust the scale bias thus making it easier for the experts to answer the questionnaire. The final form of the equation for the probability of an incident given one OFI of some type then becomes:

$$P(X_{vis}, X_{wind}, X_{stage}, X_{pos}, X_{sit}, X_{man}) = p_1 \cdot \theta \, e^{-\gamma \sum_i \beta_i \cdot \left[(1-I_1)X_i + I_1(X_i - \kappa)\right]}$$

where $I_1 = \begin{cases} 1 & \text{if } \underset{\sim}{X} \text{ corresponds to a single vessel traffic situation OFI} \\ 0 & \text{otherwise} \end{cases}$

γ = scale bias factor
κ = situational factor
θ = constant to set $OFI_1 = 1$

Data on the number of incidents in New Orleans was provided by the USCG Marine Safety Office (MSO) in New Orleans. The information came in two data bases. Collisions per river mile were compiled from 1982-1991. From river Miles 80 - 106 there was an average of 15.6 collisions per year. Allision's per mile marker from miles 91 through 101 over 1982-1991 were also available through the MSO. The average number of allisions per mile per year over this stretch (discounting allisions due to vessels that were attempting to dock) was .445 allision's per mile per year. Assuming that the number of allisions over the 26 mile length is approximately constant the average number of allision's per year over the entire 26 miles is 11.6 allisions per year.

The ratio of allisions to collisions per year can be used to calculate the difference in risk between single and dual vessel risk cases with the following assumptions.

Assume;

1) P(Allision|single vessel OFI) = $\frac{1}{2}$ P(Allision|Dual vessel OFI) given the same vessel types and weather conditions.

2) $E(P(\text{Collision}|\text{dual vessel OFI})) = \frac{E(\#\text{collisions per month})}{E(\#\text{dual vessel OFI's per month})}$

3) E(P(Allision|single vessel OFI))*E(single vessel OFI's per month) + E(P(Allision|dual vessel OFI)) * 2 E(dual vessel OFI's per month) = E(# Allision's per month)

From the simulation, the E(# single vessel OFI's per month) is 465180 and the E(# dual vessel OFI's per month) is 115311. Solving for the expected probability of collisions yields;

$$E(P(\text{Allision}|\text{single vessel OFI})) = 1.39\ E^{-6}$$
$$E(P(\text{Collision}|\text{dual vessel OFI})) = 1.13\ E^{-5}$$

The expected number of incidents due to dual states can be expressed as follows;

E(# incidents due to dual vessel OFI's) =
E(P(Collision|dual vessel OFI)) * E(#dual vessel OFI's per month) +
E(P(Allision|single vessel OFI)) * 2 E(dual vessel OFI's per month)
= 1.62 incidents per month

E(# incidents due to single vessel OFI's) =
E(P(Allision|single vessel OFI))*E(single vessel OFI's per month)
= .646 incidents per month

The ratio in the total relative probability of an incident due to dual states versus single vessel OFI's that is predicted from historical data is;

$$\frac{\text{E(\# incidents due to dual vessel OFI's)}}{\text{E(\# incidents due to single vessel OFI's)}} = \frac{1.62}{.646} = 2.5 = \frac{\sum_{i=1}^{2520} E[N_i]P_i(1-I_1)}{\sum_{i=1}^{2520} E[N_i]P_i I_1}$$

where I_1 = 1 if the OFI type is a single vessel OFI and 0 otherwise.

Another useful data source is the number of collisions over the river from mile 0 to 235 at different river stages. From 1983 - 1990 data was collected by month on the number of incidents on the river. The average river stage over the months is known from the Army Corps of Engineers data and can be directly correlated to the incident data.

TABLE B.2
RIVER STAGE AND EXPECTED NUMBER OF INCIDENTS COMPARISONS

RIVER STAGE	% TIME IN STAGE	# OF INCIDENTS AT STAGE	NORMALIZED PROBABILITY OF ACCIDENT
< 8FT.	59%	33	1.00
8-14 FT.	33%	56	3.03
> 14FT.	8%	42	9.39

The final column says that it is expected that 9.39 times as many collisions will take place in a given time period with high river stage when compared to the same time period with low river stage. It also says that 3.03 times as many incidents will happen for a given time period at 8-14ft. as opposed to below 8ft. for a given time period.

The expected number of OFI's in a typical month was generated by running 30 months of simulated data with typical inputs. The simulation generated the $\underset{\sim}{N}$ vectors and an Excel spread sheet was set up to allow the easy manipulation of the scale bias factor and situational factor until the expected number of collisions caused by dual vessel states was 2.5 times as high as single vessel states. If the situational ratio was within .01 the error was considered acceptable and a regression on the square of the difference of the normalized relative risk was performed to

determine the optimal γ (scale bias factor) and κ (situational factor). The final values are shown on the following sheet:

TABLE B.3
SCALE BIAS, SITUATIONAL, AND OFI FACTORS

FACTOR/ATTRIBUTE	VALUE
γ scale bias factor	1.4
κ situational factor	3.94
θ OFI factor	6.98
p_1 Prob. of Incident OFI_1	2.43 E^{-7}

APPENDIX C
SIMULATION MODULES

Weather data was available from two sources. Wind and visibility data was purchased from NOAA. River stage data was provided by the Army Corps of Engineers and included 13 (1981 - 1993) years of daily readings from the New Carlton Gauge. Both sets of data were analyzed to determine the appropriate updating model for the simulation.

One month was chosen as the period of time over which to collect the sums of OFI's and incidents. The main reason for this is that incident data is collected and reported monthly. The results from the simulation should be collected and reported in the same format as actual data so the experts interpreting the output from the simulation can compare the results generated in a format in which they are comfortable.

River Stage Model

In the initial data analysis it was determined that from 1981-1993 the river was in high river stage > 14 ft. eight percent of the time, in medium river stage 8 - 14 ft. thirty three percent of the time, and in low river stage < 8 ft. fifty nine percent of the time. One approach to assigning the river stage to the situational risk calculations is to generate a random number and assigning a new stage height every time the vessel positions are updated or every thirty seconds. This is not an appropriate way to generate river stages. The river rises and falls very slowly and it is rather common place to have two or three months with every day below 8ft. river stage. If every thirty seconds the simulation picks a new river stage then at the end of every month the amount of time spent at low, medium and high river stage will be very close to 59%, 33%, and 8%. We are however, interested in how dangerous a typical month can get and would like to have some of the months have a high river stage almost every day. The following analysis was performed to ensure a realistic transition of the stage values.

For all 13 years of data the first day in the year was inspected and it was determined if that day was at low medium or high river stage. Then the river stage four days later (96hrs.) was inspected and it was again determined whether the river was at high medium or low river stage. Data was tabulated for each of the stage levels over all fourteen years generating 1274 samples. The summaries are shown below.

TABLE C.1
The Percentage of Time Spent At Each River Stage

STAGE DATA	Number of Times at stage	Percentage of Time at Stage
Stage 1 (< 8ft.)	755	59%
Stage 2 (8 - 14ft.)	415	33%
Stage 3 (> 14ft.)	104	8%
Total # of Samples	1274	

When the initial starting state is considered and the probability of transitioning into another state tabulated, the resulting data can be expressed in terms of a transition matrix. Initially in this process a Dirichlet distribution on each row of the transition matrix with parameters $\alpha_{ij} = .1$ where $i = (1,2,3)$, and $j = (1,2,3)$ was defined (7).

$$f(p_{ij}|\alpha_{ij}) = \frac{\Gamma(\alpha_{1j} + .. + \alpha_{3j})}{\Gamma(\alpha_{1j})..\Gamma(\alpha_{3j})} p_{1j}^{(\alpha_{1j}-1)} .. p_{3j}^{(\alpha_{3j}-1)} \quad \text{for a fixed } j = (1,2,3)$$

The posterior distribution $f(p_{ij}|\alpha_{ij}^*)$ has a closed form dirichlet distribution with parameters (8),

$$\alpha_{ij}^* = \alpha_{ij} + \sum_{k_i = 1}^{\text{No. at Stage}} \text{(Number of transitions from stage i to stage j)}$$

By doing this the actual probability of transitioning from stage 1 to stage 3 in four days is not really 0 but a small number like .001. Below is a summary of the transitions and the transition matrix used in the simulation.

TABLE C.2
FOUR DAY INTERVAL STAGE TRANSITION DATA 1981-1993

TRANSITION DATA	Stage 1	Stage 2	Stage 3
Stage 1	720	35	0
Stage 2	35	367	13
Stage 3	0	13	91

TABLE C.3
FOUR DAY INTERVAL STAGE TRANSITION PROBABILITIES

TRANSITION MATRIX	Stage 1	Stage 2	Stage 3
Stage 1	95%	5%	0%
Stage 2	8%	88%	3%
Stage 3	0%	13%	88%

It should also be mentioned that the transition matrix was only used for the baseline run for the actual distribution of incidents in a month. The amount of time the simulation has to be run is very long when using the transition matrix because of the length of time it takes to transition from one state to another. For example, the expected amount of time spent in stage one, given that stage one was just transitioned to, is 52 days. Many of the regular runs are done without utilizing the transition matrix and picking a new stage every four days with the base rate probabilities of 59%(<8ft.), 33%(8 - 14ft.) and 8%(>14ft.). This approach is fine as long as the summary statistics are presented only on the bounds of the **mean expected number of incidents in a month** and not on the actual distribution of incidents in a month.

River Velocity Model

Every time the river stage was set the river velocity was also adjusted. Data for mean river velocity at stage was taken from Army Corps of Engineers data compiled from observations from 1941-1974. The data is simply mean surface velocity and is not adjusted in the simulation for slow and fast flowing sections of the river. For low stage (<8ft.) the river velocity is set at 3.0 mph. This velocity actually occurs at 6ft. At medium river stage (8 - 14ft.) the river velocity is set at 4.0 mph and this velocity actually occurs at 12.0 ft. At high river stage (>14ft.) the river velocity is set at 5.5 mph and this velocity actually occurs at 17 ft.

Visibility Model

As stated earlier wind and visibility data was purchased from NOAA and compiled for use in the simulation. The original questionnaire that was used to elicit expert judgment presented states with visibility above and below 1/2 a mile. The summary statistics for 1/2 mile visibility are shown below. The first traffic data that was collected was in December 1993 through September 1994. For this reason the average visibility of 1994 was used to estimate the percentage of hours in which the visibility was below .5 miles. A spread sheet was used to calculate the percentage of hours with visibility below .5 miles for every hour in every month. Their variation between months was small enough that it was felt the simulation could be run with the average monthly visibility values. Visibility runs in streaks and it was determined from inspection that changing the visibility every four hours would be appropriate. The average percentage of hours with visibility less than .5 miles at the New Orleans International airport was also calculated in a spread sheet and the values used in the simulation are 0-4 hrs. = 23%, 4-8 hrs. = 45%, 8-12 hrs. = 26%, 12-16 hrs. = 12%. 16-20hrs. = 11%, 20-24 hrs. = 12%.

TABLE C.4
% HOURS WITH VISIBILITY LESS THAN .5 MILES

	24 HOUR CLOCK TIME																							
% < .50 Miles	1	2	3	4	5	6	7	8	9	10	11	12	13	14	15	16	17	18	19	20	21	22	23	24
Jan. 94	29	32	32	29	29	29	29	45	42	32	32	29	23	19	19	23	19	13	16	16	16	19	23	32
Feb. 94	21	36	32	43	43	43	46	82	75	57	43	25	7	11	7	14	18	14	11	11	25	29	32	29
Mar. 94	23	32	35	39	45	48	55	68	65	45	32	23	23	13	6	6	6	10	10	3	3	10	13	29
Apr. 94	33	37	37	43	37	50	67	60	53	20	7	3	3	7	10	3	7	3	3	0	0	3	13	13
May 94	16	29	39	45	48	66	81	71	45	29	19	23	19	13	16	6	10	16	19	19	13	16	6	3
Jun. 94	10	13	13	13	16	55	55	48	19	10	3	6	6	23	16	10	6	10	10	6	3	6	10	6
Jul. 94	0	0	3	3	3	16	65	29	13	16	13	10	16	23	16	16	10	6	10	6	3	3	6	0
Aug. 94	10	10	10	6	19	23	65	58	35	16	19	19	19	13	10	13	13	6	13	10	6	3	6	6
Sep. 94	0	3	3	3	10	30	77	53	30	17	13	7	0	0	0	3	10	13	20	13	3	7	7	7
Oct. 94	16	26	23	23	29	42	61	61	29	26	19	19	16	19	26	19	19	16	28	10	13	13	10	19
Nov. 94	17	20	27	27	27	27	27	37	30	23	17	3	0	0	0	0	0	3	0	0	0	7	17	20
Dec. 94	32	39	45	45	45	45	48	68	58	32	19	16	10	13	16	13	10	13	10	10	16	13	16	23

The traffic logs from the Governor Nicholls light tower was analyzed to determine at what value of visibility the traffic actually stopped moving. This value ended up being about 400 Meters or .25 miles. The weather data was then reanalyzed to determine the percentage of hours with visibility below .25 miles and the four hour percentage of hour with visibility less than .25 miles are 0-4 hrs. = 4%, 4-8 hrs. = 7%, 8-12 hrs. = 5%, 12-16 hrs. = 2%. 16-20hrs. = 2%, 20-24 hrs. = 2%. The monthly summary of visibility less than .25 miles is shown below. This data was

TABLE C.5
% HOURS WITH THE VISIBILITY LESS THAN 400M

	24 HOUR CLOCK TIME																							
% < .400M	1	2	3	4	5	6	7	8	9	10	11	12	13	14	15	16	17	18	19	20	21	22	23	24
Jan. 94	13	10	10	10	10	10	10	10	10	6	3	3	0	0	0	3	3	3	0	0	6	10	6	13
Feb. 94	7	11	7	7	4	7	11	21	21	18	7	4	0	0	4	4	0	4	7	4	4	7	14	11
Mar. 94	10	6	10	16	16	16	13	26	19	13	3	6	3	0	3	3	3	6	3	0	0	0	0	6
Apr. 94	0	0	0	0	3	3	10	17	7	0	0	0	0	0	0	0	0	0	0	0	0	0	3	0
May 94	0	0	0	0	0	10	16	13	3	3	0	0	0	0	3	0	0	3	0	0	0	0	0	0
Jun. 94	0	0	0	0	0	0	0	3	0	0	0	3	3	0	0	0	0	0	0	0	0	0	0	0
Jul. 94	0	0	0	0	0	0	0	0	3	3	3	3	3	10	6	6	0	3	0	0	0	3	3	0
Aug. 94	0	0	0	0	0	0	0	6	0	3	3	3	3	6	3	6	3	0	0	0	0	0	0	0
Sep. 94	0	0	0	3	3	3	7	3	10	3	3	0	0	0	0	0	3	7	3	0	0	0	0	0
Oct. 94	3	0	0	3	0	6	6	6	10	0	0	0	3	6	10	6	10	6	6	3	3	10	6	6
Nov. 94	10	10	13	7	3	7	7	13	10	10	0	0	0	0	0	0	0	0	0	0	0	0	3	
Dec. 94	3	10	10	6	13	10	10	19	16	16	0	0	0	3	6	3	6	6	3	3	10	6	3	3

used to determine when the traffic actually stops and the .5 mile visibility data was used to set the risk state. Every four hours the visibility is checked by generating a random variable and selecting the appropriate state, below .25 miles visibility, in between .25 and .5 miles of visibility, and over .5 miles of visibility. If the visibility is less than .25 miles then arrivals are not allowed for 4 hours. This allows the river to empty out and simulates the fact that most traffic on the river stops. The visibility is checked one hour before the risk level is changed but the arrival rate is changed immediately. This allows the river to have a chance to empty out before the risk level is increased. Arrival rates will be discussed in depth later in this chapter.

Wind Model

The wind data was tabulated for percentage of hours over 25 mph for each month. The questionnaire did not have a particularly good definition for a 25 mile per hour wind. On subsequent trips to New Orleans the mariners were asked how they interpreted wind above 25 mph and most felt it was average gusts over 25 mph. The data NOAA supplied (because I asked for it that way) was the average wind speed over the hour. When the percentage of hours with wind over 25 mph was calculated, average wind speeds of 20 mph was used and it was assumed that changes of at least 5 mph must have taken place. This is a conservative assumption as an average wind speed of 15 mph can easily produce gusts of 25 mph. The summary statistics exhibit little variation for 1994 and with the exception of June. For this reason the yearly average of .008 probability that the winds exceed 25 mph for an hour was used for all hours in the simulation. The simulation checks wind every hour by choosing a random number and assigning the high wind risk factor if the number is .008 or less.

TABLE C.6
% HOURS WITH WIND GREATER THAN 25MPH

	24 HOUR CLOCK TIME																							
% <.400M	1	2	3	4	5	6	7	8	9	10	11	12	13	14	15	16	17	18	19	20	21	22	23	24
Jan. 94	0	0	0	0	0	0	0	3	0	0	0	0	3	3	6	3	0	0	3	0	3	0	0	0
Feb. 94	0	0	0	0	0	0	0	0	0	0	0	0	4	0	4	4	0	4	0	0	0	0	0	0
Mar. 94	0	0	0	0	0	0	0	0	0	0	0	0	0	3	3	3	0	0	0	0	3	0	0	0
Apr. 94	0	0	0	0	0	0	0	0	0	0	0	0	0	0	0	0	0	0	0	0	0	0	0	0
May 94	0	0	0	0	0	0	0	0	0	0	0	0	0	0	0	0	0	0	0	0	0	0	0	6
Jun. 94	6	6	6	6	6	6	6	6	6	6	6	6	6	6	10	6	6	6	6	6	6	6	6	6
Jul. 94	0	0	0	0	0	0	0	0	0	0	0	0	0	0	0	0	0	0	0	0	0	0	0	0
Aug. 94	0	0	0	0	0	0	0	0	0	0	0	0	0	0	0	0	0	0	0	0	0	0	0	0
Sep. 94	0	0	0	0	0	0	0	0	0	0	0	0	0	0	0	0	0	0	0	0	0	0	0	0
Oct. 94	0	0	0	0	0	0	0	0	0	0	0	0	0	3	0	0	0	0	3	0	0	0	0	0
Nov. 94	0	0	0	0	0	0	0	0	0	0	0	0	0	0	0	0	0	0	0	0	0	0	0	0
Dec. 94	0	0	0	0	0	0	0	0	0	0	0	0	0	0	0	0	0	0	0	0	0	0	0	0

Traffic Model

Traffic rates were the hardest data to calculate and the most analyzed by our team. Data was available from two main sources the Coast Guard Light tower log data and the Army Corps of engineers lock data monthly summaries. Other sources of traffic data (Army Corps of engineers commerce data, and the Crescent Pilots deep draft movement data) mainly corroborated the data in the two main sources. The Light tower logs were only stored on paper media and had to be converted to electronic form to be analyzed. A team member wrote a program to enter and store log data and make summary statistics. One of the most interesting aspects of the data was a rhythm to the traffic passing the Gretna and governor Nichols light towers. The total hourly average for 18 days in December of 1993 for traffic passing the Governor Nicholls tower in four hour periods is shown below:

TABLE C.7
NUMBER OF VESSELS PER HOUR PASSING THE GOVERNOR NICHOLS LIGHT TOWER FOR 18 DAYS IN DECEMBER 1993

	0 - 4 hrs.	4 - 8 hrs.	8 - 12 hrs.	12 - 16hrs.	16 - 20 hrs.	20- 24 hrs.
Up River	1.34	1.38	1.63	1.96	2.36	1.87
Down River	2.15	1.82	2.09	2.16	2.9	2.23
Both Dir's	3.49	3.2	3.72	4.12	5.26	4.1

From the data above it was decided that arrivals to the river would be modeled as a Non-homogeneous poison process with changes in arrival rates occurring every four hours. The rest of the traffic model section supports the arrival rates used in the simulation.

The breakdown of the classes of the vessels passing the tower was also made. In this case tugs with tows were considered to have 6 or less barges, and long line tows were considered to have seven or more. In the initial discussions, when the model was being developed, it was mentioned that LNIHL's did not proceed up river. The initial elicitation for the RIP values was made under this assumption. When the traffic logs were analyzed it was found that the LINHL's proceed both up and down river. Unfortunately the relative risk of upbound LINHL's was not elicited. To make up for the over sight the up bound LINHL's were simply added to the down bound LINHL totals. This left the traffic overall traffic on the river to be correct and minimized the overall error.

The variance of the class of vessels passing the tower was also analyzed and determined not to be significant. The adjusted total arrival rates in table C.8 were used for mile 80 and 106 arrivals for all times.

TABLE C.8
TOTAL NUMBER OF VESSELS PASSING GOVERNOR NICHOLS TOWER IN DECEMBER 1993

	18 Days Up River	18 Days Down River	Monthly Up River	Monthly Down River
DDRFT	236	252	406	434
SDPAS	2	1	3	2
TWTOW	483	653	832	1125
LINHL	32	54	0	148
	753	960	1242	1708

The Army Corps of Engineers Intercostal Waterway data was analyzed and the following summary data for January and December of 1993 was used for arrival data in the simulation.

TABLE C.9
TOTAL NUMBER OF BARGES TRANSITING LOWER MISSISSIPPI RIVER LOCKS IN DEC 93 AND JAN 93

	up 88	down 88	up 92.6	down 92.6	up 98.6	down 98.6
Jan-93	301	335	400	442	242	265
Dec-93	284	398	373	390	203	185
Avg	293	367	387	416	223	226

	0 - 4 hrs.	4 - 8 hrs.	8 - 12 hrs.	12 - 16hrs.	16 - 20 hrs.	20- 24 hrs.
Up River	1.34	1.38	1.63	1.96	2.36	1.87
Down River	2.15	1.82	2.09	2.16	2.9	2.23
Both Dir's	3.49	3.2	3.72	4.12	5.26	4.1

From the data above it was decided that arrivals to the river would be modeled as a Non-homogeneous poison process with changes in arrival rates occurring every four hours. The rest of the traffic model section supports the arrival rates used in the simulation.

The breakdown of the classes of the vessels passing the tower was also made. In this case tugs with tows were considered to have 6 or less barges, and long line tows were considered to have seven or more. In the initial discussions, when the model was being developed, it was mentioned that LNIHL's did not proceed up river. The initial elicitation for the RIP values was made under this assumption. When the traffic logs were analyzed it was found that the LINHL's proceed both up and down river. Unfortunately the relative risk of upbound LINHL's was not elicited. To make up for the over sight the up bound LINHL's were simply added to the down bound LINHL totals. This left the traffic overall traffic on the river to be correct and minimized the overall error.

The variance of the class of vessels passing the tower was also analyzed and determined not to be significant. The adjusted total arrival rates in table C.8 were used for mile 80 and 106 arrivals for all times.

TABLE C.8
TOTAL NUMBER OF VESSELS PASSING GOVERNOR NICHOLS TOWER IN DECEMBER 1993

	18 Days Up River	18 Days Down River	Monthly Up River	Monthly Down River
DDRFT	236	252	406	434
SDPAS	2	1	3	2
TWTOW	483	653	832	1125
LINHL	32	54	0	148
	753	960	1242	1708

The Army Corps of Engineers Intercostal Waterway data was analyzed and the following summary data for January and December of 1993 was used for arrival data in the simulation.

TABLE C.9
TOTAL NUMBER OF BARGES TRANSITING LOWER MISSISSIPPI RIVER LOCKS IN DEC 93 AND JAN 93

	up 88	down 88	up 92.6	down 92.6	up 98.6	down 98.6
Jan-93	301	336	400	442	242	266
Dec-93	284	398	373	390	203	186
Avg	293	367	387	416	223	226

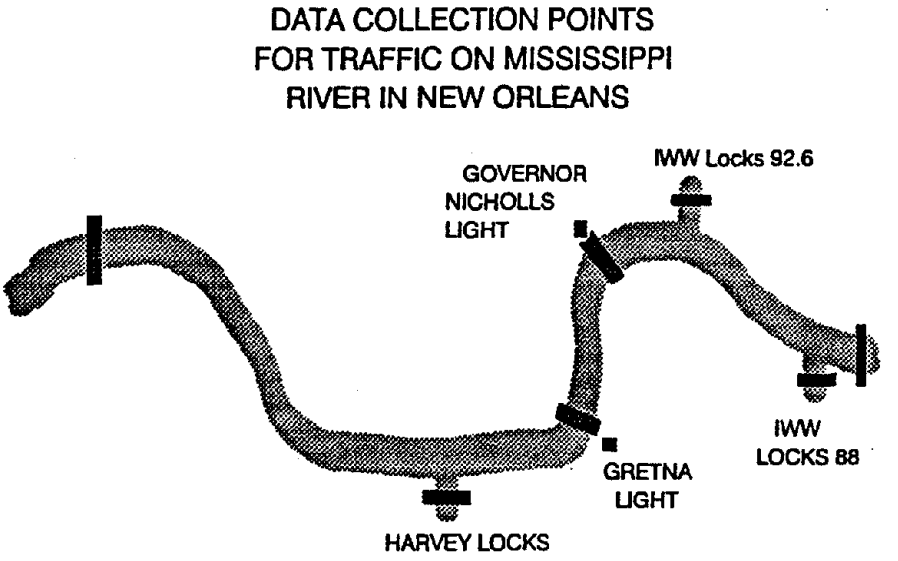

FIGURE C.1 Data Collection Points and Simulation Arrival Points

With all the traffic data available assumptions must be made about the directions of the vessels coming out of the locks and into the river to be able to calculate the average number of vessels arriving at mile 80 and mile 106 on the Mississippi. It is assumed that most of the traffic coming out of the locks at 88 goes up river and out at the locks at 92.6. It is assumed that 88% of the arrivals at 92.6 go down river and out at the locks at mile 88. The remaining 12% continues up the river and leaves at mile 106. The traffic at the Harvey locks mile 98.6 is more evenly split. It is assumed 42% head down river and leave through the 92.6 locks and the remainder head up river and leaves the zone of interest at mile 106. It is also assumed that all traffic in the IWW is due to tugs with tows. These assumptions were made by the normative experts after several observing river operations as a reasonable way to balance the actual traffic patterns on the river.

TABLE C.10
LOCK ARRIVAL DATA AND DIRECTION ASSUMPTIONS

Lock Arrivals	Total	% Up	% Down	# Up	# Down
88	293	100%	0%	293	0
92.6	416	12%	88%	50	366
98.6	222	58%	42%	93	129

It must also be mentioned that 226 extra tugs with tow were generated at mile 106 headed down river to leave at mile 98.6 through the locks to satisfy the December - January 1993 outbound vessel requirements. Solving for all these values left the following arrival totals at mile 80 and 106:

TABLE C.11
ADJUSTED % OF VESSEL CLASS FOR UP AND DOWNBOUND ARRIVALS IN DEC 93 AND JAN 93

River Arrivals	Mile 106	% Class	Mile 80	% Class
DDRFT	433	23.50%	406	34.10%
SDPAS	2	0.10%	3	0.30%
TWTOW	1256	68.30%	781	65.60%
LINHL	148	8.00%	0	0.00%

River experts were asked the average velocities of vessels relative to river current. Velocity is important because the total number of thirty second periods of the types of situations occurring is strongly dependent on how fast the vessels travel the 26 mile river length. The experts were unable to give exact velocities but were able to give ranges of velocities which are summarized below.

TABLE C.12
VELOCITIES IN MPH ASSIGNED TO VESSEL TYPES

CLASS	VELOCITY
SDPAS	9 TO 16
TWTOW	8.5 TO 15
DDRFT	12 TO 19
LINHL	8.5 TO 15

Each time an arrival is generated the class is assigned with one random number and then the velocities are assigned by using uniform distributions from the values listed in the tables above.

The last things to account for are the rhythm of the port and the portion of time that the visibility is less than .25 miles. The fact that 4% of the time arrivals would not be generated because of poor visibility and realizing that the rhythm of the port can be summarized in percent average arrivals per hour where 100% is average and the 4 hour period adjustments are as follows:

TABLE C.13
RHYTHM OF THE PORT IN % AVERAGE ARRIVALS

Rythm	0 - 4 hrs.	4 - 8 hrs.	8 - 12 hrs.	12 - 16 hrs.	16 - 20 hrs.	20 - 24 hrs.
up	76%	79%	93%	112%	134%	106%
down	97%	82%	94%	97%	130%	100%
all	88%	80%	93%	103%	132%	103%

It is then easy to solve for the average number of arrivals per hour remembering that arrivals will only occur for 692.3 hrs. a month because of low visibility. Once the average arrivals per hour

are calculate they are multiplied by the rhythm percentages of average arrivals per hour values and the following 4 hr. period arrival rates for all the arrival zones is calculated. Note, the up and down rhythm values were used for up and down arrivals respectively but, the average rhythm was used for the lock arrivals.

TABLE C.14 ARRIVAL RATE USED IN BASELINE SIMULATIONS

Arrival Rates	avg./hr.	0 - 4 hrs.	4 - 8 hrs.	8 - 12 hrs.	12 - 16 hrs.	16 - 20 hrs.	20 - 24 hrs.
down	2.65	2.561	2.168	2.489	2.573	3.454	2.656
up	1.71	1.304	1.343	1.587	1.908	2.297	1.820
88	0.423	0.371	0.340	0.395	0.438	0.559	0.436
92.6	0.601	0.527	0.483	0.562	0.622	0.794	0.619
98.6	0.320	0.280	0.257	0.299	0.331	0.423	0.330

The reciprocal of number of arrivals per hour can be taken to find the inter arrival time in hours. These are the values that were used in the simulation arrival generators.

TABLE C.15
INTER ARRIVAL TIMES USED IN BASELINE SIMULATION

Inter Arrival times	Avg. hrs.	0 - 4 hrs.	4 - 8 hrs.	8 - 12 hrs.	12 - 16 hrs.	16 - 20 hrs.	20 - 24 hrs.
down	0.377	0.391	0.461	0.402	0.389	0.290	0.377
up	0.585	0.767	0.744	0.630	0.524	0.435	0.549
88.000	2.364	2.697	2.942	2.530	2.285	1.790	2.296
92.600	1.664	1.898	2.070	1.781	1.608	1.260	1.616
98.600	3.125	3.565	3.888	3.345	3.020	2.366	3.035

One last note on the arrival rates. A quick look was taken at the variance associated with the vessel averages passing the light towers. The variance was slightly higher than the mean arrival times in many cases. This would tend to indicate slight clumping. The exponential distribution (Poison Process) has a variance which equals the mean and seems to be a good choice for inter-arrival times for this model.

☆U.S. GOVERNMENT PRINTING OFFICE: 1997 - 500-497/40014